UNIVERSITÉ DU QUÉBEC À MONTRÉAL

CONTROLLABLE SYNTHESIS AND DEVELOPMENT OF ONE-DIMENSIONAL ORIENTED CDS-BASED NANOARRAY PHOTOANODES FOR EFFICIENT PHOTOELECTROCHEMICAL HYDROGEN EVOLUTION

THESIS

PRESENTED

AS PARTIAL REQUIREMENT OF

PH.D. IN CHEMISTRY

BY

ZHIYUAN PENG

MAY 2024

UNIVERSITÉ DU QUÉBEC À MONTRÉAL

SYNTHÈSE ET OPTIMISATION DE PHOTOANODES NANOARRAY UNIDIMENSIONNELLES À BASE DE CDS POUR UNE PRODUCTION PHOTOÉLECTROCHIMIQUE EFFICACE D'HYDROGÈNE

THÈSE

PRÉSENTÉE

COMME EXIGENCE PARTIELLE

DOCTORAT EN CHIMIE

PAR

ZHIYUAN PENG

MAI 2024

ACKNOWLEDGEMENTS

I am honored to finish my Ph.D. study at Faculté des Sciences, Université du Québec à Montréal, Montreal, Canada. I do appreciate everybody who supported and helped me during my Ph.D. journey in any way. First and foremost, I would like to express my deepest gratitude to my project supervisor, Prof. Mohamed Siaj, for his irreplaceable contribution to my Ph.D. study and research. Thank you for giving me such an opportunity to join your group, where I can enrich my scientific horizons and satisfy my intellectual curiosity. Without your systematic guidance, moral support, and encouragement, my research work can not be moved so smoothly and led in the right direction. Studying here is my most valuable experience and allows me to keep moving forward.

Meanwhile, I would like to express my sincere gratitude to the delible contribution from my thesis examining committee members, whose comments and feedback helped to improve the quality of my thesis and gave me some novel inspiration. Special thanks to Prof. Frenette, Mathieu and Prof. Ricardo. Izquierdo for their work and precious insights on my early doctoral exams. Thank Prof. Jerome. Claverie from Université de Sherbrooke for his advice and for allowing me to perform part of the experiments in his lab. I would also like to acknowledge my co-supervisor, Prof. Jianming Zhang, and Prof. Yinhua Jiang from Jiangsu University, China, for their invaluable suggestions and encouragement. I do appreciate the director of the graduate programs in chemistry, Prof. Sylvain Canesi, and all teachers and technicians from UQAM.

I would like to express my appreciation to all my colleagues and group members at FEN lab. for their generous support and help throughout my Ph.D. journey. I feel lucky to be a member of such a hardworking, collaborative, and friendly group. Special thanks to my best friend and colleague, Dr. Maziar Jafari, for his unlimited help and kindness when I was new here. I am grateful to my friend and collaborator, Dr. Peipei Liu, for her direction in my experiments. I wish to acknowledge the financial assistance from the Chinese Scholarship Council for supporting my Ph.D. study here.

Last but not least, I want to express my heartfelt appreciation and gratitude to my beloved parents Shaojun Peng and Xiuling Li, my wife Yilu Su, and my baby Jinyu Peng, for their everlasting love, unconditional support, and encouragement all the time. I owe it all to you, without you nothing would be possible.

TABLE OF CONTENTS

LIST OF FIGURES

LIST OF ABBREVIATIONS

H_2	Hydrogen
PEC	Photoelectrochemical
1D	One-dimensional
CVD	Chemical vapor deposition
NRs	Nanorods
NW	Nanowire
NPs	Nanoparticles
C_{PDA}	Graphite-like carbon
PDA	Polydopamine
LSPR	Localized surface plasmon resonance
WGS	Water-gas shift
TWs	Terawatts
UV	Ultraviolet
IR	Infrared
PV	Photovoltaic
GW	Gigawatts
SPs	Semiconductor photoabsorbers
PC	Photocatalysis
PV-EC	Photovoltaic-electrocatalysis
OER	Oxygen evolution reaction
HER	Hydrogen evolution reaction

STH	Solar-to-hydrogen conversion efficiency
FTO	Fluorine-doped tin oxide
ITO	Indium-doped tin oxide
CB	Conduction band
VB	Valence band
SHR	Shockley-Read-Hall
CdS	Cadmium sulfide
MoS_2	Molybdenum sulfide
IPCE	Incident photon-to-current efficiency
ABPE	Applied biased photon-to-current efficiency
APCE	Absorbed photon-to-current efficiency
FE	Faradic efficiency
DRS	Diffuse reflectance spectrum
ALD	Atomic layer deposition
LDH	Layered double hydroxide
DFT	Density functional theory
XRD	X-ray diffractometer
XPS	X-ray photoelectron spectroscopy
UPS	UV photoelectron spectroscopy
FESEM	Field emission scanning electron microscope
TEM	Transmission electron microscopy
EDX	Energy dispersive X-ray spectroscopy
ICP-OES	Inductively coupled plasma optical emission spectrometry

PL	Photoluminescence
TRPL	Time-resolved photoluminescence
LED	Light-emitting device
PEIS	Photoelectrochemical impedance spectroscopy
RHE	Reversible hydrogen electrode
GSH	Glutathione
SAED	Selected-area electron diffraction
SnO_2	Tin dioxide
OCVD	Transient open-circuit potential decay
ECSA	Electrochemical surface-active areas
VBM	Valence band maximum
CBM	Conduction band minimum
LSV	Linear-sweep-voltammetry
SPR	Surface plasmon resonance
LO	Longitudinal optical
JCPDS	Joint committee on powder diffraction standards
Ar	Argon
GC	Gas chromatography
N_2	Nitrogen

LIST OF SYNBOLS AND UNITS

E_g	Bandgap energy
E_{CB}	Conduction band potential
E_{VB}	Valence band potential
V_{Ph}	Photovoltage
Φ_s	Semiconductor work function
Φ_R	Electrolyte work function
V_H	Helmholtz layer potential drop
$E_{F,n}$	Electron quasi-Fermi level
$E_{F,p}$	Hole quasi-Fermi level
E_f	Fermi level
V_{OC}	Open circuit voltage
P_{MAX}	Maximum power
J_{SC}	Short circuit current
$E_{oxidation}$	Semiconductor self-oxidation potential
V_{op}	Onset potential
η_{sep}	Charge separation efficiency
η_{inj}	Surface charge injection efficiency
η_{NHE}	Light-harvesting efficiency
N_D	Charge carrier concentration
E_{fb}	Flat band potential
τ_n	Average electron lifetimes

eV	Electron volt
λ	Wavelength
J	Joule
C	Coulomb
V	Volt
s	Seconds
min	Minutes
h	Hours
M	Mole/Liter
G	Gram
mg	Milligram
µg	Microgram
mL	Milliliter
µL	Microliter
nm	Nanometer
mol	Mole
mmol	Millimole
µmol	Micromole
mA/cm^2	Milliamps per square centimeter
mW/cm^2	Milliwatts per square centimeter

RÉSUMÉ

La surconsommation de combustibles fossiles a entraîné une crise énergétique mondiale sévère et une pollution environnementale accrue. Face à cette situation, la recherche de sources d'énergie alternatives et propres est devenue une priorité pour les scientifiques. Parmi les options envisagées sera l'hydrogène (H_2) qui se distingue en tant que source d'énergie potentielle, grâce à son haut rendement énergétique et ses caractéristiques écologiques. La division à l'ai de de cellule photoélectrochimique (PEC) de l'eau utilisant des matériaux photoactifs a émergé comme une méthode prometteuse pour transformer l'énergie solaire illimitée en hydrogène, de manière économique et durable. Cependant, le développement de dispositifs PEC performants, avec une haute efficacité de conversion de la lumière, nécessite la création de photoanodes semi-conductrices optimisées pour une meilleure absorption lumineuse, une excellente stabilité photochimique, une séparation efficace des porteurs de charge, et une forte réactivité redox. Le sulfure de cadmium (CdS), en particulier sous forme de nanotiges unidimensionnelles (1D), a été identifié comme un candidat exceptionnel pour la production d'hydrogène solaire. Ses atouts incluent une structure de bande énergétique adéquate, d'excellentes propriétés électriques et optiques et un chemin de transfert de charge limité minimisant la perte de porteurs. Toutefois, la rapide recombinaison des paires électron-trou photoexcitées et la photocorrosion sont des obstacles majeurs à son application pratique. Dans cette thèse, j'ai exploré la conception de nanojonctions 1D basées sur le CdS, y compris les hétérostructures de type Ⅰ, le modèle Z, et les hétérostructures améliorées par effet plasmon, pour pallier ces faiblesses et améliorer la gestion des photons et l'efficacité quantique. Cette approche a permis d'obtenir des performances PEC nettement supérieures. J'ai également étudié en détail le mécanisme qui sera possible pour l'amélioration du PEC et les voies de transfert de charge interfaciales.

La création d'hétérojonctions est une approche prometteuse qui peut améliorer significativement la séparation des porteurs de charge et l'efficacité de conversion de l'énergie solaire en hydrogène dans les cellules PEC. Cependant, cette technologie fait face à des défis liés aux interfaces de contact limitées. Dans ma première étude, j'ai utilisé la technique de dépôt chimique en phase vapeur (CVD) pour élaborer une photoanode hétérojonction CdS/MoS_2 dotée d'une nanoarchitecture inédite de type noyau-coquille. Cette structure consiste en une couche de nanofeuilles de MoS_2, cultivées directement sur des nanotiges de CdS orientées unidimensionnellement, formant ainsi un agencement plan par plan. L'épaisseur de la jonction a été optimisée en ajustant les paramètres expérimentaux, permettant de varier la charge de MoS_2 de mono à plusieurs couches. La coque MoS_2 améliore à la fois l'absorption optique et la passivation des états de piège à la surface. L'hétérojonction favorise une migration de charge unidirectionnelle, réduisant considérablement la recombinaison électron-trou, et contribuant ainsi à une efficacité quantique et un rendement accrus. La photoanode CdS/MoS_2 optimisée avec un revêtement MoS_2 de trois couches affiche une densité de photocourant et une efficacité de photoconversion significativement supérieures, surpassant le CdS pur et les hétérojonctions CdS/MoS_2 précédentes. Cette structure présente également une meilleure résistance à la corrosion et une photostabilité accrue, grâce à l'extraction rapide des trous du CdS et au transfert des sites d'oxydation de surface.

Dans le second volet du travail, j'ai conçu une hétérostructure de type Z, CdS/Au/SnO_2-S, composée de nanotiges de CdS orientées unidimensionnellement et modifiées avec des nanoparticules d'or (NP) enveloppées d'une couche de SnO_2. Cette configuration, utilisée comme photoanode, vise à optimiser l'évolution de l'hydrogène en PEC. Les NP d'or facilitent la croissance de la couche de SnO_2 et agissent comme médiateurs électroniques, améliorant le transfert de charge de SnO_2 vers CdS. Ce mécanisme de transport de charge, basé sur le schéma Z, réduit la recombinaison des charges, augmente la densité des porteurs et préserve la capacité redox. Il en résulte une densité de photocourant et une efficacité de conversion photovoltaïque améliorées, avec une meilleure résistance à la corrosion.De plus, les systèmes

PEC améliorés par les plasmons, grâce à la décoration de nanoparticules de métaux nobles (NP) sur la surface des semi-conducteurs pour former la barrière Schottky, présentent également des supériorités étonnantes en matière de conversion de l'énergie solaire.

Par conséquent, dans un troisième volet ce cette thèse, j’ai développé un réseau de nanotiges avec une structure hiérarchique plasmoniques, composé de nanotiges 1D CdS encapsulées avec une couche uniforme de carbone de type graphite (C_{PDA}) et des nanoparticules d'Au (Au NP), en tant que matériau de photoanode hautement efficace. Une méthode de réduction-graphitisation interfaciale in situ a été réalisée pour préparer la nanoarchitecture CdS/C_{PDA}/Au, où un revêtement de polydopamine (PDA) a été utilisé comme source de C et comme réducteur. La photoanode nanoréseau (*nanoarray*) CdS/C_{PDA}/Au démontre une efficacité de photoconversion supérieure avec une densité de photocourant de 8,74 mA/cm^2 et une valeur IPCE (480 nm) de 30,2 % (à 1,23 V par rapport à RHE), sous irradiation solaire simulée, qui est de 12,7 et 13,5. fois supérieur au CdS vierge. L'amélioration significative des performances du PEC bénéficie principalement de l'augmentation du rendement et de l'efficacité quantiques globaux dues à la formation du redresseur Schottky, de l'absorption de la lumière améliorée par résonance plasmonique de surface localisée (LSPR) et de l'injection favorisée d'électrons chauds à partir de l’intercouche de carbone de type graphène. Plus important encore, grâce au processus de recombinaison des porteurs de charge inhibés et aux sites de réaction d'oxydation transférés, la photoélectrode CdS/C_{PDA}/Au fabriquée affiche des durées de vie des électrons allongées et une meilleure photostabilité. Cette performance souligne son excellent potentiel pour des applications futures dans le domaine de l’ électrolyse de l'eau par photoélectrochimie (PEC).

Mots clés : Photoélectrochimique, évolution de l'hydrogène, photoanode, sulfure de cadmium, fabrication d'hétérojonctions, schéma Z, photoélectrocatalyse améliorée par plasmon, nanoarchitecture hiérarchique 1D, revêtement de carbone, type graphène, séparation de charges.

ABSTRACT

The excessive consumption of fossil fuels has resulted in the fierce issue of energy crisis and environmental pollution globally. Exploring alternative clean energy sources has thus received extensive research interest. Hydrogen (H_2), with its high energy capacity and clean attributes, is regarded as a promising and ideal candidate. In the past decades, photoelectrochemical (PEC) water splitting based on photoactive materials has attracted considerable attention for directly converting the inexhaustible solar energy into hydrogen fuels in an economical and environmentally sustainable manner. To accomplish reliable PEC devices with high photoconversion efficiency, one major challenge is still the design and manufacture of semiconductor photoanodes with wonderful light harvesting, superior photochemical stability, efficient charge carrier separation, and strong redox ability. As a typical visible-light-driven metal sulfide, cadmium sulfide (CdS), especially one-dimensional (1D) oriented CdS nanoarray, shows an excellent potential for solar hydrogen evolution due to its suitable energy band structure, great electrical/optical properties, larger aspect ratio, and confined charge transfer path with lower carrier loss. Nevertheless, the rapid bulk and surface recombination of photoexcited electron-hole pairs and severe photocorrosion restrict its practical application. In my thesis research, the rational design of 1D CdS-based nanojunctions, including conventional Type-I, Z-scheme, and plasmon-enhanced heterostructure, has been employed to overcome its intrinsic drawbacks for optimizing the overall photon management and quantum efficiency, ultimately achieving the significantly improved PEC performance. The possible PEC enhancement mechanism and interfacial charge transfer pathway are studied in detail.

Heterojunction fabrication is a promising strategy that can greatly boost the charge carrier separation and improve the solar-to-hydrogen conversion efficiency of PEC cells. However, such technology still suffers from limited contact interfaces. In my first work, the chemical vapor deposition (CVD) technique was for the first time used to construct the CdS/MoS_2 heterojunction photoanode with a unique core-shell nanoarchitecture, in which a continuous crystalline MoS_2 nanosheet layer was grown directly on 1D oriented CdS nanorods (NRs) in a plane-to-plane stacking fashion. The optimization of junction thickness with adjustable MoS_2 loading from mono to a few layers was achieved by experimental parameters variation. Herein, the MoS_2 shell plays a dual role as an optical absorption booster for more photo-exciton generation and a surface passivator of trap states. Meanwhile, the formed heterojunction helps regulate the unidirectional charge migration for a significantly suppressed electron-hole recombination process, which synergistically contributes to higher quantum yield and efficiency. As a result, the optimized CdS/MoS_2 heterojunction photoanode with 3-layered MoS_2 wrapping exhibits the highest photocurrent density and photoconversion efficiency, over a two-fold increase, compared to those of pristine CdS and the previously reported CdS/MoS_2 heterojunctions. Moreover, due to the rapid hole extraction from CdS and transferred surface oxidation sites, the present CdS/MoS_2 heterostructure demonstrates better corrosion resistance and higher photostability. The present work is expected to provide a versatile platform for exploiting the CVD technique to develop other MoS_2-based heterojunction photoelectrodes with extensive PEC applications.

Compared to the conventional semiconductor heterojunctions with the straddle charge transfer pathway, the artificial Z-schematic photosystem seems more desirable because of the promoted charge carrier separation and simultaneously preserved redox capability of photo-excitons. Thus, in my second work, an innovative pure Z-scheme heterostructure, CdS/Au/SnO_2-S, composed of 1D-oriented CdS nanorods modified with SnO_2-wrapped Au nanoparticles (NPs), was designed as a photoanode for highly efficient PEC hydrogen evolution. Systematic characterization confirms that the incorporated Au NPs not only act as the host platform to support the SnO_2 layer growth but also play a key role as the electron mediator for strengthening the vectorial charge transfer from SnO_2 to CdS. This reinforced Z-scheme charge transportation channel is favorable for suppressing the bulk charge recombination process, increasing the overall carrier density, and preserving the strong redox capability, ultimately resulting in a considerably improved photocurrent density and photo-to-current conversion efficiency with better corrosion resistance.

In addition, plasmon-enhanced PEC systems through decorating noble metal nanoparticles (NPs) on semiconductor surface to form the Schottky barrier also presents astonishing superiority in solar energy conversion. Therefore, in my third work, we develop a plasmonic hierarchical nanorod array, composed of 1D CdS nanorods encapsulated with uniformly wrapped graphite-like carbon (C_{PDA}) layer and Au nanoparticles (Au NPs), as highly efficient photoanode material. An interfacial in-situ reduction–graphitization method has been conducted to prepare the CdS/C_{PDA}/Au nanoarchitecture, where a polydopamine (PDA) coating was used as the C source and reductant. The CdS/C_{PDA}/Au nanoarray photoanode demonstrates superior photoconversion efficiency with a photocurrent density of 8.74 mA/cm^2 and IPCE value (480 nm) of 30.2 % (at 1.23 V *vs.* RHE), under simulated sunlight irradiation, which is 12.7 and 13.5 times higher than pristine CdS. The significant enhancement of PEC performance is mainly benefited from the increase of entire quantum yield and efficiency due to the formation of the Schottky rectifier, localized surface plasmon resonance (LSPR)-enhanced light absorption, and promoted hot-electron injection from interlayered graphene-like carbon. More importantly, thanks to the inhibited charge carrier recombination process and transferred oxidation reaction sites, the fabricated CdS/C_{PDA}/Au photoelectrode exhibits lengthened electron lifetimes and better photostability, illustrating its wonderful potential for future PEC applications.

Keywords : Photoelectrochemical, hydrogen evolution, photoanode, cadmium sulfide, heterojunction fabrication, Z-scheme, plasmon-enhanced photoelectrocatalysis, 1D hierarchical nanoarchitecture, carbon coating, graphene-like, charge separation.

CHAPTER 1

INTRODUCTION

1.1 Clean and renewable energy

Earth-rich and economical energy is a critical component in the operation of virtually every aspect of modern life. It drives our homes, powers our businesses, and supports the daily routines of both individuals and communities. Without energy, modern civilization would grind to a halt, and our world would be plunged into darkness. Energy already becomes the foundation of human survival and development. Since the industrial revolution, the economic energy systems have transformed dramatically and the non-renewable primary energy sources have started to dominate the world energy structure as shown in Figure 1.1a.[1, 2] According to the results in the BP Statistical Review of World Energy, 20.42 TW of the global primary energy is consumed in 2022, in which traditional fossil fuels accounted for around 76.71% share. These consisted of oil (29.61%), coal (25.07%), and natural gas (22.91%). Based on the current policy scenarios, the global energy demand from fossil fuels will keep increasing resulting from the expeditious growth of population and industrialization,[3, 4] which leads to two major concerns: (1) energy crisis (i.e., the finite reserves of fossil fuels have been hard to meet the growing energy demand and are expected to use out in the near future), and (2) environmental pollution (i.e., the extensive combustion of traditional fossil fuels commonly emit a large number of non-eco-friendly greenhouse gases, CO_2, into the atmosphere, which is mainly responsible for global warming with a series of climate changes).[5] Both of these issues already threaten the sustainable development of human society. Thus, to satisfy the global energy appetite while accomplishing carbon neutrality for a sustainable economy, emphasizing a swift transition from non-renewable fossil fuels to clean and sustainable energy resources becomes the top priority.[6]

At present, a Green Hydrogen Economy is considered the simplest and most promising way to decarbonize, wherein renewably produced hydrogen acts as the primary fuel.[7, 8] Because of its eco-friendly attribute (i.e., clean combustion by-products of H_2O and heat without carbon emission) and excellent gravimetric heating value (120 MJ/Kg), which is higher than those of mainstream energy sources (e.g., gasoline (47.5 MJ/Kg), methane (55.5 MJ/Kg), ethanol (27 MJ/Kg), and natural gas (47.1 MJ/Kg),[9] Hydrogen has been widely used in liquid fuels, power production, ammonia/fertilizer, metal refining, upgrading oil/biomass, and chemical processes. However, conventional hydrogen generation routines majorly based on thermochemical processes, like methane reformation and coal-based water-gas shift (WGS), still emit a large number of CO_2, and more importantly, its yield is also far below global energy demand.[10, 11] Therefore, discovering cost-effective and sustainable technology for carbon-free and large-scale hydrogen production is the key factor in pushing the advancement of the future hydrogen economy.

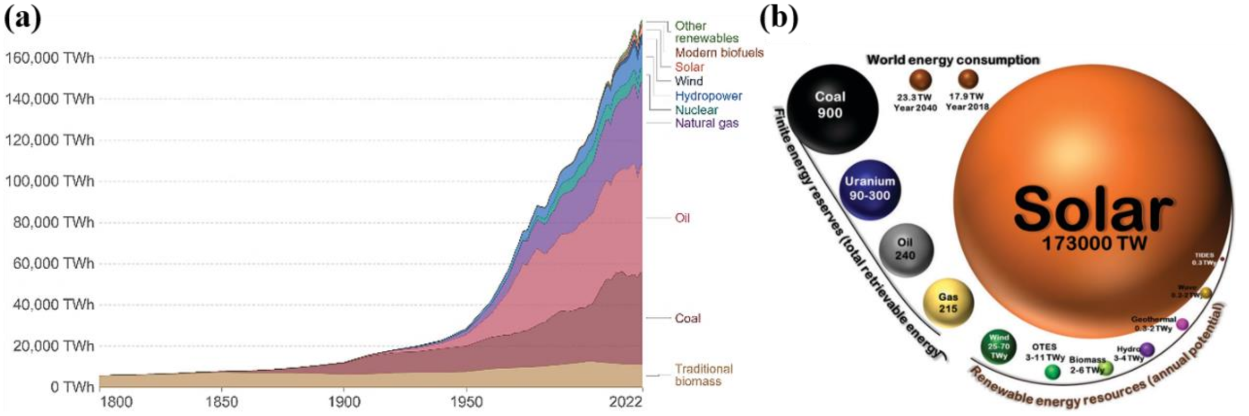

Figure 1.1 (a) Global primary energy consumption trend chart from 1800 to 2022 and (b) Global energy potential: Comparison of renewable energy (per year) with the total reserve of conventional energy sources.[2, 12]

Sunlight-driven hydrogen evolution from water splitting is a particularly appealing strategy since solar energy represents the most abundant, clean, economical, and renewable energy as shown in Figure 1.1b.[12, 13] Through calculation, a total amount of 120,000 terawatts (TW) of solar energy from sunlight irradiation strikes the earth's surface every year, which consists of around 7% of ultraviolet (UV) light, 44% of visible light, and 49% of infrared (IR) region. This value is about 6,000 times of the current global power consumption.[12, 14] However, the effective conversion of solar energy into electricity or storable hydrogen fuels for practical applications is still a long-term challenge in academia. In 2020, the direct utilization of solar energy through installed photovoltaic (PV) power was only 707.5 gigawatts (GW), far from satisfactory.[15] Considering its dispersion, diffusion, and intermittent nature, the US Department of Energy has established a 5% energy conversion target for valuable solar hydrogen generation.[16] This demands further exploration and development of economically viable, eco-friendly, and efficient solar capture and utilization approaches.

1.2 Solar hydrogen generation

Solar-driven water splitting for hydrogen evolution relies on the redox reaction of water molecules with photoinduced electron-hole pairs. From the view of thermodynamics, converting one water molecule into 1/2 O_2 and H_2 is an energetical uphill reaction and requires a change of Gibbs free energy of around 237 KJ/mol under standard conditions, corresponding to a Nernstian potential of 1.23 V per electron transferred.[17] The overall photo-assisted water splitting, i.e., proton reduction involved in the two-electron transfer process and water oxidation involved in the four-electron reaction, is displayed through the following equations:

Photoexcitation: $SPs + h\nu\ (> E_g) \rightarrow e^- + h^+$ (1)

HER (proton reduction): $2H^+ + 2e^- \rightarrow H_2$ (2)

OER (water oxidation): $2H_2O + 4h^+ \rightarrow O_2 + 4H^+$ (3)

Overall water splitting: $2H_2O \rightarrow O_2 + 2H_2\ \Delta G° = 237.2$ KJ/mol or $\Delta E° = 1.23$ eV/e (4)

Here, SPs represent semiconductor-based photo-absorbers and are the key components to accomplish solar hydrogen generation. The redox potential of water directly determines its necessary bandgap regions and energy band positions. That means that, to operate water splitting, the photon energy harvested by SPs should be above 1.23 eV, corresponding to a spectrum wavelength below 1000 nm, which requires sufficient bandgap energies ($E_g > 1.23$ eV). Simultaneously, appropriate energy band positions are also important to support the occurrence of the reaction, i.e., the conduction and valence band potential (E_{CB} and E_{VB}) should straddle the electrochemical potentials of two-half reactions ($E°(H^+/H_2)$ and $E°(O_2/H_2O)$).[18] In addition, taking the kinetic overpotential requirement (0.4-0.6 eV) for both half-reactions and free energy loss (0.3-0.4 eV) during charge carrier transport into account, the efficient bandgap value used to drive the overall water splitting should be over 1.8 eV for a single semiconductor.[17] Of course, a further expended bandgap value means less light absorption, usually leading to lower solar conversion efficiency.

To accelerate the realization of renewable solar energy into hydrogen fuels via proton/electron transfer reduction reactions, three typical photosystems, including particulate photocatalysis systems (PC), photovoltaic-electrocatalysis routes (PV-EC), and photoelectrochemical cells (PEC), have been competitively explored as shown in Figure 1.2a-c.[18] These approaches are mechanistically different from each other but share a few commonalities. Briefly, particulate photocatalysis (PC) systems are based on powder photocatalysts dispersed in the medium, which possess a significantly shorter charge transport pathway than normal charge collectors in the other photosystems.[19] Since both OER and HER half reactions directly occur on the photocatalyst surface, an independent gas separator is needed to unmix the generated H_2 and O_2, adding a certain complexity. In total, the PC system is the most affordable of these three approaches because of its simplicity and the lowest overpotential cost, but how to construct a stable and highly efficient solar-to-hydrogen (STH) conversion device is still a big challenge. Until now, the state-of-the-art STH conversion efficiency value obtained by the PC system is just around 2%, which leaves a huge development gap for practical industrial scale-up.[20] Comparatively, PV-EC and PEC technologies already achieved much higher STH efficiencies up to 30% and 13.1% using III-V semiconductor photo-absorbers (GaInP, GaInSe, GaAs, etc.).[21-24] In PV-EC tandem cells, PV panels are only employed to capture photons and produce electricity, which is then supplied to electrocatalysis. These photo-absorbers are kept away from the aqueous medium, thus photostability against corrosion is out of consideration. Although the highest STH value is recently reported by the PV-EC system, it displays a disadvantage of the highest cost and complexity in device designs. A technique map displayed in Figure 1.3 clearly elucidates the relationship between efficiency and device complexity within these three water-splitting photosystems. According to the technical analysis, the costs of hydrogen evolution by PC ($1.60 to $3.12/kg) and PEC ($4.10 to $10.10/kg) methods are significantly lower than that of PV-EC cells ($7 to $20/kg).[25-27]

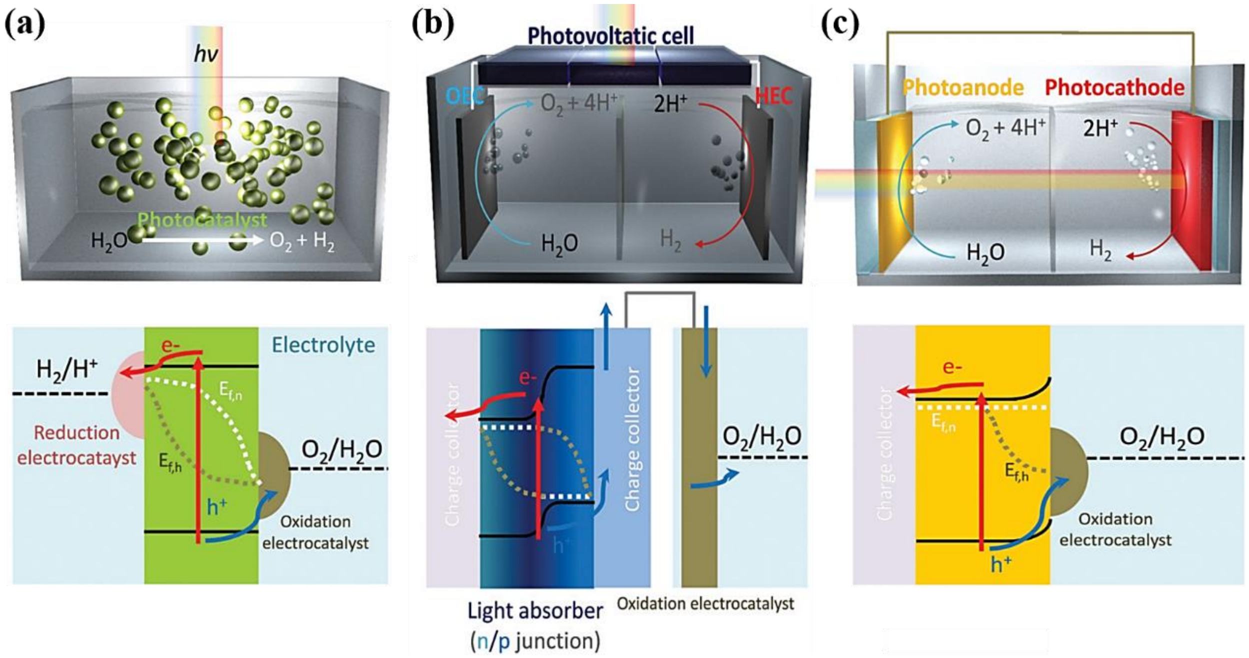

Figure 1.2 Schematic diagrams of three typical solar-driven water splitting systems and the relevant charge flow model: (a) PC, (b) PV-EC, and (c) PEC.[12]

PEC water splitting for hydrogen evolution provides a prospective strategy for direct solar energy conversion. Here, semiconductor-based photoactive materials act as photoanodes or photocathodes immersing into electrolytes, and then, water redox reaction takes part in their surface, which largely simplifies the subsequent fuel separation and collection process. More pronounced band bending along photoelectrodes endows them with better charge separation and transport efficiency, resulting in a distinct advantage of higher STH values relative to PC systems. At the same time, compared to the high cost of the

PV-EC approach, PEC cells integrate the light-harvesting and electrochemical reaction modules into a monolithic unit via a direct semiconductor-liquid junction, reducing the expense.[28] What's more, the corporation of self-bias (through a photoanode-photovoltaic or photoanode-photocathode tandem cell) or externally applied voltage into PEC configuration can make up for the overpotential deficiency and further improve the overall quantum efficiency. Over the last few years, PEC technology has been growing rapidly but is still far from practical application under the current level of development. To be competitive for market viability, high STH efficiency of over 10% and a longer lifetime of above 10 years are needed, which requires continued advancements in photoelectrode fabrications and device designs.[12]

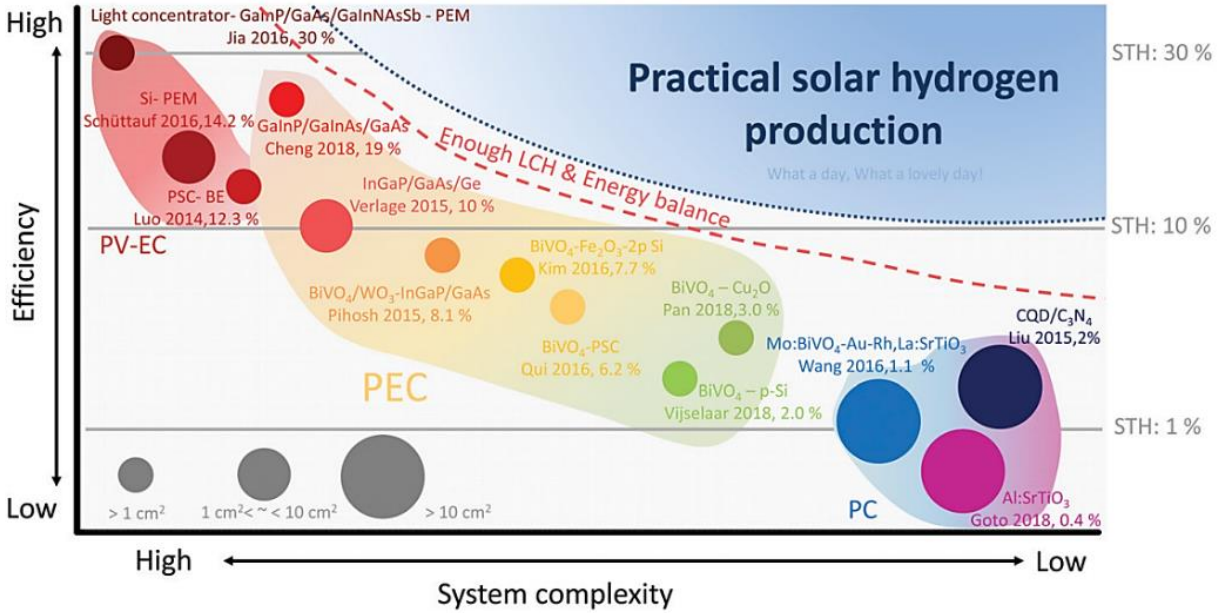

Figure 1.3 The technique map displaying the relationship between efficiency and device complexity within three solar-driven water-splitting systems.[12]

1.3 Photoelectrochemical hydrogen generation

1.3.1 Configuration and working principle of PEC water-splitting

PEC hydrogen evolution is widely regarded as an ideal approach to convert inexhaustible solar energy into storable chemical fuel which could largely relieve the increasingly serious global energy crisis and environmental problem. Semiconductor photo-absorbers as key components have always been the focus of attention. Actually, the OER phenomenon was already noticed on rutile TiO_2 electrodes under illumination as early as 1968.[29] Later, the first demonstration of solar-driven electrochemical water splitting was reported by Fujishima and Honda in 1972, using n-type TiO_2 as semiconductor photoanode, essentially marking the beginning of a new era.[30] In spite of the wonderful stability of TiO_2, the wide bandgap (~3.2 eV) limits its photo-absorption region to Ultraviolet (UV) light, leading to a low solar utilization and conversion. Therefore, significant efforts have been devoted to developing narrow-bandgap photoactive materials for more efficient PEC appliances. Thanks to these pioneering works, PEC water-splitting systems have made great progress and the recently reported STH conversion efficiency also increased to a relatively high value of approximately 19%.[22] Figure 1.4 displays several configurations of PEC cells distinguished by the functions of photoelectrodes. The basic form usually consists of a single photoelectrode (photoanode based on the n-type semiconductor or photocathode based on the p-type semiconductor) as the working electrode, Pt electrode as the counter electrode, and the simulated solar source (AM 1.5G), as shown in Figure 1.4 (a, b). This conventional PEC cell with a single photo-absorber usually needs an external bias voltage to make up for the overpotential and other energy loss. Compared to completely electrocatalytic water splitting, the photoanode substitutes the OER catalytic anode and the photocathode replaces the HER catalytic cathode to conduct the corresponding half-reactions. The introduction of photoelectrode enables the reduction and elimination of externally applied bias, where the reduced part is equal to the photovoltage (V_{Ph}) produced by photoelectrodes.[31] When V_{Ph} is higher than E (H_2/H_2O) plus overpotential requirements (~1.8 V), the PEC cell will perform unbiased water splitting. Therefore, to increase the overall V_{Ph} for achieving the spontaneous water splitting, connecting two or more photo-absorbers as a photoanode-photocathode tandem cell (Figure 1.4c), or integrating PV modules as a photoanode-photovoltaic tandem cell (Figure 1.4d) are advanced choices. Sometimes, an anion/cation exchange membrane is also used to separate the photoelectrode and counter electrode. Furthermore, conductive substrates, like silicon,[32] FTO (fluorine-doped tin oxide), or ITO (indium-doped tin oxide)-coated glasses, are normally employed to support the growth or deposition of photoactive materials for photoelectrode fabrication.

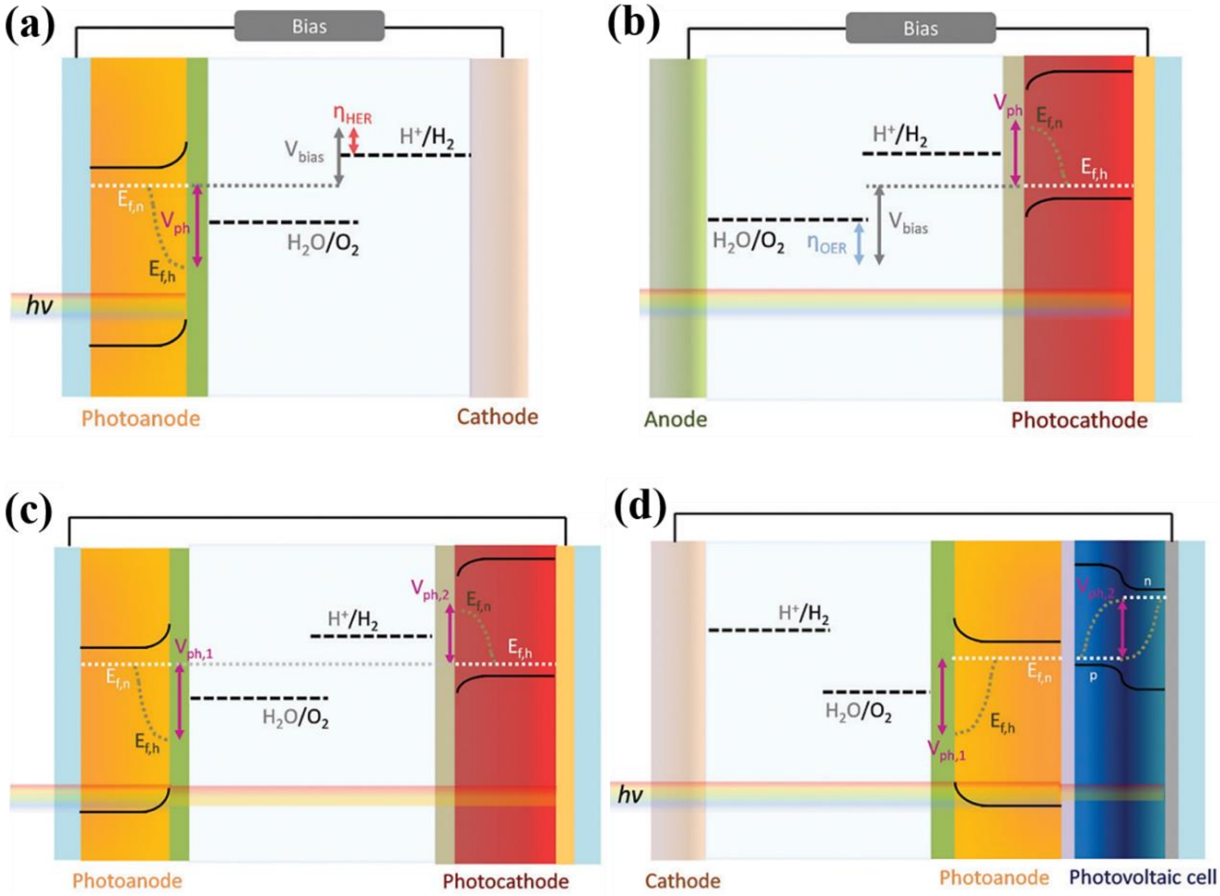

Figure 1.4 Four typical PEC water-splitting devices: (a) Photoanode-HER cathode, (b) OER anode-photocathode, (c) photoanode-photocathode tandem cell, and (d) photoanode-photovoltaic tandem device for bias-free water splitting reaction.[12]

Figure 1.5 shows the schematic illustration for the working principle of a representative PEC water-splitting process dominated by the photoanode system,[33] which majorly contains the following three steps: (i) Photoexcitation process. Under sunlight irradiation, a semiconductor photoanode captures photons with energy higher than its bandgap value ($h\nu \geq E_g$), followed by the generation of photoinduced electron-hole pairs. The electrons will be photoexcited to the conduction band (CB) and holes still remain on the valence band (VB). (ii) Charge carrier separation and transfer process. Under the synergistic effect of band bending and externally bias voltage, the separation and transfer of photogenerated charge carriers will occur. The holes (minority carriers) migrate to the photoanode surface and the electrons (majority carriers) transport to the counter electrode through the external circuit. During this step, the fast charge carrier recombination probably happens at the bulk and surface of the semiconductor, semiconductor/substrate, or semiconductor/electrolyte interface, largely limiting the overall quantum efficiency.[34] Thus, adopting effective strategies to strengthen charge separation and injection efficiency is essential to improve PEC performances. (iii) Surface redox reaction. The migrated photo-electrons on the counter electrode surface reduce H^+ to H_2, while holes accumulated on active sites of the photoanode will take part in the water oxidation reaction.[35] Besides, protons will transport from the photoanode to the counter electrode through the electrolyte, completing an electrochemical closed circuit. Relatively, for the typical PEC cell made of a p-type photocathode system, the minority carriers (photo-excited electrons) leave on the surface of the photocathode to conduct the HER process, while the majority carriers (photo-generated holes) migrate to the counter electrode involved in the OER reaction. The ideal integrated PEC cell composed of a photoanode-photocathode cell can achieve an unassisted water-splitting reaction with only solar light as the driving force.

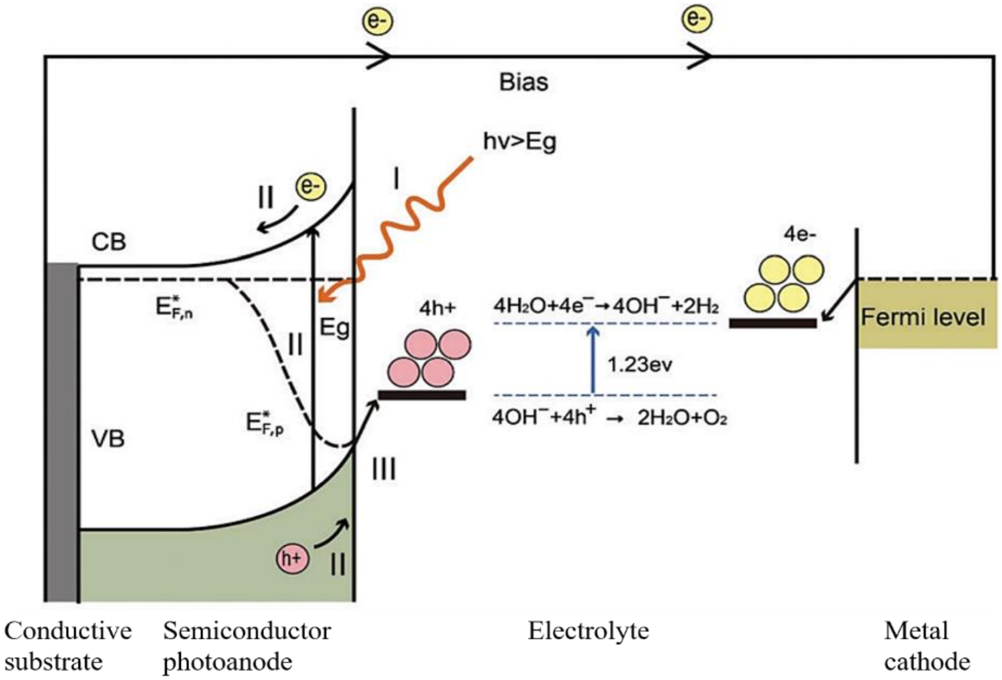

Figure 1.5 Schematical illustration for the representative PEC water-splitting process composed of the photoanode-metal cathode system. The main processes include: (i) photoexcitation, (ii) charge separation and transfer, and (iii) surface redox reactions.[33]

In addition, except for the core of PEC systems (the photo-electrolysis module), the electrolyte is also an essential component for charge transfer. Since the low electrical conductivity (around 0.055 µS/cm) of deionized pure water at 25 °C, some auxiliary ions, like salts, bases, acids, etc., are needed to dissolve into the deionized water to improve its conductivity. Noteworthily, under certain circumstances, some redox couples, such as H_2O_2, Na_2S, and Na_2SO_3, are necessary to be mixed into the electrolyte as the hole sacrificial agents,[36] where the OER process is replaced due to the more positive oxidation potential of water than other groups. The rapid consumption of photo-excited holes by sacrificial agents helps suppress surface charge carrier recombination, prevent back reaction, and photoelectrode protection. However, using sacrificial agents means additional costs in theory. To increase the economic benefits, some sacrificial organic agents represented by short-chain alcohols, carboxylic acids, and biomass-derived compounds have been developed,[9, 37] which could be dedicated to a dual purpose of producing high-value-added chemicals and simultaneous H_2 generation. Moreover, this PEC reforming process can also be employed to treat organic-containing industrial wastewater for aquatic protection. Based on the systematical elucidation of the PEC principle and process above, it is predictable that the major factors and challenges to consider for implementing a practical PEC H_2 production device include efficiency-related parameters, cost competitiveness compared to other H_2 evolution technologies, and long-term photostability.[12] Among them, how to effectively improve the solar conversion efficiency and stability of the photoelectrode is still the main research subject currently.

1.3.2 Band bending near semiconductor/electrolyte interface

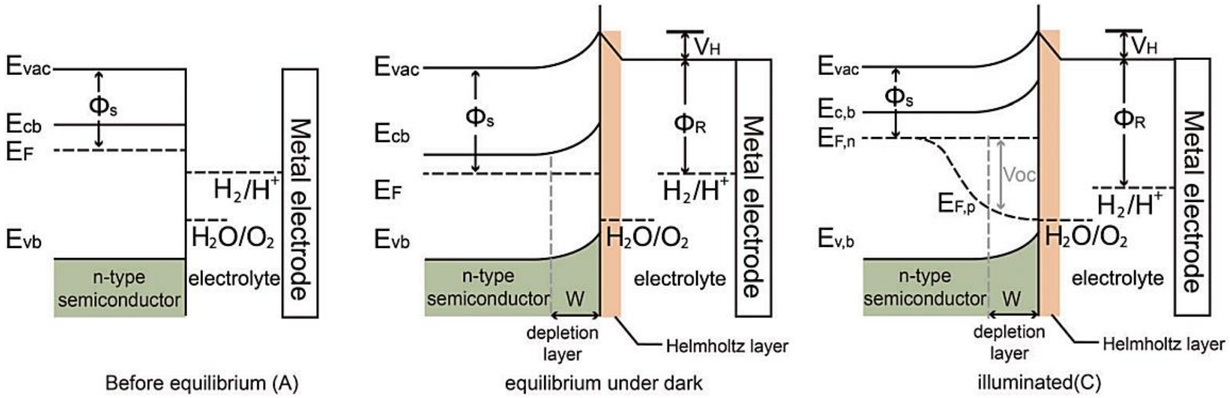

Figure 1.6 The band energetics at the photoanode/electrolyte interface before equilibration, after equilibration under darkness, and under quasi-static equilibration with steady-state sunlight irradiation. Here, Φ_s, Φ_R, V_H, $E_{F,n}$, and $E_{F,p}$ represent the semiconductor work function, the electrolyte work function, Helmholtz layer potential drop, the electron quasi-Fermi level, and the hole quasi-Fermi level, respectively.[33]

As well known, the semiconductor band diagram is made of the forbidden band (bandgap), the conduction band, and the valence band. For the undoped intrinsic semiconductor, the Fermi level (E_f) should exactly stay at the center of the band gap (mid-energy gap), where the occupation probability by electrons is half. Upon surface doping with electron donor or acceptor atoms, E_f at the surface moves towards CB for n-type semiconductors or towards VB for p-type semiconductors.[38] When the semiconductor photoelectrode and an electrolyte are in contact, the energy difference between the semiconductor Fermi level and the electrolyte redox potential will cause a charge flow from one phase to the other until reaching an equilibration, thereby forming semiconductor band bending. For the PEC water-splitting process, band bending near the semiconductor-liquid junction can supply a driving force to assist the separation and transfer of photogenerated electron-hole pairs, and therefore, a deep understanding of band bending behavior is of great importance. Figure 1.6 exhibits the band energetics at the photoanode/electrolyte interface before equilibration, after equilibration under darkness, and under quasi-static equilibration with steady-state sunlight irradiation. Observably, when a typical n-type semiconductor photoanode is immersed into the electrolyte, the electron transfer occurs at the interface until the E_f of the semiconductor is equilibrated with the redox couple of the electrolyte. After equilibration, the depletion layer (the space charge layer, W) distributed with an excess of positive charge is formed in the semiconductor, leading to an upward energy band bending. Correspondingly, an anion-dominated Helmholtz layer with a much narrower region is formed at the interface.[33] Under steady-state sunlight irradiation, non-equilibrium electron and hole populations are generated and can be denoted through a concept of the quasi-Fermi level, which represents the electrochemical potential of electrons and holes under illuminated conditions. The gradient of the quasi-Fermi level causes a built-in electric field at the semiconductor surface.[15] The voltage formed by this electric field is described as the photovoltage or the open circuit voltage (V_{OC}), which can provide a strong driving force for water oxidation. In terms of experiments, V_{OC} values can be gained by testing the potential difference between the quasi-Fermi level of hole and electron under open circuit state. The maximum power (P_{MAX}) can also be calculated by multiplying the short circuit current (J_{SC}) by the V_{OC}. In contrast, for a p-type semiconductor photocathode in the electrolyte solution, the holes as the majority carrier are depleted in the semiconductor surface, thus resulting in a downward energy band bending, which will promote the separation and transfer of photogenerated charge carriers in opposite directions. Ultimately, the minority carrier of semiconductors will dominate a redox reaction (oxidation or reduction) occurring at the photoelectrode/electrolyte interface.

1.3.3 Charge transfer behavior within semiconductor photoelectrodes

As shown in Figure 1.7, the PEC water-splitting process is dominated by several crucial steps, including photoexcitation, charge separation, transfer, and transport. Among them, the photoexcitation for the generation of charge carriers majorly depends on the photoelectronic properties of the semiconductor itself (i.e., bandgap and energy band positions). An important point to note is the matching of absorbed photon energy to the solar spectrum. The next step involves in the charge separation and transport process, which directly determines the overall quantum efficiency. During the charge transfer period within the bulk semiconductor, radiative recombination would be the only competitor ideally, where the produced photons may be reabsorbed.[39] Actually, however, charge recombination through a series of other mechanisms, such as Shockley-Read-Hall (SHR, trap-assisted) recombination, Auger recombination, and so on, is responsible for the biggest energy loss in photo-to-current conversion.[40] Besides, when the diffusion length of photoexcited charge carriers, particularly the minority carrier, mismatches with the penetration depth of sunlight, serious charge recombination will take place and result in a low PEC performance. Taking the hematite photoabsorber as an example, the diffusion length of holes is recorded to be 2-4 nm, much shorter than its characteristic light penetration depth of around 46 nm at the incident wavelength of 450 nm.[41] That means most photoinduced holes would be quenched before transfer to the semiconductor surface for redox reaction. Thereby, only the minority carriers within one diffusion length immediately adjacent to the depletion layer can be effectively separated and drift outward to the semiconductor/electrolyte interface. It is assumed that without charge carrier recombination in the depletion layer, the almost instantaneous photogenerated minority carriers current (J) can be estimated via the Gartner Equation:[42, 43]

$$J = \mathrm{e} I_0 \left(1 - \frac{e^{-\alpha W}}{1+\alpha L_n}\right) \tag{6}$$

Where I_0, e, α, W, and L_n represent the incident photon flux, the elementary charge, the absorption coefficient, the width of space charge layer, and the minority carrier diffusion length, respectively. Accordingly, a longer minority carrier diffusion length and a wider space charge region will be beneficial for a higher photocurrent density. Simultaneously, the longer lifetime (τ) and faster mobility will endow minority carriers with a longer L_n, favorable for a better charge separation efficiency.

In reality, the charge recombination process happens not only in the bulk semiconductor but also on the semiconductor surface or interface as a solid-state process.[44, 45] Even for pristine semiconductors, their surfaces, whether connecting with a metal electrode or in a vacuum, are abundant in electronic states, which are often introduced by surface defects (e.g., structural imperfections and dangling bonds). These states majorly account for the severe surface charge recombination. Other competing processes, mainly including corrosion (self-corrosion of photoelectrode induced by the parasitic chemical reaction) and side reactions (parasitic reaction competing with solar fuel production), would inhibit the surface charge transport and result in a low charge injection efficiency. Noteworthily, aside from the above unfavorable factors, chemisorbed species (e.g., reactants, intermediates, or products) on photoelectrode during surface redox reaction could also act as center sites to boost the charge recombination. As a result, adopting appropriate modification strategies to suppress these bulk and surface recombination processes is the top priority for accomplishing high-efficiently solar conversion.

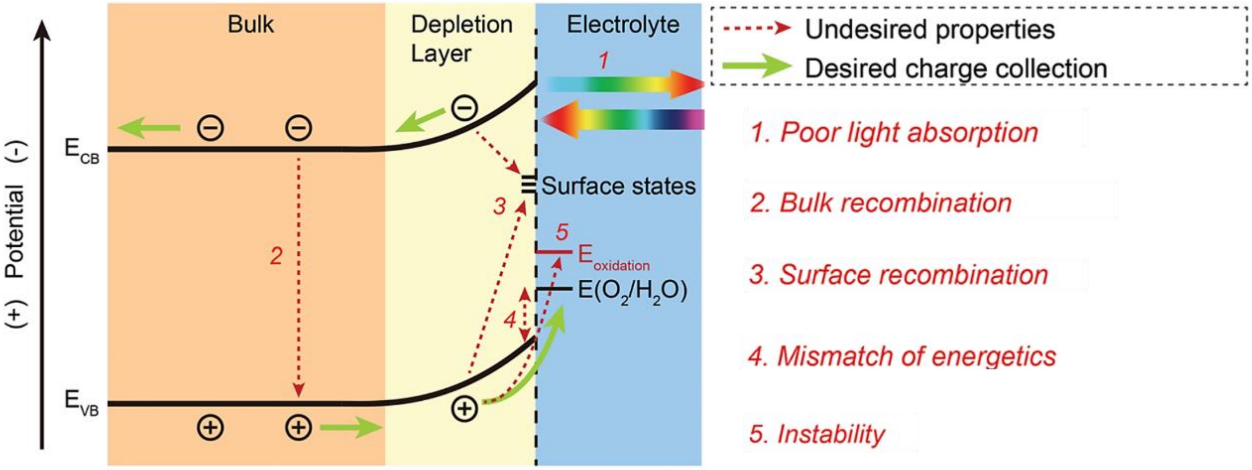

Figure 1.7 Schematical diagram of semiconductor photoexcitation, charge separation, transfer, and transport process within a typical n-type semiconductor photoanode/electrolyte PEC system. Here, E_{CB}, E_{VB}, and $E_{oxidation}$ represent the potentials of conduction band, valence band, and semiconductor self-oxidation. The dotted arrows pointed out the major undesired properties and competing processes, including poor light absorption, bulk and surface recombination, mismatch of energetics, and instability, as described in the right column.[39]

Moreover, it should be emphasized that the energetics at the solid-liquid junction need to match with the target chemical reaction, which is important for successful solar-to-fuel conversion. There are a few photoactive materials (like CdSe) that possess wonderful light absorption, charge separation, and transfer capability, but are largely limited by significantly mismatched energetics with solar water splitting. In this case, the photogenerated charge carriers with insufficient energy make it hard to drive the desired reaction forward.

1.3.4 Efficiency-related parameters involved in PEC water-splitting process

The target of photoelectrode design is to achieve the maximum photocurrent density (J_{ph}) and the minimum onset potential (V_{op}). Generally speaking, the J_{ph} value at 1.23 V vs. RHE is employed to analyze the PEC performance of photoelectrodes. The higher J_{ph} value means more photoexcitons participating in the water-splitting reaction. To better understand, the measured photocurrent density can be denoted by the following simplified charge separation and transfer process:

$$J_{ph} = J_{abs} \times \eta_{sep} \times \eta_{inj} \tag{7}$$

Where J_{abs} is the theoretical maximum photocurrent density through semiconductor photoabsorption, η_{sep} represents the bulk charge separation efficiency, corresponding to the proportion of minority carriers successfully reaching the semiconductor/electrolyte interface instead of the bulk recombination, η_{inj} is the surface charge injection efficiency, corresponding to the fraction of minority carriers successfully taking part in the desired surface reaction rather the surface recombination. Based on the above equation, the bulk and surface charge recombination process can be quantified experimentally.

Taking the n-type photoanode system as an example, H_2O_2 and Na_2SO_3 are normally used as the hole scavenger, which could be oxidized more easily than water due the much lower oxidation potential (water oxidation: $2H_2O + 4h^+ \rightarrow O_2 + 4H^+$, E°=1.23 V vs. RHE; H_2O_2 oxidation: $H_2O_2 + 2h^+ \rightarrow O_2 + 2H^+$, E°=0.68 V vs. RHE; SO_3^{2-} oxidation: $SO_3^{2-} + h^+ \rightarrow SO_3^-$, E°=0.73 V vs. RHE). Assuming the complete consumption of holes by the hole scavenger (i.e., 100% of charge injection efficiency, $\eta_{inj} = 1$), the formed photocurrent density based on the SO_3^{2-} photooxidation system can be shown as the following equation:

$$J_{so_3^{2-}} = J_{abs} \times \eta_{bulk} \tag{8}$$

Furthermore, the J_{abs} value can be confirmed according to the semiconductor light absorption data and AM 1.5G standard solar spectrum as follows:

$$P_{abs}(\lambda) = P_0(\lambda) \times (1 - 10^{-\alpha}) \tag{9}$$

$$J_{abs}\left(\frac{mA}{cm^2}\right) = \int \frac{\lambda}{1240} \cdot P_{abs}(\lambda)\, d\lambda \tag{10}$$

Where P_0 (λ) and P_{abs} (λ) correspond to the wavelength-dependent AM 1.5G standard solar power and practically absorbed solar power by the semiconductor photoanode, α is the light absorption coefficient. Integrating P_{abs} (λ) over the wavelength can gain the solar power absorbed, which is then converted to the J_{abs} value. Based on these results, the bulk and surface charge separation efficiency (η_{bulk} and η_{inj}) values can be deduced as:

$$\eta_{bulk} = \frac{J_{so_3^{2-}}}{J_{abs}} \tag{11}$$

$$\eta_{inj} = \frac{J_{ph}}{J_{so_3^{2-}}} \tag{12}$$

Except for the bulk and surface charge recombination efficiency, other efficiency-related parameters involved in solar conversion include the solar-to-hydrogen conversion efficiency (η_{STH}), incident photon-to-current efficiency (IPCE), absorbed photon-to-current efficiency (APCE), applied biased photon-to-current efficiency (ABPE), and Faradic efficiency (FE). The specific equations are listed below:

As a common indicator to compare the performance of PEC systems, η_{STH} value can be obtained by dividing the total energy produced by the total input energy (AM 1.5G), which is shown as follows:

$$\eta_{STH} = \frac{Total\ energy\ produced}{Total\ input\ energy} = [\frac{r_{\mathrm{H_2}} \times \Delta G}{P_{in} \times A}]_{\mathrm{AM1.5G}} \tag{13}$$

Where r_{H2}, ΔG, P_{in}, and A represent the hydrogen production rate (mol/s), Gibbs free energy (237 KJ/mol), incident sunlight intensity (100 mW cm^{-2}), and irradiated photoelectrode area (cm^2), respectively. Noteworthily, the η_{STH} parameter is only applicable to the two-electrode configuration without electrical bias and any sacrificial reagents.

IPCE value is widely used to evaluate the photoelectric conversion performance of photoelectrodes, which is obtained at a fixed incident light wavelength. It is normally defined as the ratio of photoexcited electrons contributing to the photocurrent versus incident photons. The formula is shown as follows:

$$IPCE\ (\lambda) = \frac{The\ number\ of\ converted\ electrons}{incident\ photons} = \frac{(\frac{J(\lambda)}{e}) \times (\frac{hc}{\lambda})}{P(\lambda)} \times 100\% \tag{14}$$

Where J (λ), e, h, c, λ, and P (λ) represent the photocurrent density at the fixed incident wavelength (mA cm^{-2}), the charge of an electron (1.602×10^{-19} C), the Planck constant (6.626×10^{-34} J s), the light speed (3×10^8 m s^{-1}), the corresponding incident light wavelength (nm), and incident light intensity (mW cm^{-2}), respectively.

The calculation of IPCE values above is based on the total number of incident photons, ignoring the optical losses from transmission and reflection, which possibly affects the accuracy of the final results. To correct this optical error, APCE values are often employed to evaluate the overall quantum efficiency. It is defined as the ratio of photoexcited electrons devoted to the photocurrent versus absorbed photons. The formula is shown as follows:

$$APCE\ (\lambda) = \frac{IPCE\ (\lambda)}{\eta_{LHE}} \tag{15}$$

Where η_{NHE} is the light-harvesting efficiency of photoelectrodes, estimated from the corresponding absorption coefficient (α):

$$\eta_{LHE} = 1 - 10^{-\alpha} \tag{16}$$

In the practical PEC measurement, a conventional three-electrode configuration is normally used to study the photoelectrode performance. The electrical energy from the externally applied bias should be removed and then, the ABPE value can be obtained as follows:

$$ABPE = \frac{J_{Ph} \times (V_{redox} - V_{bias})}{P_{light}} \times 100\% \tag{17}$$

Where J_{Ph} represents the generated photocurrent density from the PEC device (mA cm^{-2}), V_{redox} refers to the redox potential of water splitting (1.23 V vs. RHE), V_{bias} is the actual device voltage, P_{light} corresponds to the intensity of incident light (100 mW cm^{-2}).

The Faradic efficiency (EF) is regarded as the most common approach to determine if the obtained photocurrent density results from the water splitting rather than photoelectrode corrosion or other competing reactions. It is defined as the ratio between the practical evolved gas amount and the theoretical evolved gas amount calculated from the measured photocurrent density. The formula is listed below:

$$FE = \frac{Experimental\ O_2\ or\ H_2\ evolution}{Thoretical\ O_2\ or\ H_2\ evolution} = \frac{N}{(\frac{J_{Ph} \times A \times T}{Z \times F})} \times 100\% \tag{18}$$

Where N is the experimentally generated gas amount analyzed by gas chromatography (GC, mmol), J_{Ph} represents the actual photocurrent density (mA cm^{-2}), A is the photoelectrode area (cm^2), T is the photoreaction times (s), Z is the transferred electrons amount required for generation a gas molecular (2 for H_2 and 4 for O_2), F is Faraday constant (96 485.33 C mol^{-1}).

1.4 Strategies for highly-efficient photoelectrode design

Rationally designing semiconductor photoelectrodes with much higher performance is the top priority in developing the PEC technology for efficient solar hydrogen synthesis. According to the PEC water splitting process mentioned above and the expression formula of photocurrent density in section 1.3.4, three major factors limiting the PEC performance of semiconductor photoelectrodes include solar energy absorption capability, charge separation, and charge injection efficiency. In the past decades, plenty of theoretical and experimental studies have been carried out to explore a series of feasible modification strategies, such as novel photocatalyst development, chemical doping/vacancy enriching,[46, 47] nanostructuring,[48] surface reconstruction,[49] noble metal deposition,[50] heterojunction fabrication,[51] dye sensitization,[52] co-catalyst decoration,[53] etc., to accomplish the purposes of enhancing spectrum absorption range and suppressing the bulk and surface charge carrier recombination for much higher quantum yield and efficiency.[54, 55] As proven, a single modification strategy or photoactive material is hard to simultaneously satisfy all three aspects, and combining two or more methods can achieve a higher goal. Herein, the detailed description will be performed separately below.

1.4.1 Efficient light absorption

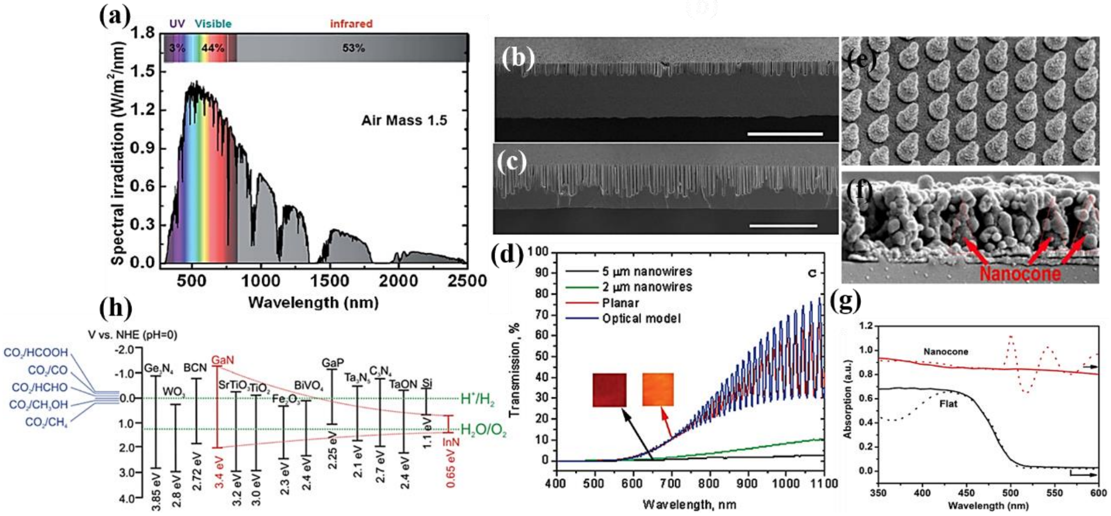

Figure 1.8 (a) Solar spectral distribution based on the AM 1.5 global irradiation.[56] (b, c) The SEM images of 2.5 µm and 5 µm Si nanowire array on 7.5 µm Si windows and (d) the corresponding transmission spectra.[57] The blue line corresponds to the optical spectrum of the planar Si window. (e, f) The SEM images of the pre-designed $SiO_x/Pt/SnO_2$ nanocone arrays and Mo:$BiVO_4$ on its surface, and (g) the UV-vis optical absorption spectra of Mo:$BiVO_4$ on nanocone arrays and FTO glasses.[49] The simulated absorption spectra are presented in the dotted line. (h) Energy band position of InGaN in comparison with some commonly reported semiconductors, which continuous and directly depended on the concentration of doped In.[58]

Photoexcitation for the charge carrier generation is the basis of the PEC water-splitting reaction. A narrow spectrum response regime and low quantum yield is the common issue restricting the PEC activity of some photoactive materials. Taking the anatase-phase TiO_2 photoanode as an example, it possesses the advantages of high photo-to-electron conversion efficiency and excellent physicochemical stability but is still limited by its wide bandgap value of around 3.2 eV. That means only UV light with a wavelength shorter than 400 nm can be absorbed by TiO_2 photoelectrode, occupying less than 5% of the total solar energy (Figure 1.8a),[56] which results in a low solar utilization for practical PEC water splitting.[59] Similar issue also arises in some other wide-bandgap semiconductors, like ZnO, SnO_2, ZnS, $SrTiO_3$, etc. Several approaches have been demonstrated effective to overcome this drawback, mainly including the following points: (i) Exploring narrow-bandgap semiconductor materials instead of wide-bandgap materials. Over the past decade, a large number of novel semiconductor or solid-solution photoactive materials have been developed as promising substitutes for TiO_2, such as CdS, α-Fe_2O_3, $BiVO_4$, Ag_3PO_4, Si, InP, CdSe, MoS_2, $Ga_xZn_{1-x}O_yN_{1-y}$, $AgInS_2$-ZnS, $CuInS_2$-ZnS, etc.,[60-63] which already extend the solar spectrum absorption regime from UV to visible light and even near-infrared light.

(ii) Strengthening light harvesting through reducing reflection. As demonstrated in previous reports, reflection-induced optical loss is significantly obvious within the planar semiconductor photoelectrode, leading to a low PEC performance. Two major methods are used to address this challenge. One approach involves constructing well-designed nanostructures on the photoelectrode surface to weaken reflection. For instance, Garnett et al. proved that the optical path length of solar irradiation was remarkably enhanced via carefully adjusting the density and diameter of Si nanowires (NWs). Because of the structure merits, the maximum reached up to 73 times higher than the Si thin film with the same thickness as shown in Figure 1.8b-d.[57] Maiolo et al. reported that Si nanowires with a length of 10~30 µm showed a significantly higher photovoltage and photocurrent density than Si planar samples under the 1,1'-dimethylferrocene $(Me_2Fc)^{+/0}$ redox system.[64] Furthermore, Dai et al. also synthesized the Si NW arrays using the Ag-assisted etching method, which exhibited a strong broadband anti-reflection feature with a reflectance of approximately 0%. In contrast, the Si planar film presents a high sunlight reflectance of 19% at the film-water interface.[65] The other strategy is to arrange suitable conductive substrates with unique architectures underneath the semiconductor photo-absorber, which is aimed at recycling the incident photons for higher solar utilization. For example, Qiu et al. separately deposited mesoporous Mo:$BiVO_4$ on the surface of the pre-designed SiO_x/Pt/SnO_2 nanocone substrate and flat substrate (Figure 1.8e-g), where the nanocone structure showed a stronger sunlight trapping resulting from multiple incident scattering.[49] The relevant simulations to the electromagnetic wave distribution (at λ=500 nm) over Mo:$BiVO_4$ samples on these two substrates illustrated theoretically that the nanocone region helped the diffraction and redistribution of incident photons, due to the distance of neighboring nanocones matching with the incident light wavelength. The corresponding UV-vis optical absorption spectra also verified the above results. Similarly, Wang et al designed and fabricated a CdS nanorod@SnO_2 nanobowl (NR@NB) array photoanode through in-situ growing CdS NRs on the inner surface of the SnO_2 NBs.[66] This novel hierarchical NR@NB architecture contained multi-scattering centers, enhancing the overall light harvesting capability. As a result, a dramatically improved PEC performance with the photocurrent density of 3.8 mA cm^{-2} at 1.23 V vs RHE is obtained, which is 2.5 times as high as that of the pristine CdS NR array. These two methods to reduce the optical loss can be employed to other semiconductor photoactive materials. Taking nanostructuring as an example, various semiconductor photoelectrodes, such as Si, metal sulfides, metal oxides, and metal nitrides, with precisely controlled morphologies and dimensions have been achieved until now. Noteworthily, except for reducing the optical reflection, structure engineering can also increase the surface-active sites, and suppress the bulk charge carrier recombination by shortening the diffusion length of minority carriers. Simultaneously, the major existing drawback is the enlargement of the photoelectrode/electrolyte interface area, easily leading to a more severe surface charge quench. Therefore, future strategy should be devoted to balancing strengths and weaknesses.

(iii) Narrowing bandgap via ion-doping or vacancy enriching. It has been proven feasible to narrow the bandgap of semiconductor materials through chemical doping with metal or non-metal atoms (e.g., Ni, Co, V, Cr, Pt, N, W, Mo, F, S, etc.).[56] For example, Yang et al. designed a core-shell S-doped "black" rutile TiO_2 photoabsorber, which is prepared by first forming a disordered TiO_{2-x} shell outside TiO_2 nanoparticles via molten Al reduction process and subsequently, doping sulfur into the vacancy-enriched shell layer by annealing procedure at H_2S atmosphere.[67] Diffuse reflectance spectrum (DRS) results demonstrated its bandgap value being 1.3 eV narrower than that of pure rutile TiO_2. After spin-coated on the FTO substrate for photoelectrode fabrication, the as-prepared S-doped rutile TiO_2 photoanode exhibited an increased photocurrent density at 1.23 V by a factor of nearly 30 compared with the pristine rutile TiO_2 and its onset potential also shifted negative by 280 mV. A better understanding example of regulating the energy band structure by changing the compositions is displayed in metal nitrides. Taking the GaN photoelectrode as an instance, it possesses lots of advantages, such as early onset potentials, a good fill factor, and suitable energy band positions for water-splitting reactions. However, the wide bandgap value (3.4 eV) limits its practical PEC performance. The pioneering reports pointed out that incorporating the additional metal In during the synthetic process can effectively reduce the bandgap value from 3.4 eV to 0.65 eV (pure GaN to pure InN), as shown in Figure 1.8h.[58] The variation of bandgap values is continuous and directly dependent on the concentration of doped In. The photostability of InGaN becomes the key challenge for its PEC water-splitting application. At present, changing the compositions to narrow the bandgap of semiconductor materials is one of the most prevalent strategies to enhance light absorption. By carefully adjusting the compositions, the spectrum absorption can be extended easily from UV to near-infrared region. However, the traditional solution-based synthetic methods make it hard to obtain stable and high-quality materials with low-defects, leading to unsatisfied solar conversion efficiency. Therefore, the long-term focus of such a strategy is still to develop a low-cost and reliable technique for solving the above issue.

(iv) The last common strategy used to broaden the spectrum absorption range involves coupling wide bandgap materials with narrow bandgap semiconductors.[56] Over the past years, great attention has been focused on this method. For instance, Mayer et al. designed a dual-absorber photoanode, fabricated by direct atomic layer deposition (ALD)-growing α-Fe_2O_3 thin film on the surface of Si NWs in a conformal fashion.[68] Owing to the narrower bandgap of Si (1.1 eV) compared with that of α-Fe_2O_3 (2.1 eV), the underlying Si NWs can supplementally absorb the incident photons transiting through the superficial α-Fe_2O_3 layer, thereby making full solar utilization. At the same time, the proper band alignment between them contributed to an appreciable band-bending depth, creating a larger photovoltage and promoting the rapid electron flow from the α-Fe_2O_3 layer to the inner Si NWs. Ultimately, the as-obtained dual-absorber photosystem presented a low turn-on potential of around 0.6 V and a significantly higher photoresponse compared to the photoelectrode with only α-Fe_2O_3 film on the FTO substrate. A similar result is proven by other composite photosystems, like the TiO_2/g-C_3N_4 combination, in which g-C_3N_4 thin film was deposited on the surface of TiO_2 nanorods.[69] In comparison with the pristine TiO_2, a clear red-shifted absorption edge is detected in the TiO_2/g-C_3N_4 heterostructure. Besides, the building of n/n heterojunction can also facilitate the directional charge carrier immigration between TiO_2 and g-C_3N_4. The synchronously improved quantum yield and efficiency ultimately enable a higher photocurrent density (1.15 mA cm^{-2} at 1.23 V vs RHE) in 0.1 M Na_2SO_4 electrolyte, 2.6 times higher than that of the pure TiO_2. Through analyzing these cases, an important note to consider in such a strategy is to manage charge flows. The disordered charge transport pathway within the junction will cause a great waste of photoexcitons even though the combination photosystem has a strong optical absorption. In reality, up to now, how to construct the intimate interface contact with high-speed charge transfer channels between two semiconductor phases remains a challenge. What's more, some metal nanoparticles and dye molecules can also be employed as photosensitizers to assist the light harvesting of wide bandgap semiconductors and achieve a series of advancements.

1.4.2 Enhancing the charge separation efficiency

The second critical factor affecting the overall solar conversion is the bulk charge carrier separation and transfer efficiency. Obtaining a high PEC water splitting performance demands an efficient separation of photo-excitons as well as rapid transportation to the appropriate active sites for the desired surface reaction.[70] To realize this goal, a series of methods and strategies are developed to minimize the charge loss within the bulk semiconductor, mainly including morphology design (matching the short diffusion length of minority carrier), elemental doping (increasing the donor/acceptor carrier concentration to accelerate the charge collection), crystal facet reengineering, various types of heterojunction fabrication, etc. Among them, constructing a heterojunction through combining two or more semiconductors with a well-coordinated band alignment is one of the most essential and prevalent strategies to promote the charge separation and transfer.

Herein, we will focus on elucidating the types, principles, and working mechanisms of heterojunction fabrication.

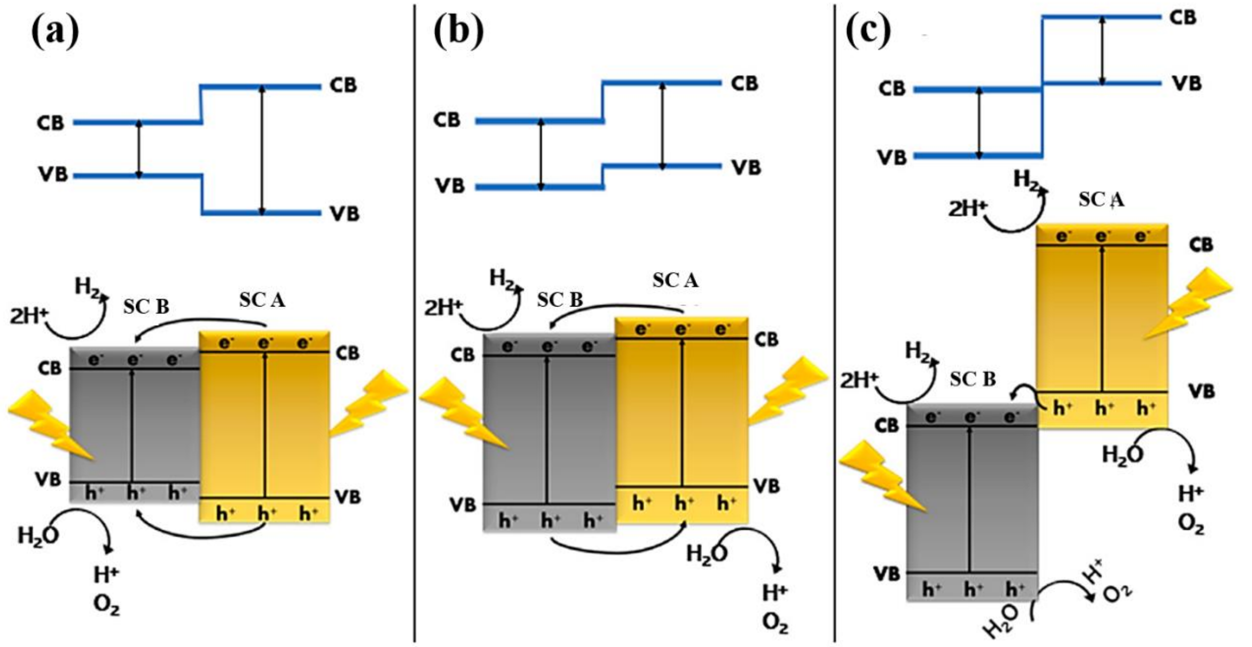

Figure 1.9 Schematic diagrams of semiconductor heterojunctions classified by energy band alignment: (a) Type-I, (b) Type-II, and (c) Type-III heterojunctions.[71]

A heterojunction is formed by two or more semiconductors in direct contact, which represents the contact interface inducing the facile charge transport between semiconductors. Heterojunction fabrication generally requires similar crystal structures, lattice spacing, and thermal expansion coefficients.[72] The mismatched lattice within the heterojunction easily causes weak bonding at the interface and generates defects, unfavorable for the charge transfer. Since the divergence in energy band structures, the semiconductor-based heterojunction can be classified into the following three types: (i) Type-I with straddling bandgap junctions (Figure 1.9a), where both photoexcited electrons and holes with transfer from semiconductor A to semiconductor B without any external bias. The accumulated photogenerated charge carrier will undergo a serve recombination process because of the narrower bandgap. In theory, the construction of Type-I heterojunction is not a good choice to enhance the PEC performance. (ii) Type-II with staggered bandgap junctions (Figure 1.9b), where the existence of energy gradient will drive the movement of photogenerated electrons and holes in the opposite direction, leading to the spatial separation and accumulation of electrons and holes in different semiconductors.[73] Therefore, the Type-II heterojunction fabrication via integrating wide and narrow bandgap materials is regarded as an effective approach to simultaneously improve the overall sunlight absorption and carrier dynamics.[74-76] During the past decades, a series of Type-II heterostructures with different nanoarchitectures have been explored, like stacking planar film, core/shell nanorods, quantum dots-decorated nanowires, etc. Compared with the single photo-absorber, these Type-II heterostructures, such as CdS/TiO_2,[77, 78] ZnO/CdS,[79, 80] CdS/MoS_2,[81] WO_3/$BiVO_4$,[82, 83] Ag_2S/CdS,[84] Ni_3S_2/CdS,[85] Co_3O_4/TiO_2,[86] CuS/WS_2,[87] Si/MoS_2,[88] $AgVO_3$/Mo:$BiVO_4$,[89] TiO_2/In_2S_3/CdS,[90] CdS/Cu_2O,[91] SnS_2/$CuInS_2$,[92] CdS/CdO,[93] WO_3/$BiVO_4$/$BiFeO_3$,[94] $BiVO_4$/Sb-SnO_2,[95] WO_3/$CdIn_2S_4$,[96] ZnO/TiO_2/CuO, etc.,[97] all demonstrated higher PEC performance and solar conversion efficiencies. (iii) Type-III with broken bandgap junctions (Figure 1.9c), where no directional charge transfer occurs.[72] Based on the above description, it is noticed that energy band alignments between semiconductors should be first considered when fabricating a heterojunction. A matched energy band position can accelerate the charge transfer for a better water-splitting reaction while a mismatched band alignment would form an energy barrier at the contact interface, causing the severe charge recombination behavior. Therefore, selecting suitable semiconductors with matched energy band structure become the top priority but is not easy.

Recently, Z-scheme heterojunction fabrication has attracted dramatic attention due to its various advantages. Unlike the traditional Type-II heterojunctions, separating photoexcited electrons and holes by sacrificing their redox potential, a powerful Z-scheme heterojunction not only improves the carrier dynamics but also preserves the strong oxidation and reduction ability of photoexcitons. Simply speaking, the Z-scheme heterojunction refers to the Z-shape charge transfer mechanism after the semiconductor photoexcitation, which is generally classified into three types: ionic, all-solid-state, and direct Z-scheme heterostructures (Figure 1.10).[72, 98-100] The detailed contents are described below.

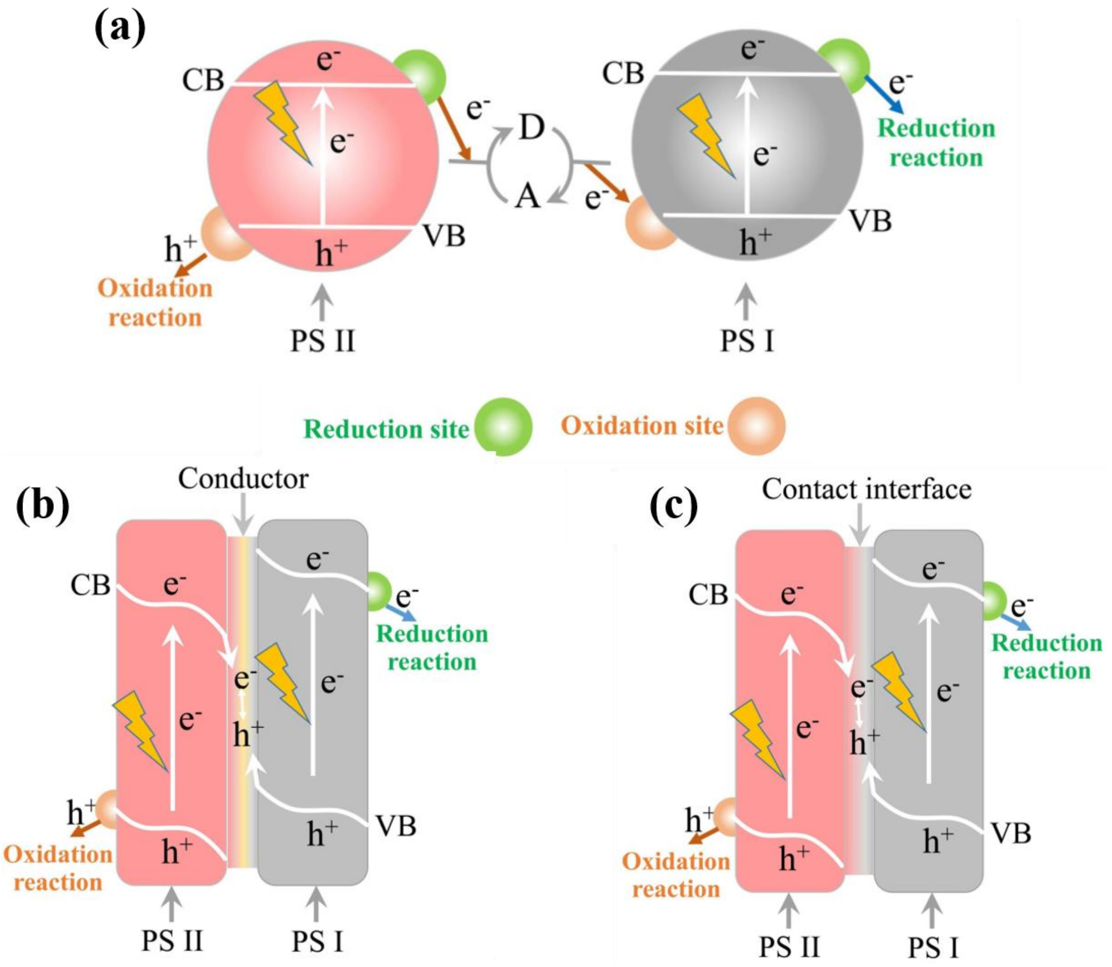

Figure 1.10 (a) ionic-state Z-scheme heterojunction, (b) all-solid-state Z-scheme heterojunction, and (c) direct Z-scheme heterojunction.[101]

The concept of ionic-state Z-scheme heterojunction was first introduced and applied in 1979. In such a special heterojunction, two semiconductors are not in direct contact. Redox shuttle ions will act as the electron mediator to accelerate the charge transfer, where the electron donor and acceptor will react respectively with the CB electrons of one semiconductor and the VB holes of the other semiconductor, indirectly inducing the charge recombination process. The separately remaining photoexcited electrons and holes in two semiconductors with the higher redox potential will take part in the photolysis of water. The common redox shuttle ions include Fe^{3+}/Fe^{2+}, NO_3^-/NO_2^-, IO_3^-/I^-, $[Co(phen)_3]^{3+/2+}$, $[Co(bpy)_3]^{3+/2+}$, etc. However, several serious drawbacks, such as the easy occurrence of back reaction, light-shielding effect of shuttle ions, and narrow scope of application, limit its prospects of development. To overcome these issues, an improved Z-scheme heterojunction of all-solid-state is explored and replaces its function. In general, a typical all-solid-state Z-scheme heterojunction consists of a metal nanoparticle as the electron mediator and two semiconductor photoabsorbers with the matched band alignment. Among them, the metal electron mediators with the ohmic contact, like Au, Ag, Pt, Cu, W, Cd, rGO, etc., play a key role in charge carrier transfer, which will work as the recombination centers to directly quench the photoexcited electrons and holes respectively from two different semiconductors. Some inspiring works have demonstrated the effectiveness of all-solid-state Z-scheme heterojunction in PEC water-splitting applications. For example, Wen et al., designed and fabricated a highly-active three-dimensional ZnO/Au/g-C_3N_4 Z-scheme heterojunction photocathode.[102] Through the time-resolved photoluminescence and electrochemical impedance characterizations, it is confirmed that Au nanoparticles act as the electron mediator to promote the vertical Z-scheme charge transfer between ZnO and g-C_3N_4. As a result, the formed ZnO/Au/g-C_3N_4 Z-scheme heterostructure showed a significantly increased PEC H_2 production efficiency. The other convincing case involves using undamaged large-area rGO film as the electron mediator to construct the ZnO quantum dots/rGO/$FeVO_4$ pure Z-scheme heterojunction.[103] The results indicated that the pure Z-scheme heterojunction can effectively promote the spatial charge separation and simultaneously, retain their redox capability. However, the strategy of all-solid-state Z-scheme heterojunction also suffers from the light-shielding effect of the electron mediator and the bad long-term stability. Thus, further development is necessary.

To actualize the prospect of this strategy, the unique direct Z-scheme heterojunction mimicking nature photosynthesis is developed. In such a heterojunction, when two semiconductors with different energy levels are in direct contact, the electron drifting behavior takes place until reaching an equilibrated Fermi level. Then, the localized electrons and holes on two sides of the interface will induce the formation of the space charge layer (band bending) with the built-in electric field. Under sunlight illumination, the formed built-in electric field will drive the rapid recombination process between the CB electrons and VB holes with the weaker redox potential from different semiconductors. In the meanwhile, the water oxidation and reduction reaction will separately occur at the CB and VB with the higher redox potential. Comparatively, the no-mediator Z-scheme heterostructure presents the obvious superiority, in which the direct charge transfer through the contact interface can largely shorten carrier diffusion length, strengthen the charge recombination, and increase the built-in photovoltage. As a result, the inherent shortcomings in the ionic or all-solid-state Z-scheme heterojunctions are well overcome. Some representative examples, such as black phosphorus/monolayer $BiWO_4$,[104] black phosphorus/red phosphorus,[105] Sb_2Se_3/Fe_2O_3,[106] etc. direct Z-scheme heterojunctions, have been displayed by the previous reports. At present, the construction and characterization of direct Z-scheme heterojunctions is still challenging and attracts great researchers' interest.

Except for the conventional and Z-scheme heterojunctions mentioned above, there are also some other special nanojunction fabrications in favor of facilitating the separation and transportation of photoexcited charge carriers, mainly including semiconductor p-n junctions, semiconductor/metal junctions, semiconductor/carbon nanomaterial junctions, and facet isotype heterojunctions.[107] Although so many approaches and strategies have been put forward and exploited, the practical efficiency improvement is still very limited, far from the scale-up industrial application. Therefore, there is still much work to be done and more factors should be considered to make a reliable alternative PEC device.

1.4.3 Improving the surface charge injection efficiency

The third critical factor affecting the overall solar-to-hydrogen conversion is the surface charge injection efficiency, which generally involves the following three major aspects: surface catalysis, photovoltage, and surface recombination. Their working mechanisms are intricately interconnected. For example, better surface catalysis commonly implies a faster forward charge output and reduced surface charge recombination. Also, the higher photovoltage means a much more efficient charge separation with the remarkably suppressed surface charge recombination. In terms of this, several strategies have been exploited to improve the above three functionalities. One of the most straightforward approaches is to decorate the passivation layer on the photoelectrode surface. For example, a series of metal oxides, like Al_2O_3, In_2O_3, and Ga_2O_3 thin layers, have been coated on the hematite photoanode via the urea hydrolysis CBD process, where the hematite/electrolyte interface is replaced by the hematite/oxide/electrolyte interface.[108] Through implementing this idea, it is expected to weaken the Fermi level pinning effect and passivate the surface defect states, thereby improving the overall photovoltage and decreasing the turn-on potential. As tested, Ga_2O_3 film as a better and highly efficient passivation layer can cathodically shift the onset potential by 0.4 V, which is majorly attributed to the matched crystal structure between hematite and Ga_2O_3. In addition, except for reducing the surface recombination, the versatile passivation layer can also act as the protection layer to improve the overall photostability and as the catalytic layer to strengthen the surface reaction kinetics. The key challenge is to select the suitable passivation material via analyzing the origins of surface recombination.

Loading redox cocatalysts is the other common and prevalent approach to improve the utilization of superficially photogenerated charge carriers. In general, even though the semiconductor photoabsorber possesses the suitable energy band structure for water splitting reaction, the formed intermediate species on most photoelectrode surfaces will produce a large energy barrier to O_2/H_2 generation, thereby an overpotential is needed to overcome this kinetic barrier and drive the desired water oxidation/reduction reactions.[33, 109-111] In this case, the main role of cocatalysts is to provide the reaction active sites for lowing the activation energy and also, suppress the surface charge recombination via rapidly accepting the photoexcited electrons or holes. Noteworthily, with the aid of cocatalysts, the surface reaction sites vary from the semiconductor/electrolyte interface to the cocatalyst/electrolyte interface, which can effectively avoid the back reaction and simultaneously protect the semiconductor photoabsorber from photocorrosion.[112]

According to the divergence of function features, cocatalysts can be classified into oxidation catalysts or reduction catalysts. For the water-splitting reaction, they are also denoted as oxygen or hydrogen evolution cocatalysts. Generally speaking, hydrogen evolution cocatalysts mainly consist of noble metal materials (e.g., Pt, Au, Ag, Ru, Pb, Ir, Ni, and their alloys) and non-noble metal materials, such as MoS_2, Ni_2P, NiO_x, etc. In particular, Pt was regarded as one of the most effective HER cocatalysts due to its Gibbs free energy of hydrogen absorption near zero.[113] Oxygen evolution cocatalysts are mainly composed of transition metal oxides (e.g., RuO_x, CoO_x, IrO_x, MnO_x, etc.), metal boron or phosphates (e.g., Co-Pi and Ni-Bi), metal-based (oxy)hydroxide (e.g., FeOOH, CoOOH, NiOOH), and the layered double hydroxide (LDH), like the CoAl-LDH material.[114, 115] Although a great number of HER or OER cocatalysts have been developed, appropriately integrating cocatalysts with well-architected photoelectrodes to facilitate the desired surface redox reactions is still a difficulty for the design of PEC devices. Unlike the electrocatalytic hydrolysis process, the core of PEC devices is the semiconductor photoabsorber, thus enabling maximum sunlight harvesting by minimizing the light-shielding effect from cocatalyst loadings is important.[116] Furthermore, selecting the suitable cocatalyst deposition methods to avoid damage to the semiconductor scaffold and simultaneously, optimizing the contact interface between the semiconductor and cocatalysts to boost the interfacial charge transfer dynamics are also of great importance.

In addition, some other special surface treatment methods, such as the surface reconstruction via changing the crystal structure of the semiconductor surface to reduce the surface defect state,[117] forming buried p-n junction for increasing the band bending and photovoltage,[118] surface hydrogen-treatment for enriching vacancies,[119] are also proven effective for improving the surface charge injection efficiency and desired surface reaction kinetics, which will not be introduced in detail here.

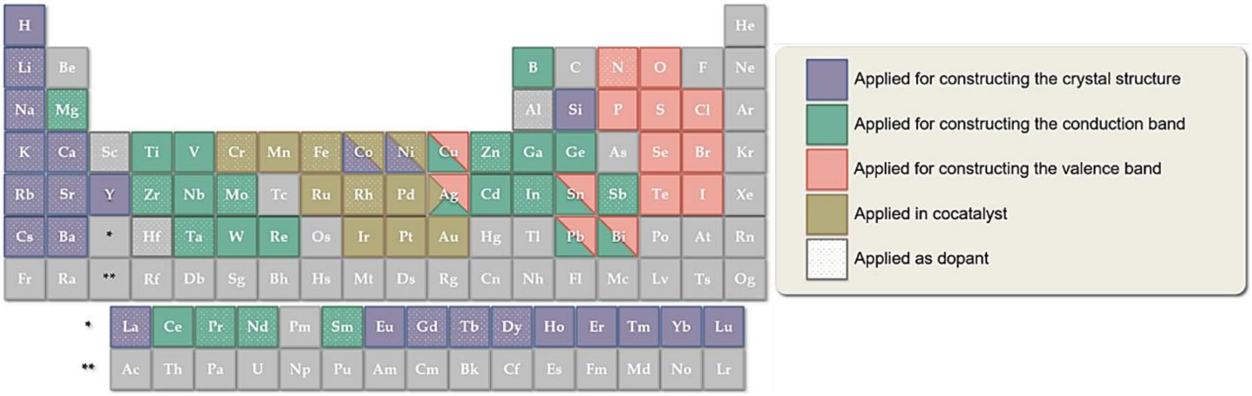

Figure 1.11 Elemental composition and their roles in semiconductor photoabsorbers.[120]

1.5 Semiconductor photoactive materials for PEC hydrogen evolution

As the core of PEC devices, semiconductor-based photoabsorbers are always the focus of the photoelectrode design. Since the pioneering development of TiO_2 photoanode in 1979, various semiconductor photoactive materials have been investigated and employed for PEC water-splitting, achieving great progress. As proven, an ideal photoelectrode material should possess the following characteristics: (i) Suitable bandgap and energy band potentials. As mentioned above, when combining the redox potential of water-splitting with the overpotential requirement and the possible thermodynamic energy loss, the efficient bandgap value for a single semiconductor photoabsorber should be over 1.8 eV, corresponding to the absorption wavelength of approximately 800 nm. Considering the energy density distribution of the solar spectrum (5% of UV, 43% of visible light, and 52% of near-infrared light) and the rapidly dropping sunlight intensity below 390 nm, the maximum bandgap value should be within 3.2 eV. In theory, a bandgap value of around 2.0 eV is preferred for enabling sufficient sunlight harvesting in the visible region and optimal solar utilization. Additionally, the matched band edge positions with the oxidation and reduction potentials of water are also important to support the occurrence of the reaction. However, practically, seldom semiconductors can meet these requirements at the same time. Adopting suitable modification strategies listed above to tune the energy band structure is inevitable; (ii) High bulk charge separation and transport efficiency; (iii) Rapid surface charge injection and superior catalytic activity. The above three factors directly determined the overall quantum yield and efficiency of a semiconductor photoelectrode. Apart from these, the wonderful photoelectrode material should also be composed of earth-abundant elements and possess photochemical stable, low-cost, and non-toxic properties for its future industrial application.

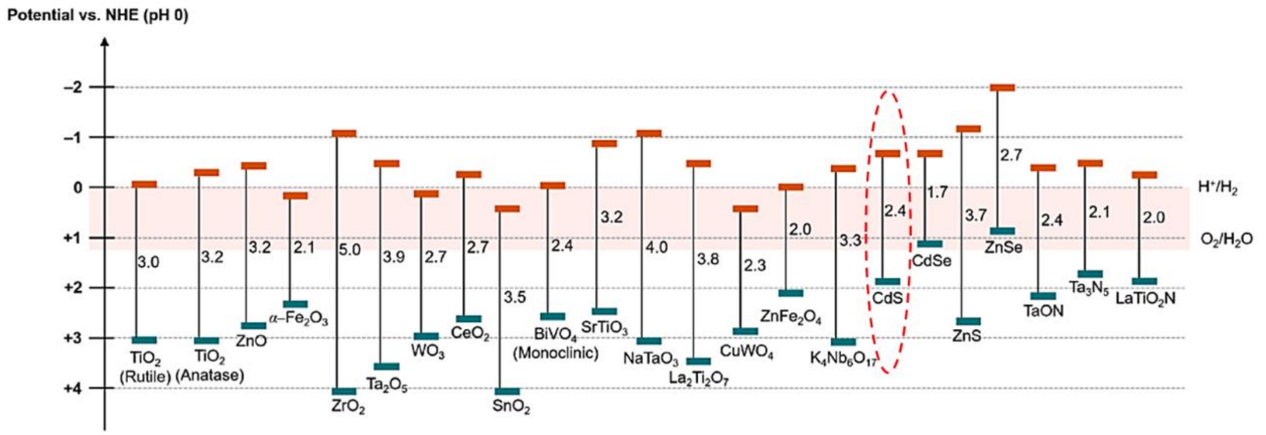

Figure 1.12 The energy band structure of CdS in comparison with the water redox potentials and those of other commonly reported semiconductor photocatalysts.[120]

1.5.1 Semiconductor-based photoanode materials

In a typical PEC system, the anodic water oxidation process, involved in the complex exchange of four electrons to produce one oxygen molecule, usually acts as the rate-limiting step in catalysis, largely affecting the entire solar-to-hydrogen conversion. Therefore, seeking desirable photoanode materials with wonderful optical absorption, sufficient overpotential, excellent charge separation, and transport efficiency is urgently demanded but still remains challenging. The photoanode materials usually consist of n-type semiconductors, where the band bending with the formed electric field can drive the holes toward the photoanode surface for the desired oxidation reaction. Over the past decades, the most commonly used photoanode materials belong to the classic binary metal oxides, composed of the O^{2-} anion and transition metal cations with d^0 configurations (Ti^{4+}, Zr^{4+}, V^{5+}, Ta^{5+}, Nb^{5+}, and W^{6+}), as shown in Figure 1.11.[120] Due to the high electronegativity of the oxygen constitute, these binary-metal oxide photoanodes, like TiO_2 (E_g: ~3.2 eV) and WO_3 (E_g: ~2.7 eV), can be prepared easily and also relatively stable during the PEC water-splitting process, thereby gaining great attention.[30, 121] However, these metal oxides with empty *d* bands generally have highly positive valence band levels (at around +3 V vs RHE at pH=0), dictated directly by O 2p orbitals, making their bandgaps too large to efficiently harvest the solar energy. In terms of this, a large number of novel semiconductors with narrow bandgaps and wide sunlight absorption regimes, such as oxides, oxy-halides, oxynitrides, metal chalcogenides, chalcopyrites, Silicon, carbon-based semiconductors, etc., have emerged as visible-light-driven photoanodes for the efficient solar hydrogen evolution. For instance, metal oxides with d^n band cations often present narrow bandgap values and good photostability stability. The representative examples are Fe_2O_3 (E_g: ~2.1 eV) and Co_3O_4 (E_g: ~1.3 eV), whose bandgaps are largely affected by *d-d* transitions.[122] However, since the low polaron conductivity (Polaron is defined as the electrons that are self-trapped in a local lattice distortion induced by the electron's own charge), the problems of short carrier mobility and slow charge separation usually appear over this class of metal oxides. Besides, coupling *s*^{2} band cations (e.g., Bi^{3+} and Sn^{2+}) with *d*^{0} cations can also tune the bandgaps of metal oxides and give rise to a smaller bandgap by creating more negative VBs than O 2p orbitals.[123] A typical example is $BiVO_4$, which has a narrow bandgap of around 2.4 eV and is reported as one of the most promising photoanode materials for PEC application. In addition to modifying the VB levels using the metal cations, introducing a higher-lying *p*-band energy level by replacing oxygen anions with nitrogen or sulfide anions can also decrease the bandgaps. Taking the typical tantalum oxide (Ta_2O_5) as an example, its valence band maximum (VBM) shifts to the more negative potentials after nitrification. The relevant DFT calculation of electronic band structures proved that the VBMs of Ta_2O_5, TaON, and Ta_3N_5 predominantly consist of O 2p, N 2p + O 2p, and N 2p orbitals, respectively.[124] Accordingly, the formed products, TaON and Ta_3N_5, present the narrower bandgaps of around 2.5 eV and 2.1 eV, and their sunlight absorption edges are also extended to approximately 500 nm and 600 nm, respectively. As a potential photoanode material, TaON shows high electron mobility and appropriate VB position for water oxidation but always suffers from the bad thermodynamic stability. Apart from (oxy)nitrides, metal chalcogenides are also deemed as particularly promising candidates for the fabrication of visible-light-driven photoanodes. Because of their VBs consist of the higher-lying *p* orbitals than oxygen, these metal chalcogenides usually have narrow bandgaps and visible-light absorption capability. Noteworthily, Cadmium sulfide (CdS) as a typical metal chalcogenide exhibits excellent charge separation and transport properties, simultaneously possessing the matched band alignment with water redox potential, which has been used as a high-performance photoanode material for decades. Herein, we will also use CdS with highly oriented nanostructure as the host materials for further modification. Its crystal structure and recent progress are described below.

1.5.2 1D CdS nanoarray photoanode

As one of the most important II-VI semiconductor compounds, CdS possesses fantastic electronic and optoelectronic properties and is widely applied in different fields of flat band displays, sensors, thin film transistors, logic gates, light emitting diodes, non-linear optical devices, lasers, near-field optical lithography, etc.[125] Over the recent decades, CdS photoactive material has also received much attention in PEC research owing to its fundamental material characteristics, mainly including the narrow direct bandgap (~2.4 eV at 300 K, capable of light absorption up to 520 nm), suitable energy band structure (straddling well with the water redox potentials), high electron mobility, and excellent charge transport properties. Meanwhile, its negative conduction band potential is about 0.6 V less than the H^+/H_2 energy level (Figure 1.12),[120] which allows the spontaneous hydrogen reduction process. More importantly, the CdS surface can be readily functionalized using various ligands, which not only endow them with either hydrophilic or hydrophobic features but also benefit their interconnection with other functional materials.[126, 127] As a result, CdS is deemed as a particularly promising photoanode material for PEC hydrogen production, and its synthesis and improvement have always been a hot research spot.

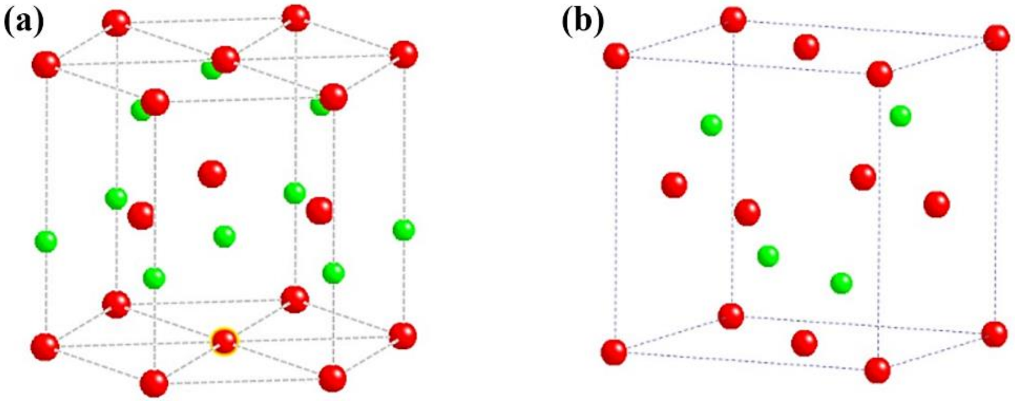

Figure 1.13 Two crystal structure of CdS: (a) hexagonal (wurtzite) and (b) cubic (zinc blende). Red and green balls represent Cd and S atoms.[128]

As well known, CdS can exist in both cubic (zinc blende) and hexagonal (wurtzite) crystal structures, where these two phases are similar in some aspects. As displayed in Figure 1.13, the stacking model in the close-packed planes of zinc blende is followed by the repeated ABCABCABC pattern, whereas in that of wurtzite is presented by the repeated ABABAB pattern.[125, 128] Wurtzite CdS is usually thermodynamically more stable and can be defined as a couple of alternating planes consisting of tetrahedrally coordinated S^{2-} and Cd^{2+} ions stacking along the *c*-axis. Thus, CdS deposited at a higher temperature above 473 K generally exhibits the hexagonal structure and shows a cubic structure at a lower temperature. The other major structural feature of CdS involves its polar surfaces. The basal plane is the most famous polar surface. The oppositely charged ions induce positively charged Cd (0001) and negatively charged S $(000\bar{1})$ polar surfaces, causing a dipole moment, which can lead to spontaneous polarization along the *c*-axis and surface energy divergence.[129] Furthermore, the anisotropic growth of wurtzite CdS predominantly originates from the discrepancy over surface energies, surface polarity, and chemical activity of different crystallographic planes.

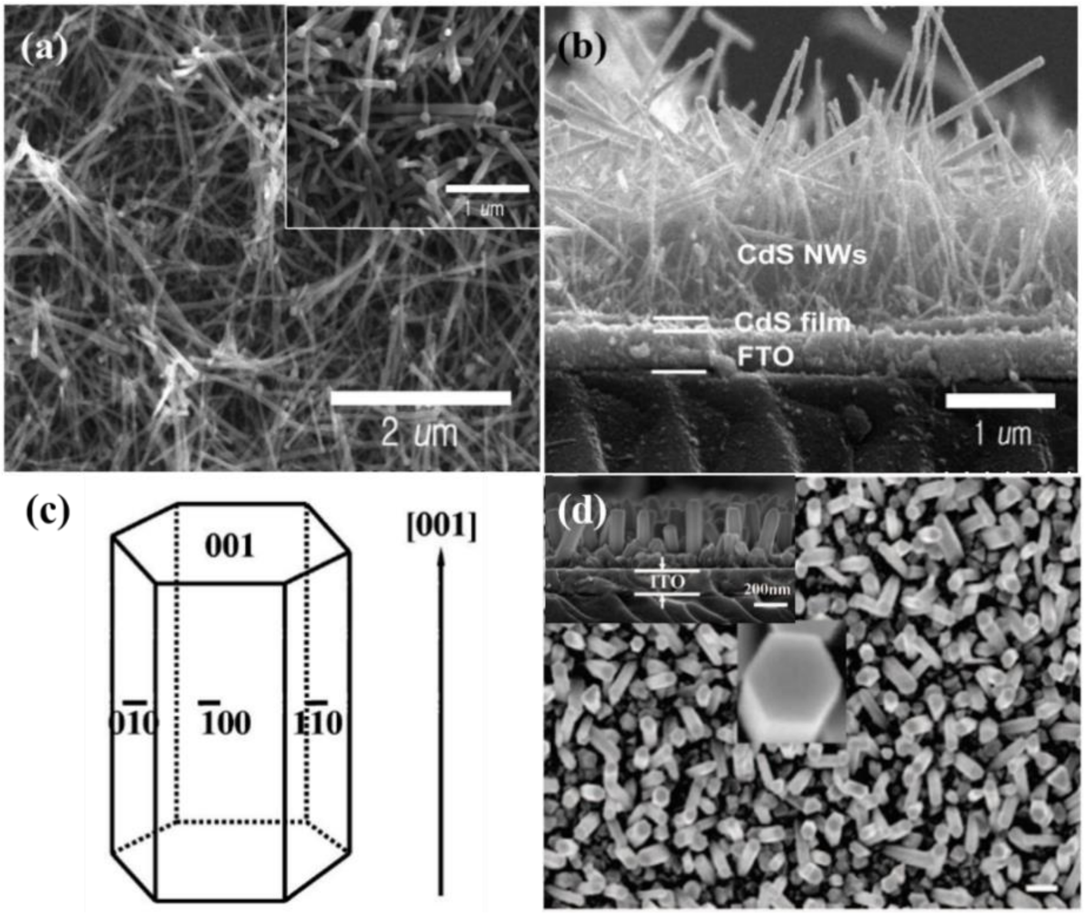

Figure 1.14 (a, b) The top-view and cross-sectional SEM images of CdS nanowire arrays on the FTO substrate reported.[130] (c) The preferential [001] crystal growth of CdS nanorod and the corresponding SEM images.[131]

As an important branch of CdS-based PEC research, the one-dimensional CdS nanoarray photoanode has stimulated a growing interest because of its unique optical, structure, and electronic features. As mentioned above, nanostructuring with well-defined size and shape plays a key role in determining the PEC performance of semiconductor photoabsorber. Particularly, 1D nanostructures are ideal systems for investigating dimensionality-dependent functional properties.[125, 127, 129] The pioneering studies pointed out that compared with the thin film and block material, 1D CdS nanoarrays illustrate the following advantages: (i) A high aspect ratio. Generally, a typical 1D CdS nanostructure, especially a nanorod, is fabricated with a high length-to-diameter ratio, which is capable of improving light anti-reflectance and scattering properties, thereby enhancing the overall sunlight harvesting capability. (ii) Efficient charge collection. The building of the high-oriented 1D nanostructure defines a direct charge transport pathway along the long axis (hundreds of nanometers). Considering the sufficient electron diffusion length of around 0.65 µm in CdS, the photogenerated electrons can be effectively collected by the substrate for PEC hydrogen evolution. (iii)

Better bulk charge separation. The 1D nanostructure can shorten the diffusion length of minority carriers (holes for CdS), and readily match it with the penetration depth of sunlight, thereby reducing the radiative recombination and promoting the bulk charge separation. (iv) lager specific surface area and more exposed surface-active sites. Therefore, combining the intrinsic structural characteristics of CdS with the above merits of 1D nanostructure, 1D CdS nanoarray photoanode exhibits great prospects for future practical application. According to previous reports, the fabrication of 1D CdS nanostructure primarily depends on the anisotropic growth of crystals and the surface energies of terminating facets. Barth et al. indicated that the assistance of surfactant is essential for the preparation of 1D structure, which helps to modulate the specific surface energy of the growing structure.[132] The final morphology is mainly owing to the crystallographic phases and the balance between thermodynamic and kinetic growth regimes. The past decades have witnessed explosive development in the preparation approaches of 1D CdS powder samples, such as hydrothermal/solvothermal, colloidal micellar, chemical vapor deposition, physical evaporation, template-assisted methods, etc.[127] However, only a few researches on the growth of vertical-aligned 1D CdS nanoarray on the conductive substrate have been reported yet. For example, Qian et al. successfully synthesized 1D CdS nanowire arrays on the Cd-foil through a solvothermal process.[133] Xu et al. fabricated the vertical-aligned CdS nanorod arrays on the ITO substrate via the electrodeposition with the anodic aluminum oxide as a template.[134] Sung et al. grow CdS nanowire arrays on FTO substrate by the solution-liquid-slide (SLS) method using Bi catalysts (Figure 14a and b).[130] Comparatively, Chen et al. put forward a template-free and facile one-step hydrothermal approach to prepare 1D CdS nanorod arrays on ITO substrate (Figure 14c and d), where the glutathione was used as the capping agent to limit the growth of low-energy facets.[131] This method largely reduces the preparation complexity of 1D CdS nanoarrays and increases its applicability for further modification.

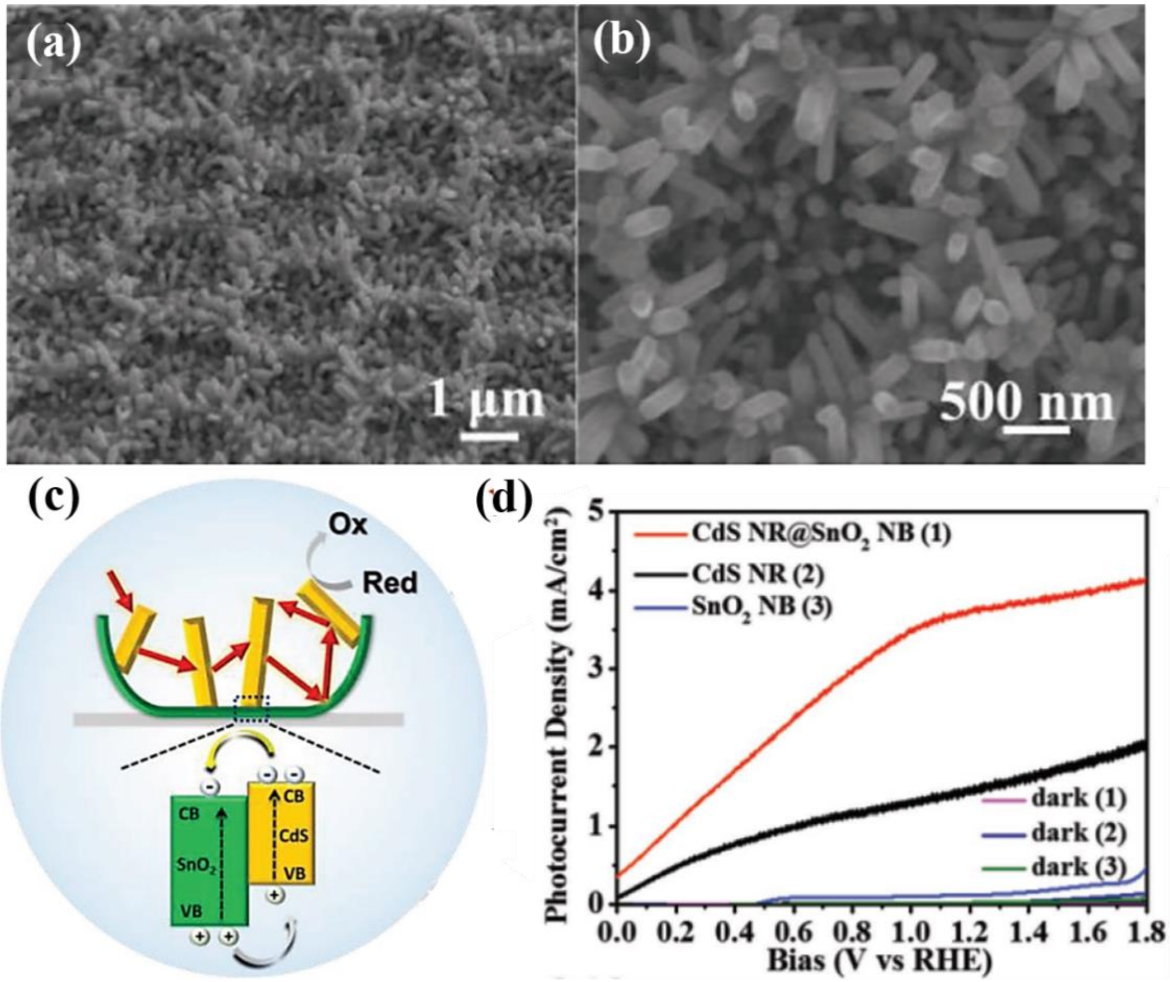

Figure 1.15 (a, b) The SEM images of CdS nanorod@SnO_2 nanobowl heterojunction photoanodes; (c) The charge flow model; (d) PEC performance evaluation based on LSV curves.[66]

Although the huge structural advantages and development potential of the 1D CdS nanoarray photoanode, its practical solar conversion efficiency is far from satisfactory due to the rapid bulk and surface recombination of photoexcited electron-hole pairs. In addition, photostability is the other concern associated with the PEC hydrogen evolution of CdS photoanode. Due to the lower oxidation potential of S^{2-}, it is readily self-oxidized by surface-accumulated photogenerated holes, resulting in the occurrence of severe photocorrosion. To overcome these shortcomings, a series of surface modification strategies have been examined. Among them, the fabrication of 1D CdS-based heterojunctions is one of the most prevalent methods for boosting the charge carrier separation and improving the solar-to-hydrogen conversion efficiency. For instance, Cho et al. reported a Z-scheme heterojunction photoanode composed of CdS/CdO core-shell nanorod array.[135] Through the relevant Mott-Schottky and open-circuit potential analysis, it is proven that when the CdO shell thickness is equal to or smaller than the width of the space charge region, the formed CdS/CdO nanorod photoanode exhibits the highest photovoltage. As a result, this optimum

CdS/CdO Z-scheme heterojunction photoanode exhibits a considerably improved photocurrent density, up to ~ 4.35 mA cm^{-2} at 0 V vs SCE. Wang et al. successfully synthesized a CdS nanorod@SnO_2 nanobowl heterojunction photoanode via the hydrothermal process as shown in Figure 1.15. The unique hierarchical nanoarchitecture contributes to the enlarged surface area, improved light harvesting, and enhanced charge separation/collection efficiency, ultimately leading to much higher photocurrent density of 3.8 mA cm^{-2} at 0 V vs RHE. Further coating the SiO_2 thin layer on the photoanode surface can enhance the overall photostability. Zhu et al. prepared a novel p-n heterojunction photoanode via directly sensitizing 1D CdS nanorod array with p-type β-$Ni(OH)_2$ nanoparticles.[136] Experiments demonstrated that the unique band structure and the fabrication of the p-n junction are favorable for the separation and transfer of photoexcited charge carriers, suppressing the charge recombination, prolonging the carrier lifetime, and simultaneous photoanode protection. Finally, the fabricated β-$Ni(OH)_2$@CdS core-shell photoanode shows a drastically enhanced H_2 production rate, reaching up to 762.5 μmol h^{-1}, 8 times higher than that of the pure CdS photoanode. In spite of great progress having been made on the fabrication of 1D CdS-based photoelectrodes, the obtained PEC performance is distant from the industrial scale. Indeed, intrinsic charge transfer and photoconversion still need further improvement by employing new modification strategies and optimizing the interface junctions.

1.6 Thesis objectives

As mentioned above, to accomplish a reliable PEC device for highly efficient photoconversion, one major challenge is still the design and manufacture of semiconductor photoanodes with wonderful light harvesting, superior photochemical stability, efficient charge carrier separation, and strong redox ability. As a typical visible-light-driven metal sulfide, cadmium sulfide (CdS), especially one-dimension (1D) oriented CdS nanoarray, shows an excellent potential for solar hydrogen evolution due to its suitable energy band structure, great electrical/optical properties, larger aspect ratio, and confined charge transfer pathway for lower carrier loss. Nevertheless, the rapid bulk and surface recombination of photoexcited electron-hole pairs and severe photocorrosion restrict its practical application. Therefore, in my thesis research, 1D CdS nanorod arrays on the FTO substrate are used as the host material. To overcome its intrinsic drawbacks, the rational design of 1D CdS-based nanojunctions, like conventional Type-I, Z-scheme, and plasmon-enhanced heterostructure, has been employed to optimize the overall photon management and quantum efficiency, ultimately achieving the significantly improved PEC performance. The possible PEC enhancement mechanism and interfacial charge transfer pathway have been discussed in detail. The objectives of this thesis are listed as follows:

(1) In our first project, the conventional heterojunction fabrication is selected to modify the pure 1D CdS

nanoarray photoanode. To overcome the limited contact interfaces, the chemical vapor deposition (CVD) technique was for the first time used to construct the CdS/MoS_2 heterojunction photoanode with a unique core-shell nanoarchitecture, in which a continuous crystalline MoS_2 nanosheet layer was grown directly on one-dimensional (1D) oriented CdS nanorods (NRs) in a plane-to-plane stacking fashion. The optimization of junction thickness with adjustable MoS_2 loading from mono to a few layers was achieved by experimental parameters variation. Systematic characterizations show that the MoS_2 shell plays a dual role as an optical absorption booster for more photo-exciton generation and a surface passivator of trap states. Meanwhile, the formed heterojunction helps regulate the unidirectional charge migration for a significantly suppressed electron-hole recombination process, which synergistically contributes to the significantly improved photocurrent density and photostability. This work is expected to provide a versatile platform for exploiting the CVD technique to develop other MoS_2-based heterojunction photoelectrodes with extensive PEC applications.

(2) In our second project, an innovative pure Z-scheme heterostructure, CdS/Au/SnO_2-S, composed of 1D oriented CdS nanorods modified with SnO_2-wrapped Au nanoparticles (NPs), was designed as a photoanode for highly efficient PEC hydrogen evolution. Systematic studies confirm that the incorporated Au NPs not only act as the host platform to support the SnO_2 layer growth but also play a key role as the electron mediator for strengthening the vectorial charge transfer from SnO_2 to CdS. This reinforced Z-scheme charge transportation channel is favorable for suppressing the bulk charge recombination process, increasing the overall carrier density, and preserving the strong redox capability, ultimately resulting in a considerably improved photocurrent density and photo-to-current conversion efficiency with better corrosion resistance.

(3) In our third project, we designed a plasmonic hierarchical nanorod array, composed of oriented 1D CdS nanorods decorated with uniformly wrapped graphite-like carbon (C_{PDA}) layer and Au nanoparticles (Au NPs), as highly efficient photoanode material. An interfacial in-situ reduction–graphitization method has been conducted to prepare the CdS/C_{PDA}/Au nanoarchitecture, where a polydopamine (PDA) coating was used as the C source and reductant. The formed plasmon-enhanced CdS/C_{PDA}/Au nanoarray photoanode demonstrates a superior photoconversion efficiency with significantly improved photostability. The underlying PEC enhancement mechanism was studied thoroughly. This work provides an effective strategy to in-situ reduce plasmonic metals and optimize the interfacial connection between noble metals and the semiconductor, which is instructive for designing and fabricating other plasmon-enhanced PEC systems for improved solar energy conversion

CHAPTER 2

MATERIALS AND CHARACTERIZATIONS

2.1 Chemicals and reagents

In this thesis, the mainly involved chemicals were listed as follows: cadmium nitrate tetrahydrate ($Cd(NO_3)_2·4H_2O$, 98% purity, Sigma-Aldrich), thiourea (NH_2CSNH_2, ≥ 99% purity, Sigma-Aldrich), molybdenum trioxide (MoO_3, ≥ 99.5% purity, Sigma-Aldrich), sulphur powder (S, ≥ 99% purity, Sigma-Aldrich), glutathione ($C_{10}H_{17}N_3O_6S$, ≥ 98% purity, Sigma-Aldrich), tris(hydroxymethyl)- aminomethane ($NH_2C(CH_2OH)_3$, ≥ 99.8% purity, Sigma-Aldrich), hydrochloric acid (HCl, 37% purity, Sigma-Aldrich), dopamine hydrochloride ($C_8H_{12}ClNO_2$, Sigma-Aldrich), Gold (III) chloride solution ($HAuCl_4$, 30 wt.%, Sigma-Aldrich), Tin (II) chloride ($SnCl_2$, 98%, Sigma-Aldrich), methanol (CH_3OH, ≥ 99.8%, Sigma-Aldrich), ethanol (C_2H_6O, 95%, Sigma-Aldrich), sodium sulfide nonahydrate ($Na_2S·9H_2O$, 98% purity, Sigma-Aldrich), sodium sulfite (Na_2SO_3, 98% purity, Sigma-Aldrich). All these commercially available chemicals were utilized directly without any purification. Fluorine-doped tin oxide (FTO) conductive glass substrates (15 Ω/sq) and deionized water (18.2 MΩ) were used throughout the whole material preparation and PEC measurements.

2.2 Material characterization techniques

In our study, various physical characterization methods were used to measure the optical properties, morphologies, compositions, and nanostructures of the as-prepared photoanodes, which are listed as follows: The exploration of crystallinity and structural features was taken on an X-ray diffractometer (Bruker D8 advance, Cu-Kα, λ = 1.5406 Å) and Raman spectrometer (Renishaw confocal microscope) with the excitation laser of 532 nm. The surface chemical compositions were precisely analyzed by X-ray photoelectron spectroscopy (XPS PHI 5600-ci, Eden Prairie, MN, USA) with a monochromatized Al Kα small-spot irradiation. Surface work functions were determined by UV photoelectron spectroscopy using a He-I photon source (21.2 eV) The microstructure and surface morphologies were cautiously collected via a JSM7600F field emission scanning electron microscope (FESEM) and a Multimode8 (Bruker) atomic force microscope (AFM). Transmission electron microscopy (TEM) and high-resolution TEM investigations were conducted on a Jeol JEM-2100F TEM instrument equipped with the energy-dispersive X-ray detector (STEM-EDX). Photophysical information was obtained on a Lambda 750 UV-visible spectrometer. Inductively coupled plasma optical emission spectrometry (ICP-OES, Agilent Technologies, 5100) was employed to detect the relevant metal elemental contents in the as-prepared CdS/Au/SnO_2-S photoanode. A PE LS-45 fluorescence spectrometer was applied to record the photoluminescence (PL) spectra at room temperature using a 375 nm excitation wavelength. The time-resolved PL (TRPL) data was collected using a time-correlated single photon counting system with a pulsed diode laser (375 nm, Edinburgh Instruments FLS900). Besides, the PL method was also selected to detect the hydroxyl radical (·OH) formed during the photoreaction process, and terephthalic acid was used as the probe molecule. Specifically, powder photocatalysts scraped from FTO substrates were dispersed into a mixed aqueous solution (5 mL) of terephthalic acid (0.5 mM) and NaOH (2 mM) under vigorous stirring, which was then irradiated by simulated sunlight (AM 1.5G) for 3 h. After the photoreaction, a 315 nm excitation wavelength was used to look at the solution with a QuantaMaster 40 spectrofluorometer.

CHAPTER 3

ENGINEERING INTERFACIAL BAND HOLE EXTRACTION ON CHEMICAL-VAPOR-DEPOSITED MOS_2/CDS CORE-SHELL HETEROJUNCTION PHOTOANODE: THE JUNCTION THICKNESS EFFECTS ON PHOTOELECTROCHEMICAL PERFORMANCE

Zhiyuan Peng[a], Yilu Su[a], Maziar Jafari[a] and Mohamed Siaj[a*]

Published article for this study: Engineering interfacial band hole extraction on chemical-vapor-deposited MoS_2/CdS core-shell heterojunction photoanode: The junction thickness effects on photoelectrochemical performance, *J. Mater. Sci. Technol.* 167 (2023) 107-118. https://doi.org/10.1016/j.jmst.2023.05.036

Department of Chemistry and Biochemistry, Université du Québec à Montréal, Montréal QC, H3C 3P8, Canada

*Corresponding author, E-mail: siaj.mohamed@uqam.ca

This Chapter has been shown in the following manuscript: (Zhiyuan Peng et al., 2023).

3.1 Abstract

Heterojunction fabrication is a promising strategy that can greatly boost the charge carrier separation and improve the solar-to-hydrogen conversion efficiency of photoelectrochemical (PEC) cells. However, such technology still suffers from limited contact interfaces. In this study, the chemical vapor deposition (CVD) technique was for the first time used to construct the CdS/MoS_2 heterojunction photoanode with a unique core-shell nanoarchitecture, in which a continuous crystalline MoS_2 nanosheet layer was grown directly on one-dimensional (1D) oriented CdS nanorods (NRs) in a plane-to-plane stacking fashion. The optimization of junction thickness with adjustable MoS_2 loading from mono to a few layers was achieved by experimental parameters variation. Systematic characterizations show that the MoS_2 shell plays a dual role as an optical absorption booster for more photo-exciton generation and a surface passivator of trap states. Meanwhile, the formed heterojunction helps regulate the unidirectional charge migration for a significantly suppressed electron-hole recombination process, which synergistically contributes to higher quantum yield and efficiency. As a result, the optimized CdS/MoS_2 heterojunction photoanode with 3-layered MoS_2 wrapping exhibits the highest photocurrent density and photoconversion efficiency, over a two-fold increase, compared to those of pristine CdS and the previously reported CdS/MoS_2 heterojunctions. Moreover, due to the rapid hole extraction from CdS and transferred surface oxidation sites, the present CdS/MoS_2 heterostructure demonstrates better corrosion resistance and higher photostability. The present work is expected to provide a versatile platform for exploiting the CVD technique to develop other MoS_2-based heterojunction photoelectrodes with extensive PEC applications.

3.2 Introduction

In the last few decades, scientists have focused most on converting and storing solar energy to meet the large increase in energy needs.[17, 137, 138] Photoelectrochemical (PEC) hydrogen evolution is considered as a promising technology that can effectively convert renewable solar energy into stored chemical fuels.[139, 140] Semiconductor-based photoanodes as critical components should possess narrow electronic band gaps for better spectrum utilization and matched band edge potentials for hydrogen production. Since the first discovery of the PEC effect on a TiO_2 photoelectrode, plenty of metal oxides with varied nanostructures have been developed as photoactive materials. While most of them suffer from two major drawbacks related to weak optical absorption and extremely short photo-exciton lifetimes.[89, 141-144] Alternatively, metal sulfides and nitrides with appropriate energy band structures are widely studied for PEC applications because of stronger light harvesting and better electrical properties.[145-147] As a typical visible-light-driven metal sulfide, CdS has emerged as an attractive photoanode material with a direct bandgap of around 2.4 eV, capable of light absorption up to 520 nm. Meanwhile, the negative conduction band potential is about 0.6 V less than the H^+/H_2 energy level, which allows the spontaneous hydrogen reduction process.[90, 148, 149] Nevertheless, the actual photoconversion efficiency of CdS itself is very low due to the rapid bulk and surface recombination of photoexcited electron-hole pairs. Furthermore, its severe photocorrosion attributed to the self-oxidation of S^{2-}induced by holes also slows down its large-scale industrialization.[150, 151] To overcome these limitations, various modifications have been examined. Typically, structural control design, particularly one-dimensional oriented CdS architecture, has been utilized to define the charge transfer pathways with less carrier loss and to facilitate ion diffusion with reduced bulk charge recombination.[135, 152, 153] Another strategy for improving PEC performance involves the deposition of noble-metal nanocrystals with lower Fermi levels, such as Ru,[154] Au,[155] and Pt nanocrystals,[156] which is beneficial for increasing overall conductivity, suppressing surface charge recombination, and extending carrier lifetimes by inducing Schottky-junction-driven charge transportation. Considering their prohibitive cost and scarcity, employing inexpensive and earth-abundant substitute co-catalysts to promote interfacial charge flow is thus desired. What's more, the heterojunction fabrication method by coupling with other photosensitizers to induce a well-coordinated energy band alignment has proven its effectiveness for constructing unidirectional charge transfer channels.[93, 157, 158] In particular, building a CdS-based core-shell heterojunction with two-dimensional (2D) materials as shells can not only passivate the surface trap state but also boost the hole extraction through an easier carrier transfer pathway.[158-161]

Transition-metal dichalcogenides (TMDCs) with typical 2D layered structures receive considerable attention for their superior mechanical, optical, and exciting electronic properties.[162-166] For instance, molybdenum disulfide (MoS_2), composed of a sandwich stacked S-Mo-S layer linked by van der Waal interaction, has demonstrated a higher catalytic potential compared to Pt for hydrogen evolution reaction.[113, 167] This reactivity is attributed directly to the low hydrogen absorption energy of the MoS_2 layer edges.[168, 169] Great efforts have thus been devoted to exposing more active surface areas for improving the catalytic activity. Recently, some progress has been made by loading few-layered 2H-MoS_2 nanosheets on CdS to create MoS_2/CdS heterojunctions with significantly enhanced photocatalytic properties. It was found that the introduced MoS_2 was favorable for the effective charge carrier separation and the interior CdS protection.[159, 161, 170-172] However, the reported CdS/MoS_2 composites are majorly focused on the photocatalytic powder assemblies and the novelties of PEC systems are rarely reflected by these CdS/MoS_2 heterojunctions. Indeed, the resulting photogenerated charge transfer and photoconversion still need improvement through strengthening MoS_2 adhesion to hosting core materials and forming intimate interface contacts. Such a step is hardly accomplished by facile solution growth methods reported above.[173] Fortunately, the direct CVD growth of co-catalysts on host materials has been demonstrated available for interface junctions' optimization to achieve lower charge transfer resistance and higher quantum efficiency.[174, 175] In addition to the interface contacts' influence, the electrical conductivity of the used material acts as another critical factor to govern the overall PEC performance. Compared to semiconducting MoS_2 (2H phase), metallic MoS_2 (1T phase) with better conductivity usually exhibits higher charge transport capability, thus resulting in better carrier kinetic behavior for PEC applications.[176-178]

To realize these motivations, we report a new and facile fabrication method of CdS/MoS_2 core-shell heterostructures for solar-driven hydrogen evolution. A hierarchical continuous, uniform, and controlled number of layers of dual-phase (2H & 1T) MoS_2 nanoflakes are deposited on single-crystal CdS NRs via one-step CVD techniques. Systematic studies demonstrate the growth of plane-to-plane junctions between crystalline MoS_2 and CdS NRs leading to effective charge transport channels for boosting carrier mobility. The influence of loaded MoS_2 layer numbers on PEC activities is also investigated in detail. Compared to pristine CdS NRs, we found that for a better photoconversion (over two-fold higher) the optimal number of deposited MoS_2 layers on CdS NRs is three. The optimized MoS_2 loading can not only promote more photoexciton generation for a higher quantum yield but suppress charge carrier recombination in both the bulk and CdS surface for increased quantum efficiency.

3.3 Experimental section

3.3.1 Preparation of the CdS/MoS_2 heterojunction photoanode

1D CdS nanorod arrays were first grown hydrothermally on fluorine-doped tin oxide glass substrates (FTO, 15 Ω/sq) in accordance with our previous report.[151] 0.5 mM of Cd $(NO_3)_2H_2O$, 0.5 mM of thiourea, and 0.2 mM of glutathione were thoroughly dissolved in 20 mL of deionized water to make a precursor solution. Next, clean FTO substrates (2.5 cm × 1.0 cm) were placed vertically in a 25 mL Teflon container filled with the obtained precursor solution. The hydrothermal process was performed in a Muffle oven at 200 °C for 4 h. After that, the FTO substrate with a coated bright yellow layer was taken out and rinsed gently with nanopure water and ethanol, and then dried at 80 °C for 24 h overnight in ambient conditions.

The CdS/MoS_2 heterojunction was fabricated via the in-situ CVD growth of dual-phase MoS_2 layers onto the surface of CdS photoanodes. During the whole CVD process (Figure 3.1a), molybdenum trioxide (MoO_3, 10 mg, as the Mo source) and sulphur powder (200 mg, as the S source) were loaded into two different porcelain boats, which were separately placed in the upstream (Zone I) and downstream (Zone II) heating zones. FTO substrates with the CdS coating were placed face-down to the MoO_3 powder. Before the reaction, the CVD system was flushed with high-purity Ar gas (~100 sccm) for 30 mins to obtain an oxygen-free atmosphere. Later, Zone II was set to 550 °C at a ramp rate of 30 °C/min, whereas the Ar flow rate was reduced to 20 sccm. Zone I was heated to 220 °C in 10 minutes after Zone II reached the desired temperature. Both zones were stabilized at their specific temperature for 15 mins to support material deposition. In particular, through piling 0, 3, 6, or 8 slices of 1 mm glass plates in the bottom of the porcelain boat as the supporting base of the MoO_3 powder, the vertical distances between the CdS coating and the Mo source were easily adjusted to 11, 8, 5, and 3 mm. The resulting distinct-layered MoS_2 attachment (1, 2, 3, and 5 layers) were respectively labeled as CdS/MoS_2-1L, 2L, 3L, and 5L. Also, pure stacked MoS_2 nanosheets with a few layers were deposited on the glass side of FTO substrates with a fixed distance of 8 mm between each of them. The details of characterization technologies are listed in the Annex A.

3.3.2 PEC measurements

A conventional three-electrode device on an electrochemical workstation (SP-200 Potentiostat) was employed to measure the relative PEC and EC measurements. The obtained samples on FTO substrates with a fixed coating area of 1.0×1.0 cm^2 were used as the working electrodes. Ag/AgCl (3 M KCl) and Pt wire acted as the reference and counter electrodes. The light source was an LED solar simulator (LSH-7320 ABA) and the illumination intensity was calibrated to 100 mW/cm^2. The mixed $NaSO_3$/Na_2S (0.35 M/0.25 M, pH = 12.5) aqueous solution was applied as the electrolyte. The photoresponse (*I-V* curves) of as-prepared photoanodes was obtained by linear sweep voltammetry at a scan rate of 20 mV/s under darkness, steady, or chopped solar illumination. Amperometric *I-t* performance was recorded at 0 V vs Ag/AgCl with six on/off illumination cycles (10 s). The incident photon-to-current efficiency (IPCE) tests were executed at a bias of 0 V vs Ag/AgCl under monochromatic light exposure from 320 to 700 nm. Photoelectrochemical impedance spectroscopy (PEIS) was conducted between 10^5 to 1 Hz at the open circuit potential. Capacitance analysis was performed at 1 kHz under darkness over the voltage range from -1 to 0 V vs Ag/AgCl. The long-term photostability of the pristine CdS and representative CdS/MoS_2-3L heterojunction photoanodes was recorded at 0 V vs Ag/AgCl under one sun illumination. The evolved hydrogen was quantitatively analyzed using a gas chromatograph (Perkin Elmer Clarus 580) and the corresponding Faradic efficiency was estimated according to equation A3.3. Besides, for comparison purposes, some potentials were calibrated against the reversible hydrogen electrode (RHE) based on the Nernst equation (Equation A3.1).

3.4 Result and discussion

3.4.1 Structural characterization

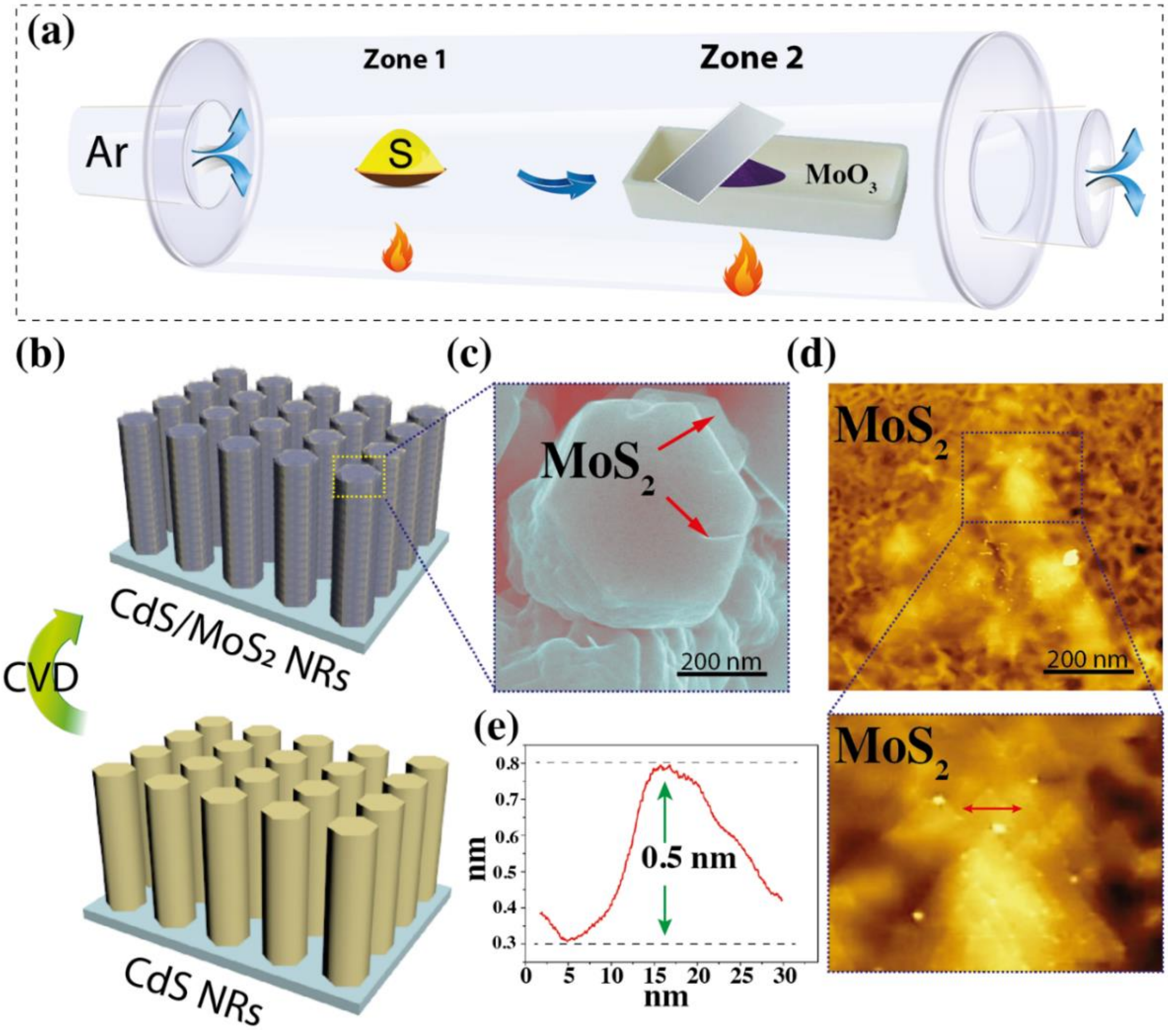

Figure 3.1 (a) CVD MoS_2 heterojunction growth for CdS/MoS_2 photoanode preparation on FTO substrates. (b) Illustration of the fabrication process of CdS/MoS_2 photoanode. (c) SEM image showing the MoS_2 growth on CdS NRs. (d) AFM image of MoS_2 on CdS surface and (e) height profiles of bare MoS_2 nanosheets.

The CdS/MoS_2 core/shell nanostructures are prepared via a two-step synthetic strategy. First, one-dimensional CdS nanorod arrays are synthesized on FTO substrates by a facile hydrothermal process, in which thiourea was used as S source and to provide the ligand for forming stable Cd-based complex compound.[171] During the growth process, glutathione (GSH) was used as a capping agent for growing well-oriented CdS nanorod structures.[131] Second, the MoS_2 shells with mono/few-layered stacking structures are deposited on CdS nanorods via CVD technology (Figure 3.1b and c). The number of MoS_2 layers could be tuned by varying the vertical distance between the CdS substrate and the molybdenum source. We found that the CdS/MoS_2 heterojunction photoanode composed from three layers of MoS_2 shells demonstrates the optimal PEC performance (see below) and is systematically characterized. As a control experiment for MoS_2 growth, pure MoS_2 nanosheets were deposited on the FTO-free substrate and their atomic force microscopy (AFM) profile is displayed in Figure 3.1d and e. The MoS_2 CVD growth on the FTO-free glass side showed a stack of well-known triangular monolayer MoS_2 nanoflakes with a thickness of around 0.5 nm, which matches well with previous reports and will assistively evaluate the layer numbers of wrapped MoS_2 shells outside CdS cores.[179-180]

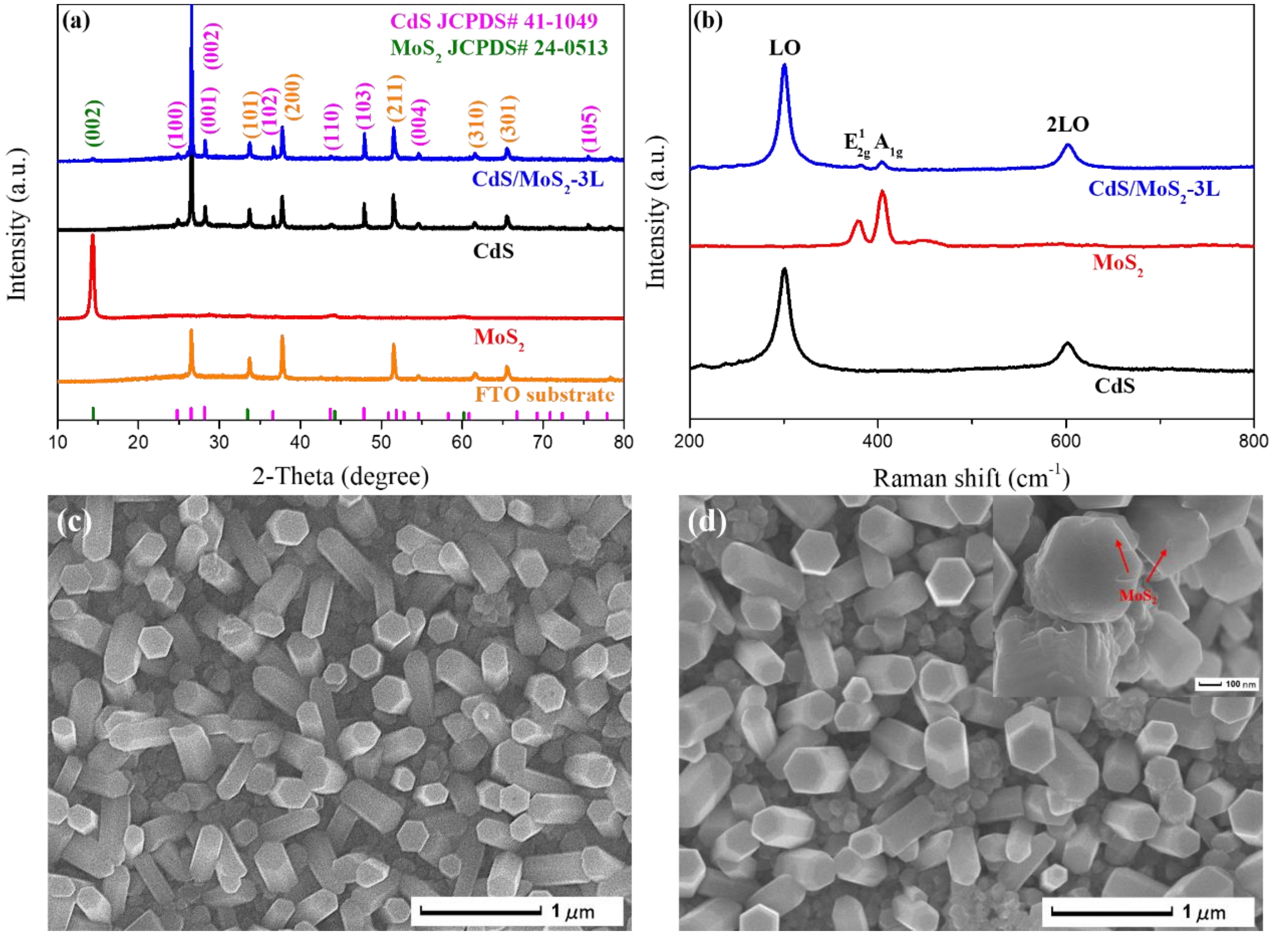

Figure 3.2 (a, b) X-ray diffraction patterns and Raman spectra of pure CdS NRs, MoS_2 nanoflakes and CdS/MoS_2 nanostructures. (c, d) SEM images of CdS NRs on FTO substrates before and after CVD-grown MoS_2 shells.

X-ray diffraction (XRD) measurements were performed to confirm the crystallographic structures of as-prepared CdS/MoS_2 heterojunctions (Figure 3.2a). Except for FTO substrate diffraction peaks (orange curve), all remaining peaks can be attributed to hexagonal wurtzite structure of CdS NR arrays (S.G. P63mc, JCPDS no. 41-1049). The significantly enhanced peak at 26.6º, corresponding to the (002) crystal plane of CdS, indicates its preferable [001] growth direction.[181] The XRD data (red curve) for pure MoS_2 nanoflakes delineates an intense diffraction peak at 14.1º resulting from the highly oriented (002) plane of hexagonal MoS_2 structure (S.G. P-6m2, JCPDS no. 24-0513).[147] Crystal structures of the prepared CdS/MoS_2-3L were confirmed by XRD spectrum (Figure 3.2a, blue line), No appearance of any ambiguous reflection or extra peaks belonging to other phased and disordered structures suggests its high purities. Besides, through the calculation of the Scherrer formula,[182] the crystallite sizes of CdS nanorods before and after MoS_2 loading present little gap, indicating the well-preserved CdS crystallinity during the CVD process. Raman analysis was further employed to confirm the phase composition of CdS/MoS_2 photoanode. Raman spectra of CdS/MoS_2 nanorods (Figure 3.2b, blue line) show two distinct characteristic peaks of bare CdS NRs at 300 cm^{-1} and 600 cm^{-1} associated with its longitudinal optical (LO) phonon and overtone (Figure 3.2b, black line), as well as the phonon vibration modes at 382.2 cm^{-1} and 403.7 cm^{-1} corresponding to in-plane (E^1_{2g}) and out-of-plane (A_{1g}) lattice vibration of 2H-MoS_2 (see Figure 3.2b, red line) .[183-185] Noticeably, the slight blueshift of E^1_{2g} and redshift of A_{1g} occur relative to pure MoS_2 nanoflakes (vibration modes at 379.1 cm^{-1} and 405 cm^{-1}) after CVD-grown MoS_2 shells on CdS NRs. The smaller wavenumber difference ($\Delta \sim 21.5$ cm^{-1}) of MoS_2 peaks in the CdS/MoS_2-3L heterojunction (compared to $\Delta \sim 25.9$ cm^{-1}) indicates fewer stacking layers (<10) of MoS_2 shells outside CdS NRs,[171] which may play an important role in PEC hydrogen generation performance. The field emission scanning electron microscopy (FESEM) images display the surface morphological changes of CdS NRs after the CVD growth of MoS_2 shells. As shown in Figure A3.1a, highly ordered and vertically aligned CdS NRs are successfully deposited on FTO substrates via the hydrothermal method. The amplified SEM image (Figure 3.2c) reveals the resulting CdS in the shape of hexagonal nanorods with smooth surfaces, which is in line with the surface energy minimization. The average diameter of CdS NRs is determined to be about 200 nm. The mean thickness of CdS films is also estimated at around 760 nm by the SEM cross-section image (Figure A3.1b). FESEM image of representative CdS/MoS_2-3L NRs is shown in Figure 3.2d, which exhibits a subtle morphological difference (a slightly increased outer diameter) from that of bare CdS NRs. From the enlarged morphology (insert in Figure 3.2d), it is observed that the surface of the CdS/MoS_2-3L photoanode presents certain wrinkled features attributed to the continuous and tightly wrapped MoS_2 shells. Moreover, the semitransparent properties of exposed MoS_2 nanoflakes further confirm its few-layered 2D structure.

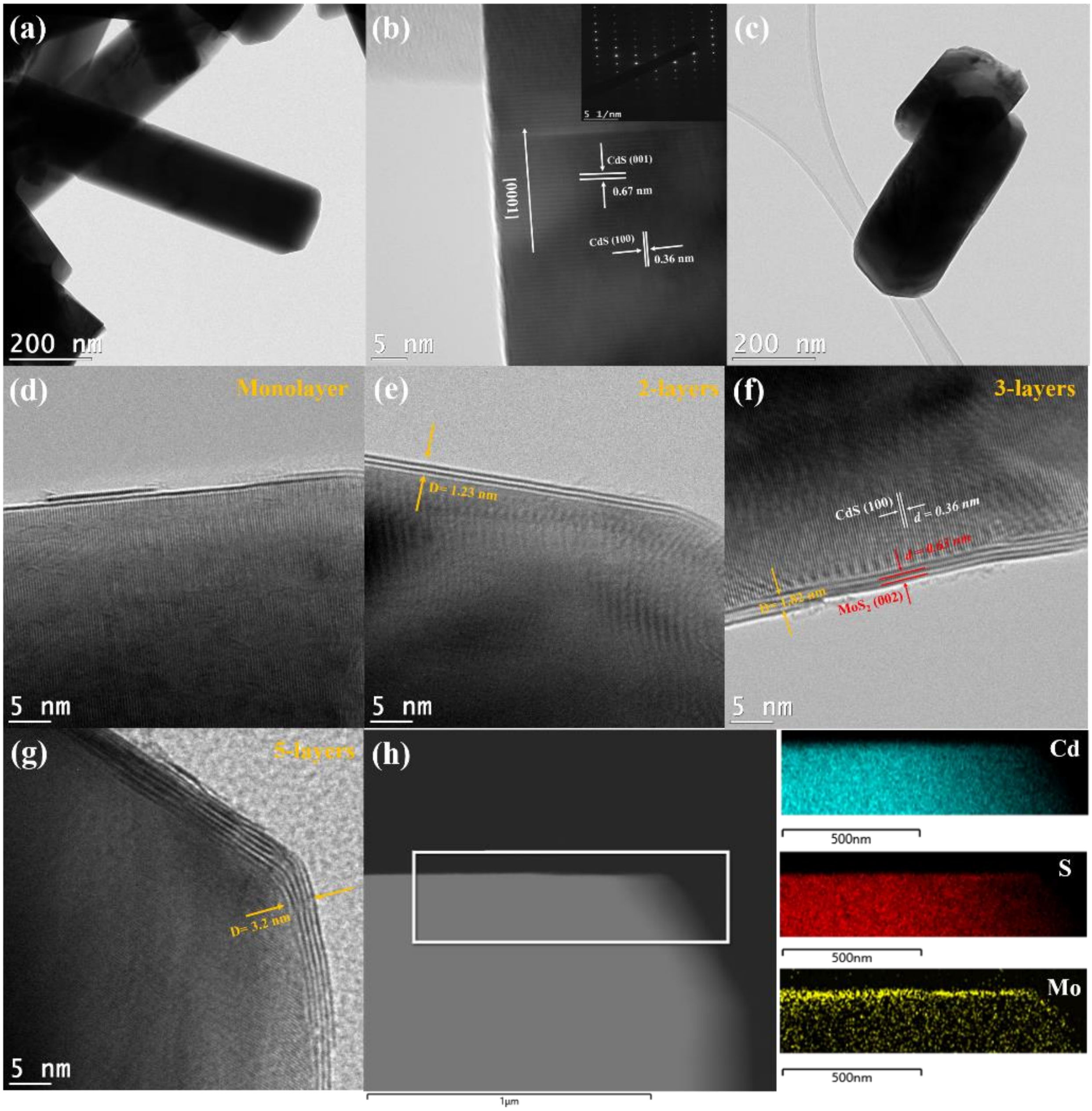

Figure 3.3 (a) Bright-field and (b) High-resolution TEM images of single-crystalline CdS NRs. (c) Low-magnification TEM image of representative CdS/MoS_2-3L NRs. (d-g) High-resolution TEM images of CdS/MoS_2 heterojunctions with distinct layer numbers of MoS_2 shells. (h) STEM image of a CdS/MoS_2 NR and the corresponding elemental mapping analysis.

Transmission electron microscopy (TEM) and high-resolution TEM images provide more detailed information on the nanostructure of as-prepared CdS and CdS/MoS_2 NRs. As shown in Figure 3.3a, the pristine CdS NR presents a smooth and faceted surface without grain boundaries and has a diameter of approximately 188 nm, which is in good agreement with the SEM results above. The HRTEM image (Figure 3.3b) and corresponding selected-area electron diffraction (SAED, as the insert) pattern in the dot array reveals its single-crystalline nature, which is beneficial for the higher electron mobility.[159, 186] The clear lattice fringes with spacing (*d*) of 0.67 nm and 0.36 nm correspond to the oriented (001) and (100) planes of hexagonal CdS, respectively, suggesting the obtained CdS grows along with the [001] direction.[181] After CVD-grown MoS_2 shells, the representative CdS/MoS_2-3L photoelectrode (Figure 3.3c) still exhibits a rodlike structure but with rippling edges. Figure 3.3d-g displays the HRTEM images of CdS/MoS_2 NRs prepared with an adjusted vertical distance between the CdS coating and Mo source (1.1, 0.8, 0.5, and 0.3 mm). The corresponding low-resolution TEM images are shown in Figure A3.2a-d. It is clearly observed that the CdS NRs in all photoanodes are uniformly covered by flake-shaped MoS_2 shells in a layer-by-layer mode. Such a strong adhesion between CdS cores and MoS_2 shells could greatly accelerate charge transfer and form numerous active sites, thus leading to better overall performance.[178, 187] The typical lattice fringe with an interplanar distance of 0.63 nm matches the crystallographic (002) plane of MoS_2, further verifying that the as-grown MoS_2 shell is crystalline. Each parallel line in MoS_2 lattice fringes represents a layer number in MoS_2 shells, which is well consistent with the height profile of MoS_2 (Figure 3.1e).[171, 188] This result confirms that mono/few layers (1, 2, 3, and 5 layers) of MoS_2 nanoflakes can be precisely deposited on faceted CdS NRs through the CVD method. Moreover, a close look at the interface in Figure 3.3f shows that the continuous MoS_2 lattice fringe directly connects to the (100) lattice plane of CdS cores, implying an intimate contact. In general, the charge transfer kinetics are highly dependent on the drift and diffusion process through MoS_2 shell layers.[181, 189] Such an intimate interfacial junction of crystalline MoS_2 flakelike shells uniformly grown on single-crystalline CdS NRs would be favorable for boosting the charge migration and separation. In addition, STEM imaging and EDX mapping for the selected area were also carried out to identify the elemental composition of representative CdS/MoS_2 NRs. The EDX spectra in Figure A3.3 illustrate the existence of Cd, S, and Mo elements, and the homogenous distribution of Mo element (Figure 3.3h), which confirms the successful MoS_2 wrapping on CdS NRs.

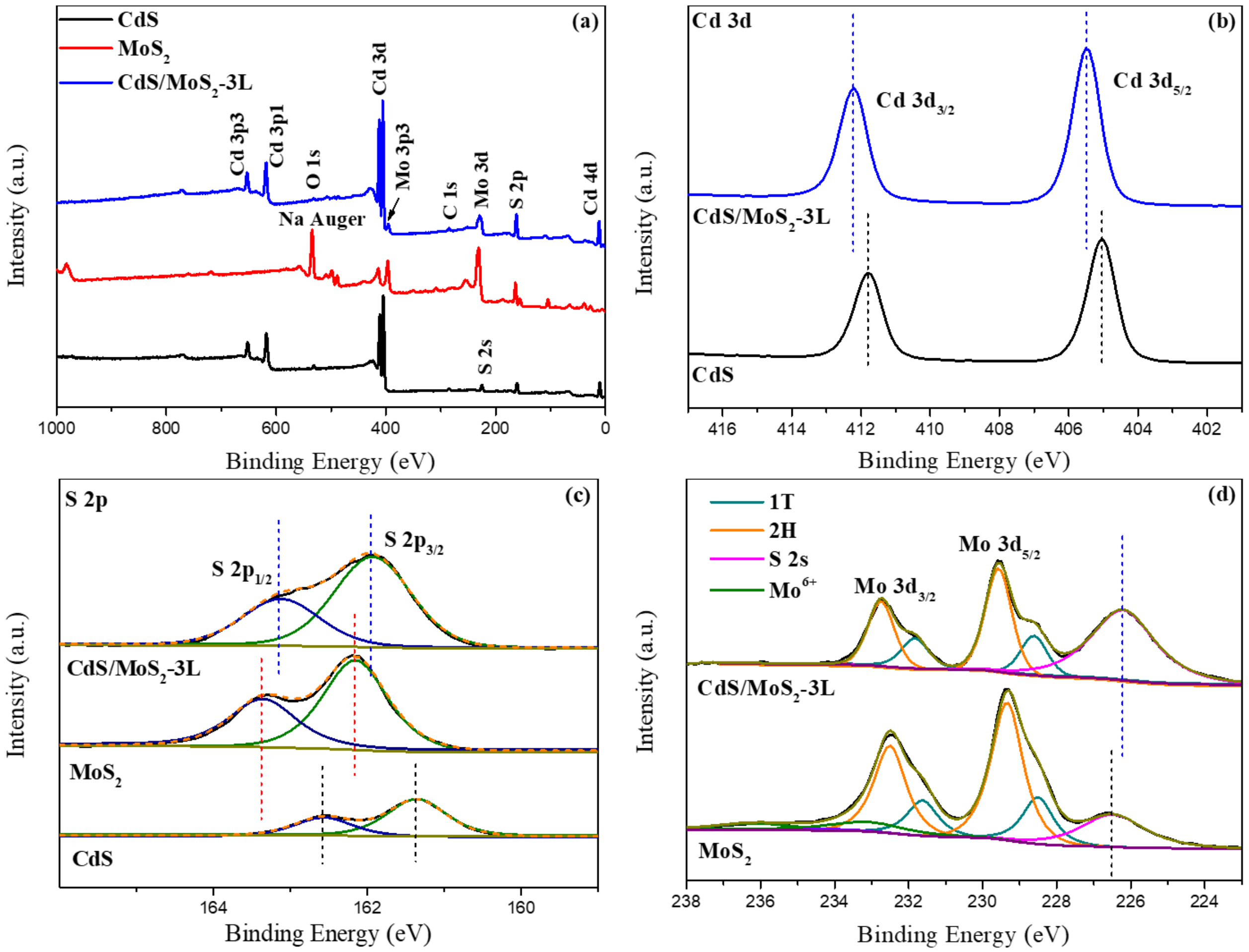

Figure 3.4 (a) XPS survey scan of the pristine CdS NRs, MoS_2 nanoflakes and CdS/MoS_2 core shell nanostructure. (b-d) High-resolution XPS spectra in Cd 3d, Mo 3d and S 2p regions.

To study the surface chemical states of the representative CdS/MoS_2-3L heterojunction, XPS analysis was performed (see Figure 3.4). Consistent with the EDX results above, the typical survey scan (Figure 3.4a) further corroborates the presence of Cd, S, and Mo elements in CdS/MoS_2-3L NRs, where Mo and S originate from the outer MoS_2 shell. The high-resolution XPS spectra in Cd 3d region (Figure 3.4b) indicate two dominant peaks of Cd $3d_{3/2}$ and Cd $3d_{5/2}$ located respectively at 412.2 eV and 405.5 eV.[190] Compared with the Cd signal at 411.7 eV and 405 eV in the pristine CdS NRs, the slight positive shift (by 0.5 eV) in the CdS/MoS_2 heterojunction suggests a decreased electron density.[191] The S 2p spectrum (Figure 3.4c) of CdS/MoS_2 NRs can be well-deconvoluted into two peaks at 163.1 eV and 161.9 eV, corresponding to the spin-orbits of S $2p_{1/2}$ and S $2p_{3/2}$. Similarly, the S 2p peak shifts to higher binding energy compared to those of the pristine CdS. Noticeably, a negative offset towards lower binding energy occurs relative to the S 2p signal of bare MoS_2 nanoflakes, which provides powerful evidence of strong interfacial interactions between CdS and MoS_2.[192] Specifically, the electrons will be injected from CdS cores to MoS_2 shells after intimate contact because of the sub-equilibrium state of their Fermi levels. Further, the Mo 3d in CdS/MoS_2 NRs is also detected with two prominent peaks around 232.8 eV (Mo $3d_{3/2}$) and 229.6 eV (Mo $3d_{5/2}$), and two satellite peaks at 231.8 eV and 228.6 eV, which delineate the formation of dual-phase (2H & 1T) MoS_2 shells via the CVD process.[193] The strong signal at the binding energy of 226.2 eV corresponds to S 2s from sulfides, which also presents a negative shift compared to the bare MoS_2. The small peak at 236.1 eV (green curve) in the pure MoS_2 is assigned to the Mo^{6+} oxidation state attributed to surface oxidation reaction under ambient conditions,[159] but disappeared in CdS/MoS_2 heterojunctions.

3.4.2 Optical properties

The optical properties of as-obtained bare CdS, MoS_2, and the representative CdS/MoS_2-3L nanostructure were characterized by UV-vis-NIR diffuse reflectance spectroscopy (DRS). As depicted in Figure A3.4, the growth MoS_2 film exhibits a wonderful light harvesting capacity from the near-infrared to ultraviolet region. The appearance of two characteristic peaks between 600 nm and 700 nm (2.06-1.77 eV) occurs from the K-point of Brillouin zone and the broad peak around 400 nm (3.1 eV) results from direct band transition.[183, 194] The pristine CdS NRs show a visible absorption edge at 524 nm, which is in accordance with previous literature.[195] With MoS_2 shells on the surface of CdS cores, the absorption intensity is overall enhanced, owing to the contribution of the narrower band-gap of MoS_2. Meanwhile, the absorption band edge of the CdS/MoS_2 heterojunction (Figure A3.4) red-shifts to a longer wavelength (534 nm) than that of bare CdS NRs, indicating the effectively broadened utilization of solar energy. In addition, the estimated band gap energies according to the Kubelka-Munk transformation are displayed in Figure A3.5. The calculated direct band-gap value (E_g) for CdS is 2.31 eV and the indirect E_g value for MoS_2 is around 1.67 eV. As analyzed above, the introduction of MoS_2 nanoflakes as shells can indeed improve the overall light absorption ability, which in turn enhances the overall quantum yield and photon-to-charge conversion efficiency, thus leading to better photoelectric performance.

3.4.3 PEC performance measurements

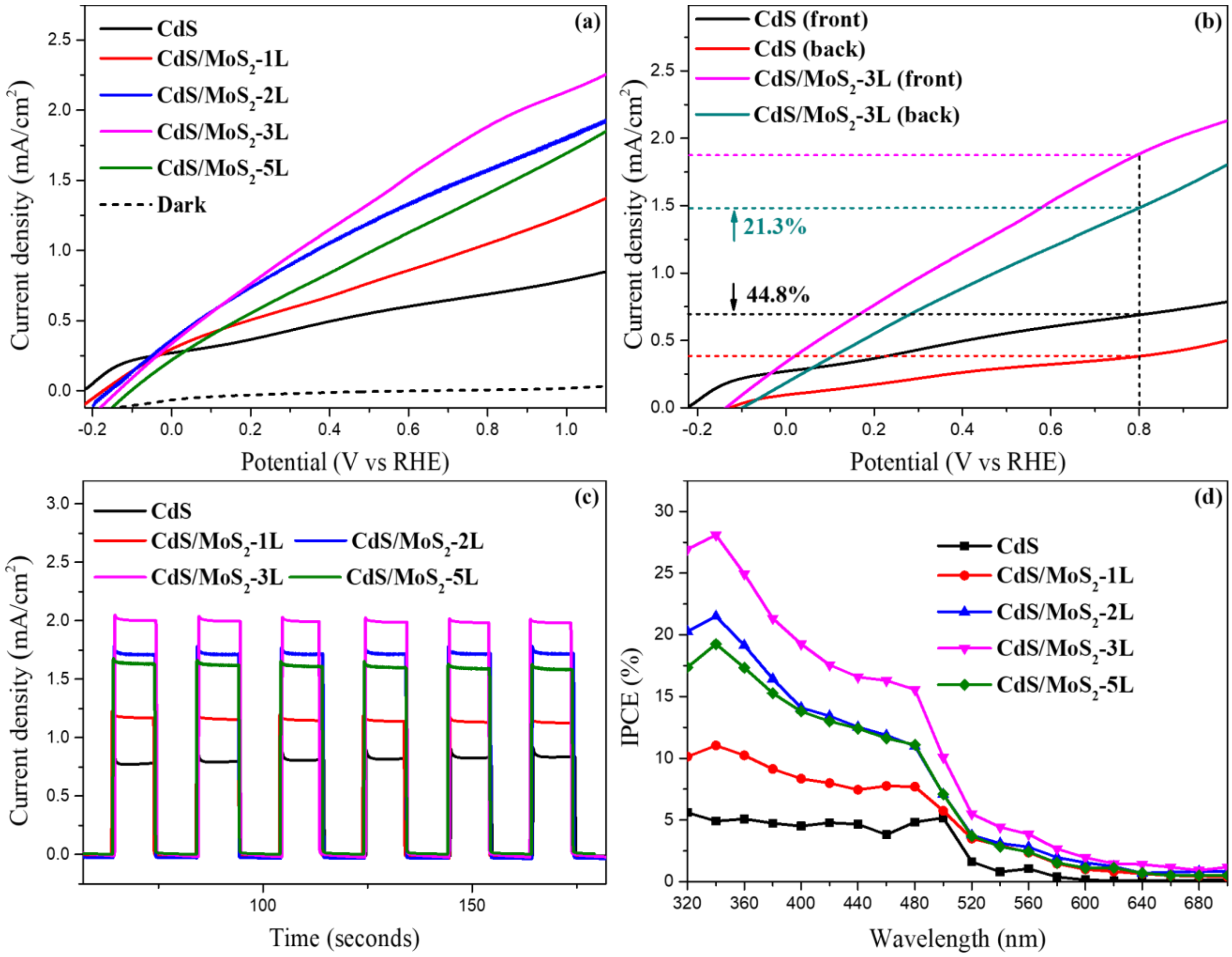

Figure 3.5 Photoelectrochemical (PEC) performance of the pristine CdS and CdS/MoS$_2$ heterojunctions with varied layer numbers of MoS$_2$ shells. (a) Current density versus applied potential in darkness and AM 1.5G solar light irradiation (100 mW/cm^2). (b) Chopped linear scan voltammetry (LSV) curves under back and front irradiations. (c) Photoresponse measurements at 1 V vs RHE. (d) IPEC plots at an applied bias of 0 V vs Ag/AgCl for all photoanodes.

To study the PEC performance of as-fabricated heterojunction photoanodes, a series of photoelectrochemical measurements were carried out. The photocurrent density as a function of applied voltage obtained by linear sweep voltammetry was recorded under darkness and 1 sun front-side irradiation. Note that the bare MoS$_2$ film shows ultra-low photoactivity (Figure A3.6). Further, as revealed in Figure 3.5a, the negligible dark current suggests a great charge transfer resistance of CdS NR arrays, while the diffusion resistance was dramatically reduced under irradiation as shown in Figure A3.7. This phenomenon is the result of the high electron mobility in the system. The photocurrent curves of all photoanodes exhibit a promptly upward trend when the potential sweeps to the positive side. Comparatively, the pure CdS NRs arrays present an unsatisfactory photoresponse due to the fast electron-hole recombination. On the other hand, the formed CdS/MoS_2 heterojunctions after CVD-grown MoS_2 shells show higher photocurrent densities. Interestingly, the loading layers of MoS_2 have a significant influence on the overall PEC performances in terms of the resulting photocurrent densities. The optimum three-layered MoS_2 shell in the heterojunction of CdS/MoS_2-3L NRs possesses optimum saturation relative to those of other MoS_2 loadings. Conceivably, excessive MoS_2 wrapping would shield the optical absorption of CdS cores and hinder the hole extraction, thus incurring a decreased photo response. As depicted in Figure 3.5a, the optimized CdS/MoS_2-3L heterojunction exhibits a saturated photocurrent density of 2.14 mA/cm^2 at 1 V vs RHE, which is approximately 2.74 times higher than that of the pristine CdS film at the identical applied bias. Meanwhile, it is observable that the open-circuit potential (OCP) of CdS/MoS_2-3L NRs (-0.14 V vs RHE) displays a slight positive shift relative to that of the pristine CdS NRs (-0.21 V vs RHE). The lower negative value of the OCP signifies fewer trapped electrons in the heterostructure.[181, 196] Additionally, polarization curves of the as-obtained photoanodes were also measured under chopped solar light irradiation as shown in Figure A3.8. Compared to the *J-V* curves obtained in continuous illumination (Figure 3.5a), negligible divergency in photocurrent densities confirms good photochemical stability of the as-obtained films. Moreover, CdS/MoS_2 heterojunctions also show a higher cathodic dark current in negative potentials than that of bare CdS, indicating the improved electrocatalytic HER ability.

Hole transfer behavior was initially evaluated via comparing the difference in photocurrent density between front-side and back-side irradiation, as shown in Figure 3.5b. Front-side photocurrent density of the pristine CdS NRs is 44.8% higher than the back-side photocurrent density at 0.8 V vs RHE, suggesting extremely low hole extraction and high charge carrier recombination close to the bottom-end of nanorods.[192] By contrast, a halving difference (only 21.3%) in photocurrent densities was experimentally detected over core-shell CdS/MoS_2 NRs. Such difference reveals that the heterojunctions effectively accelerate the separation of photo-induced electron-hole pairs in bulk semiconductor and improve the overall oxidation kinetics. This behavior is primarily due to the formed built-in electric field, lower charge transfer resistance, and more active areas, as described in greater detail later. Further, the less negative offset of onset potential for the CdS/MoS_2 heterojunction under front-side illumination also verifies the analysis above.

To examine the instantaneous photocurrent response, chronoamperometric I-t curves were recorded under 7 times of periodic on-off solar illumination without applied voltage, as displayed in Figure 3.5c. Noticeably, all photoanodes show prompt and repetitive photoresponse with remarkable stability within a few cycles. A significant enhancement in photocurrent densities for all core-shell CdS/MoS_2 heterojunction NRs can be detected compared to that of the pristine CdS NRs. Noteworthily, the CdS/MoS_2-3L heterojunction with three layers of MoS_2 shells demonstrates the optimal photocurrent response for PEC hydrogen production, which agrees with the LSV results above. To further investigate the affiliation of PEC activity with respect to wavelength, incident photon-to-current efficiencies (IPCE, equation A3.2) of the as-fabricated photoanodes were measured under monochromatic light illumination at 0 V vs Ag/AgCl. As depicted in Figure 3.5d, all CdS/MoS_2 heterojunctions illustrate significantly increased IPCE values within UV and vis regions in comparison to the pristine CdS NRs. In particular, the core-shell CdS/MoS_2-3L heterojunction NRs manifest a maximum conversion efficiency of approximately 28.1% at a wavelength of 340 nm, which is 5.7 folds compared to pristine CdS NRs. Besides, above 520 nm, the IPCE of CdS NRs sharply declines till disappearing, whereas the heterojunction of CdS/MoS_2-3L still presents a clear photoconversion efficiency. This red-shift phenomenon mainly derives from the broadened optical absorption due to the wrapping of narrow band-gap MoS_2 shells, which matches with the DRS analysis above. On the basis of the aforementioned results, it is concluded that coupling 1D CdS NRs with few-layered MoS_2 nanoflakes via a suitable structural engineering strategy can significantly improve the PEC performance. Through the comparison with recently reported CdS/MoS_2 heterostructures and CdS-based photosystems (listed in Table A3.1), 1D core-shell CdS/MoS_2-3L heterojunction with outstanding PEC activity illustrates a certain superiority.

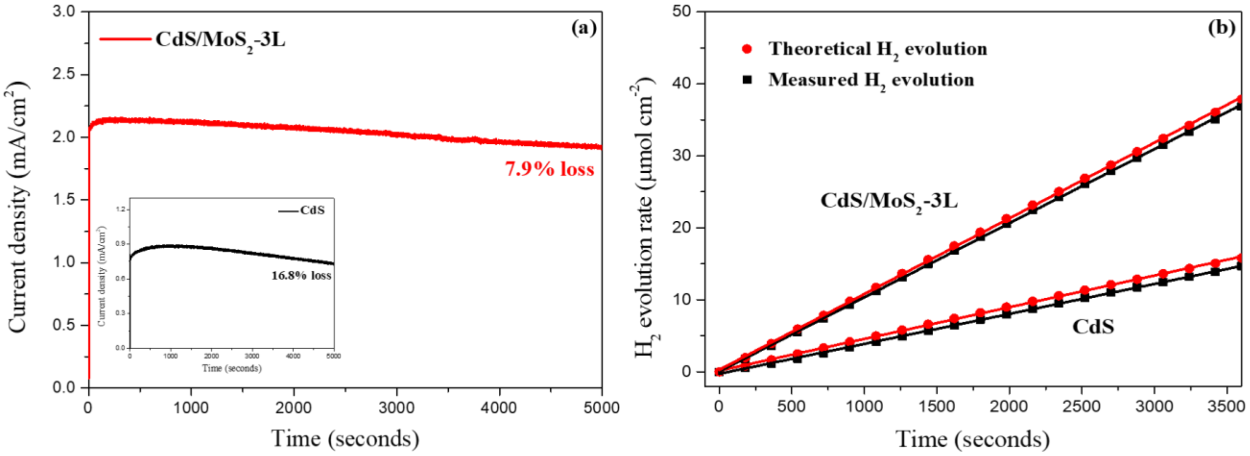

Figure 3.6 (a) Long-term photostability measurements by chronoamperometry and (b) PEC H_2 generation vs reaction times over the bare CdS NRs and the representative CdS/MoS_2-3L heterojunction at 0 V vs Ag/AgCl under 1 sun illumination. A mixture of $NaSO_3$ and Na_2S (pH = 12.5) was used as the electrolyte.

Long-term photostability is an important metric of photoelectrodes for evaluating their future practical application. As displayed in Figure 3.6a, photocurrent densities as a function of time were probed under continuous solar light irradiation for 5000 seconds without bias. The bare CdS NRs demonstrate unfavorable photostability with rapid degradation starting from the experiment and dropping by 16.8 % after 5000 s because of the serious self-corrosion of CdS by holes during the PEC surface oxidation process. In comparison, the core-shell CdS/MoS_2 heterojunction NRs perform very well with inhibited photocurrent attenuation (7.9% loss). This desirable result could be attributed to the establishment of a suitable junction between these two semiconductors with high-speed charge transfer channels, leading to the effective separation and extraction of VB holes in CdS. Besides, as revealed in the SEM image and XRD pattern of the CdS/MoS_2-3L heterojunction after testing (Figure A3.9), no apparent variation in micromorphology and crystal structure is observed in comparison with those of freshly-prepared CdS/MoS_2-3L NRs, further substantiating its useful photochemical stability. The above analysis provides evidence that CVD-grown MoS_2 nanoflakes as shells increase the overall PEC performance and protect the CdS cores from photocorrosion. Furthermore, the produced H_2 was quantified using a gas chromatograph in an interval of 3 mins. Figure 3.6b demonstrates the correlation of measured amounts with the theoretical calculation from the observed photocurrent density (the detailed calculation is listed in equation A3.3 and A3.4). The production maximum of H_2 was analyzed to be 36.8 μmol after 1 h of illumination at 1 cm^2 of the CdS/MoS_2-3L heterojunction photoanode, and the average generation rate reached 0.618 μmol min^{-1} cm^{-2}, which is over two-fold higher than that of the bare CdS NRs. Notably, both the CdS and CdS/MoS_2-3L heterojunction photoanodes present a high Faradic efficiency of over 90%, signifying that the appearance of photocurrent is mainly due to the PEC hydrogen evolution reaction.

3.4.4 PEC enhancement analysis and mechanism discussion

Various electrochemical measurements and characterizations were carried out in order to gain insight into the underlying mechanism for the enhanced PEC performance in CdS/MoS_2 heterojunctions. First, Mott-Schottky analysis was performed at a fixed frequency of 1 kHz to estimate the charge carrier concentration (N_D) and the flat band potential (E_{fb}), which was calculated via the equation A3.5 listed in supporting information. As shown in Figure 3.7a, the linear regions in Mott-Schottky plots of the bare CdS and CdS/MoS_2-3L give positive slopes, indicating their n-type characteristics.[197] Apparently, the bare CdS presents a much steeper slope with a relatively low donor density ($\sim 4.03\times10^{17}$ cm^{-3}). The fabrication of heterojunction through CVD-grown MoS_2 shells on CdS NRs manifests a higher donor density ($\sim 9.3\times10^{17}$ cm^{-3}) and it is over 2 times larger than that of CdS NRs. The significant increase can contribute to improved electrical conductivity and charge transport in the semiconductor interface,[198] which may play an important role in photocurrent enhancement. The result is caused by the presence of conductive 1T phase MoS_2 and the formation of the built-in electric field, so that the unidirectional charge transfer channels could be constructed between the bulk CdS and MoS_2 layers, thus leading to the effective separation of photoinduced electron-hole pairs and a larger N_D value. On the other hand, the less surface defect density from the passivation effect of MoS_2 wrapping can also help to reduce carrier recombination. In addition, the flat band potentials (E_{fb}) were collected from the x-intercepts via extrapolating the linear part of $1/C^2$ versus V plots. When compared to CdS NRs, a clear positive shift in the E_{fb} value in a CdS/MoS_2-3L heterojunction signifies less electron trapping and higher quantum efficiency,[107] in line with the LSV results above. (Flat band potential is defined as the potential of a semiconductor/electrolyte interface at which there is no net charge on the semiconductor surface.)

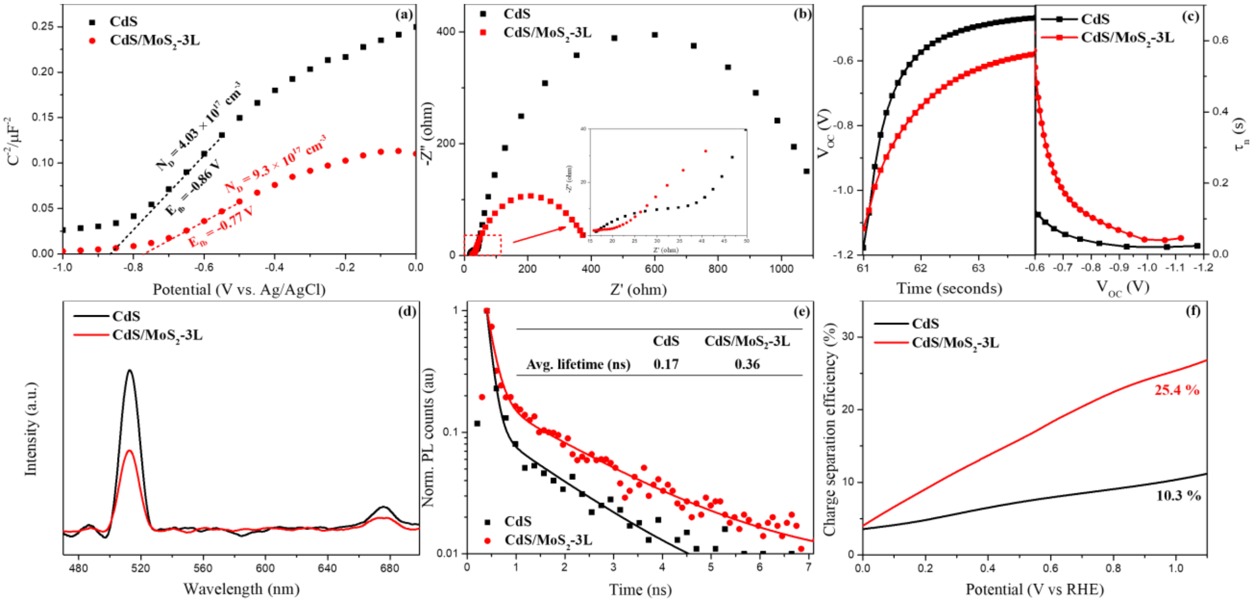

Figure 3.7 (a) Mott-Schottky plots collected at a fixed frequency of 1 kHz, (b) Nyquist impedance spectroscopy at open circuit potential under simulated solar light irradiation, (c) OCVD results with calculated average electron lifetimes, (d) photoluminescence (PL), (e) time-resolved photoluminescence (TRPL) and (f) charge separation efficiency over the pristine CdS and representative CdS/MoS$_2$ heterojunction NRs.

To deeply explore the charge transfer kinetics in the bulk semiconductor and interface, the Nyquist plots of the bare CdS and representative CdS/MoS$_2$-3L heterojunction NRs at open-circuit voltage were obtained via electrochemical impendence spectroscopy (EIS) under 1 sun irradiation. Normally, the charge carrier separation efficiency and electron transfer are associated with the arc radius of Nyquist plots. As depicted in Figure 3.7b, both CdS and CdS/MoS$_2$-3L NRs present two semicircles, and smaller semicircles appear in the heterojunction of CdS/MoS$_2$-3L, suggesting better charge transport in this system. Figure A3.10 illustrates the equivalent circuit fitted from the EIS spectra and the related parameter values are listed in Table A3.2, in which R_s represents the series resistance between FTO substrates and semiconductor films, R_{Bulk} corresponds to the charge transfer resistance within the bulk semiconductor involved in the charge trapping, and R_{ct} corresponds to the charge transfer resistance at the electrode/electrolyte interface dependent on the hole transport process. It can be observed that all photoelectrodes have low R_s values (below 16 Ω), confirming effective interfacial contact between FTO substrates and CdS NRs. As expected, in comparison with those of the bare CdS, smaller R_{Bulk} (10.6 Ω) and R_{ct} (366.3 Ω) values appearing in the heterojunction of CdS/MoS_2-3L manifest the prolonged carrier lifetime and higher electron transfer efficiency. This behavior can be mainly ascribed to the synergistic effect of using the MoS_2 wrapping to build a heterojunction that subdues the severe carrier recombination in the bulk or surface states and facilitates the hole extraction from the CdS host, thus leading to an improved photocurrent density in the heterostructure. The mixed phases of 2H & 1T MoS_2 could also be devoted to the better electrical conductivity. In addition, the thicker MoS_2 shell with 5-layered MoS_2 loading displays almost identical bulk resistance (R_{Bulk}), but with a bigger R_{ct} value, because of the extended hole immigration pathway, which well-explains the slightly decreased photoresponse in CdS/MoS_2-5L heterojunction NRs. To further monitor the charge carrier recombination behavior, the transient open-circuit potential decay (OCVD) measurements were conducted. As shown in the left region of Figure 3.7c, the open-circuit voltages (V_{OC}) of both CdS and CdS/MoS_2-3L NRs substantially decay and decrease to lower voltages once illumination is ceased, based on which the average electron lifetimes (τ_n) were determined according to the equation A3.6. The right region of Figure 3.7c provides the transformed electron lifetime profiles. Apparently, the CdS/MoS_2-3L heterojunction NRs display a gentler V_{OC} decay and a significantly prolonged electron lifetime relative to the bare CdS NRs. Such a result confirms that the CdS NRs modification with MoS_2 shells for the heterojunction fabrication can indeed be favorable for charge transfer and separation, resulting in the higher quantum efficiency. Moreover, the above results are also verified by the normalized *I*-*T* plots and kinetic process shown in Figure A3.11 and the corresponding discussion. Because the CdS/MoS_2-3L photoanode presents a longer decay time, using MoS_2 wrapping as a heterojunction can effectively reduce the trapping process of photogenerated electrons and facilitate the hole extraction.[89]

The overall photogenerated electron-hole recombination process and charge-trapping effect were thoroughly analyzed by photoluminescence spectroscopy (PL). The PL spectra data of the pristine CdS and representative CdS/MoS_2-3L heterojunction are shown in Figure 3.7d. Bare CdS NR arrays exhibit a strong and sharp emission peak at 512 nm due to intrinsic band transmission and a weak and broad emission peak at approximately 680 nm due to surface trap states,[181, 199] where the self-trapped excitons in the bulk CdS can hardly move to the surface, resulting in high carrier bulk recombination. Following CVD-grown MoS_2 shells on CdS NRs for heterojunction fabrication, significantly quenched PL intensities of more than 50% are observed on both band and trap-state emission peaks of CdS/MoS_2-3L NRs, implying a reduced recombination and trapping process of photoexcited electron-hole pairs in this system. As a result, the CdS/MoS_2-3L heterojunction has a higher quantum efficiency and can liberate more photo-excitons for optimized PEC hydrogen evolution. Moreover, to assess the carrier dynamic of CdS/MoS_2-3L heterojunction NRs, the time-resolved photoluminescence (TRPL) curves were analyzed and fitted with a biexponential decay model according to equation A3.8 and A3.9. All parameter values are summarized in

Table A3.3. The fitted TRPL spectra in Figure 3.7e illustrate that the average exciton lifetime of the CdS/MoS_2-3L heterojunction (0.36 ns) is longer than that of bare CdS NRs (0.17 ns). The profoundly increased lifetime is well consistent with the result of PL quenching in the heterojunction of CdS/MoS_2 and provides indisputable evidence that the introduction of dual-phase MoS_2 as a heterojunction can achieve the rapid spatial separation of photogenerated charge carries across the bulk and interface.

On the basis of the above results, the charge separation efficiency was quantified in accordance with the equation: $\eta_{sep} = J_{Ph}/J_{Max}$, in which J_{Ph} is obtained from the polarization curves and J_{Max} corresponds to the theoretical maximum photocurrent density. The surface limitation has already been excluded by assuming the complete consumption of surface holes using the sacrificial agent ($NaSO_3$ and Na_2S). Light harvesting efficiency (LHE) and J_{Max} were calculated through equation A3.10 and A3.11, and the results are shown in Figure A3.12 and A3.13. It is noticed that CdS/MoS_2-3L heterojunction NRs present a higher integrated photocurrent density (J_{Max}: 8.4 mA/cm^2) than that of the bare CdS (7.6 mA/cm^2), majorly resulting from its better optical absorption. Figure 3.7f exhibits the resulting η_{sep} as a function of applied potential. The architected CdS/MoS_2-3L NRs manifest an obviously enhanced charge separation efficiency from 10.3% to 25.4% at 1 V vs RHE, in comparison to the bare CdS, directly proving the boosted carrier anti-recombination behavior in this heterostructure.

On account of the unique structural features of the formed core-shell nanoarchitecture, it is speculated that CdS/MoS_2-3L NRs should possess the higher active areas. In order to test this point of view, the electrochemical surface-active areas (ECSA) of the pure CdS and CdS/MoS_2-3L NRs were determined via the electrochemical double-layer capacitance (C_{dl}) at non-Faradaic potentials (Figure A3.14).[27, 63] To our delight, the CdS/MoS_2-3L heterojunction photoanode has a higher Cdl value, nearly 1.5 times as high as that of the pure CdS. Considering the proportional correlation between ECSA and C_{dl} value, it is reasonably concluded that the CVD-grown MoS_2 shells as a heterojunction not only improve the overall carrier efficiency but also increase the surface-active area, which is beneficial for the promoted surface oxidation reaction.

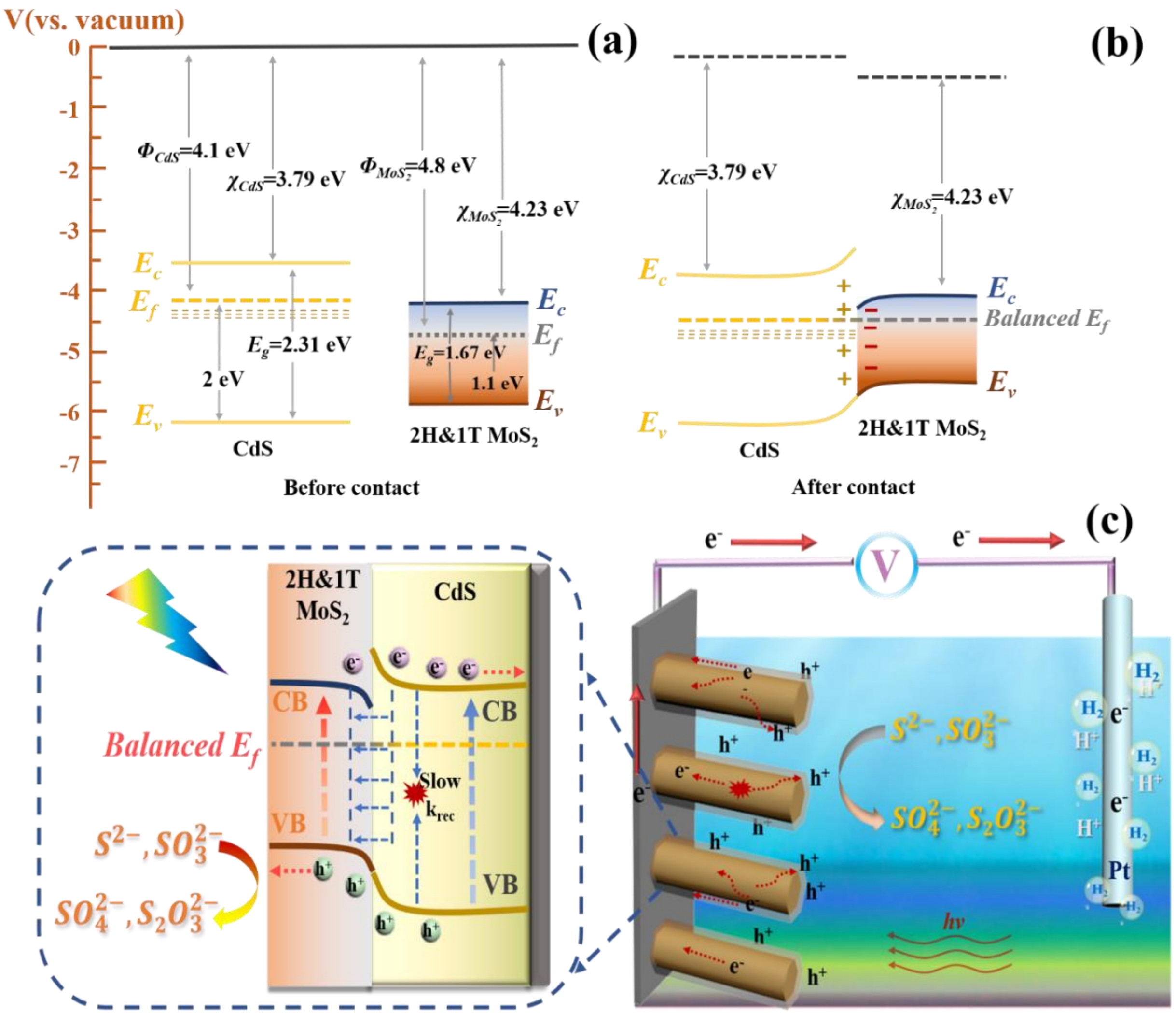

Figure 3.8 The energy band alignment diagram of MoS_2 and CdS (a) before and (b) after interface contact at thermal equilibrium in darkness. (c) Schematic illustration of electron-hole transfer models over the 1D CdS/MoS_2 heterojunction under 1 sun illumination.

To reveal the possible PEC operation mechanism for hydrogen evolution reaction, the detailed energy-band structures of CdS and MoS_2, and energetics of interfacial charge transfer over the CdS/MoS_2 heterojunction are discussed and shown in Figure 3.8a and b. To be specific, the ultraviolet photoelectron spectroscopy (UPS) results are displayed in Figure A3.15, where the Fermi levels (E_f) of CdS and few-layered MoS_2 nanoflakes with respect to vacuum level are determined to be 4.1 eV and 4.8 eV through subtracting the spectrum edge of secondary electrons from the excitation energy (21.2 eV). The valence band energies relative to the Fermi levels are read through extrapolating the linear portions of low binding energy areas and the resulting valence band maxima (E_v) of CdS and MoS_2 are calculated to be 6.1 eV and 5.9 eV. Later, based on the adopted bandgaps from Tauc plots (DRS spectra, Figure A3.4) and E_v values, the conduction band edges (E_c) of both semiconductors are identified above (Figure 3.8a). While CdS NRs and MoS_2 shells are in intimate physical contact, a charge carrier rectification process will occur at the interface because of their mismatched energy-band structures. The rapid electron transfer of CdS cores to MoS_2 shells causes the Fermi levels to rearrange until they reach a thermodynamical equilibrium, resulting in the expected band bending and space charge layer (Figure 3.8b). Therefore, a typical Type-I heterojunction can be formed, where photogenerated holes in the valence band (VB) of CdS cores can be unidirectionally driven to the VB of MoS_2 for significantly suppressed carrier recombination. In terms of the information on the energy-band alignment and charge carrier separation analyzed above, the possible electron-hole transfer model over CdS/MoS_2 heterojunction NRs for highly-efficient PEC hydrogen production is proposed in Figure 3.8c. Under solar irradiation, both semiconductors can be photoexcited by absorbing photons with higher energies than their bandgaps and producing electron-hole pairs. Owing to the presence of the built-in electric field, the photogenerated holes in the VB of CdS cores can be rapidly extracted, and the gathered holes on the MoS_2 surface will participate in the surface oxidation reaction. Note that the promoted transferred VB holes of CdS can effectively avoid its self-corrosion for better photostability. Furthermore, by applying a bias voltage, the electrons in the CB of MoS_2 are driven toward the opposite direction and converge on the retained electrons in the CB of CdS, then migrate toward the counter electrode for hydrogen production. As a result, the formed CdS/MoS_2 heterojunction demonstrates a higher PEC performance compared to the bare CdS. Ultimately, the considerably enhanced PEC activity is attributed to the CVD-grown MoS_2 shells. The formed shell is acting as the photosensitizer, which significantly improves the overall light absorption strength and range, which helps to generate more photo-excitons for a higher quantum yield. In addition, both the passivation effect and the fabricated heterojunction with the intimate interface contact can restrain the carrier recombination rate (K_{rec}) for better charge transfer and separation, thus causing a higher quantum efficiency. Furthermore, because of the difference in electrical conductivity between the mixed metallic 1T and semiconducting 2H phases of MoS_2, it is expected that photoinduced holes will transport within the shell via an energetically favorable pathway,[178] potentially improving the overall charge transfer kinetics.

3.5 Conclusion

In summary, a hierarchically core-shell CdS/MoS_2 heterojunction photoanode is successfully fabricated by directly depositing MoS_2 on CdS NRs using CVD methods. The resulting structural analysis confirms that mono/few-layered MoS_2 nanoflakes with a mixed phase of semiconducting 2H and metallic 1T are continuous and intimate deposited on single-crystal CdS NR arrays in a plane-to-plane stacking fashion. Through adjusting the working distance during the CVD process, the optimal junction thickness with precise MoS_2 loading is identified and the formed CdS/MoS_2 photoanode with three-layered MoS_2 shells presents the highest photocurrent density (2.14 mA/cm^2 at 1 V vs RHE) and photoconversion efficiency, with respect to other single component and compounds. This significant enhancement in photoelectrochemical performance predominantly results from the construction of CdS/MoS_2-3L heterostructure which increases the overall light harvesting capability, passivates the surface trapping state, and provides unidirectional channels for better charge separation. More importantly, the uniformly adhered MoS_2 shells also serve as a protective layer, beneficial for photoanode protection and improved photostability. This work highlights the function of the CVD-assisted strategy in preparing ultrathin catalytic/co-catalytic materials for surface engineering applications.

3.6 Supporting information

The supplementary material related to the formulas used in this study and analytic characterizations is available in Annex A and on the website: https://doi.org/10.1016/j.jmst.2023.05.036

3.7 Contribution of authors to this paper:

Zhiyuan Peng, as the first author of this paper, designed this project, performed most of experiments, analyzed the data, and wrote the full manuscript.

Yilu Su conducted the partial PEC performance measurements, structural characterization, and the corresponding result analysis.

Maziar Jafari took part in the preparation of few-layered MoS_2 nanosheets and performed all AFM tests.

Prof. Mohamed Siaj, as the corresponding author, contributed to the feasible analysis of project, the preparation and correction of manuscripts, and the final submission process.

CHAPTER 4

ENCAPSULATION OF TIN OXIDE LAYERS ON GOLD NANOPARTICLES DECORATED ONE-DIMENSIONAL CDS NANOARRAYS FOR PURE Z-SCHEME PHOTOANODES TOWARDS SOLAR HYDROGEN EVOLUTION

Zhiyuan Peng[a], Yilu Su[a], and Mohamed Siaj[a*]

Published article for this study: Encapsulation of tin oxide layers on gold nanoparticles decorated one-dimensional CdS nanoarrays for pure Z-scheme photoanodes towards solar hydrogen evolution, *Appl. Catal. B: Environ.* 330 (2023) 122614. https://doi.org/10.1016/j.apcatb.2023.122614.

Department of Chemistry and Biochemistry, Université du Québec à Montréal, Montréal QC, H3C 3P8, Canada

*Corresponding author, E-mail: siaj.mohamed@uqam.ca

This Chapter has been shown in the following manuscript: (Zhiyuan Peng et al., 2023).

4.1 Abstract

Despite their high potential for solar energy conversion into chemical fuels, most artificial all-solid-state Z-scheme photosystems have disordered structures and focus on power photocatalytic water splitting applications rather than photoelectrochemical (PEC) cells. Herein, an innovative pure Z-scheme heterostructure, CdS/Au/SnO_2-S, composed of one-dimensional (1D) oriented CdS nanorods modified with SnO_2-wrapped Au nanoparticles (NPs), was designed as a photoanode for highly efficient PEC hydrogen evolution. Systematic characterization confirms that the incorporated Au NPs not only act as the host platform to support the SnO_2 layer growth but also play a key role as the electron mediator for strengthening the vectorial charge transfer from SnO_2 to CdS. This reinforced Z-scheme charge transportation channel is favorable for suppressing the bulk charge recombination process, increasing the overall carrier density, and preserving the strong redox capability, ultimately resulting in a considerably improved photocurrent density and photo-to-current conversion efficiency with better corrosion resistance.

4.2 Introduction

The finite fossil fuels on Earth have been hard to burden with the growing requirements of continuous urbanization and industrialization, causing an increase in scientific interest in the search for alternative and renewable energy sources.[17, 74, 200, 201] Hydrogen (H_2), with its high energy capacity and clean attribute, is regarded as a promising and ideal candidate.[13, 202] In the past decades, photoelectrochemical (PEC) water splitting based on photoactive materials has attracted considerable attention for directly converting the inexhaustible solar energy into hydrogen fuels in an economical and environmentally sustainable manner.[140, 203, 204] To accomplish reliable PEC devices with high photoconversion efficiency, one major challenge is still the design and manufacture of semiconductor photoelectrodes with ideal light harvesting, superior photochemical stability, efficient charge carrier separation, and strong redox ability.[102, 205, 206] Although a variety of affordable photoactive materials have been developed, it is proven difficult for the single-component semiconductor to satisfy all the above physicochemical characteristics. In addition, their performances are greatly limited due to serious charge recombination in bulk, surface, and interface, leading to a decline in the internal quantum efficiency.[207] Recent efforts have been devoted to the construction of semiconductor heterojunctions (usually Type-II heterostructure) to improve the carrier separation efficiency. However, the straddle charge transfer pathway will always weaken the redox ability of photo-generated electron-hole pairs, in which the charge carriers are driven into the conduction band (CB) and valence band (VB) of coupled semiconductors, respectively.[103, 208]

Comparatively, the artificial Z-schematic photosystem inspired by green plant photosynthesis is more desirable because it can not only improve the overall quantum efficiency but also retain the original strong redox capability by extinguishing electrons/holes with weaker redox potential.[102, 209] In 2006, the concept of an all-solid-state Z-scheme photocatalytic system was proposed and rapidly developed,[210] which usually comprises oxidation/reduction evolving semiconductors and the electron shuttle by using noble-metal particles (Au,[102, 211-213] Ag,[214, 215] Cd [216] and Pt [217]) and carbon-based additives like graphene oxide or reduced graphene oxide.[103, 218] Nevertheless, until now most of the fabricated Z-scheme photosystems are disordered and focus on the power photocatalytic water splitting rather than PEC cells.[219, 220] The direct contact of semiconductor components due to the inevitable aggregation of power samples will induce an undesirable back reaction, and puzzle the precise charge transport mechanism resulting from the coexistence of non-Z-scheme and Z-scheme models.[103, 221] In fact, the critical factor in building an all-solid-state Z-scheme system is to realize the dynamic equilibrium of photoexcited charge carriers between two semiconductor components, which is believed not to be readily reached by a facile adjustment of semiconductor ratios if two semiconductor components are not totally detached by electron mediators.[222] Thus, to avoid the adverse non-Z-scheme charge transfer, various types of spatially separated Z-scheme PEC cells have been well designed for an unassisted overall water splitting,[203, 223-225] where two photoelectrodes (such as n-type photoanode and p-type photocathode) are in series and their majority carriers can recombine in the ohmic interfacial layer. Despite the efficient charge separation and preserved redox potentials, such a configuration, requiring light illumination and co-catalysts for both photoelectrodes, would greatly complicate the preparation process of PEC devices and curb its practical application. So, it is of great importance to come up with an all-solid-state Z-scheme photoelectrode in which the two semiconductor parts are completely separated by electron mediators for pure Z-scheme charge transfer while the carrier dynamic equilibrium can be easily reached by changing the ratios of the used semiconductors.

For an efficient PEC hydrogen evolution reaction, photoactive materials are essential, and their catalytic performance is strongly dependent on band structures. The cadmium sulfide (CdS) with a favorable bandgap value (~2.4 eV) and sufficient CB level for the reduction of H^+ shows an excellent potential for solar conversion.[158, 226-228] Hence, distinct CdS nanostructures with varied morphologies have been explored as photoanodes for PEC hydrogen evolution. In particular, one-dimensional oriented CdS architecture, like nanowire or nanorod, demonstrates relatively better PEC activity than other nanostructures, owing to its large length-to-diameter ratio and defined charge transport pathway with less electron loss.[228-231] However, as mentioned above, pure CdS photoelectrodes also suffer from excessive charge carrier recombination. In addition, the self-oxidation of S^{2-} caused by photoexcited holes prior to the surface oxidation reaction results in severe CdS photocorrosion and poor photostability.[232, 233] Therefore, a large number of efforts have been focused on exploiting effective methods and strategies to push forward the advancement of CdS, mainly including co-catalyst loading,[234] plasmon metal decorations,[228, 235] and heterojunction constructions (Type-

II, Z-scheme and p-n junctions).[66, 210, 229] Nevertheless, to the best of our knowledge, there have been no attempts and published reports regarding the fabrication of 1D CdS-based pure Z-scheme photoanodes toward excellent hydrogen evolution. Accordingly, in this work, we designed an innovative pure Z-scheme photoanode system, composed of a 1D hierarchical CdS/Au/SnO_2 nanorod array, for highly efficient PEC hydrogen production. The spectrum-defined hydrolysis-precipitation approach is first proposed and employed to selectively encapsulate the SnO_2 layer on Au NPs for achieving the spatial separation of CdS and SnO_2. Here, the embedded Au NPs not only work as the host platform to support the attachment of the SnO_2 layer but also serve as the electron transfer mediators to profoundly promote the charge transfer from SnO_2 to CdS. This vectorial charge transportation helps to neutralize the VB holes of CdS and undermines the bulk recombination process of charge carriers, which is necessary for photoanode protection and the optimization of overall quantum efficiency. Meanwhile, the concentrated electrons in the CB of CdS with higher reductive power will drive faster hydrogen generation. As a result, the architected CdS/Au/SnO_2 photoanode exhibits significantly enhanced photo-to-current conversion efficiency, PEC property, and photostability compared to the pristine CdS.

4.3 Experimental section

4.3.1 Fabrication of Au-coated CdS nanorod arrays

First, CdS nanorod arrays were prepared via a one-step hydrothermal process based on our previous studies.[228] Briefly, 0.5 mM of $Cd(NO_3)_2{\cdot}4H_2O$, 0.5 mM of thiourea, and 0.2 mM of glutathione were dissolved in 20 mL of deionized water and stirred until a clear solution was obtained, then transferred to a 25 mL Teflon-lined autoclave. Later, a fresh FTO substrate (2.5×1.0 cm^2) was cleaned with acetone, deionized water, and ethanol and placed in the autoclave wall, followed by the hydrothermal treatment at 200 °C for 4 hours. Finally, the formed sample after washing and drying, was annealed at 400 °C for 1 h in nitrogen atmosphere for standby.

Subsequently, a facile in-situ reduction strategy was applied to evenly deposit Au nanoparticles on the surface of CdS nanorods. In detail, the prepared CdS nanorods on FTO substrates were immersed vertically into a mixture containing 10 mL of nanopure water and 10 mL of ethanol as the reducing agent. Then, different volumes (50, 100 and 200 µL) of $HAuCl_4$ solution (5 mM) were dropped into the reaction system. After holding for 2 h at room temperature, the Au-coated CdS nanorod arrays were washed slightly with deionized water and dried at 80 °C for about 12 h. Lastly, the formed electrodes were placed into a muffle furnace and subjected to a heat treatment at 400 °C for 1 h under N_2 flow at a heating rate of 20 °C min^{-1}. The loading amount of Au nanoparticles was tuned by varying the $HAuCl_4$ content in the precursor solution, and the corresponding samples were labeled as CdS/Au-0.5, 1, and 2, respectively.

4.3.2 Fabrication of selectively SnO_2-encapsulated CdS/Au photoanodes

Selectively decorating a SnO_2 layer on obtained CdS/Au electrodes was achieved through a spectrum-defined hydrolysis-precipitation approach. Typically, FTO substrates with CdS/Au were soaked vertically into $SnCl_2$ methanol solution (30 mL, 20 mM), followed by the addition of 50 µL of NaOH solution (0.5 M) under gentle stirring. Later, the above photodeposition system was irradiated by a LED solar simulator (with a calibrated irradiation intensity of 100 mW/cm^2) coupled with a 550 nm long-wave-pass filter. Upon photoreaction completion, the formed products were washed with ethanol, dried with N_2 flow, and then calcinated at 200 °C for 1 h in air for later characterizations. Here, photodeposition times (0.5, 1, and 2 h) were employed to adjust the loading thickness of the SnO_2 layer on the Au surface, and the final-obtained photoelectrodes were marked as CdS/Au/SnO_2-S0.5, CdS/Au/SnO_2-S1, and CdS/Au/SnO_2-S2, respectively. For comparison, SnO_2-coated CdS and fully SnO_2-wrapped CdS/Au nanorod arrays were prepared by essentially identical procedures but with full-spectrum irradiation for 1 h, which were renamed as CdS/SnO_2 and CdS/Au/SnO_2-F.

4.3.3 PEC measurements

An electrochemical workstation (SP-200 Potentiostat) coupled with a conventional three-electrode quartz cell (as-fabricated samples as working electrodes, Ag/AgCl (3 M KCl) as the reference electrode, and a Pt wire as the counter electrode) was employed to collect photoelectrochemical information. The efficient coating areas on FTO substrates were controlled at around 1.0 × 1.0 cm^2. A mixed $NaSO_3$(0.35 M) and Na_2S (0.25 M) aqueous solution (pH = 12.5) was applied as an electrolyte for all PEC and electrochemical experiments. An LSH-7320 ABA LED Solar Simulator with a calibrated irradiation intensity of 100 mW/cm^2 was used as the light source to provide the natural spectrum. The polarization curves of as prepared photoanodes from -1.2 to 0.4 V (vs. Ag/AgCl) were recorded at a sweep rate of 20 mV/s under darkness, chopped illumination, or continuous sunlight illumination. The transient I-t measurements at a constant bias of 0 V vs. Ag/AgCl were executed under chopped sunlight illumination with eight on/off cycles (20 s). The incident photon-to-current efficiency (IPCE) measurements were carried out at an applied bias of 0 V vs. Ag/AgCl using an aligned monochromator with a wavelength range of 320-700 nm. Electrochemical impedance spectroscopy (PEIS, 1-10^5 Hz) was performed at the open circuit potential with or without sunlight irradiation. Capacitance analysis over as prepared photoelectrodes was conducted at 1 kHz in darkness, ranging from -1 to 0 V vs. Ag/AgCl. The photostability of bare CdS and CdS/Au/SnO_2-S photoanodes was tested at 0 V under AM 1.5G irradiation. During the above process, the production of hydrogen in the gaseous phase of the sealed quartz PEC cell was collected and detected by a calibrated gas chromatograph (Perkin Elmer Clarus 580) and Ar was used as the carrier gas. Besides, some measured electrode potentials with respect to Ag/AgCl have been converted to those versus the reversible hydrogen electrode (RHE) through the Nernst equation for better comparison (Equation B4.1).

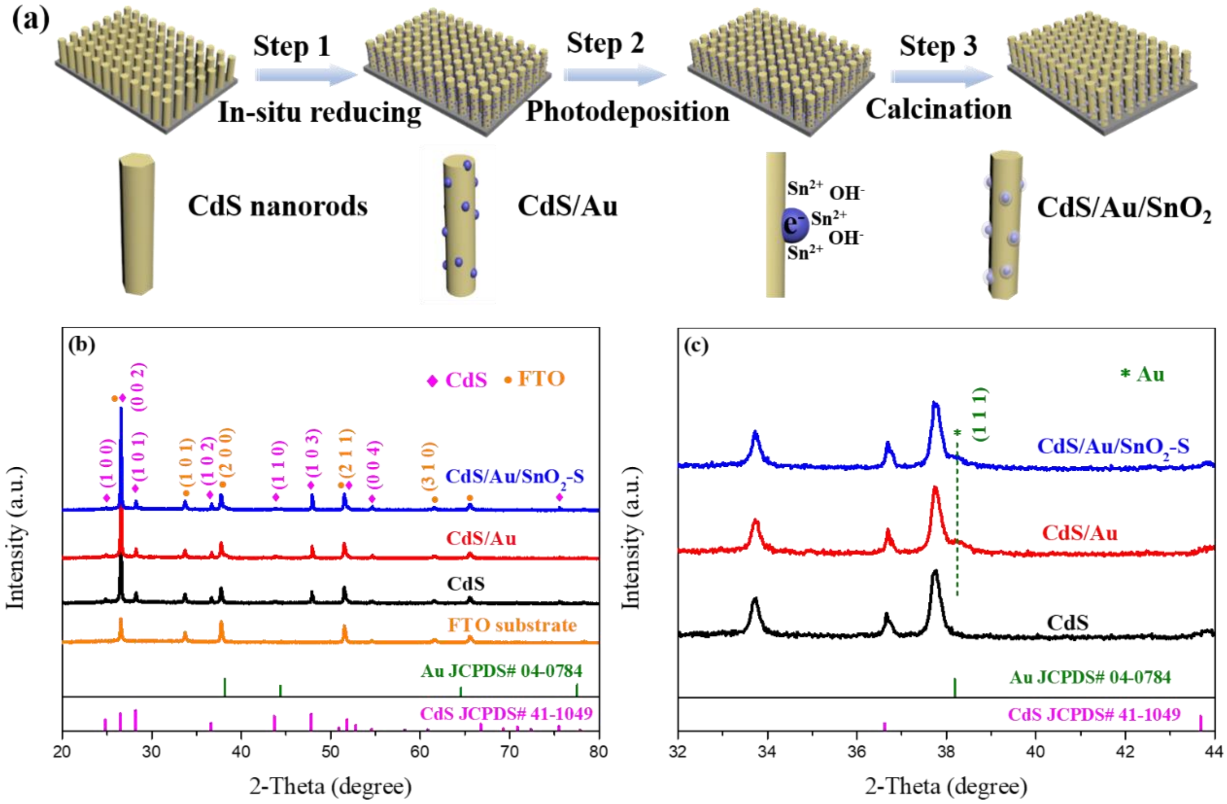

Figure 4.1 (a) Schematic diagram for the synthetic route of 3D hierarchical CdS/Au/SnO_2 photoanodes. (b) X-ray diffusion patterns of as-fabricated CdS, CdS/Au, and CdS/Au/SnO_2-S photoelectrodes. (c) Partial enlarged XRD patterns.

4.4 Result and discussion

4.4.1 Structural analysis

The fabrication of Z-scheme hierarchical CdS/Au/SnO_2 heterojunction photoanodes is schematically depicted in Figure 4.1a. Au NPs are firstly dispersed onto the surface of vertically aligned CdS nanorods with ethanol as the reducing agent. Following this, a facile photoassisted hydrolysis-precipitation approach is employed to selectively encapsulate the SnO_2 layer on Au NPs. In a typical process, surface plasmons of Au NPs can be photoexcited under visible light irradiation (with a wavelength higher than 550 nm) and then decay to generate hot electrons above their Fermi level.[236, 237] The electron-charged Au provides a large number of active sites for the approach and binding of Sn^{2+} via the electrostatic interaction.[211] Afterward, the attached Sn^{2+} on the Au surface would combine with OH^- due to the addition of NaOH and be thus hydrolyzed to be $Sn(OH)_2$. Upon heat treatment in an air atmosphere, the intermediate hydroxide will be further dehydrated and oxidized to form SnO_2. Since the irradiated photon energy is insufficient for CdS photoexcitation, the controlled growth of the SnO_2 layer will focus majorly on the Au surface, ultimately leading to the conformation of selectively SnO_2-encapsulated CdS/Au Z-scheme heterostructures. Similarly, one sun illumination will enable the fabrication of fully SnO_2-wrapped CdS/Au photoanodes, where photooxidation reaction will occur synchronously on the surface of CdS with better SnO_2 deposition.

To investigate the composition and crystallographic features of as-fabricated CdS/Au/SnO_2 Z-scheme heterojunctions, X-ray diffraction (XRD) analysis was performed and shown in Figure 4.1b. Apart from characteristic peaks belonging to the FTO substrate, other diffraction peaks of the pristine CdS photoanode match well with those of hexagonal wurtzite CdS,[229, 238] corresponding to JCPDS Card No. 41-1049. A few auxiliary impurity peaks confirm its high quality. Meanwhile, the significantly enhanced characteristic peak around 26.6° mainly arises from the (002) crystal plane of CdS, indicating its preferential longitudinal growth along the [001] direction.[181, 195] Notably, the introduction of the Au coating and the SnO_2 layer displays a negligible influence on the CdS diffraction pattern. Figure 4.1c shows the partially enlarged XRD patterns of bare CdS, CdS/Au, and CdS/Au/SnO_2-S photoelectrodes. One weak diffraction signal at 2θ values of 38.2 ° is detected and corresponds to the (111) diffraction of the cubic Au (JCPDS No. 04-0784),[239-240] implying the successful loading of metallic Au. Considering the diffraction interference of FTO substrates, the presence of SnO_2 encapsulation will not be discussed here.

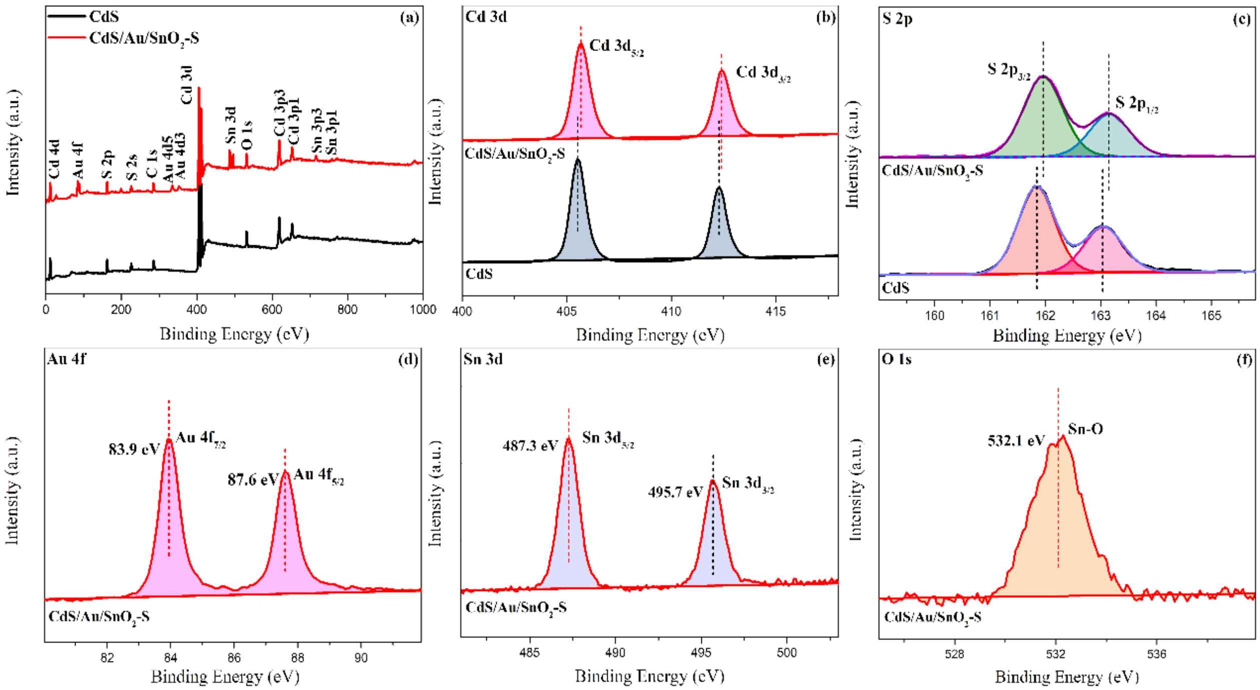

Figure 4.2 (a) Comparative XPS survey scan of as-prepared CdS and CdS/Au/SnO$_2$-S photoanodes: (b-f) Relative high-resolution XPS spectra of Cd 3d, S 2p, Au 4f, Sn 3d, and O 1s regions.

Comparative XPS studies were carried out to thoroughly probe the surface elemental compositions and chemical states of the hierarchical CdS/Au/SnO$_2$ photoanode. The survey XPS spectrum of as-obtained pure CdS and CdS/Au/SnO$_2$ Z-scheme heterostructure is given in Figure 4.2a. Except for the Cd and S signals, the appearance of intense Au and Sn peaks in the CdS/Au/SnO$_2$ heterostructure is also distinctive compared with those of the CdS. High-resolution XPS spectra are displayed in Figure 4.2b-f. Two prominent peaks at binding energies of 405.5 and 412.4 eV correspond to Cd 3d$_{5/2}$ and Cd 3d$_{3/2}$ spin-orbits, demonstrating the cadmium oxidation state (Cd^{2+}) in CdS.[241, 242] The fitting results for S 2p spectrum (Figure 4.2c) illustrate two characteristic peaks at 161.8 and 163 eV, consistent with the metal-sulfur bonds as the orbits of S 2p$_{3/2}$ and S 2p$_{1/2}$. Noticeably, both Cd 3d and S 2p peaks of the CdS/Au/SnO$_2$ heterostructure show a positive shift to higher binding energies, indicative of the decreased electron density on the CdS and the formation of strong interfacial interaction.[192] As for the Au region (Figure 4.2d), binding energies appearing at 83.9 and 87.6 eV are designated to Au 4f$_{7/2}$ and Au 4f$_{5/2}$, evidently manifesting the coating of Au NPs. More importantly, the Sn 3d spectrum (Figure 4.2e) with two bands located at 487.3 and 495.7 eV is also detected in the hierarchical CdS/Au/SnO$_2$ structure, which can be assigned to Sn 3d$_{5/2}$ and Sn 3d$_{5/2}$ spin-orbits. The splitting energy of 8.4 eV suggests the valence state of element tin (Sn^{4+}).[207, 243] Correspondingly, the XPS signal of O 1s near 532.1 eV is attributed to crystal lattice oxygen in Sn-O. As a result, the above analysis provides convincing evidence for the successful fabrication of Au-coating and SnO$_2$-encapsulation in a CdS/Au/SnO$_2$ heterostructure.

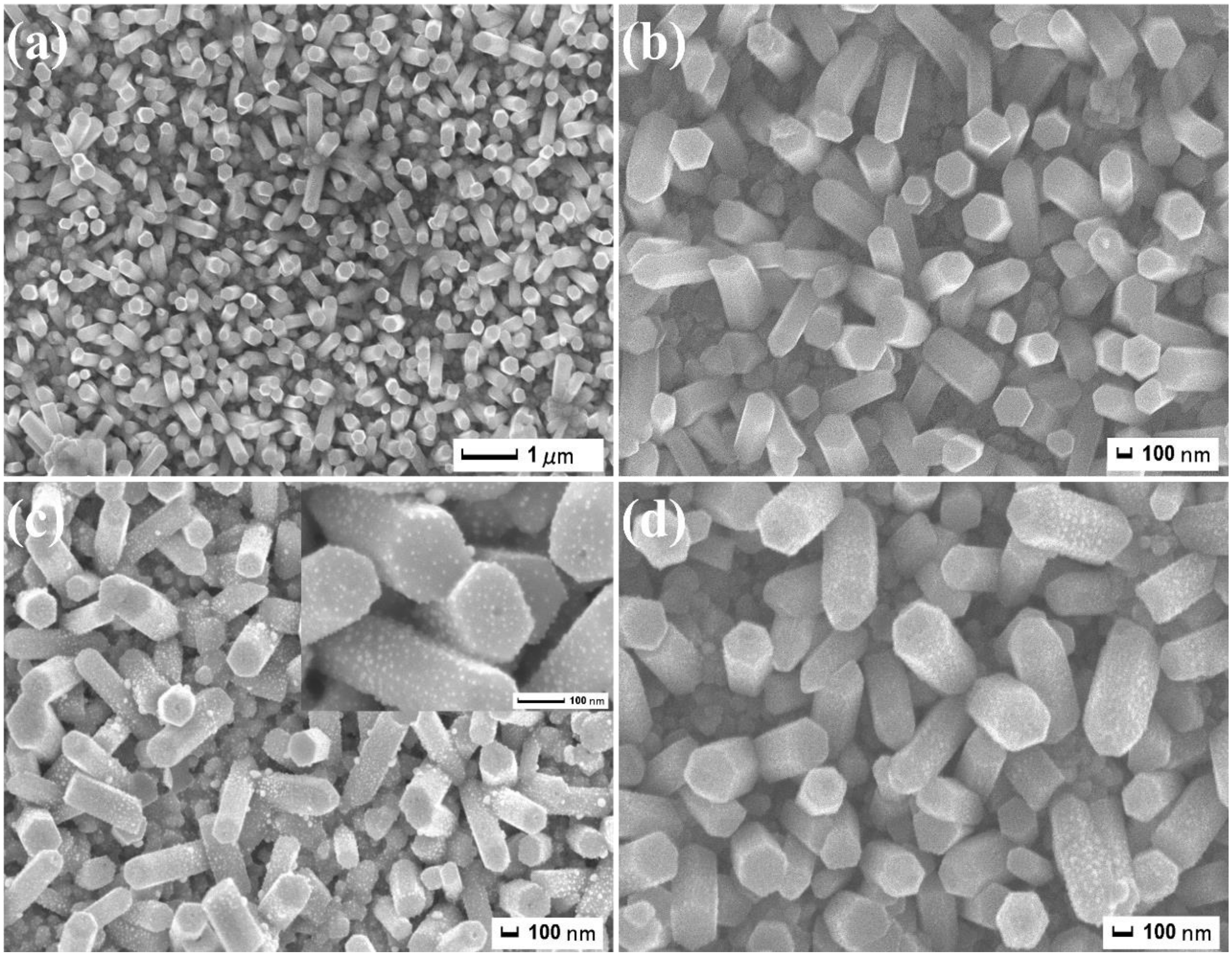

Figure 4.3 Top-view SEM images of (a, b) the bare CdS, (c) CdS/Au, and (d) hierarchical CdS/Au/SnO_2 nanorod arrays.

The typical SEM observations were developed to verify the morphologies of as-synthesized photoelectrodes. The low magnification SEM image in Figure 4.3a reveals that the pristine CdS arrays featured as the 1D hexagonal rod-like shape almost vertically grow on the FTO substrate. From high magnification and cross-sectional SEM images (Figure 4.3b and B4.1), it can be observed that the bare CdS nanorod possesses a relatively smooth surface with a diameter distribution from 100 to 300 nm, and the length scale is approximately 760 nm. After the in-situ reducing procedure, plenty of Au nanoparticles with an average size of 10 nm are well deposited on both the side and top surface of CdS nanorods (Figure 4.3c). The as-fabricated CdS/Au/SnO_2 heterostructure (Figure 4.3d) exhibits an analogously morphological characteristic as that of CdS/Au nanorod arrays, but with slightly increased particle sizes, demonstrating the favorable stability of the whole microstructure during the photoassisted hydrolysis-precipitation process.

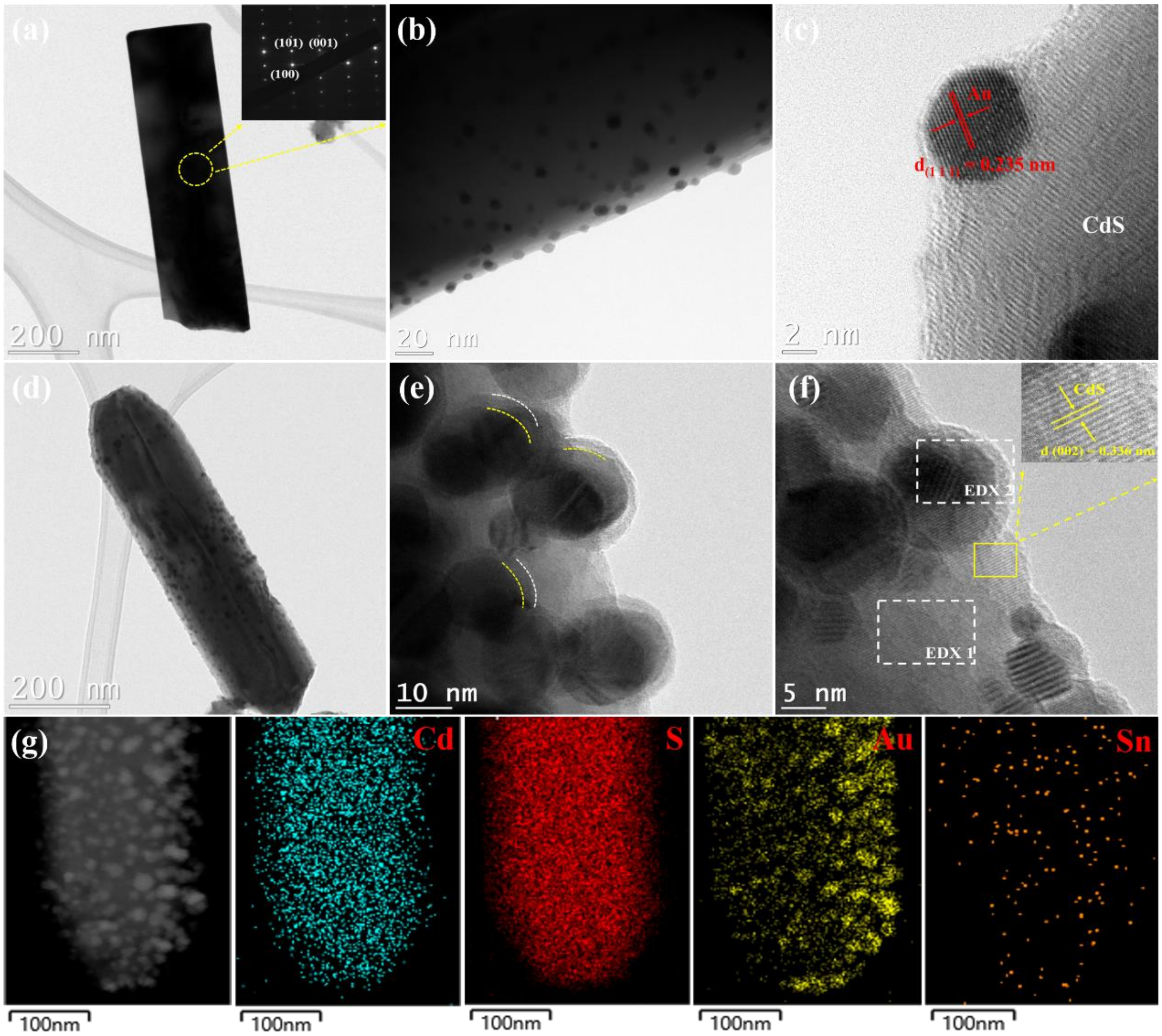

Figure 4.4 (a) Low magnification TEM image and SAED pattern (insert) of the single-crystalline CdS nanorod. (b) Bright field and (c) HRTEM images of the Au-modified CdS nanorods. (d, e) Low magnification TEM and (f) HRTEM images of hierarchical CdS/Au/SnO_2 nanorods. (g) STEM image of CdS/Au/SnO_2 photoelectrode and the related EDX elemental mapping analysis.

TEM and HRTEM characterizations were applied to observe the detailed microstructures of CdS/Au/SnO_2-S photoanodes and confirm the location of SnO_2 encapsulation. As shown in Figure 4.4a, the CdS nanorod with the faceted and smooth surface has been successfully prepared through the hydrothermal process. The selected-area electron diffraction (SAED) pattern shown in the insert reveals its single-crystalline feature, which might endow it with high electron mobility for improving charge carrier transfer.[181] The detected 6.79, 3.58, and 3.16 Å spacings correspond to the (001), (100), and (101) crystal planes of hexagonal CdS, respectively. A clear interplanar distance of 0.67 nm shown in Figure B4.2b is related to {001} the basal plane of CdS crystals, indicating its [001] growing direction. From the low magnification TEM image of

CdS/Au nanorods (Figure 4.4b), a large amount of consecutively distributed Au nanoparticles with well-proportioned particle sizes (in the range of 5-20 nm) can be readily distinguished on the pristine CdS nanorod surface, which is in a good agreement with the above SEM observations. The corresponding HRTEM image (Figure 4.4c) presents the intimate interface connection between Au NPs and CdS nanorods with the exposed (111) crystal plane.[244] In addition, a SnO_2 wrapped CdS core-shell nanostructure was also fabricated via the photoassisted hydrolysis-precipitation process, but with full-spectrum illumination, and the related HRTEM image is displayed in Figure B4.3. Obviously, the bare CdS nanorod is absolutely covered by a uniform SnO_2 sheath layer with a thickness of ~2 nm and a typical lattice distance of 0.335 nm can be assigned to its (110) crystal face. This compelling result proves that the photodeposition can indeed achieve the SnO_2 encapsulation on the photoactive material surface. Furthermore, Figure 4.4d displays the low magnification TEM image of the CdS/Au/SnO_2 heterostructure. Upon the in-situ reducing and photodeposition process, the sample CdS/Au/SnO_2-S still maintains the 1D rod-like microstructure without any deformation. Figure 4.4e illustrates that the external SnO_2 passivation layer tightly attaches to the surface of Au NPs, signifying the successful fabrication of hierarchical CdS/Au/SnO_2 heterojunction architecture. To further examine whether the deposition sites of SnO_2 are primarily on Au NPs, the TEM-EDX analysis with distinct regions taken from Figure 4.4f (EDX1 concentrated on the bare CdS region and EDX2 focused on the CdS/Au/SnO_2 region) was performed, and the results are presented in Figure B4.4. Apparently, area 1 is composed of Cd, S, Au, Sn, and O elements, but area 2 only contains Cd and S elements, which directly suggests the successful selective deposition of the SnO_2 layer on the Au surfaces of the CdS/Au nanorod. In general, the charge drift and diffusion behavior of a heterojunction are highly dependent on its structural features. Herein, such a special junction with uniform SnO_2 layers selectively covered on the Au surface of CdS/Au nanorods would be favorable for the realization of a Z-scheme charge transport mechanism, as discussed later. Ultimately, the energy dispersive X-ray spectroscopy (EDX) elemental mapping of Cd, S, Au, and O elements was recorded according to the HADDF-STEM image in Figure 4.4g, and the correlative elemental distribution expresses a similar architecture as that of the CdS/Au/SnO_2-S photoanode. Based on the above results, it is convinced that the strategy developed here can accomplish the selective encapsulation of the SnO_2 layer on Au NPs through varying the spectrum of irradiation.

4.4.2 Optoelectronic properties

The optical properties of as-obtained photoelectrodes were tested, and the resulted UV-vis absorption spectra are presented in Figure B4.5. The pristine CdS nanorod arrays exhibit a remarkable visible-light harvesting capacity with a steep absorption onset of approximately 518 nm due to their intrinsic narrow bandgap.[135, 245] Upon the decoration of Au NPs, an apparent absorption enhancement in the visible region accompanied with a slightly redshifted spectrum can be observed over the CdS/Au photoanode. The broad absorption band detected at 615 nm is mainly owing to the surface plasmon resonance effect of Au NPs.[204] After the SnO_2 encapsulation, CdS/SnO_2 and CdS/Au/SnO_2-S photoelectrodes show similar absorption edges to bare CdS and CdS/Au nanorod arrays, but with the higher light sensitization below their absorption edge, which may be attributed to the higher absorption of scattered light by CdS.[66] It is believed that the prepared CdS/Au/SnO_2 photoanode with better light harvesting will obtain a higher quantum yield for PEC hydrogen evolution. In addition, the bandgap energies of as-fabricated photoelectrodes were estimated according to the Kubelka-Munk equation, and the calculated values (Figure B4.5b) correspond to 2.29, 2.29, 2.25, and 2.25 eV, respectively.

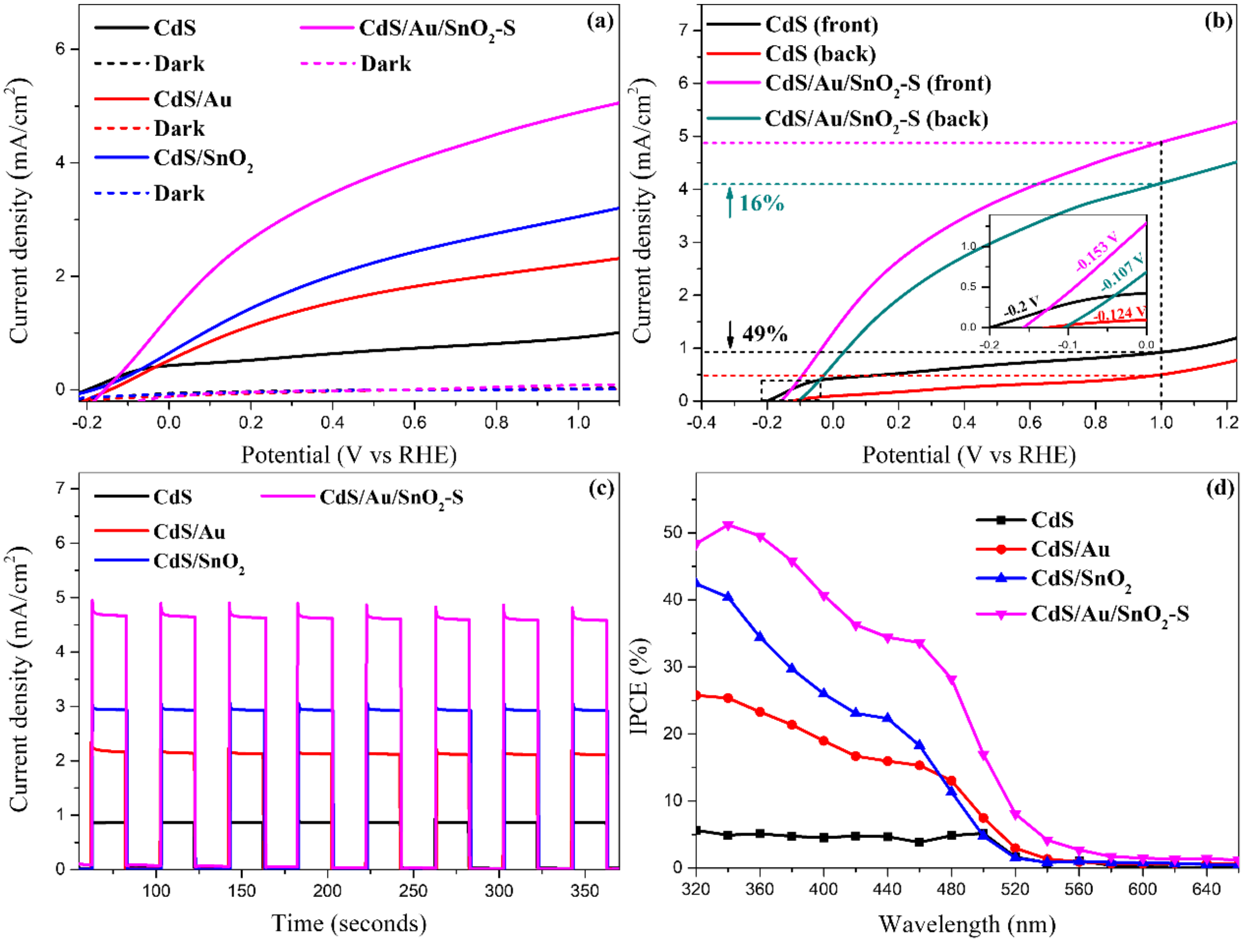

Figure 4.5 Photoelectrochemical measurements on as-obtained CdS, CdS/Au, CdS/SnO_2, and CdS/Au/SnO_2-S photoanodes. (a) LSV curves under simulated sunlight irradiation (100 mW/cm^2) and darkness. (b) The comparable current density-voltage curves under front or back side illumination. (c) Photoresponse tests at 0 V vs. Ag/AgCl under chopped light irradiation (8 cycles with 20 s of interval). (d) IPCE plots.

For studying the PEC hydrogen evolution activities of as-fabricated photoelectrodes, the linear-sweep-voltammetry (LSV) curves were recorded using a conventional three-electrode configuration under one sun illumination. Initially, the impact of the loading amount of Au NPs on the photoelectrochemical performance of the pristine CdS nanorod arrays is systematically discussed (Figure B4.6), and the optimal $HAuCl_4$ content is determined. Conceivably, excessive Au NPs coating would shield the light absorption of the CdS host and incur a profoundly inhibited photoresponse. Figure 4.5a and B4.7 display the comparative polarization curves of the bare CdS, CdS/Au, CdS/SnO_2, and CdS/Au/SnO_2-S photoanodes with the photocurrent density as a function of voltage under dark, chopped, and continuous simulated sunlight irradiation. Apparently, the dark scans from -0.2 to 1.1 V vs. RHE only exhibit the ignorable current density, implying their high charge transport resistance. Under one sun illumination from the front side, the photocurrent density of all photoelectrodes promptly increases with the raised applied bias. It is worth noting that the bare CdS nanorod array shows an unsatisfactory photoresponse with a considerably low photocurrent density (0.91 mA/cm^2 at 1 V vs. RHE), due to its fast quantum recombination rate. After being coupled with an encapsulated SnO_2 layer, the resulting core-shell CdS/SnO_2 heterostructure possesses an evidently improved photocurrent density (3.06 mA/cm^2 at 1 V vs. RHE) within the whole positive potential. Considering their matched energy band alignment and the higher conduction band (CB) potential of the CdS host (as demonstrated later),[207, 229] a direct Z-scheme charge transfer route should be more suitable here than the conventional type-II heterojunction mode. Interestingly, the incorporation of Au NPs as the electron mediator can contribute to the higher PEC activity and result in a dramatically enhanced photocurrent density up to 4.87 mA/cm^2 (at 1 V vs. RHE), which may be attributed to the further promoted charge carrier separation efficiency. Besides, controlling samples with different photodeposition times for the SnO_2 encapsulation were fabricated and tested in Figure B4.8 for the maximum PEC properties. From the ICP-OES analysis, the loaded Au and SnO_2 contents in the optimal CdS/Au/SnO_2-S electrode were determined to be 2.75 and 7.49 wt.%, respectively. Figure 4.5b displays the difference in the photocurrent density between the front and back sides of the irradiation (100 mW/cm^2) for evaluating the separation and transfer processes of photoinduced holes. Obviously, the front-side photocurrent density of the bare CdS nanorod array was found to be 49% higher than the back-side photocurrent density at an applied bias of 1 V vs. RHE, suggesting the high internal consumption of holes from the nanorod bottom (near the FTO substrates).[192, 246] This phenomenon means that holes are easily recombined with photogenerated electrons during the charge carrier transport process in the bulk semiconductor. By contrast, the largely reduced difference in photocurrent density (16 %) over CdS/Au/SnO_2-S heterostructure reveals that the rational construction of the heterojunction can effectively suppress the charge carrier recombination behavior and allow more electrons to smoothly transfer into the counter electrode for hydrogen evolution. Such behavior is also certified by its less positive offset of onset potential (the insert).

Chronoamperometric I-t curves were obtained under AM 1.5G irradiation (100 mW/cm^2) without the applied bias for evaluating the instantaneous photoelectric behavior. As found in Figure 4.5c, all fabricated photoelectrodes present a reliable and reproducible photocurrent response over repetitive on/off cycles of sunlight irradiation. Compared with the bare CdS nanorod array, both CdS/Au and CdS/SnO$_2$ yield a substantially higher photocurrent density, which might result from the passivation effect of Au NPs and the establishment of direct Z-scheme charge transport channels (as proved later). Notably, the 1D hierarchical CdS/Au/SnO$_2$-S heterostructure demonstrates the maximum photocurrent generation for PEC hydrogen evolution, which is consistent with the above LSV analysis. Further, to investigate the correlation of photoactivity with respect to the incident wavelength, the IPCE tests (Equation B4.2) were performed under monochromatic light illumination at 0 V vs. Ag/AgCl. As shown in Figure 4.5d, the pristine CdS photoanode presents a relatively low photo-to-current conversion efficiency below 510 nm because of its rapid charge carrier recombination process. Upon the encapsulation of the SnO$_2$ layer with a high electron mobility,[66] the formed CdS/SnO$_2$ core-shell heterostructure exhibits a dramatically improved photoactivity from UV to visible light region, which may be ascribed to the enhanced optical absorption, facilitated charge separation and transport. After incorporating Au NPs as the electron mediator, its photoconversion efficiency is further improved and the corresponding IPCE plot presents a slight redshift, matching well with the result of UV-vis absorption analysis. Noticeably, the IPCE curve of the CdS/Au/SnO$_2$-S photoanode increases sharply in the UV region and reaches a maximum at a wavelength of 340 nm, which may be closely associated with the activation of Z-scheme charge transfer channel. Ultimately, the well-designed CdS/Au/SnO$_2$-S heterostructure demonstrates the optimal conversion efficiency (51.2 %) that is 10.4 times higher than that of the bare CdS photoanode. Based on these PEC performance measurements, it is believed that coupling the 1D CdS nanorod array with Au NPs and SnO$_2$ layer through an appropriate structured engineering strategy could accomplish the leap in photoelectrochemical activity. Moreover, through a comparison with reported similar CdS-based heterojunctions (Table B4.1), the novel 1D hierarchical CdS/Au/SnO$_2$-S photoanode with the extremely excellent PEC activity demonstrates a certain superiority.

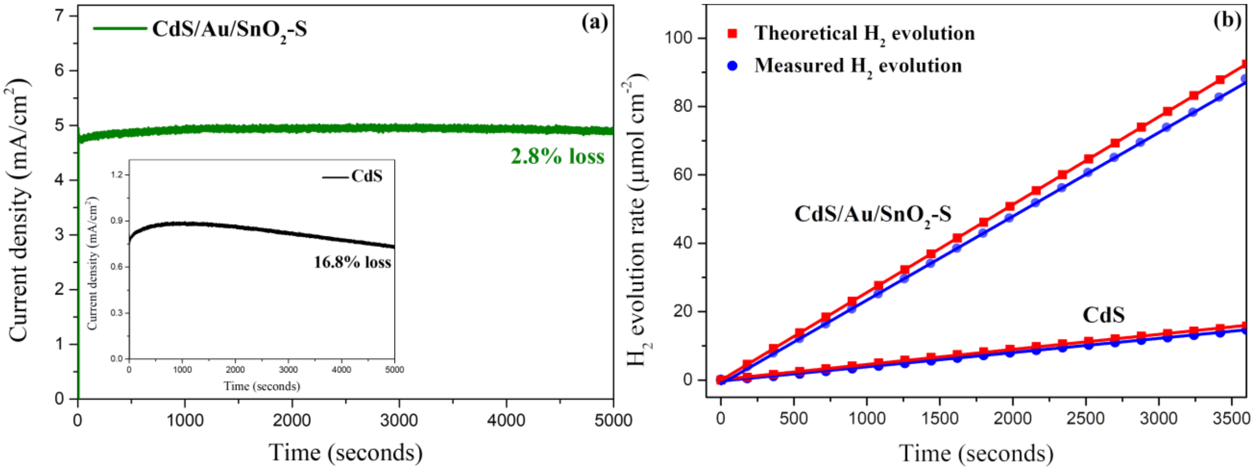

Figure 4.6 (a) Long-term photostability and (b) time-dependent PEC hydrogen evolution over the pristine CdS and hierarchical CdS/Au/SnO_2-S photoanodes under one sun irradiation (100 mW/cm^2) at 0 V versus Ag/AgCl.

Long-term photostability and durability are crucial factors in evaluating the practical application of as-obtained PEC cells. Thus, the time-dependent photocurrents (Figure 4.6a) over the pristine CdS and hierarchical CdS/Au/SnO_2-S photoanodes were systematically examined under one sun irradiation without bias. As expected, the photocurrent density of the bare CdS decays rapidly with the prolonged irradiation time and the high attenuation ratio (16.8 % loss) in a period of 5000 s could be mainly owing to its highly susceptible photocorrosion. By sharp contrast, the hierarchical CdS/Au/SnO_2-S heterostructure exhibits better stability (2.8 % loss) and the photocurrent density still retains at around 4.9 mA/cm^2 after 5000 s of continuous sunlight illumination, which possibly results from the efficient charge carrier separation and speedy extraction of VB holes in CdS. In addition, the cycled SEM image and XRD pattern (Figure B4.9a and b) after the long-time photoreaction displays tiny micromorphological and crystal structural variations compared to the original sample, further confirming the wonderful photostability of the as-fabricated CdS/Au/SnO_2-S photoelectrode. The above results experimentally reveal that the rational incorporation of Au NPs and SnO_2 layer can not only devote to the higher PEC performance but also protect the CdS host from photo-corrosion. In addition, the generated hydrogen was collected and quantified every 3 mins with a gas chromatograph, and the working areas of each photoelectrode were limited to 1 cm^2 with the identical experimental condition above. The detected H_2 amounts versus time is recorded in Figure 4.6b. Both CdS and CdS/Au/SnO_2-S photoanode present nearly linear increments in the yields of hydrogen. Relatively, the CdS/Au/SnO_2-S heterojunction possesses a much higher average H_2 generation rate (1.47 μmol min^{-1} cm^{-2}) corresponding to its larger photocurrent density. Through comparing the measured H_2 amount with the theoretical H_2 production, the calculated Faradaic efficiency of CdS/Au/SnO_2-S photoanode reaches up to

95.3 % (Equation B4.4), signifying that the hydrogen evolution reaction is responsible for the appearance of PEC photocurrent.

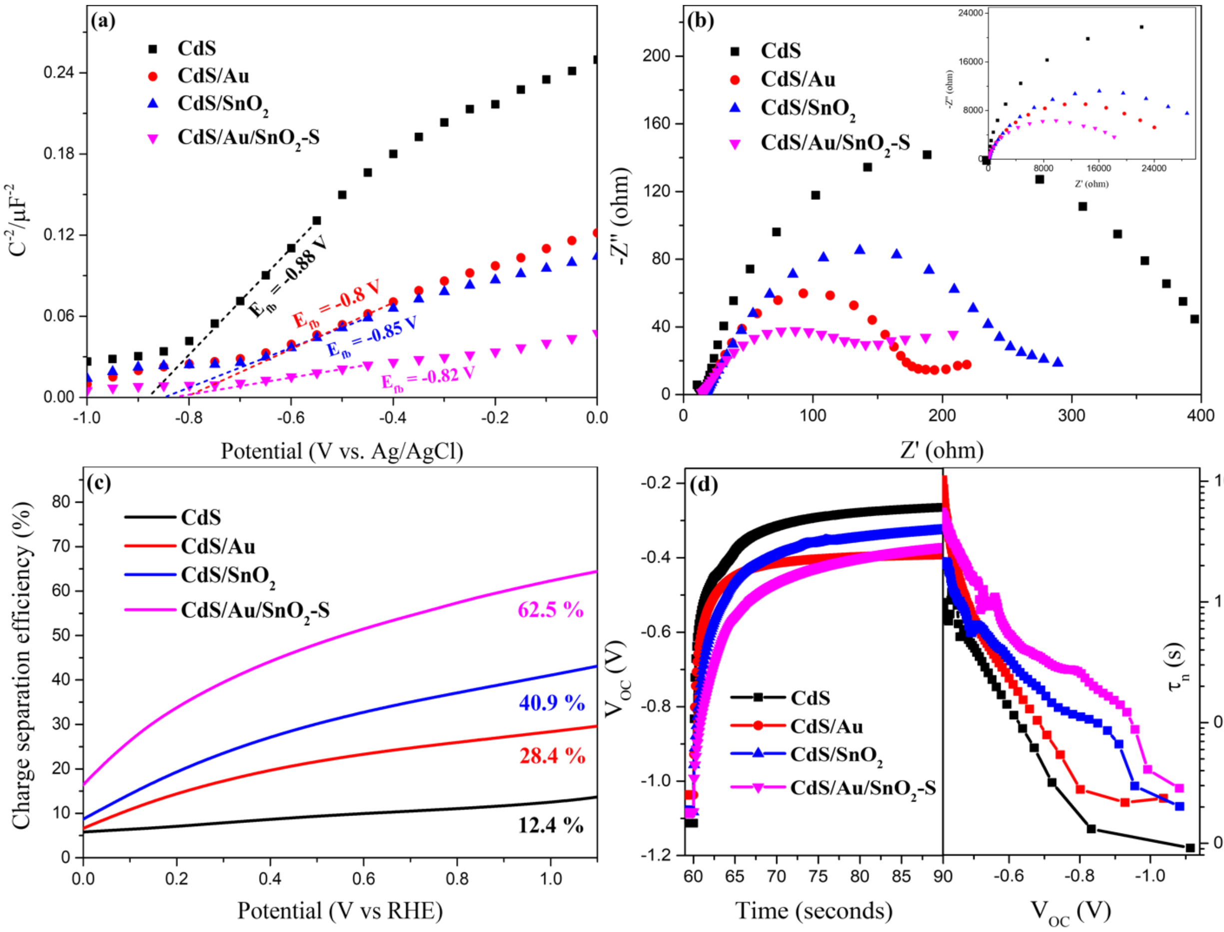

Figure 4.7 (a) Mott-Schottky plots recorded at a frequency of 1 kHz, (b) Nyquist plots at the open circuit potential under darkness and one sun irradiation, (c) charge separation efficiency, (d) the open-circuit photovoltage decay curves (left), and calculated electron lifetimes (right) of as-prepared photoelectrodes.

4.4.3 PEC enhancement analysis

To obtain a deep insight into the charge migration behavior responsible for the significant PEC enhancement, a series of electrochemical measurements were carried out. Mott-Schottky tests were first performed at a fixed frequency of 1 kHz with an applied bias from -1 to 0 V vs. AgCl under darkness. As shown in Figure 4.7a, the M-S plots of all as-fabricated photoelectrodes present positive slopes, proving their n-type semiconductor characteristics. In the meantime, it is readily observable that the incorporation of Au NPs and SnO_2 layer leads to a progressively reduced slope, signifying the increased charge carrier density.[107] To be specific, the donor density (N_D) of the pristine CdS, CdS/Au, CdS/SnO_2, and CdS/Au/SnO_2-S photoelectrodes were calculated to be 4.04×10^{17}, 9.5×10^{17}, 1.12×10^{18}, and 2.85×10^{18} cm^{-3}, respectively (Equation B4.5). The higher donor density of hierarchical CdS/Au/SnO_2-S over 7 times higher than that of bare CdS further demonstrates the dramatically improved charge separation efficiency and better electrical conductance. It is speculated that this phenomenon is mainly caused by the formation of Z-scheme heterostructure (see below), so that the VB holes of CdS will be effectively captured by the CB electrons of the SnO_2 layer under the effect of the built-in electric field, thus leading to the suppressed electron-hole recombination process and higher N_D value. Besides, the passivation of Au NPs may also be favorable for the reduced surface state density along with less charge carrier recombination. Moreover, the flat-band voltage (E_{fb}) was read through the x-intercept from the extrapolated linear part of C^{-2} *vs* the applied bias voltage. Compared with the bare CdS, a distinctive positive shift in the E_{fb} value of the CdS/Au/SnO_2-S heterostructure means less electron-trapping process and higher quantum efficiency.[107, 247]

Electrochemical impendence spectra were recorded both under darkness and one sun irradiation to further analyze the charge transfer kinetics in the as prepared photoelectrodes. Figure 7b and B4.10 present the obtained Nyquist plots and the associated equivalent circuit, which contains two resistances (R_s and R_{Bulk}): series resistance from the PEC cell and charge transfer resistance in the bulk component. Among them, CdS/Au and CdS/SnO_2 photoanodes exhibit a smaller semicircle radius in the high-frequency region, corresponding to a lower R_{Bulk} than that of the pristine CdS, indicating the boosted charge carrier transport process.[248] As expected, upon the incorporation of Au NPs and a SnO_2 layer, the hierarchical CdS/Au/SnO_2-S heterostructure with the smallest arc radius demonstrates the lowest resistance, thus allowing the more effective electron migration from SnO_2 to CdS. In addition, this result could also be confirmed by PL spectra, as shown in Figure B4.11. The bare CdS nanorod array displays a strong visible band emission located at 515 nm and a relatively broad trap-state emission centered at around 680 nm.[181, 195] In contrast to that of the CdS, the PL intensity of the as-fabricated CdS/Au/SnO_2-S photoanode is sharply quenched on both band and surface trap state emission peaks, implying a largely suppressed bulk and trap-state-mediated carrier recombination process in the heterostructure because of the Z-scheme heterojunction fabrication and the passivation effect of Au NPs. Assuming the complete capture of photoinduced holes accumulated on the photoelectrode surface by the hole scavenger (Na_2S/Na_2SO_3), the quantitative charge separation efficiency was calculated according to the following equation: $\eta_{sep} = J_{Ph}/J_{Max}$, where J_{Max} (Equation B4.6 and B4.7) represents the maximum theoretical photocurrent density (Figure B4.12). Following the UV-vis absorption spectra, the integrated photocurrent densities (J_{Max}) of the pristine CdS, CdS/Au, CdS/SnO_2, and CdS/Au/SnO_2-S photoelectrodes are determined to be 7.44, 7.81, 7.38, and 7.87 mA/cm^2, respectively. Figure 4.7c displays the correlation for the calculated charge separation efficiency as a function of the applied bias voltage. Obviously, the architected CdS/Au/SnO_2-S photoanode illustrates the highest separation efficiency in comparison to other photoelectrodes, up to 62.5 % at 1 V vs. RHE, directly verifying the promoted photoexciton anti-recombination process in this heterostructure. It is noteworthy that the above analysis also reveals the important bridging role of embedded Au NPs on linking the SnO_2 layer to the CdS host for elevating the electron transport.

The instantaneous open-circuit voltage decay (OCVD) tests were applied to quantitatively evaluate the promoted charge separation efficiency and prolonged electron lifetimes. All photoelectrodes underwent a 30 s of sunlight illumination to gain a steady open-circuit voltage (V_{OC}), and subsequently, the decayed V_{OC} curves as a function of time were examined in darkness, as displayed in Figure B4.13 and the left image of Figure 4.7d. The strongest V_{OC} decay observed in pristine CdS is majorly owing to the rapid bulk charge carrier recombination.[244, 249-250] Comparatively, both Au decoration and SnO_2 wrapping result in effectively alleviated V_{OC} decay. With Au NPs, its surface passivation and formation of a Schottky rectifier in the plasmonic CdS/Au heterostructure will drive the delocalized holes to Au NPs for surface oxidation, thus preventing the charge carrier recombination, as proved previously.[228, 244] With the SnO_2 layer, the conformation of the direct Z-scheme heterojunction (as analyzed later) will aid the rapidly vectorial charge migration from the SnO_2 layer to the CdS host, liberating the conduction band (CB) electrons of the CdS host and valence band (VB) holes of the SnO_2 layer for higher carrier density. It is worth noting that the utilization of embedded Au NPs in the middle of a core-shell CdS/SnO_2 nanostructure causes a very gentle V_{OC} decay, indicating further accelerated charge transfer and separation. The related decay lifetimes were calculated and shown in Figure B4.13. Furthermore, the corresponding electron lifetimes (τ_n) were deduced in accordance with the V_{OC} decay rate (Equation B4.8), and the results are shown in the right image of Figure 4.7d. Obviously, the architected CdS/Au/SnO_2-S heterostructure demonstrates a substantially prolonged lifetime compared to other photoelectrodes, which is well consistent with the above analysis. All previous results reasonably conclude that the rational incorporation of Au NPs and SnO_2 layer can advance charge separation and transfers, elongate electron lifetime, and benefit the outstanding PEC hydrogen evolution and photostability.

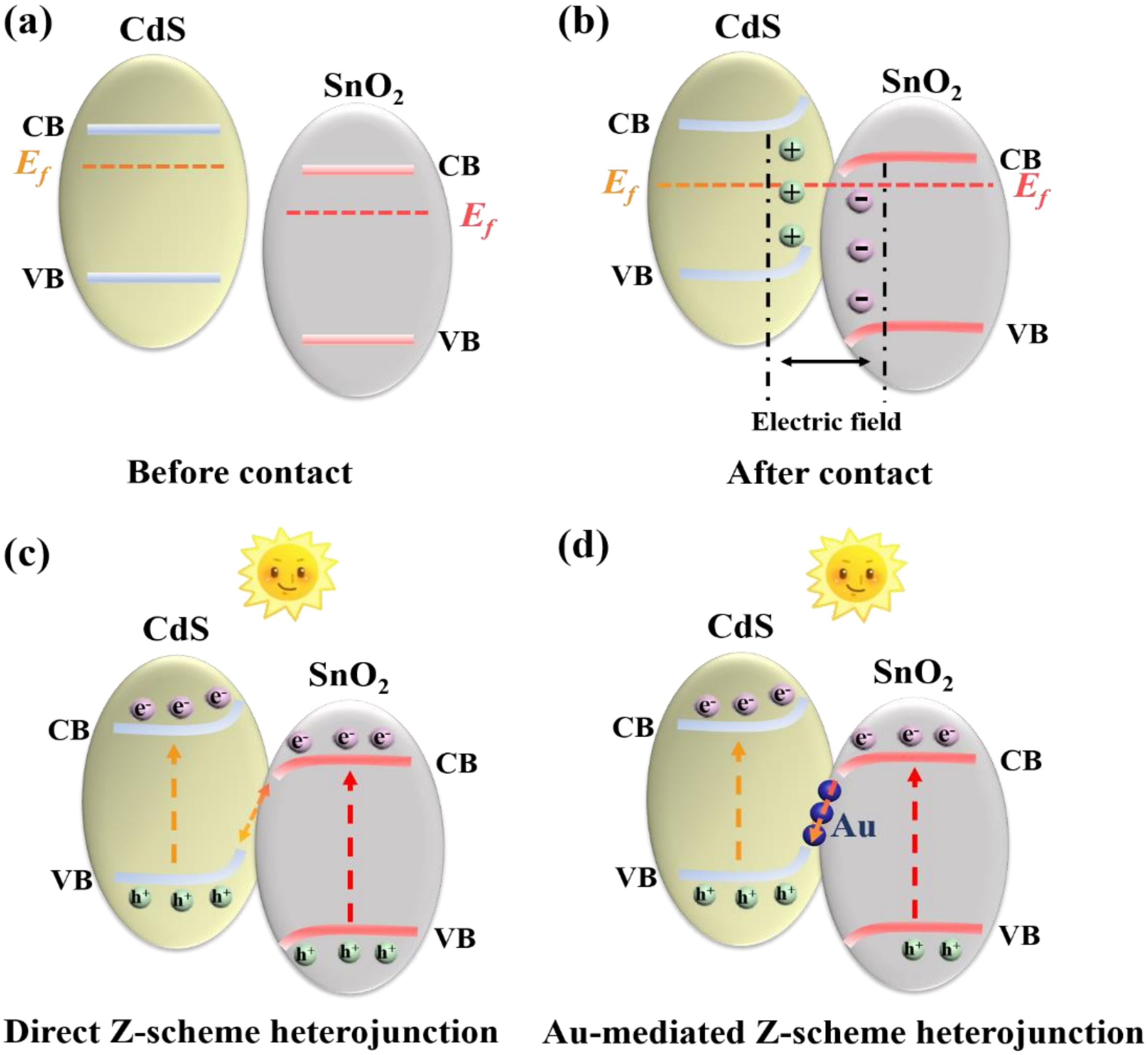

Figure 4.8 Schematic illustrations of the band alignment of CdS and SnO_2 (a) before and (b) after contact. The charge transport behavior of (c) direct CdS/SnO_2 Z-scheme heterostructure and (d) Au-mediated CdS/SnO_2 Z-scheme heterojunction.

4.4.4 Au-mediated Z-scheme PEC mechanism

To elucidate the higher charge separation efficiency in hierarchical CdS/Au/SnO_2-S heterostructure, the energetics of charge transport and a possible PEC catalytic mechanism were explored and proposed. In general, the charge carrier transfer behavior between semiconductors is determined by the interfacial energy-band bending, which is highly dependent on their Fermi levels and band structures.[102, 207, 251-253] Herein, the work function and valence band maximum (VBM) values of CdS and SnO_2 were characterized by ultraviolet photoelectron spectroscopy (UPS, Figure B4.14a and B4.14b). Additionally, based on their optical bandgaps, the corresponding conduction band minimum (CBM) positions of CdS and SnO_2 were calculated to be -3.72 and -4.26 eV. As a result, a staggered band alignment among them is built as shown in Figure B4.15, which matches well with previous reports.[195, 207] As can be seen, the CdS host (-4.06 eV) demonstrates a higher Fermi energy level than SnO_2 (-4.83 eV). When they make direct contact, a charge migration process from CdS to SnO_2 will occur until a balanced energy level is reached, thus inducing the formation of a distinct built-in electric field. Meanwhile, the band edge of CdS will present an upward bending at the contact interface while a downward bending is presented on that of SnO_2, ultimately disrupting the straddle charge transfer channels from CdS to SnO_2 (Type-II pathway), as shown in Figure 4.8a and b. Subsequently, under sunlight irradiation, the presence of the built-in electric field will drive the photogenerated electrons in CB of SnO_2 to recombine with the holes in VB of CdS at the interface. The retained photoexcited charge carriers with higher redox potentials in CB of CdS and VB of SnO_2 will participate in the PEC system cycles, which illustrates a direct Z-scheme catalytic mechanism (Figure 4.8c). Pioneering studies have pointed out that the introduction of the metallic polar surface in direct binary Z-scheme photoactive systems through a rational structural engineering strategy will be favorable for a strengthened Z-scheme transport kinetic and improved PEC performance. Therefore, Au NPs with a higher work function (-5.30 eV) are selected as electron mediators to accelerate the vectorial charge immigration from SnO_2 to CdS and perfect the Z-scheme transfer process (Figure 4.8d), which has been confirmed by the further promoted charge separation efficiency in the CdS/Au/SnO_2-S heterostructure compared to the binary CdS/SnO_2 (as analyzed above).

In order to further confirm the Z-scheme charge transfer route, the hydroxyl radicals (·OH) produced during the photoreaction were detected with terephthalic acid as the PL probe. As displayed in Figure 4.9a, all fabricated photocatalysts present clear PL signals at around 425 nm, indicating the generation of hydroxyl radicals, which can be explained by comparing the energy band positions of CdS and SnO_2 with the redox potential of $OH^-/\cdot OH$. Figure 4.9b exhibits the specific band alignment between CdS and SnO_2, and the relative redox potential of $O_2/\cdot O^-_2$ (-0.3 V vs. NHE) and $OH^-/\cdot OH$ (2.8 V vs. NHE). Obviously, the photoexcited holes in the VB of SnO_2 with the higher oxidation potential can directly produce hydroxyl radicals, and photoinduced electrons in the CB of CdS are able to facilitate the generation of superoxide radicals ($\cdot O^-_2$), indirectly producing hydroxyl radicals. Accordingly, if the charge transport route in the binary CdS/SnO_2 heterostructure majorly complies with the conventional Type-II pathway (Figure B4.16), neither superoxide radicals nor hydroxyl radicals will be generated, which is contrary to the above PL results. Compared with that of the bare CdS, a stronger PL signal is clearly observed in the CdS/SnO_2, revealing the more generation of hydroxyl radicals (·OH). This result evidently clarifies the efficient release of charge carriers with enough redox potentials in CB of CdS and VB of SnO_2, suggesting the successful construction of the direct Z-scheme heterojunction. More importantly, the introduction of Au NPs as charge mediators could further promote the directional charge transfer from SnO_2 to CdS, leading to higher quantum efficiency, which is verified by the highest PL intensity of the CdS/Au/SnO_2-S heterostructure. When the discussion of energy bands and PL characterization are taken together, it seems likely that the charge-carrier immigration process in the CdS/Au/SnO_2-S photoreaction system follows a Z-scheme catalytic model rather than the usual straddles band transfer.

Based on the aforesaid analysis, the rational charge carrier transport mechanism for the overall PEC hydrogen evolution over the hierarchical CdS/Au/SnO_2-S heterostructure was proposed in Figure 4.9c. Under one sun irradiation, electron-hole pairs can be first photo-generated on both CdS and SnO_2. Owing to the more negative Fermi level of Au NPs, the photoexcited electrons in the CB of SnO_2 will rapidly travel into Au NPs. Meanwhile, since the VB potential of CdS is lower than the Fermi level of Au NPs, the gathered electrons in Au NPs will then directionally transfer to the CdS host, readily recombining with its VB holes. Thus, the photoinduced electrons and holes in the CdS host can be effectively separated through the collaboration with Au NPs and the SnO_2 layer, which is favorable for suppressing the charge carrier recombination process, reducing the bulk resistance, prolonging the electron lifetimes, and largely improving the photoelectric response. Note that Au NPs mainly function as the electron mediator to accelerate the vectorial charge immigration from SnO_2 to CdS. As a result, the effective release of electrons in CB of CdS with a stronger reduction ability will pass through the external circuit to the counter electrode for highly efficient hydrogen evolution, while the accumulated holes in VB of SnO_2 take part in the surface oxidation reaction. It should be mentioned that the promoted consumption of VB holes in the CdS host can also avoid its S^{2-} self-oxidation for better photoanode protection and long-term stability.

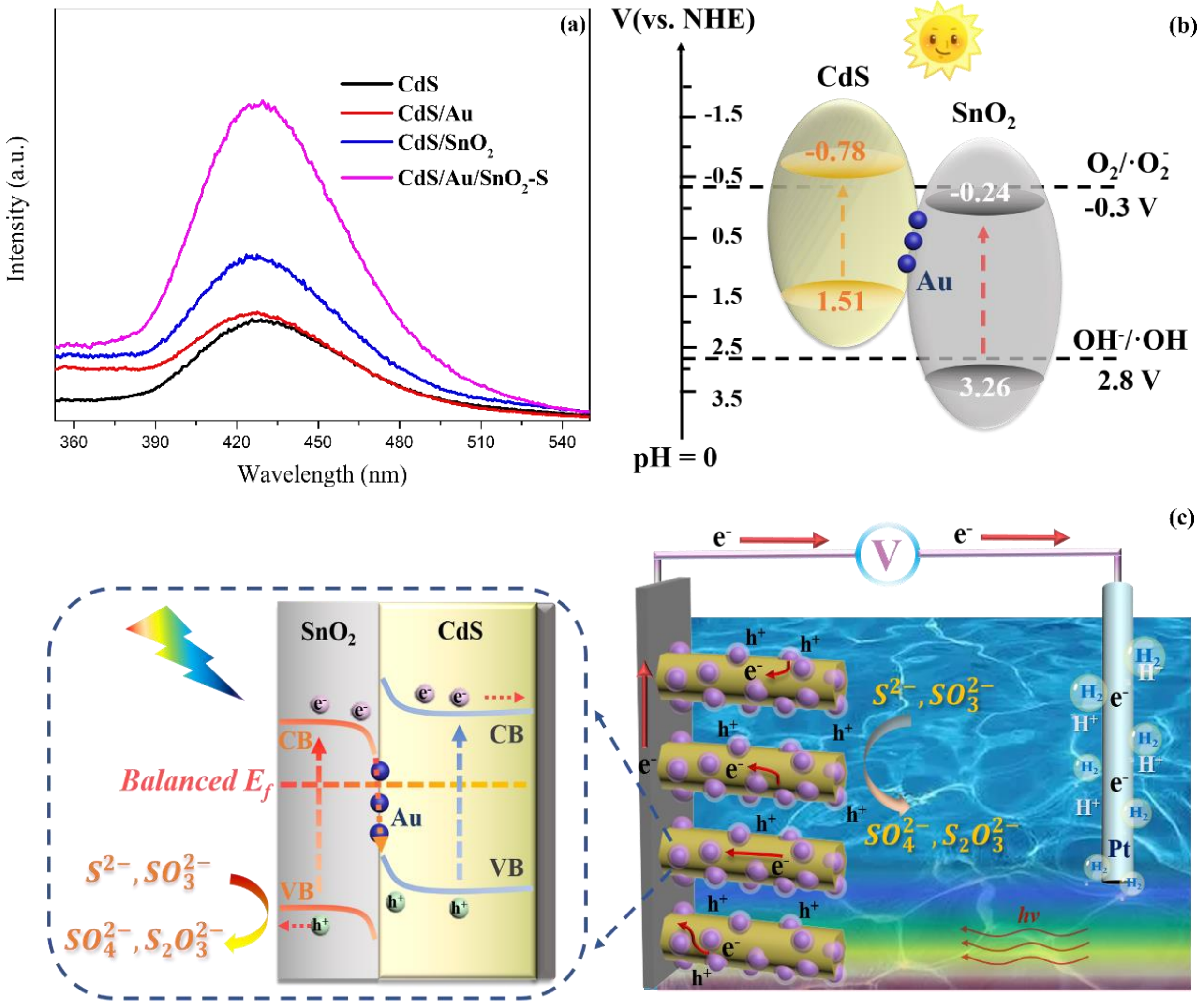

Figure 4.9 (a) Comparative PL spectra for the detection of hydroxyl radicals (·OH) over the CdS, CdS/Au, CdS/SnO_2, and $CdS/Au/SnO_2$-S photocatalysts. (b) Band alignment between CdS and SnO_2, and the relative redox potential of $O_2/\cdot O_2^-$ and $OH^-/\cdot OH$. (c) Schematic diagram of charge transfer mechanism for the overall PEC hydrogen evolution over the $CdS/Au/SnO_2$-S photoanode.

Herein, we would like to emphasize that the configuration variance plays an unignorable role in interfacial charge transport and PEC performance enhancement of the all-solid-state Z-scheme $CdS/Au/SnO_2$ photoanode. To confirm the structural superiority of the hierarchical $CdS/Au/SnO_2$-S photoanode, full-spectrum illumination was used to fabricate the complete SnO_2-wrapped 1D CdS/Au nanorod array ($CdS/Au/SnO_2$-F) for comparison. As displayed in the TEM observations of the $CdS/Au/SnO_2$-F sample (Figure B4.17), the SnO_2 passivated layer is not only photo-deposited on the Au surface but also attached to CdS nanorods, verifying the formation of the complete encapsulation configuration. Meanwhile, the comparative LSV curves and PL detection (Figure B4.18a and b) reveal that the fully encapsulated $CdS/Au/SnO_2$-F photoanode exhibits a relatively lower photocurrent density (3.86 vs.

4.87 mA/cm^2 at 1 V vs. RHE) and less generation of hydroxyl radicals than the hierarchical CdS/Au/SnO$_2$-S heterostructure. Combining the straddle band alignment of SnO$_2$ and CdS, it can be reasonably postulated that their direct contact in the CdS/Au/SnO$_2$-F might give rise to a typical Type-II charge transfer pathway, where a limited portion of photogenerated electrons in CB of CdS can migrate to SnO$_2$ due to the higher CB potential of CdS. Since the deposited SnO$_2$ is spatially separated from the conductive substrate, these disoriented electrons in SnO$_2$ cannot be driven to the counter electrode for hydrogen evolution, thus causing the deteriorated PEC performance. In addition, the partial construction of Type-II heterojunctions is also responsible for the weaker PL signal for the detection of ·OH. Conceivably, the core-shell CdS/SnO$_2$ sample without electron mediators will devote more energy to the higher ratio of straddle charge transport. Such behavior ultimately accounts for its lowest photoresponse compared to that in CdS/Au/SnO$_2$-F and CdS/Au/SnO$_2$-S photoelectrodes. The above analysis also implies the imperfect direct Z-scheme heterojunction built in binary CdS/SnO$_2$ sample and its disordered charge transfer.

4.5 Conclusion

In summary, a novel 1D hierarchical CdS/Au/SnO$_2$-S nanostructure has been successfully fabricated and demonstrated as a pure Z-scheme photoanode for highly efficient PEC hydrogen evolution. Compared to the pristine CdS, plasmonic CdS/Au, and direct Z-scheme CdS/SnO$_2$ heterostructures, the hierarchical CdS/Au/SnO$_2$-S photoanode presents the highest photocurrent density and photo-to-current conversion efficiency. This significantly improved PEC performance mainly depends on the effectiveness of strengthened vectorial Z-scheme charge transfer from the CB of SnO$_2$ to the VB of CdS using Au NPs as charge mediator, which is in favor of the promoted charge separation, increased carrier density, and preserved strong redox capability. More importantly, thanks to the undermined VB holes of CdS and transferred surface oxidation sites, the resulting Z-scheme CdS/Au/SnO$_2$-S photoanode exhibits better corrosion resistance and photostability, illustrating its great potential for future applications. In addition, for comparison, a complete SnO$_2$-encapsulated CdS/Au (CdS/Au/SnO$_2$-F) photoelectrode was also fabricated by full-spectrum irradiation, which exhibits the decreased photo-response and weakened generation of hydroxyl radicals because of the disordered charge transfer. It is thus concluded that the absolute separation of semiconductor components by charge mediators can favor to the construction of pure all-solid-state Z-scheme heterojunctions for better PEC properties. The present work gives a deep insight into the use of the all-solid-state Z-scheme photoanode for PEC hydrogen generation and provides a valuable strategy to design and fabricate other pure Z-scheme photoelectrodes, which is helpful to push forward the advancement of Z-scheme photosystems for their practical applications.

4.6 Supporting information

The supplementary material related to the formulas used in this study and analytic characterizations is available in Annex B and on the website: https://doi.org/10.1016/j.apcatb.2023.122614.

4.7 Contribution of authors to this paper:

Zhiyuan Peng, as the first author of this paper, designed this project, performed most of experiments, analyzed the data, and wrote the full manuscript.

Yilu Su conducted the partial PEC performance measurements, structural characterization, and the corresponding result analysis.

Prof. Mohamed Siaj, as the corresponding author, contributed to the feasible analysis of project, the preparation and correction of manuscripts, and the final submission process.

CHAPTER 5

ONE-DIMENSIONAL CDS/CARBON/AU PLASMONIC NANOARRAY PHOTOANODES VIA IN-SITU REDUCTION-GRAPHITIZATION APPROACH TOWARDS EFFICIENT SOLAR HYDROGEN EVOLUTION

ZhiYuan Peng [a], Jianming Zhang [b], Peipei Liu [c], Jerome.Claverie [c], Mohamed Siaj [a,*]

Published article for this study: One-dimensional CdS/carbon/Au plasmonic nanoarray photoanodes via in situ reduction–graphitization approach toward efficient solar hydrogen evolution, *ACS Appl. Mater. Interfaces* 13 (2021) 34658-34670. https://doi.org/10.1021/acsami.1c04006.

a. Department of Chemistry and Biochemistry, Université du Québec à Montréal, Montréal QC, H3C 3P8, Canada

b. School of Chemistry and Chemical Engineering, Jiangsu University, Zhenjiang, Jiangsu, 212013, China

c. Département de Chimie, Université de Sherbrooke, 2500 Blvd de l’Université, Sherbrooke, J1K2R1 Qc, Canada

*Corresponding author, E-mail: siaj.mohamed@uqam.ca

This Chapter has been shown in the following manuscript: (Zhiyuan Peng et al., 2021).

5.1 Abstract

Photoelectrochemical (PEC) hydrogen evolution has been acknowledged as a promising “green” technique to convert solar energy into clean chemical fuel. Photoanode plays a key role in determining the performance of PEC systems, spurring numerous efforts to develop advanced materials as well as structures to improve photoconversion efficiency. In this work, we report the rational design of a plasmonic hierarchical nanorod array, composed of oriented one-dimensional (1D) CdS nanorods decorated with uniformly wrapped graphite-like carbon (C_{PDA}) layer and Au nanoparticles (Au NPs), as highly efficient photoanode material. An interfacial in-situ reduction–graphitization method has been conducted to prepare the CdS/C_{PDA}/Au nanoarchitecture, where a polydopamine (PDA) coating was used as the C source and reductant. The CdS/C_{PDA}/Au nanoarray photoanode demonstrates superior photoconversion efficiency with a photocurrent density of 8.74 mA/cm^2 and IPCE value (480 nm) of 30.2 % (at 1.23 V *vs.* RHE), under simulated sunlight irradiation, which is 12.7 and 13.5 times higher than pristine CdS. The significant enhancement of PEC performance is mainly benefited from the increase of entire quantum yield and efficiency due to the formation of Schottky rectifier, localized surface plasmon resonance (LSPR)-enhanced light absorption and promoted hot-electron injection from interlayered graphene-like carbon. More importantly, thanks to the inhibited charge carrier recombination process and transferred oxidation reaction sites, the fabricated CdS/C_{PDA}/Au photoelectrode exhibits lengthened electron lifetimes and better photostability, illustrating its wonderful potential for future PEC application.

5.2 Introduction

The excessive consumption of fossil fuels has resulted in the fierce issue of energy crisis and environmental pollution globally. Exploring alternative clean energy sources has thus received extensive research interest.[74, 254] Hydrogen (H_2) with higher energy density, carbon-free, and renewable features is expected to be the promising candidate to replace fossil fuel.[202, 255] Water splitting driven by sunlight using photoelectrochemical cells (PEC) has been deemed as one of the most prospective techniques for hydrogen generation, which could directly convert the interminable solar energy into green chemical energy in an eco-friendly and cost-effective way.[140, 256] Photo-responsive semiconductors have been widely used as key materials to construct photoelectrodes and their properties, such as bandgap width, band edge position, physiochemical stability, charge carrier mobility, and diffusion length, show significant effects on the photoconversion efficiency of PEC cells.[92, 211, 257, 258] Great efforts have thus been devoted to developing advanced PEC photoelectrodes for simultaneously satisfied maximum solar light utilization, superior photoconversion efficiency, and long-term photostability. [259, 260]

As a classic visible-light-response semiconductor, Cadmium sulfide (CdS) has been widely investigated as the photoanode material for PEC hydrogen evolution owning to its narrow bandgap (~2.4 eV) and sufficiently negative conduction-band potential for thermodynamic H_2 production.[158, 226, 227, 261] Nonetheless, there are still many challenges remaining that are yet to be met before the development of their practical application. The main issues include the immoderate surface recombination of photoexcited electron/hole pairs and the fierce photo-corrosion from self-oxidation of S^{2-} induced by accumulated holes, which result in the low photoconversion efficiency as well as the instability of CdS photoelectrode.[232, 233, 262] The most prevalent strategy to address these problems is to conjugate CdS with the secondary photoactive component to form a heterostructure, devoted to higher charge separation efficiency and anode protection. Nevertheless, the actual effectiveness of most heterojunctions is limited by lower oxidation reaction kinetics due to more negative valence band potential and reduced energy from conquering the barrier height.[236] Therefore, it is imperative to explore a strategy to simultaneously achieve more efficient charge separation and faster surface reaction.

Pioneering researches point out that the morphology of CdS, surface hybridization, and the hierarchy configuration of different components all show an important impact on the performance of the CdS photoanode. For example, CdS nanorods or nanowires with highly oriented one-dimensional (1D) structures usually possess better photoelectric response, mainly due to their confined charge transfer path with less carrier loss,[158, 238, 263] compared with the non-oriented counterparts. Hybridization of the CdS with diverse nanomaterials, like carbon materials (e.g. graphene or carbon nanotube) and metallic NPs (e.g. Cu or Au NPs), is developing rapidly owing to its significantly improved photoactivity.[155, 264-266] Since graphene/graphite presents high conductivity, the photoinduced charge carriers of CdS will be separated efficiently and the electrons can be transported rapidly.[267] In addition, different from other hybridizing materials, carbon offers the intrinsic merits of being stable, low-cost, and easily obtained from vast types of raw materials.[268] Thus, endowed with high chemical stability and electrical conductivity, CdS/C hybrids are expected as highly efficient photocatalysts. Moreover, the decoration of metal NPs on the semiconductor surface to form the Schottky barrier has presented astonishing superiorities, mainly including facilitating charge carrier transfer and separation, building new oxidation reaction sites, and improving photostability.[244, 269-271] Compared to other noble metallic NPs, Au NPs show better visible light absorption, photostability, and corrosion resistance. More importantly, if well designed, the unique surface plasmon resonance (SPR) effect of Au NPs can induce strong interfacial near field to boost the generation and transfer of hot-electron, leading to the enhancement of photon harvest as well as photoconversion efficiency, which has urged Au-modified photoactive materials to be excellent electrodes for photovoltaic and PEC application.[236, 272] However, the conventional hybridization/decoration methods all undergo complex synthesis including multistep conjugation with various precursors and linkers, which largely increases the difficulty of obtaining the precise configuration in a controlled fashion. Simultaneously, the high surface energy of unfixed Au NPs brings about its easy agglomeration feature, leading to a shortened lifetime and decayed catalytic activity.[239, 273] Therefore, developing a facile and efficient approach is urgent to implement the stable surface functionalization of CdS materials with C and Au NPs, for improving their quantum efficiency and photostability.

Polydopamine (PDA), originating from dopamine self-polymerizing in an alkaline solution, bears a large number of catechol groups, which renders its wonderful affinity towards semiconductor materials and metal NPs.[274-276] The presence of abundant reductive groups (e.g. phenolic and amine groups) and its internal compact flexible matrix can endow PDA a great potential as the reduction sites for the in-situ formation and immobilization of Au NPs.[239] Simultaneously, the C_{PDA} layer formed by PDA calcination was reported to possess multi-layer graphene-like structure with excellent electroconductivity, which has been applied to accelerate the charge carrier transfer of photoelectrodes (e.g., g-C_3N_4, $BiVO_4$, Si) for better PEC hydrogen generation.[274-276] More importantly, the surface C_{PDA} coating has been proven to be capable of preventing FeP electrodes from oxidation with considerably improved corrosion resistance under electrocatalytic reaction conditions.[277] Accordingly, herein we report a PDA-assisted interfacial in-situ reduction-graphitization approach to prepare CdS/C_{PDA}/Au nanoarray for efficient PEC hydrogen evolution and photoanode protection. Through this strategy, the thickness of uniform carbon layer and the decoration of Au NPs can be precisely controlled by experimental design. Systematic studies indicate that the superior photoconversion efficiency of the CdS/C_{PDA}/Au benefits from the facilitated charge carrier separation, lengthened electron lifetime, and hot-electron injection, upon the introduction of C layer and plasmonic Au NPs. Moreover, because of the wonderful chemical stability of coated shell C_{PDA}, the passivation effects of Au NPs, and the formation of Schottky barrier, the fabricated CdS/C_{PDA}/Au photoanode displays better PEC durability and significantly improved photostability than bare CdS.

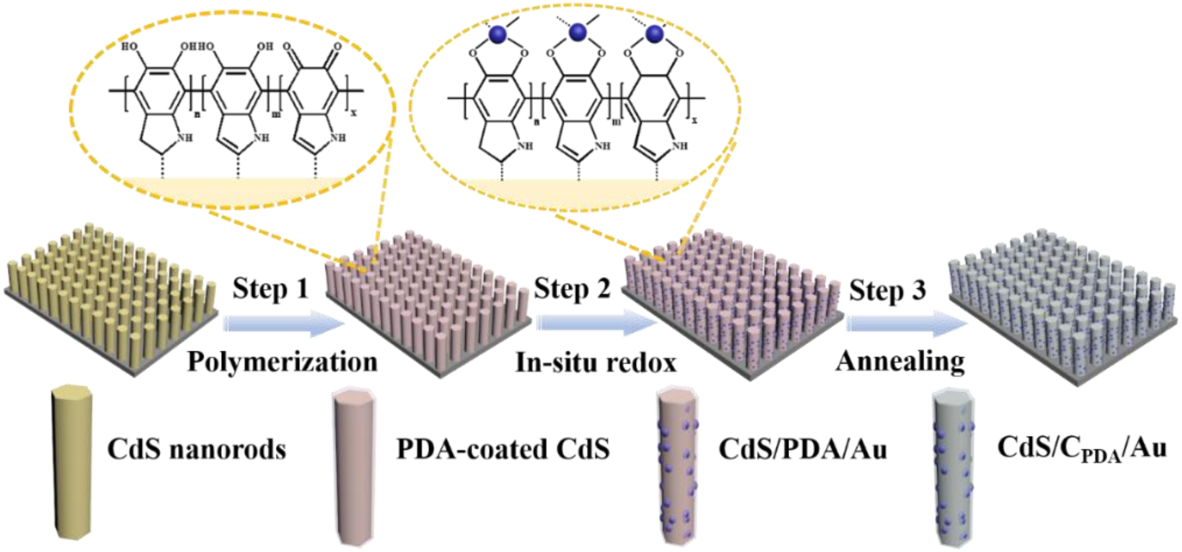

Figure 5.1 The synthetic route and formation process of C$_{PDA}$ and Au NPs decorated CdS nanorod arrays.

5.3 Experimental section

5.3.1 The fabrication of CdS nanorod arrays

The CdS nanorod arrays were in-situ synthesized on the surface of FTO glasses through a hydrothermal process according to the previous report, but with tiny modifications.[150] Firstly, the native FTO-coated substrates were put sequentially into acetone, deionized water, and ethanol for ultrasonic cleaning, and followed with drying in nitrogen flow. Subsequently, the fresh FTO glass was immersed vertically into a 25 mL Teflon-lined stainless steel autoclave containing 20 mL of $Cd(NO_3)_2·4H_2O$ (0.154 g, 25 mM/L), thiourea (0.038 g, 25 mM/L) and glutathione (0.0615 g, 10 mM/L) aqueous solution. Finally, the thus-obtained solution was treated hydrothermally at 200 °C for 4 hours and then annealed at 450 °C for 2 hours under a stream of argon (50 sccm) for standby.

5.3.2 The synthesis of C$_{PDA}$-coated CdS nanorod arrays

The C$_{PDA}$-coated CdS nanorod arrays were fabricated via a simple self-polymerization/graphitization route. In detail, the obtained CdS nanorod arrays were submerged into 40 mL tris-hydrochloric acid buffer solution (pH = 8.5) composed of 0.8 g tris(hydroxymethyl)-aminomethane and 21 mL of 0.1 M dilute HCl solution. Next, 0.2 g dopamine hydrochloride was dispersed evenly into the above mixture with gentle magnetic stirring and the whole in-situ self-polymerization process was maintained for 1, 2, 3, and 4 hours, marked as CdS/PDA-n. After washing and drying, these prepared electrodes were put into the muffle furnace and calcinated at 450 °C for 2 hours under a stream of argon (50 sccm), labeled as CdS/C$_{PDA}$-1, CdS/C$_{PDA}$-2, CdS/C$_{PDA}$-3 and CdS/C$_{PDA}$-4, respectively.

5.3.3 The preparation of Au-deposited CdS/C_{PDA} nanorod arrays

The Au nanoparticles were deposited directly on the surface of CdS/PDA nanorods via the dip/redox method. Typically, the synthesized CdS/C_{PDA} nanorods were dipped vertically into 20 mL $HAuCl_4$ aqueous solution and holden on 2 hours at room temperature. After slightly rinsing with deionized water and blowing with nitrogen flow, the products were transferred into a vacuum drying oven at 60 ℃ for 12 hours. Subsequently, the treated electrodes were calcinated at 450 ℃ for 2 hours in argon flow (50 sccm) to obtain the final CdS/C_{PDA}/Au nanorod arrays. As a result, these CdS/C_{PDA}/Au samples with different amounts of Au nanoparticles were renamed as CdS/C_{PDA}/Au-0.5, CdS/C_{PDA}/Au-1, CdS/C_{PDA}/Au-2 and CdS/C_{PDA}/Au-3, corresponding to the 0.5, 1, 2 and 3 mM $HAuCl_4$ aqueous solution, respectively.

5.3.4 PEC measurements

The electrochemical performance and PEC measurements were operated in a conventionally homemade three-electrode configuration system with as-prepared samples (the coating surface area on FTO substrate ~ 1 cm^2) as working electrodes, a standard Ag/AgCl (3 M KCl) as reference electrode and a Pt wire as counter electrode, respectively. A mixed aqueous solution (0.35 M $NaSO_3$ and 0.25 M Na_2S, pH = 12.5) was utilized as an electrolyte throughout the whole experiment. Partial potentials were converted into reversible hydrogen electrode (RHE) potentials using the Nernst equation for better comparison. A standard sunlight simulator with 100 mW/cm^2 of calibrated irradiation intensity was chosen as the illumination source to simulate the natural continuous spectrum. The linear sweep voltammetry (LSV) curves were recorded from -1.15 V to 0.25 V vs Ag/AgCl with a scan rate of 20 mV/s. The transient photo-response tests were performed under chopped solar light irradiation with several on/off cycles of 20 s. The incident photo-to-current conversion efficiency (IPCE) of as-prepared samples was obtained via the photoelectric response measurements at a bias of 1.23 V vs RHE under monochromatic light illumination with different wavelengths, ranging from 360 nm to 700 nm at a fixed interval of 20 nm. The electrochemical impendence spectra (PEIS) were tested under darkness and solar light irradiation at the open circuit potential and the frequency range was 1 Hz-10^5 Hz. Mott-Schottky plots were collected at the frequency of 1 kHz, 2 kHz, and 3kHz in darkness within the potential of -1-0 V vs Ag/AgCl. Afterward, the photostability of as-fabricated electrodes was tested at an applied bias of 0 V vs Ag/AgCl under one sun illumination.

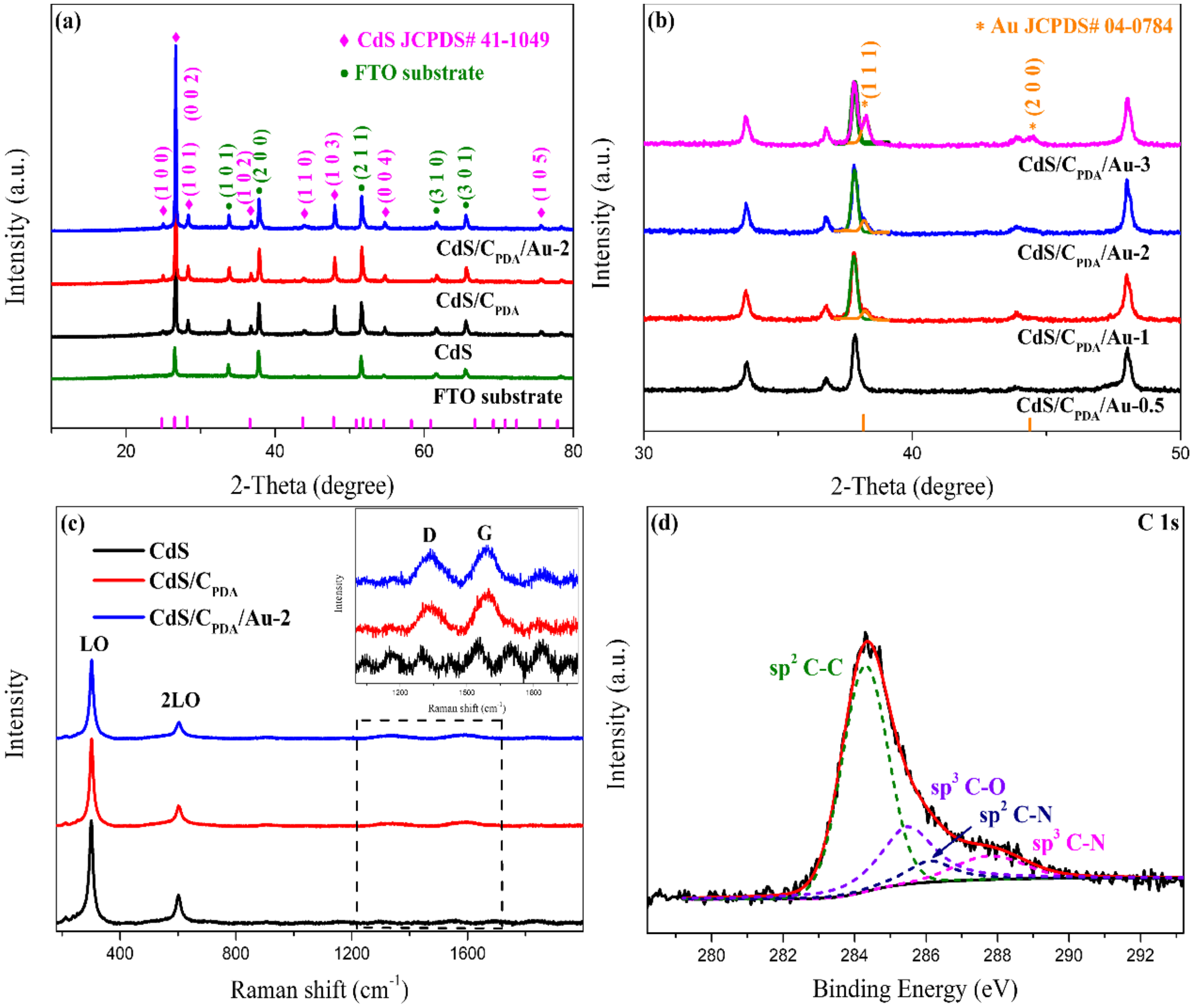

Figure 5.2 The XRD patterns of (a) bare CdS, CdS/C$_{PDA}$ and CdS/C$_{PDA}$/Au-2; (b) CdS/C$_{PDA}$/Au-n (c) Raman spectra; (d) High-resolution XPS spectrum of C 1s over obtained CdS/C$_{PDA}$/Au-2 photoelectrode.

5.4 Result and discussion

5.4.1 structural characterization

The interfacial in-situ reduction-graphitization fabrication of the plasmonic nanoarray photoanode is illustrated in Figure 5.1. First, a simple encapsulation/self-polymerization process is implemented to the 1D CdS nanorod arrays grown on FTO substrates (see Figure C5.3 for SEM images of nanorod array). An adsorption of dopamine hydrochloride molecules on the CdS surface has taken place, due to the existence of catechol groups; meanwhile, a self-polymerization process is triggered upon the adsorption to form a layer of PDA around the CdS surface, leading to the acquisition of CdS/PDA. In the second step, an interfacial in-situ reduction process is conducted to form Au NPs on the nanorod surface, enabled by the dual function of PDA as a linker and reductant. Once the CdS/PDA nanorods are immersed in HAuCl$_4$

solution, Au^{3+} ions can be captured by the phenolic and amine groups on PDA coating and reduced into metallic Au. The internal porous cross-linked PDA structure could also confine the Au growth to distribute Au NPs uniformly on its surface, eventually resulting in the formation of CdS/PDA/Au.[270] Following the encapsulation-reduction, a calcination step is then performed to convert PDA into a uniform C layer on the CdS surface under an inert atmosphere and preserves the original Au attachment to yield CdS/C_{PDA}/Au structures. Also, this ultimate annealing process could further improve the crystallinity of Au NPs and promote the phase transition of crystal CdS from cubic to wurtzite structure.

The X-ray diffraction was applied to characterize the crystallographic structure and purity of as-obtained CdS, CdS/C_{PDA}, and CdS/C_{PDA}/Au-n photoanodes (n varies from 0.5 to 3, indicating the content of Au). As shown in Figure 5.2a, except for the characteristic peaks arising from the FTO substrates, all the other diffraction peaks (noted as♦) can be accurately indexed to the crystallites of CdS (JCPDS# 41-1049), demonstrating the successful synthesis of CdS nanomaterials on FTO glasses.[229, 238] One strongest diffraction peak around 26.6° is mainly assigned to the (002) lattice phase of hexagonal CdS, suggesting the preferential perpendicular growth to the substrates.[195] The diffraction features of the CdS are nicely preserved after further surface modification to form either CdS/C_{PDA} or CdS/C_{PDA}/Au upon the in-situ reduction-graphitization. Figure 5.2b exhibits the XRD patterns of CdS/C_{PDA}/Au-n photoanodes with different Au contents. Two obvious characteristic peaks at 38.3 ° and 44.5 ° are assigned to (111) and (200) Bragg diffractions of cubic Au (JCPDS# 04-0784).[239] Simultaneously, the diffraction intensity enhances gradually with the concentration increase of $HAuCl_4$ solution due to the formation of more metallic Au. Additionally, the absence of C_{PDA} diffraction signals may be owing to its low coating contents and weak crystallinity.[270]

Raman and XPS characterization were conducted to identify the presence of the carbon component and analyze its surface chemical state. As displayed in Figure 5.2c, two typical vibration modes centered at 300 cm^{-1} and 600 cm^{-1} are related to the CdS longitudinal optical (LO) phonon and its overtone.[150, 278] Meanwhile, two additional characteristic peaks (insert from Figure 5.2c) for D band at 1332 cm^{-1} and G band at 1597 cm^{-1} could be detected after the graphitization of PDA, which are derived from the disordered structure and stretching of C-C bonds, respectively.[103, 276, 279] For the high-resolution XPS spectrum of C 1s region (Figure 5.2d), two constituent peaks located at 284.3 eV and 285.5 eV are attributed to sp^2 C-C and sp^3 C-O structure. The other two signals with higher bands of 286.1 eV and 287.8 eV originate possibly from the sp^2 C-N and sp^3 C-N structure, respectively.[280] Correspondingly, the N 1s characteristic peaks (Figure C5.1) at 399.7 eV and 400.8 eV may arise from pyrrolic and pyridinic nitrogen, suggesting the existence of N-doping carbon components in the C_{PDA} layer.[281, 282] The above Raman and XPS analysis provide convincible evidence for the formation of C_{PDA}-coating on CdS and its N-doped graphite-like structure. Furthermore, the survey XPS spectrum (Figure C5.2a) indicates the CdS/C_{PDA}/Au-2 sample is composed of Cd, S, C, and Au elements. In the high-resolution spectrum of the Cd region (Figure C5.2b), two typical characteristic peaks appearing at binding energies of 405.6 eV and 412.3 eV are related to the Cd $3d_{5/2}$ and Cd $3d_{3/2}$ spin-orbits, assigned to the oxidation state of cadmium (Cd^{2+}). The decomposed S 2p spectrum (Figure C5.2c) shows two substantial peaks at 161.2 eV and 162.4 eV, which can be attributed to the orbits of S $2p_{3/2}$ and S $2p_{1/2}$ in metal-sulfur bonds of CdS. The two bands (Figure C5.2d) at 83.9 eV and 87.6 eV in the Au 4f region can be ascribed to Au $4f_{7/2}$ and Au $4f_{5/2}$, directly verifying the in-situ growth of Au NPs. As a result, it can be reasonably concluded that through the in-situ reduction-graphitization approach, the CdS/C_{PDA}/Au photoanode has been prepared successfully.

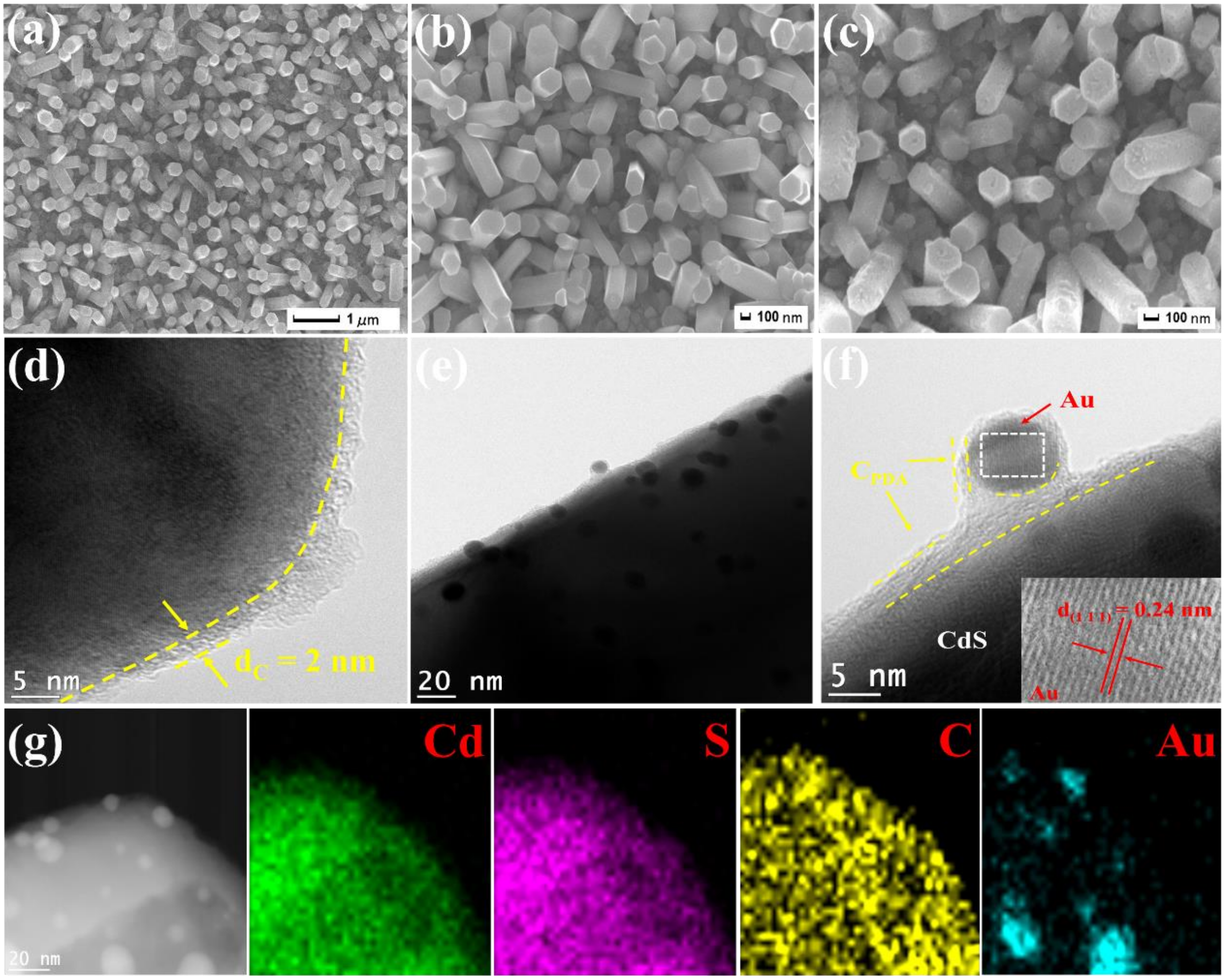

Figure 5.3 Field-emission SEM images of (a) bare CdS, (b) CdS/C_{PDA}, and (c) CdS/C_{PDA}/Au-2. TEM and HRTEM images of (d) CdS/C_{PDA}, (e) CdS/C_{PDA}/Au samples and (f) CdS/C_{PDA}/Au photoelectrodes. The insert taken from the white square displays the magnified lattice fringe image of Au NPs. (g) HAADF STEM image of Au-loaded CdS/C_{PDA} photoanode and the corresponded elemental mappings.

SEM observations were used to examine the morphology of the modified CdS electrodes. The top-view (Figure 5.3a and S5.3a) and cross-section (Figure C5.3b) SEM images demonstrate the typical 1D rod-like structure of pristine CdS array with hexagonal cross-section nearly aligned vertically over the whole FTO substrates. The diameters of as-fabricated nanorods range from 100 to 300 nm and the average length is about 760 nm. After self-polymerization/graphitization procedures, sample CdS/C_{PDA} (Figure 5.3b) shows an extremely smooth surface due to the uniform wrapping of the external carbonaceous layer. The SEM image (Figure 5.3c) of the obtained CdS/C_{PDA}/Au displays a similar feature as that of the bare CdS array, but with plenty of nanoparticles attached on the CdS surface, indicating the whole structure is not damaged over the in-situ reduction-graphitization process. All corresponding characteristic peaks (Cd, S, C, and Au elements) were also detected over the selective region from EDS analysis (Figure C5.4) of the CdS/C_{PDA}/Au-2 sample, demonstrating the successful encapsulation of C_{PDA} and Au NPs. TEM and HRTEM were used to further investigate the microstructure and crystallization of single nanorods. As displayed in Figure C5.5a, CdS nanorods with well-defined grain boundaries have been synthesized via the hydrothermal method. Figure 5.3d shows the TEM images of the CdS/C_{PDA} nanorod. A continuous and ultrathin carbon layer with a thickness of 2 nm (marked with a yellow line) coated with the CdS nanorod is easily observable. The TEM image of CdS/C_{PDA}/Au-2 (Figure 5.3e and C5.5c) illustrates the evenly deposited Au NPs on the photoanode surface with the average diameter of 10 nm, and its well-proportioned size and consecutive distribution may derive from the constraint effect of PDA matrix. The intimate interface contact was further confirmed through the HRTEM observation of CdS/C_{PDA}/Au-2 (Figure 5.3f). It is obvious that the interlayered C_{PDA} avoids the direct contact of Au NPs and CdS nanorod with a separation of 2 nm, which would lead to a different interaction between Au NPs and CdS from the direct contact and be discussed later. Simultaneously, due to the diffusion of soft PDA along with solid surface during the reduction of Au ion and subsequent graphitization process, the attached Au NPs are fully covered with 1 nm of C_{PDA} film, favoring the fixation and protection of Au. The distinct lattice spacing of 0.24 nm was well related to the (111) plane of marginal Au, which is matched well with XRD analysis.[236, 244] Besides, the HADDF-STEM image (Figure 5.3g) provides a clearer contrast for distinguishing the geometrical distribution of Au nanoparticles over single CdS/C_{PDA}/Au-2 nanorod. The correlative EDX elemental mapping (Cd, S, C, and Au elements) is recorded and displays the corresponding elemental distribution. On the basis of the above SEM, TEM, and HRTEM results, it has been proven that the PDA-assisted in-situ reducing/graphitization strategy could effectively decorate well-defined Au nanoparticles on 1D CdS nanostructure.

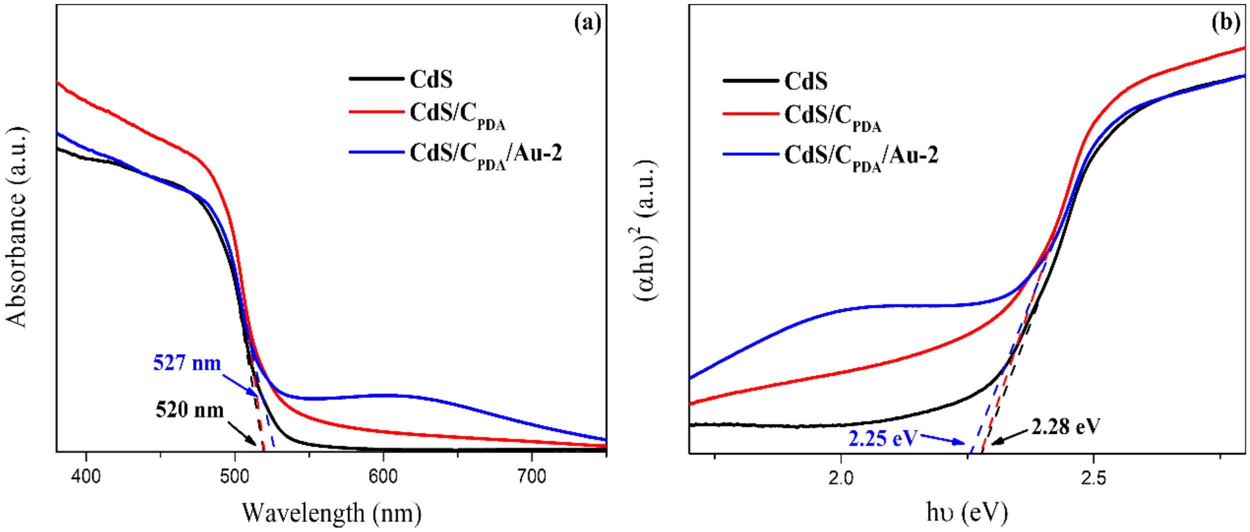

Figure 5.4 (a) UV-vis absorption spectra and (b) Tauc plots of bare CdS, CdS/C_{PDA} and CdS/C_{PDA}/Au-2 photoelectrodes.

5.4.2 Optical properties

The UV-vis absorption spectroscopy was applied to explore the optical properties of as-fabricated CdS, CdS/C_{PDA}, and CdS/C_{PDA}/Au photoelectrodes. As depicted in Figure 5.4a, bare CdS nanorod arrays present a wonderful visible-light absorption capacity with a spectral limitation of up to 520 nm, which matches well with its intrinsically narrow bandgap.[135, 245] After the coating of carbonized PDA film, CdS/C_{PDA} photoanode presents a similar absorption edge but with a higher visible light sensitization as compared to bare CdS, which is mainly due to the assisted extra light absorption from the surface N-doped carbon layer.[283, 284] Upon the attachment of Au NPs, the absorption spectrum of CdS/C_{PDA}/Au exhibits a slight redshift with a broad absorption band around 610 nm due to the surface plasmonic interaction between CdS and deposited Au. Here, a weakened absorbance appearing at 380-540 nm may result from the reflection effect of Au NPs. Moreover, the bandgap energies of these electrodes were estimated using the Kubelka-Munk equation, assuming a direct bandgap of CdS. As shown in Figure 5.4b, the measured bandgap values for pure CdS, CdS/C_{PDA}, and CdS/C_{PDA}/Au photoelectrodes are approximately 2.28, 2.28, and 2.25 eV, respectively. Based on the above results, it is believed that PDA-assisted decoration of Au NPs can effectively improve the overall light harvesting ability and induce a better visible-light sensitivity, then leading to a higher quantum yield for photoelectrochemical hydrogen production.

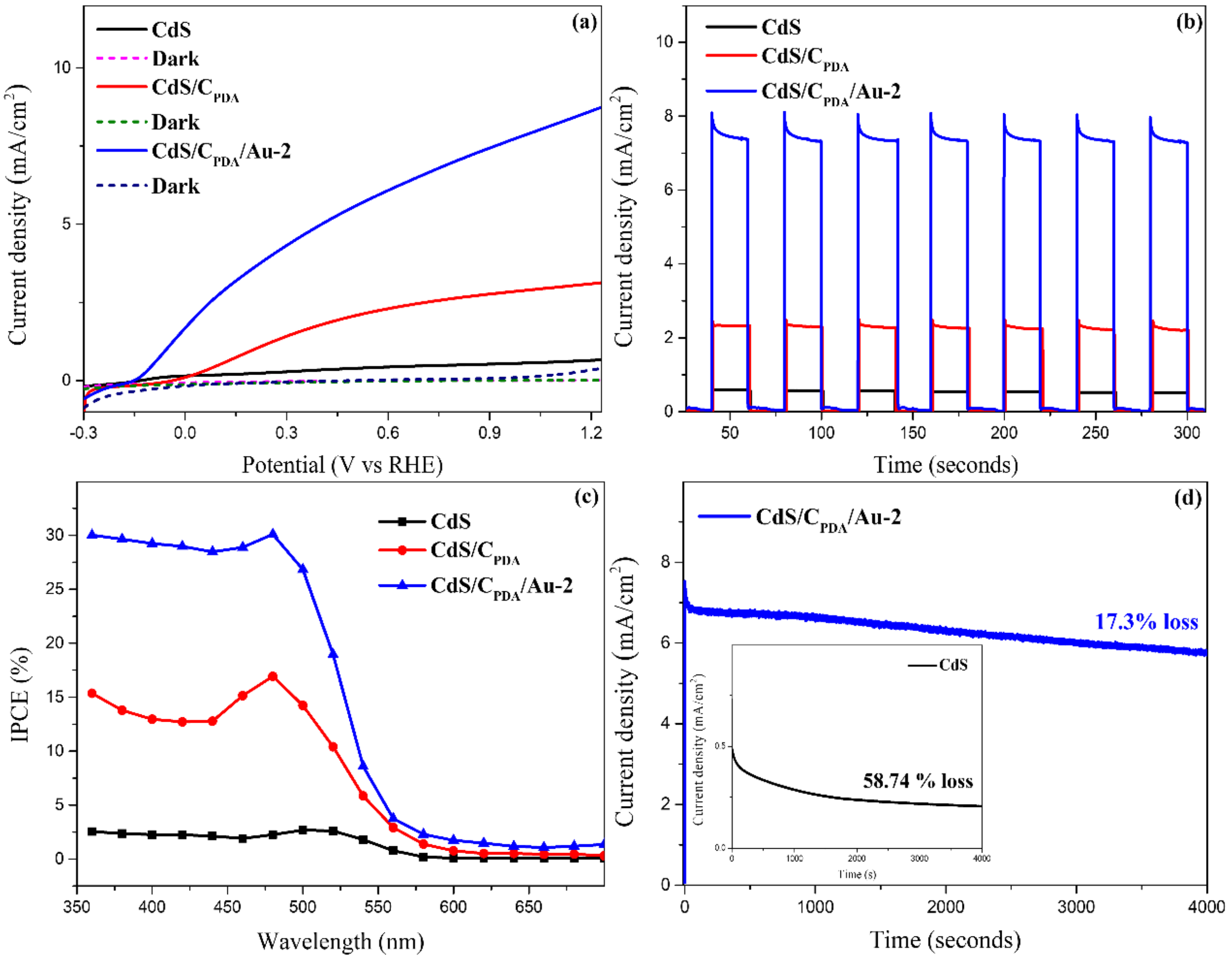

Figure 5.5 (a) LSV curves of bare CdS, CdS/C$_{PDA}$ and CdS/C$_{PDA}$/Au-2 photoelectrodes under darkness and one sun irradiation (100 mW/cm^2); (b) Transient photocurrent response; (c) IPCE spectra under monochromatic light illumination; (d) Photostability and durability measurements.

5.4.3 PEC performance tests

The linear-sweep-voltammetry (LSV) measurements (scan rate: 20 mV/s) were performed under one sun irradiation (100 mW/cm^2) to evaluate the PEC HER activities of as-obtained electrodes. Initially, the effect of C$_{PDA}$ thickness over the PEC performance of CdS nanorod arrays was studied by controlling the DA-polymerization times (1, 2, 3, and 4 hours) and the corresponding LSV curves were shown in Figure C5.6. The CdS/C$_{PDA}$-2 possesses the highest photocurrent density when the polymerization time is optimized to 2 hours. Further extended DA encapsulation times to 3 or 4 hours leads to a sharp decrease in photocurrent density because the excessive carbon layer may suppress the light absorption of CdS, lengthen the hole migration distance, and transform into carrier recombination centers.[275] Figure 5.5a and S5.7 displays the comparison of LSV curves for bare CdS, CdS/C$_{PDA}$, and CdS/C$_{PDA}$/Au-2 photoelectrodes under darkness, continuous, and chopped solar light illumination. The corresponding overpotential and the photocurrent density at the applied bias of 1.23 V vs. RHE were listed in Table C5.1. Obviously, all these electrodes show negligible photo-response in darkness. Under the front-side irradiation, bare CdS photoanode presents only a small photoresponse with an unsatisfied photocurrent density of 0.69 mA/cm^2 due to the fast recombination of photoinduced electron/hole pairs and low carrier migration. By contrast, the introduction of the carbon layer shows a significant increase in its PEC performance and the photocurrent density of CdS/C$_{PDA}$ reaches around 3.12 mA/cm^2, which may result from the promoted interfacial charge transfer due to its wonderful electric conductivity. More importantly, the CdS/C$_{PDA}$/Au electrode fabricated by the incorporation of Au NPs on CdS/C$_{PDA}$ nanorod arrays demonstrates the highest photo-response of 8.74 mA/cm^2 at 1.23 V vs RHE, which is 12.7 and 2.8 folds of bare CdS and CdS/C$_{PDA}$ electrodes. The remarkable enlargement in PEC performance may be mainly attributed to the further improved quantum yield and photoinduced charge carrier separation efficiency. Interestingly, an apparent anodic shift of overpotential (about 100 mV) over bare CdS can be checked after the encapsulation of graphitized PDA film. This phenomenon demonstrates that the wrapped C$_{PDA}$ mainly acts as the conducting layer for charge transport rather than oxidation co-catalysts, signifying that the C$_{PDA}$ layer could effectively transport the photo-generated holes only with the higher driven force from the applied potential. Fortunately, the decoration of Au nanoparticles makes up for this negligible defect through its passivation effect and the formed electrical field, which could effectively accelerate hole transporting and improve surface reaction kinetics of photoanode. As a result, the as-fabricated CdS/C$_{PDA}$/Au PEC system obtains a higher photo-response under relatively lower applied potentials and exhibits a wonderful competitiveness compared to the previously reported CdS-based PEC systems, as listed in Table C5.2. Additionally, the LSV curves for CdS/C$_{PDA}$/Au-n photoanodes with different loading amounts of Au NPs are shown in Figure C5.8. It is believed that the suitable Au deposition can contribute to the reinforcement of the entire PEC system. What's more, the transient photo-response measurements were performed at the applied bias of 0 V vs Ag/AgCl under the hand-chopped solar irradiation (100 mW/cm^2). The photocurrent density with respect to time were shown in Figure 5.5b. All these fabricated electrodes demonstrate superior photo-switching properties and wonderful stability within 7 on-off cycles. As expected, the CdS/C$_{PDA}$/Au photoanode possesses the maximum photocurrent density (7.4 mA/cm^2 at 0 V vs Ag/AgCl) than those of bare CdS and CdS/C$_{PDA}$ nanorod arrays, which matched well with the LSV results.

The wavelength-dependent photoelectrical activities were investigated via IPCE measurements under monochromatic light irradiation at the applied potential of 1.23 V vs. RHE. As shown in Figure 5.5c, the IPCE plots of the three electrodes follow their absorption spectra perfectly. Compared to bare CdS and CdS/C$_{PDA}$ nanorod arrays, the CdS/C$_{PDA}$/Au-2 photoanode presents the highest conversion efficiency throughout the UV-to-visible spectral region ($360 < \lambda < 680$ nm). The maximum IPCE value reaches up to

30.2% upon the incident-light wavelength of 480 nm, showing 13.5 times higher than that of the CdS photoanode. Meanwhile, the IPCE difference before and after the decoration of Au nanoparticles was calculated and depicted as a function with λ. Figure C5.9 and the insert show a slight IPCE increasement (about 1%) at the range of 560 nm to 640 nm with a peak around 610 nm, corresponding to the SPR band observed in the UV-visible spectra (from Figure 5.4a). This truth reveals evidently that the plasmonic effect between Au and CdS can definitely advance the improvement of photoconversion efficiency. Simultaneously, the huge enhancement over 12% below 500 nm may be due to localized electric-field amplification effect and effective surface passivation of Au NPs,[244] which will be analyzed later.

To further explore the photostability and durability of the obtained photoelectrodes, chronoamperometric photoelectrolysis measurements were carried out at the applied bias of 0 V vs Ag/AgCl under AM 1.5G solar illumination (100 mW/cm^2). As shown in Figure 5.5d, the bare CdS photoanode exhibits a fast attenuation in photocurrent density (58.74 %) at the given irradiation time (4000 seconds) because of its high surface carrier recombination and photocorrosion during the oxidation reaction. By sharp contrast, only 17.3 % loss over the CdS/C$_{PDA}$/Au sample is checked and the whole photocurrent density still maintains at a relatively high level (5.8 mA/cm^2) after illumination, which may be assigned to the superior chemical stability of coated C$_{PDA}$ layer and Au, the increased carrier separation efficiency and transferred oxidation reaction sites from CdS surface to Au. To deeply confirm the structure stability of CdS/C$_{PDA}$/Au photoelectrode, the SEM and XRD comparisons were performed after the long-term photoreaction, and the results were depicted in Figure C5.10a and b. Evidently, the micromorphology of CdS/C$_{PDA}$/Au is well retained as uniform nanorod arrays and its crystal structure shows negligible variation after the PEC HER process, further verifying its wonderful photochemical stability. The above analysis illustrates that the deposition of graphitized PDA film and Au can not only improve the overall quantum efficiency but also protect the semiconductor from photocorrosion. Moreover, the generated H_2 was analyzed quantitatively by gas chromatograph, and its content was detected every 3 min during the above chronoamperometric measurements for the CdS/C$_{PDA}$/Au-2 sample (geometric working area ~ 1 cm^2). The fifth sampling (817th s of solar irradiation) was set as the starting point to calculate the theoretical H_2 evolution and the corresponding H_2 moles detected before were calibrated to zero for more accurate Faradaic efficiency. Figure C5.11 displays the comparison between calculated theoretical and measured H_2 evolution. Obviously, the H_2 productivity shows a nearly linear increase with a production rate of 1.84 μmol min^{-1} cm^{-2} in the entire 3600 s of continuous operation. The associated Faradaic efficiency was calculated to be 96.3 %, indicating that the generated photocurrent is mainly devoted to the H_2 evolution reaction with relatively high stability.

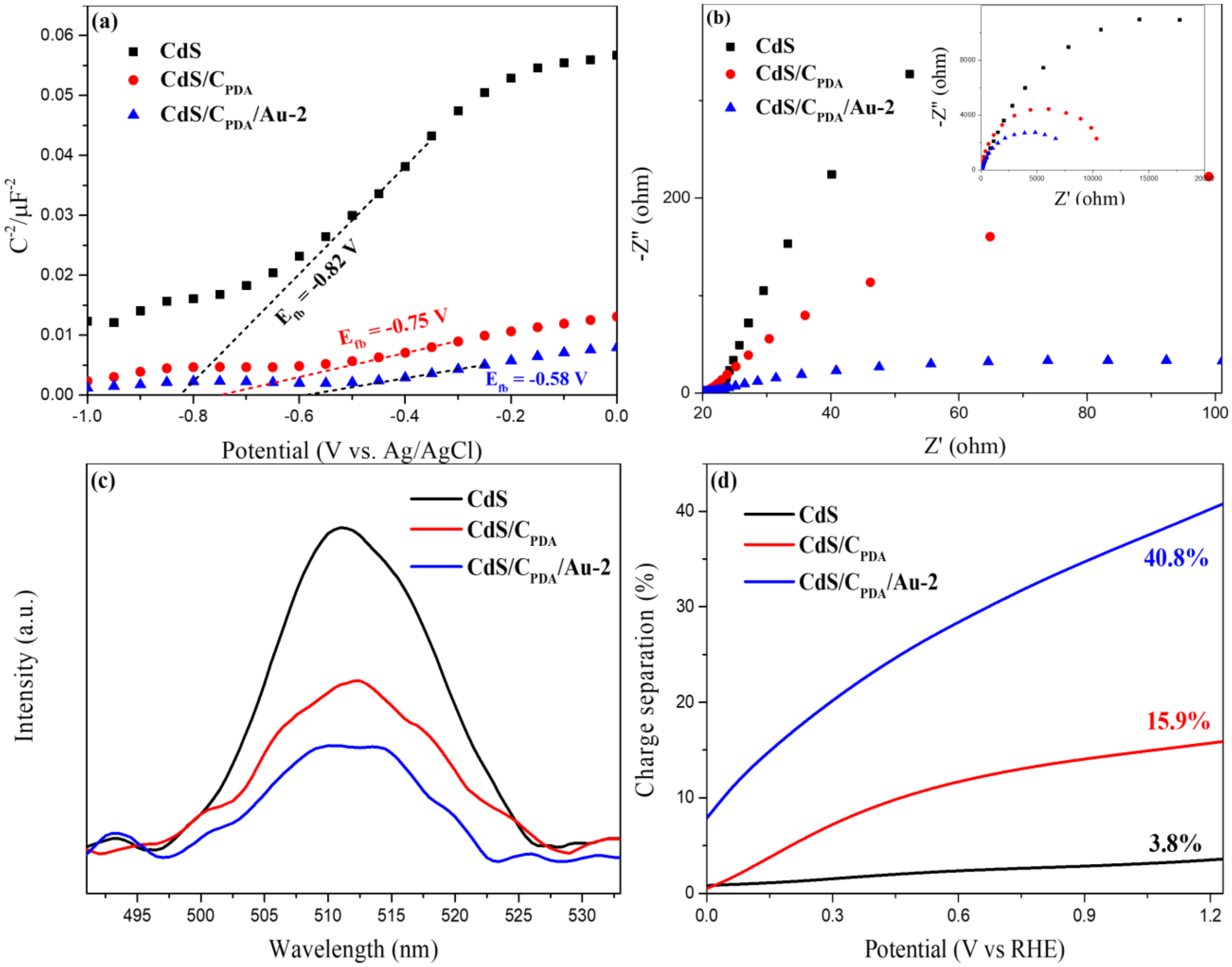

Figure 5.6 (a) Mott-Schottky plots, (b) EIS spectra under darkness (insert) and AM 1.5G solar irradiation (100 mW/cm^2), (c) PL spectra and (d) charge separation efficiency of bare CdS, CdS/C$_{PDA}$ and CdS/C$_{PDA}$/Au-2 photoelectrodes.

5.4.4 PEC enhancement analysis and result comparison

Interfacial charge recombination behavior of as-fabricated photoanodes displays a direct influence on their PEC performance, which could be evaluated by transient photocurrent decay at the beginning of each interval (shown in Figure 5.5b). Generally, the photocurrent decay with time and subsequently formed transient spikes mainly stem from charge loss and could be described in the following two possible ways: The photoinduced holes accumulate on the surface of electrode and recombine with the charge on the conduction band of semiconductor prior to the capture by a scavenger. The other possibility is that the photogenerated electrons may be caught by the electron acceptors in electrolytes such as S_2^{2-}, rather than transported to the counter electrode for HER.[94, 285] Here, the normalized plots and kinetic process were calculated and shown in Figure C5.12. The plots of ln D versus time exhibit approximately the first-order linearity, signifying the decay process mainly originating from the surface recombination of photogenerated charge carriers.[89, 286] For better comparison, the transient decay times of as-fabricated photoelectrodes were taken where ln D = -1. The results reveal that the recorded decay times are about 0.19 s, 0.24 s, and 0.7 s for the pristine CdS, CdS/C_{PDA}, and CdS/C_{PDA}/Au photoelectrode. Obviously, the CdS/C_{PDA}/Au array possesses the longest decay time and slowest carrier recombination rate, finally achieving the significantly enhanced PEC performance. Furthermore, this comparison over different decay times also elucidates that the incorporation of Au plays a leading role in weakening the surface recombination process compared to the coating of C_{PDA} layer, which could be explained by the transfer rectification of charge carriers.

To acquire a deep understanding on PEC enhancement of the as-prepared CdS/C_{PDA}/Au-2 system, varied electrochemical measurements were performed. Mott-Schottky plots were first applied to examine their flat-band potentials (E_{fb}) and carrier density (N_D). As shown in Figure 5.6a and S5.13, all these CdS-based photoanodes present positive slopes, confirming their n-type semiconductor features. Their E_{fb} is obtained through extrapolating the linear part to the transverse axis and the specific values are listed in Table C5.3. The E_{fb} of bare CdS nanorod arrays displays a slight positive shift after the introduction of C_{PDA} and Au nanoparticles, implying an increased band bending. Correspondingly, N_D values for CdS, CdS/C_{PDA}, and CdS/C_{PDA}/Au-2 photoelectrodes are calculated to be 1.4×10^{18} cm^{-3}, 7.9×10^{18} cm^{-3} and 1.2×10^{19} cm^{-3}, respectively. Noticeably, the deposition of C_{PDA} and Au can significantly enhance the overall carrier density, leading to higher electrical conductance and quantum efficiency.

The electrochemical impendence spectroscopy (EIS) was carried out to further study the charge transfer process and resistance of as-prepared photoelectrodes. Figure 5.6b and its insert show the measured Nyquist plots with or without 1 sun irradiation (100 mW/cm^2) and the relevant equivalent circuit is presented in Figure C5.14, where three parameters (R_s, R_{Bulk}, and CPE) represent series resistance between semiconductor and charge collector (FTO), electron transfer resistance within the bulk component and constant phase element, respectively. As displayed in Figure 5.6b, the semicircles in the high-frequency region correspond to R_{Bulk} and their radius decreases with the following sequence: CdS > CdS/C_{PDA} > CdS/C_{PDA}/Au-2, indicating that CdS/C_{PDA}/Au with the smallest semicircle possesses the lowest charge transfer resistance and highest HER reaction kinetic, which is coincided well with the analyzed carrier density above. The insert shows the compared impendence spectra in darkness, illustrating that solar energy has a vital influence on the PEC cell. The dramatic charge-transfer resistance is related to their ignorable dark-currents.

PL signals depend on the recombination of photogenerated charge carriers and are applied to evaluate the overall quantum efficiency. Figure 5.6c presents the PL spectra comparison with the exciting wavelength of 375 nm. Bare CdS nanorod arrays show a strong and broad emission peak around 512 nm on account of surface-defect-related recombination for trapped electron-hole pairs. Compared to pure CdS, the CdS/C_{PDA}/Au-2 photoelectrode with the decoration of C layer and Au displays a sharply diminished PL intensity, further confirming the promoted carrier transfer and separation.[287, 288] Ultimately, in order to quantitatively analyze carrier migration behavior, charge separation efficiency (η_{Bulk}) was calculated based on the formula: $\eta_{Bulk} = J_{Ph}/J_{Max}$, in which J_{Ph} indicates the photocurrent density obtained from the above LSV results and J_{Max} indicates the theoretical maximum photocurrent (shown in Figure C5.15). Figure 5.6d reveals the highest separation efficiency of as-fabricated CdS/C_{PDA}/Au-2 photoanode around 40.8% at 1.23 V vs RHE, nearly 11 times as that of bare CdS. Through the above discussion, it is evidently determined that the introduction of C_{PDA} layer and Au could indeed favor the charge separation and subsequent quantum efficiency, as the C_{PDA} coating promotes the charge transfer due to its good conductivity and Au nanoparticles further improve the separation of photoinduced holes and suppresses the carrier recombination.

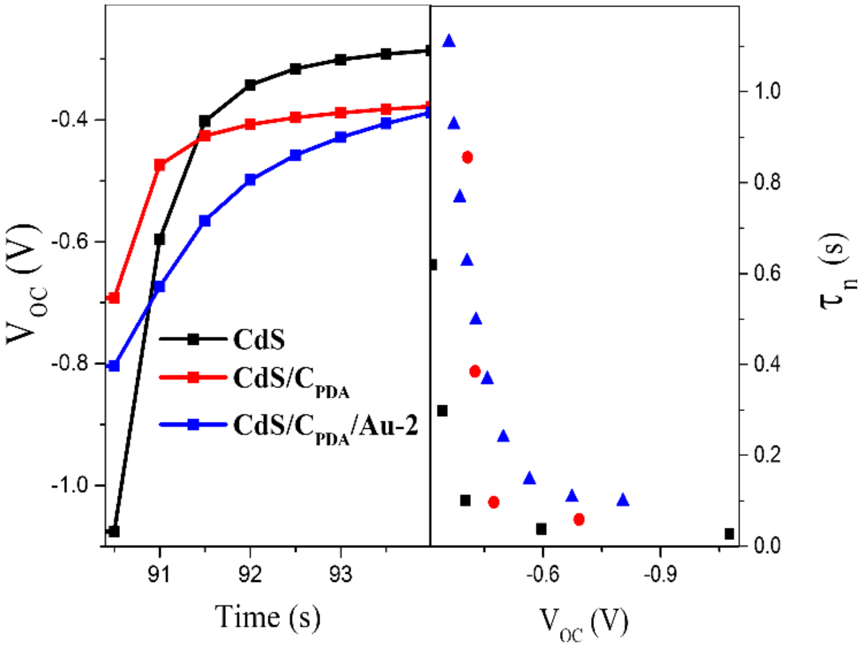

Figure 5.7 The transient OCVD measurements (left) and the corresponding average electron lifetimes (right) for bare CdS, CdS/C_{PDA} and CdS/C_{PDA}/Au-2 photoelectrodes.

The electron lifetime acts as a crucial parameter determining the entire PEC behavior of photoelectrodes. Based on the above PL, normalized I-t decay pattern, and EIS analysis, it has been revealed that the coating of C_{PDA} and Au decoration can effectively promote charge transport, enhance carrier separation efficiency, and prolong the electron lifetimes. Here, this conjecture is further demonstrated quantitatively via the open-circuit voltage decay (OCVD) tests. The as-prepared samples were treated with 1 sun illumination (100 mW/cm^2) for 60 s to obtain a stable open-circuit voltage (V_{OC}) and then, the decay curves were measured without irradiation. The left figure in Figure 5.7 shows the function between the V_{OC} and time. The pure CdS displays the fastest V_{OC} decay rate because of the surface accumulated holes strongly recombining with photoinduced electrons. Comparatively, the V_{OC} decay is greatly alleviated with the coating of C_{PDA}, indicating the wonderful conductivity of coated carbon can effectively drive charge to the counter electrode. The further inhibited decay degree is observed after the Au decoration, which is attributed to its better conductivity and the formation of a localized electrical field resulting in the rapid transport of holes. Additionally, the average charge lifetimes (τ_n) are calculated and listed as a function of V_{OC} decay in the right figure of Figure 5.7. It is determinable that the CdS/C_{PDA}/Au exhibits the longest lifetime compared with those of bare CdS and CdS/C_{PDA} photoanodes, well accordance with the previous analysis. Therefore, it is reasonably concluded that the modification of C_{PDA} and Au can indeed prolong the charge carrier lifetime and favor better PEC performance and photostability.

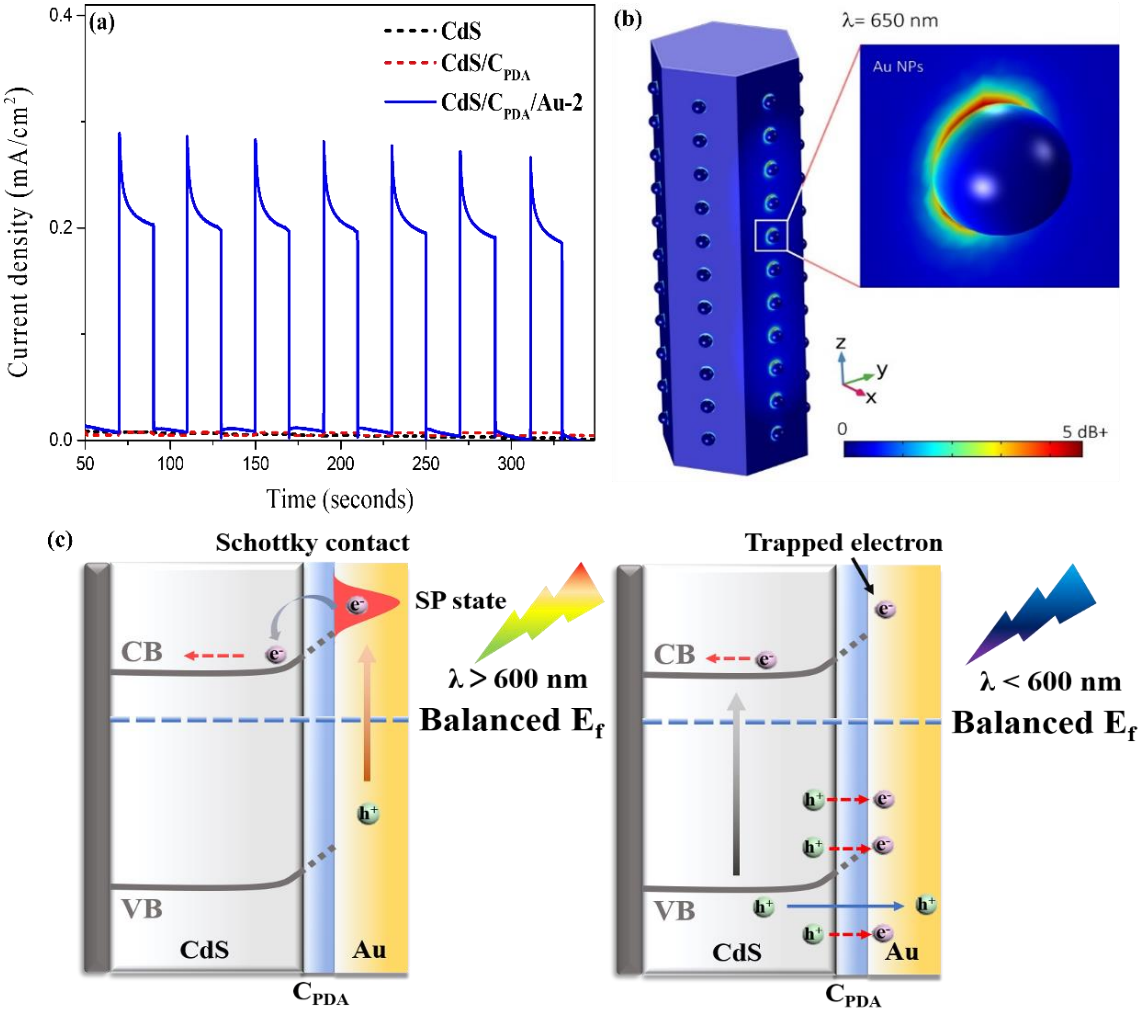

Figure 5.8 (a) Chronoamperometric I-t measurements at 0 V vs Ag/AgCl under one sun irradiation (100 mW/cm^2) equipped with a 600 nm long-wave-pass filter. (b) The near-field distribution of CdS/C_{PDA}/Au-2 with an incident light wavelength of 650 nm. (c) The schematic diagram of interface contact in CdS/C_{PDA}/Au PEC system with the incident light wavelength beyond or below 600 nm.

Additionally, to evaluate the possible photoelectric response induced by SPR effects and analyze the role of Au decoration, the chronoamperometric I-t measurements under visible-light illumination with λ> 600 nm were performed. As displayed in Figure 5.8a, bare CdS and CdS/C_{PDA} samples present the ignorable photo-response behavior. After the decoration of Au, the photocurrent density of CdS/C_{PDA}/Au-2 illustrates a significant enhancement with the current density of ~ 0.21 mA/cm^2. Considering the size constraint (< 50 nm) of Au NPs and unsatisfied photon energy for photoexcitation of CdS, resonant photon scattering, and localized electric-field enhancement mechanism can be excluded here.[236] Therefore, it is convinced that the

SPR-induced hot electron transport from Au NPs to CdS mainly contributes to the improved PEC performance of CdS/C_{PDA}/Au-2 photoelectrode in the spectral region of λ > 600 nm, in consistent with the analysis of IPCE results and UV-vis spectra. FEM analysis and simulation were conducted to calculate the near-field distribution and further verify the plasmon-enhanced photoresponse. Figure C5.16 shows the calculated absorption spectrum, which is in good agreement with the experimental measurements. Figure 5.8b presents the simulated electric field distribution at λ = 650 nm, where an intense near field at the metal-semiconductor interface can be observed, which can greatly increase the light absorption and boost the hot electron generation/injection, with an enhancement factor of > 5 dB. On the basis of the above results and analysis, the interface contact and possible electron transfer process between Au and CdS/C_{PDA} are explored and the schematic diagram is shown in Figure 5.8c. When CdS/C_{PDA}/Au-2 photoelectrode is exposed to visible light at λ> 600 nm, surface plasmons in Au NPs are photoexcited and generate electron-hole pairs. Here, Au working as the electron trap could effectively drive interfacial hot electrons migrating through the C_{PDA} layer to adjacent CdS, then leading to an improved PEC activity. While the wavelength of incident light is below 600 nm, the localized electric field formed by the trapped electrons in Au nanoparticles and generated holes in the semiconductor would play a crucial role in the separation of charge carriers and considerable photoconversion enhancement. As a result, un-localized holes will transfer onto the Au surface for oxidation reaction and the photoexcited electrons will be collected on the substrate, which would be beneficial for the prolonged charge lifetimes and photoanode protection.

To elucidate the superiorities of the PDA-assisted reduction-graphitization strategy and explore the influence of carbon coating on the performance of CdS-based photoanode, CdS/Au sample was fabricated with ethanol as a reducing agent. As shown in the SEM image of CdS/Au (Figure C5.17 and insert), compared with the CdS/C_{PDA}/Au sample, the size and distribution of Au on CdS are less uniform with fierce agglomeration. The I-t measurement under visible light irradiation with λ > 600 nm (Figure C5.18a) illustrates that the as-prepared CdS/Au photoanode without carbon coating shows a decreased photocurrent density. Moreover, a sharply cathodic spike (Figure C5.18b) can be observed when the light is off, which is attributed to a back reaction from the recombination process of hot electrons and holes. The introduction of carbon could largely reduce cathodic current and suppress the occurrence of back reaction, directly demonstrating that the carbon coating can effectively promote the extraction of hot electrons from Au to CdS. Besides, the CdS/Au photoanode also exhibits a largely attenuated LSV curve (Figure C5.18c) under one sun irradiation compared with that of CdS/C_{PDA}/Au, signifying the significant effect of interfacial carbon layer on the overall PEC performance. In addition to benefiting charge transfer and PEC performance, the decoration of C_{PDA} can also improve the overall photostability. As displayed in Figure C5.18d, CdS/Au presents a higher photocurrent loss by 38.9 % over 4000 s of photoelectrolysis, which could result from the absence of carbon isolation between CdS and electrolyte. Therefore, the unique advantage of PDA and graphitized carbon layer can be reasonably summarized as follows: Firstly, the coated PDA layer acts as a supporter, favoring the reduction and fixation of metallic Au; secondly, it works as the charge acceptor and transporter to accelerate the hot electron extraction and lengthen carrier lifetime; thirdly, it serves as an isolation layer to protect CdS from photocorrosion, prevent the direct contact of CdS and Au and reverse transfer of photoinduced charge carrier.

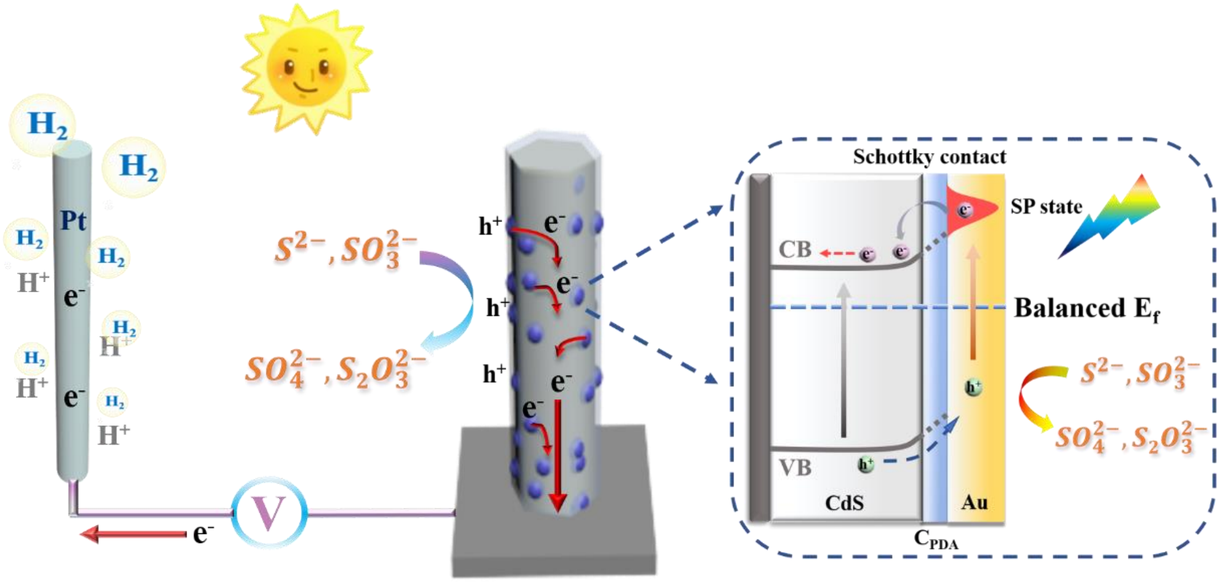

Figure 5.9 The mechanism sketch of PEC hydrogen generation over 1D-oriented CdS/C_{PDA}/Au heterostructure.

On the basis of these observations and discussions, a possibe schematic illustration of electron transfer path for the significantly enhanced PEC hydrogen evolution performance over the CdS/C_{PDA}/Au heterostructure has been proposed and presented in Figure 5.9. Upon the PDA-assisted attachment of Au on CdS nanorod arrays, the SPR interaction between Au and CdS will improve the entire light-harvesting strength and range, which helps to the generation of more photoinduced electron/hole pairs. In the meantime, because of the difference in Fermi levels, a carrier transfer rectification process will occur at the metal/semiconductor interface, where the free electrons on the CdS rapidly transport to Au surface until the matched energy level, leading to the formation of a space charge layer and Schottky barrier.[244, 283, 289, 290] The bands of CdS will exhibit upwards bending due to the higher work function of Au.[102, 238, 290] Ultimately, the produced Schottky barrier and energy band bending will induce the increased charge carrier separation efficiency, minimize the electron-hole recombination, and prolong the carrier lifetimes. Specifically, under simulated sunlight irradiation, both CdS and Au can be photoexcited to generate electron/hole pairs. Then, the interfacial hot electron from Au will be injected into the internal CdS conduction band through conquering the Schottky barrier or the tunneling effect, migrating to the counter electrode for hydrogen production. The accumulated holes on the Au surface would oxidize S^{2-} to S_2^{2-} ions, where the direct oxidation reaction sites on Au NPs could effectively protect CdS from photocorrosion. Here, the introduction of scavenger (SO_3^{2-}) is to avoid the back reaction. During the whole process, the role of C_{PDA} layer is to accelerate the hot electron extraction, inhibit the reverse transport of charge carriers, and lengthen electron lifetimes. As a result, all the aforementioned factors are devoted to the outstanding PEC hydrogen evolution activity of the as-prepared CdS/C_{PDA}/Au photoanode.

5.5 Conclusion

In summary, the novel plasmon-enhanced CdS/Carbon/Au nanoarray photoanode was successfully fabricated via a facile interfacial in-situ reduction–graphitization method, where the creative introduction of PDA layer could not only grow and fix metallic Au NPs with precise configuration but also function as C precursor for its intimate attachment. Thanks to the LSPR effect, the formed 1D-oriented CdS/C_{PDA}/Au photoelectrode shows remarkably enhanced light harvesting and quantum yield. Meanwhile, compared to the pristine CdS, the photocurrent density and photoconversion efficiency over CdS/C_{PDA}/Au electrode both achieve impressive growth owing to the building of intense localized electric field, hot-electron injection, and promoted charge carrier separation at metal/semiconductor interface. Besides, the PL, normalized I-t plots, and OCVD analysis further confirm the lengthened electron lifetimes because of the largely suppressed charge carrier recombination process. More importantly, the modification by the C_{PDA} layer and Au NPs significantly enhances entire photostability and durability through isolation effect and highly efficient hole transporting. This work here provides an effective strategy to in-situ reduce plasmonic metals and optimize the interfacial connection between noble metals and the semiconductor, which is instructive for designing and fabricating other plasmon-enhanced PEC systems for improved solar energy conversion.

5.6 Supporting information

The supplementary material related to the formulas used in this study and analytic characterizations is available in Annex C and on the website: https://doi.org/10.1021/acsami.1c04006.

5.7 Contribution of authors to this paper:

Zhiyuan Peng, as the first author of this paper, designed this project, performed most of experiments, analyzed the data, and wrote the full manuscript.

Peipei Liu conducted the IPCE measurements of all samples, and the corresponding result analysis.

Prof. Jianming Zhang, Prof. Jerome. Claverie, and Prof. Mohamed Siaj (the corresponding author) contributed to the preparation and correction of manuscripts, and the final submission process.

CHAPTER 6
CONCLUSIONS AND PERSPECTIVES

6.1 Conclusions

The PEC hydrogen evolution provides a promising strategy for directly converting solar energy to storable green chemical fuels in an economical and eco-friendly manner. The development of high-performance and stable semiconductor photoanodes is still the key challenge to accomplish a reliable PEC device. In our thesis, the highly oriented 1D CdS nanorod array was selected as the host material. To overcome the intrinsic drawbacks of the pristine CdS, further surface modifications through coupling with other semiconductor photoactive materials or noble metals to construct special nanojunctions have been proven effective in improving its overall optical absorption capability, charge separation, and transport efficiency, and photocorrosion resistance, ultimately achieving a dramatically enhanced photocurrent density and stable solar hydrogen production.

In Chapter 3, a hierarchically core-shell CdS/MoS_2 heterojunction photoanode is successfully fabricated by directly depositing MoS_2 on CdS NRs using CVD methods. The resulting structural analysis confirms that mono/few-layered MoS_2 nanoflakes with a mixed phase of semiconducting 2H and metallic 1T are continuous and intimate deposited on single-crystal CdS NR arrays in a plane-to-plane stacking fashion. Through adjusting the working distance during the CVD process, the optimal junction thickness with precise MoS_2 loading is identified and the formed CdS/MoS_2 photoanode with three-layered MoS_2 shells presents the highest photocurrent density (2.14 mA/cm^2 at 1 V vs RHE) and photoconversion efficiency, with respect to other single component and compounds. This significant enhancement in photoelectrochemical performance predominantly results from the construction of CdS/MoS_2-3L heterostructure which increases the overall light harvesting capability, passivates the surface trapping state, and provides unidirectional channels for better charge separation. More importantly, the uniformly adhered MoS_2 shells also serve as a protective layer, beneficial for photoanode protection and improved photostability. This work highlights the function of the CVD-assisted strategy in preparing ultrathin catalytic/co-catalytic materials for surface engineering applications.

In Chapter 4, a novel 1D hierarchical CdS/Au/SnO_2-S nanostructure has been successfully fabricated and demonstrated as a pure Z-scheme photoanode for highly efficient PEC hydrogen evolution. Compared to the pristine CdS, plasmonic CdS/Au, and direct Z-scheme CdS/SnO_2 heterostructures, the hierarchical CdS/Au/SnO_2-S photoanode presents the highest photocurrent density (4.87 mA/cm^2 at 1 V vs. RHE) and photo-to-current conversion efficiency (51.2% at 340 nm). This significantly improved PEC performance mainly depends on the effectiveness of strengthened vectorial Z-scheme charge transfer from the CB of SnO_2 to the VB of CdS using Au NPs as charge mediator, which is in favor of the promoted charge separation, increased carrier density, and preserved strong redox capability. More importantly, thanks to the undermined VB holes of CdS and transferred surface oxidation sites, the resulting Z-scheme CdS/Au/SnO_2-S photoanode exhibits better corrosion resistance and photostability, illustrating its great potential for future applications. In addition, for comparison, a complete SnO_2-encapsulated CdS/Au (CdS/Au/SnO_2-F) photoelectrode was also fabricated by full-spectrum irradiation, which exhibits the decreased photo-response and weakened generation of hydroxyl radicals because of the disordered charge transfer. It is thus concluded that the absolute separation of semiconductor components by charge mediators can favor to the construction of pure all-solid-state Z-scheme heterojunctions for better PEC properties. The present work gives a deep insight into the use of the all-solid-state Z-scheme photoanode for PEC hydrogen generation and provides a valuable strategy to design and fabricate other pure Z-scheme photoelectrodes, which is helpful to push forward the advancement of Z-scheme photosystems for their practical applications.

In Chapter 5, the novel plasmon-enhanced CdS/Carbon/Au nanoarray photoanode was successfully fabricated via a facile interfacial in-situ reduction–graphitization method, where the creative introduction of PDA layer could not only grow and fix metallic Au NPs with precise configuration but also function as C precursor for its intimate attachment. Thanks to the LSPR effect, the formed 1D oriented CdS/C_{PDA}/Au photoelectrode shows remarkably enhanced light harvesting and quantum yield. Meanwhile, compared to the pristine CdS, the photocurrent density and photoconversion efficiency over CdS/C_{PDA}/Au electrode both achieve impressive growth owing to the building of intense localized electric field, hot-electron injection, and promoted charge carrier separation at metal/semiconductor interface. Besides, the PL, normalized I-t plots, and OCVD analysis further confirm the lengthened electron lifetimes because of the largely suppressed charge carrier recombination process. More importantly, the modification by the C_{PDA} layer and Au NPs significantly enhances entire photostability and durability through isolation effect and highly efficient hole transporting. This work here provides an effective strategy to in-situ reduce plasmonic metals and optimize the interfacial connection between noble metals and the semiconductor, which is instructive for designing and fabricating other plasmon-enhanced PEC systems for improved solar energy conversion.

6.2 Future perspectives

In this thesis, a series of surface modification approaches, like conventional Type-I, Z-scheme, and plasmon-enhanced heterostructure fabrication, have been employed to optimize the 1D CdS nanoarray photoanode for improving its optoelectronic performance and photocorrosion resistance. Although these well designed, 1D CdS-based photoanodes have presented great progress, there are still some issues that need to be solved and further optimized for accomplishing the better PEC application. The future advancement for the fabrication of CdS-based photoanodes can be focused on the following potential directions:

(1) Further extend the light-harvesting range. According to the criterion for a practical application, the solar energy conversion efficiency over PEC cells should reach 10% or higher. That requires a wider optical absorption wavelength region to 600-700 nm by the composed PEC systems. Therefore, further strengthening the photon management of CdS-based photoanodes by ion doping to regulate the energy band positions or constructing a dual-photoabsorber PEC system is inevitable. In addition, connecting the CdS-based photoanodes and appropriate photocathodes or PV panels in the series is also a good choice for achieving a highly efficient unassisted solar hydrogen generation.

(2) Further improve the quantum efficiency. In addition to the above approaches, some other modification strategies, such as chemical doping, surface reconstruction, p-n junction, nanostructure optimization, nano-interfacing, etc., could also be attempted to promote the efficient bulk charge carrier separation and further optimize the overall quantum efficiency for better photoconversion.

(3) Until now, photostability of CdS-based photoanode is still the primary issue that needs to be solved. In this thesis, a series of well-designed 1D CdS-based photoanodes have been fabricated and exhibit the improved photocorrosion resistance in some extent but is also far from the requirement of scale-up. In future work, we will try to deposit a passivation overlayers (such as Al_2O_3, Ga_2O_3 or In_2O_3) or some cocatalysts on CdS surface for photoanode protection. Meanwhile, we are testing some other more stable photoactive materials with the unique nanoarchitecture and surface modifications, like $BiVO_4$ nanopyramid arrays, for better and long-term PEC solar conversion.

(4) Increase the applicability of CdS-based PEC systems. The currently used electrolytes for CdS-based photoanodes are strong alkaline and contain the hole scavengers (Na_2S+Na_2SO_3), which is used to consume the photogenerated holes accumulated on photoanode surface. Although the utilization of hole scavengers can improve the overall PEC performance and inhibit the occurrence of CdS self-corrosion, it also causes a large waste of photoexcitons, additional cost, and single functional product (H_2).

Therefore, in future work, we will focus on the exploration of other types of electrolytes to rationally exploit the holes on the surface of CdS-based photoanodes for obtaining high-value-added products, achieving dual-functional or even multifunctional PEC applications.

ANNEXE A
SUPPLEMENTARY FILE FOR CHAPTER 3

Engineering interfacial band hole extraction on chemical-vapor-deposited MoS_2/CdS core-shell heterojunction photoanode: The junction thickness effects on photoelectrochemical performance

Zhiyuan Peng, Yilu Su, Jafari, Maziar and Mohamed Siaj*

Department of Chemistry and Biochemistry, Université du Québec à Montréal, Montréal QC, H3C 3P8, Canada

*Corresponding author, E-mail: siaj.mohamed@uqam.ca

Analytical characterization

The exploration of crystallinity and structural features was taken on an X-ray diffractometer (Bruker D8 advance, Cu-K α, λ = 1.5406 Å) and Raman spectrometer (Renishaw confocal microscope) with the excitation laser of 532 nm. The surface chemical compositions of as-prepared photoanodes were precisely analyzed by X-ray photoelectron spectroscopy (XPS PHI 5600-ci, Eden Prairie, MN, USA) with a monochromatized Al Kα small-spot irradiation. Surface work functions of bare CdS nanorod arrays and MoS_2 thin film were determined by UV photoelectron spectroscopy using a He-I photon source (21.2 eV). The microstructure and surface morphologies were obtained with a JSM7600F field emission scanning electron microscope (FESEM) and a Multimode8 (Bruker) atomic force microscope. Transmission electron microscopy (TEM) and high-resolution TEM investigations were conducted on a JEOL JEM-2100F TEM instrument equipped with the energy-dispersive X-ray detector (STEM-EDX). Photophysical information was obtained on a Lambda 750 UV-visible spectrometer. A PE LS-45 fluorescence spectrometer was applied to record the photoluminescence (PL) spectra at room temperature using a 375 nm excitation wavelength. The time-resolved PL (TRPL) data was collected using a time-correlated single photon counting system with a pulsed diode laser (375 nm, Edinburgh Instruments FLS900).

Formula used in this work

1. Nernst equation

Partial measured potentials are converted to the reversible hydrogen electrode (RHE) potentials using the following equation:

$$E_{RHE}=E_{Ag/AgCl}+ 0.059\,pH + E^{0}_{Ag/AgCl} \tag{A3.1}$$

Where E_{RHE} and $E_{Ag/AgCl}$ are related to the potential vs. RHE and vs. Ag/AgCl, $E^{O}_{Ag/AgCl}$ is 0.197 V at 25 °C.

2. Incident photon-to-current efficiencies (IPCE)

Incident photon-to-current efficiencies (IPCE) can be calculated as follows:[291]

$$IPCE=\frac{1240\times J_{\lambda}\ (mA\cdot cm^{-2})}{\lambda\ (nm)\times P_{\lambda}(mW\cdot cm^{-2})}\times 100\% \tag{A3.2}$$

Where λ, J_{λ} and P_{λ} are respectively related to the incident-light wavelength, the measured photocurrent density and irradiation intensity.

3. Faradaic efficiency

The theoretical moles of hydrogen produced can be calculated according to the following equation:

$$n_{H_2}(theoretical)=\frac{Q}{zF}=\frac{I\times t}{zF} \tag{A3.3}$$

Where n_{H_2} represents the theoretical moles of hydrogen produced, Q is total charge passed during the testing process, z is the number of electrons for producing one molecule, which is 2 for H_2, F is the Faraday constant (96 485.33 C mol^{-1}), I is the photocurrent density and t is the testing time in seconds.

The corresponding Faradaic efficiency can be obtained as follows:

$$\eta_{Faradaic}=\frac{n_{H_2}(\text{measured})}{n_{H_2}(\text{theoretical})}\times 100\% \tag{A3.4}$$

Here, the measured H_2 evolution via gas chromatography after 3600 s is 3.685×10^{-5} mol and the theoretical H_2 evolution is 3.787×10^{-5} mol over the core-shell CdS/MoS_2 heterostructure. Consequently, the related Faradaic efficiency can be was calculated to be 97.3 %.

4. Mott-Schottky (M-S) analysis

The donor densities are estimated via the Mott-Schottky formula:[292]

$$N_D=\frac{2/e\varepsilon\varepsilon_0}{d(1/C^2)/dV} \tag{A3.5}$$

Where e is electron charge, ε_0 and ε represent vacuum permittivity (8.85×10^{-12} F m^{-1}) and relative dielectric constant of CdS (8.6). C and V correspond to the space charge capacitance and applied potential from M-S curves.

5. OCVD electron lifetimes

The average charge lifetimes (τ_n) are evaluated according to the following equation:[238, 244]

$$\tau_n = \frac{K_B T}{\mathrm{e}}(\frac{\mathrm{d}V_{OC}}{\mathrm{d}_t})^{-1} \tag{A3.6}$$

Where the K_BT, e and $\mathrm{d}V_{OC}/\mathrm{d}t$ are defined as the thermal energy, elementary charge, and derivative of OCVD transient.

6. The normalized plots of In D vs. t.

The normalized plots and kinetic process are conducted using the following equation:[94]

$$D=\frac{(I_t\text{-}I_s)}{(I_i\text{-}I_s)} \tag{A3.7}$$

Where I_t is the photocurrent at the time t, I_s represents the stable-state photocurrent and I_i denotes the photocurrent spikes.

7. Calculation of exciton lifetimes in TRPL

To assess the recombination kinetics of photogenerated charge carriers, TRPL decay spectra are fitted to the following biexponential decay equation:

$$PL(t) = A_1 e^{-t/\tau_1} + A_2 e^{-t/\tau_2} + \Delta A_0 \tag{A3.8}$$

Where τ_i belongs to decay time and A_i corresponds to decay amplitude. All fitting parameters all listed in Table S3. The average photoexciton lifetimes are calculated as follows:[181, 194]

$$\tau_{Avg.} = \frac{A_1\tau_1^2 + A_2\tau_2^2}{A_1\tau_1 + A_2\tau_2} \tag{A3.9}$$

8. Light harvesting efficiency (LHE)

Light harvesting efficiency (LHE) of as-fabricated photoanode is calculated from UV-vis spectra based on the following formula:[89]

$$LHE=1-10^{-A(\lambda)} \tag{A3.10}$$

Where $A(\lambda)$ is the absorbance at specific wavelength λ.

9. Theoretical maximum photocurrent (J_{Max})

Theoretical maximum photocurrents (J_{Max}) of as-obtained photoanodes are obtained according to the following equation:[89]

$$J_{abs} = \int \frac{\lambda}{1240} \cdot \varphi AM\ 1.5G(\lambda) \cdot LHE(\lambda) d\lambda \tag{A3.11}$$

In which λ, φAM 1.5G (λ) and LHE (λ) represent wavelength (nm), AM 1.5G solar spectrum and light harvesting efficiency, respectively.

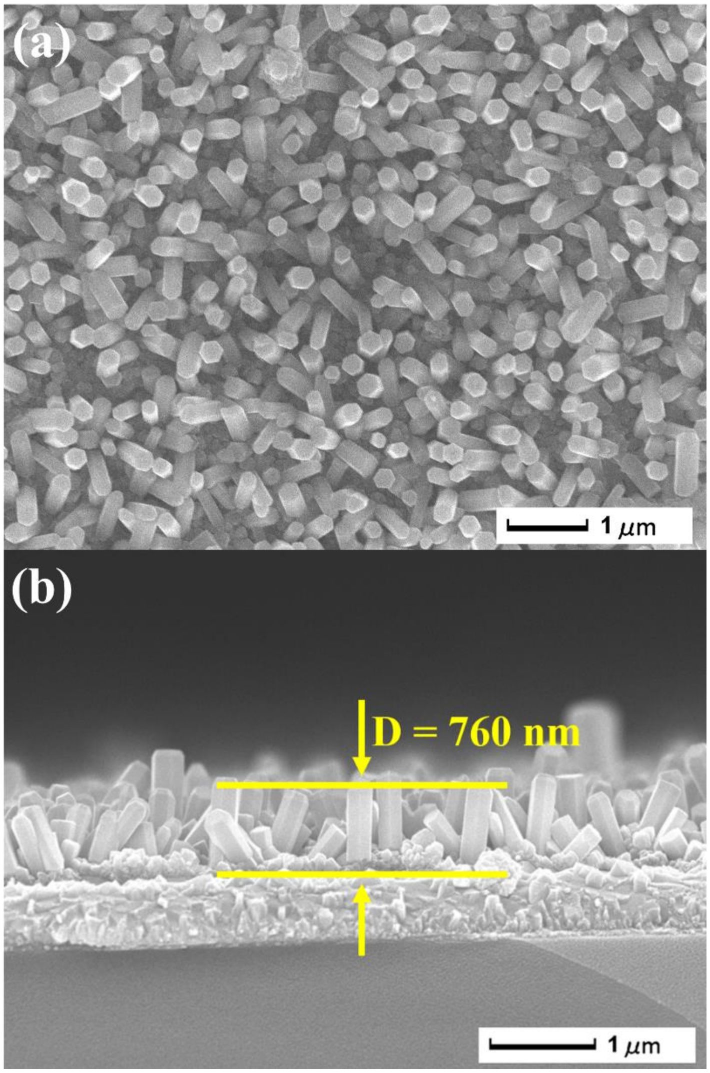

Figure A3.1 (a) The low-magnified and (b) cross-sectional SEM images of CdS photoanode.

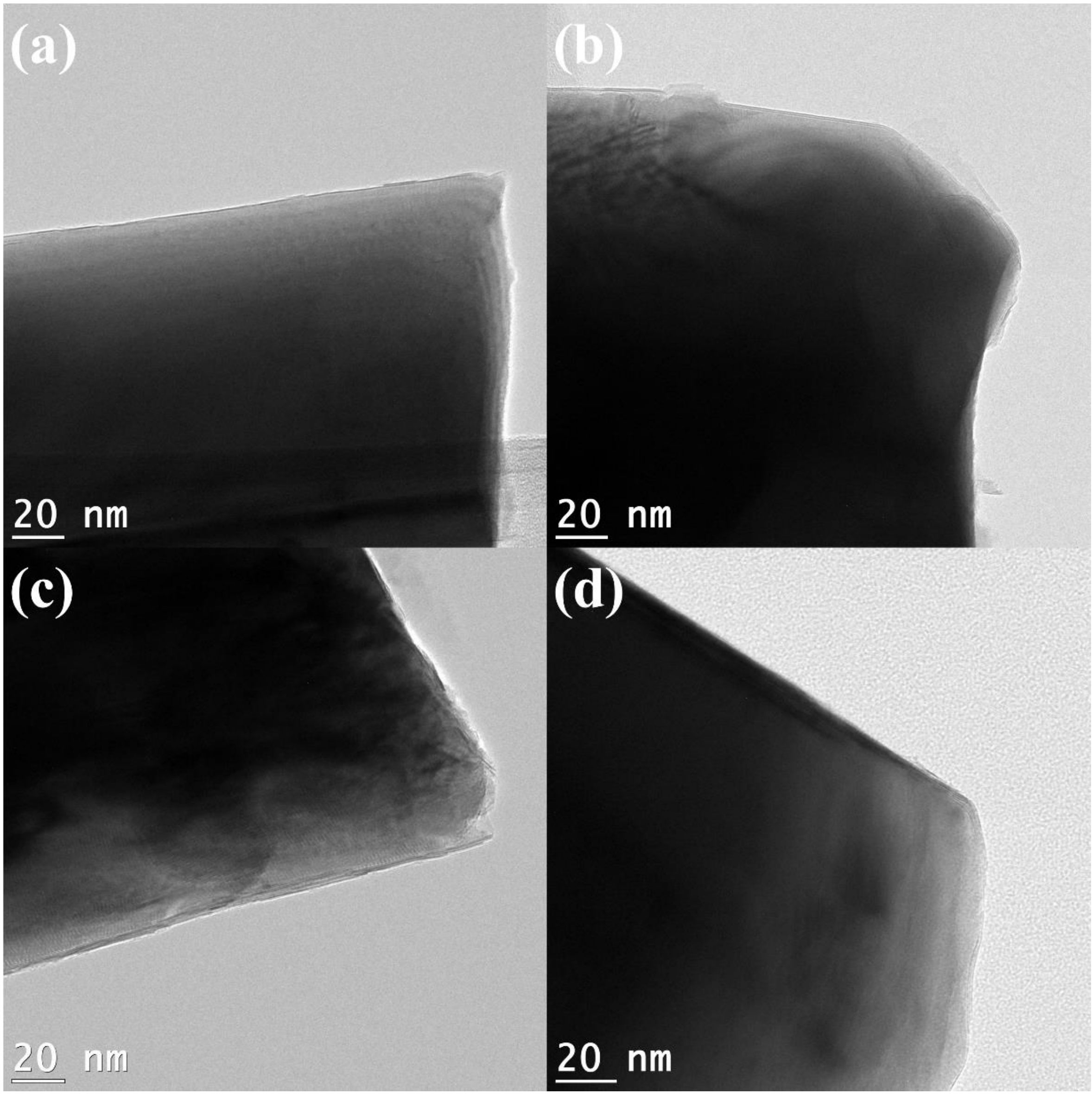

Figure A3.2 (a-d) low-resolution TEM images of CdS/MoS$_2$ heterojunctions with distinct layer numbers of MoS$_2$ shells.

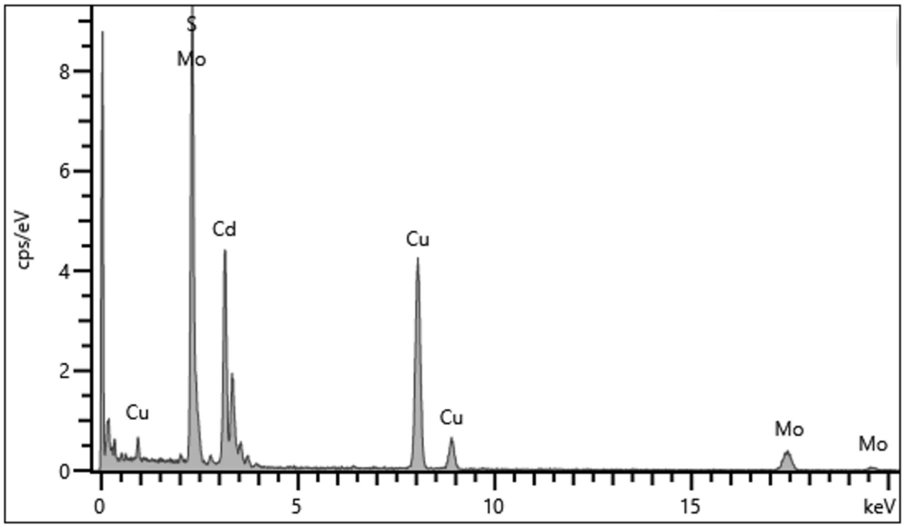

Figure A3.3 The EDX analysis of representative CdS/MoS$_2$-3L NR heterojunction.

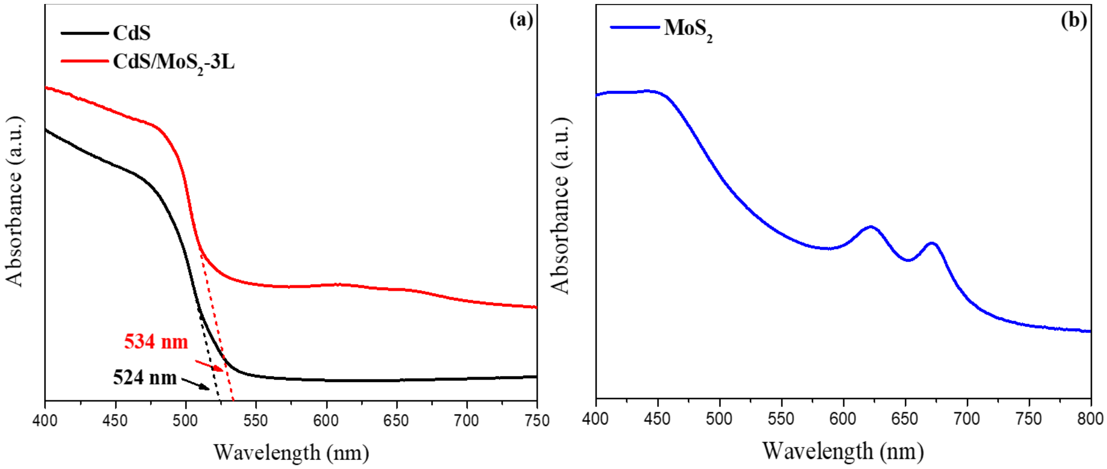

Figure A3.4 UV-vis absorption spectra of (a) bare CdS NRs, representative CdS/MoS$_2$-3L NRs and (b) MoS$_2$ nanoflakes.

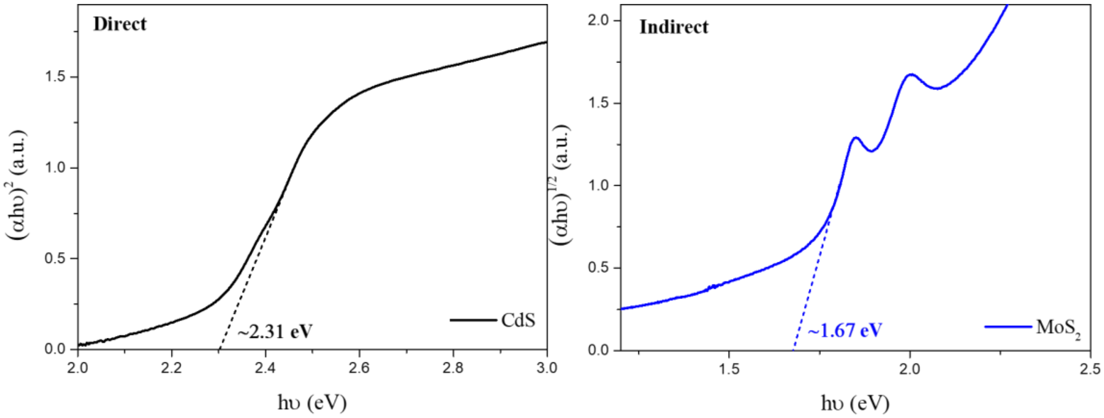

Figure A3.5 Tauc curves of the pristine CdS and MoS_2 nanoflakes.

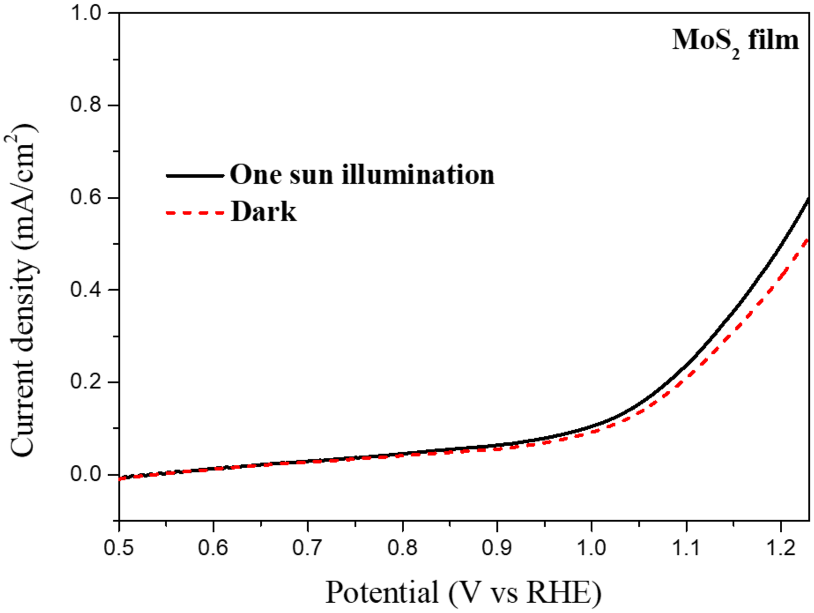

Figure A3.6 The polarization curves of MoS_2 film under darkness and one sun illumination.

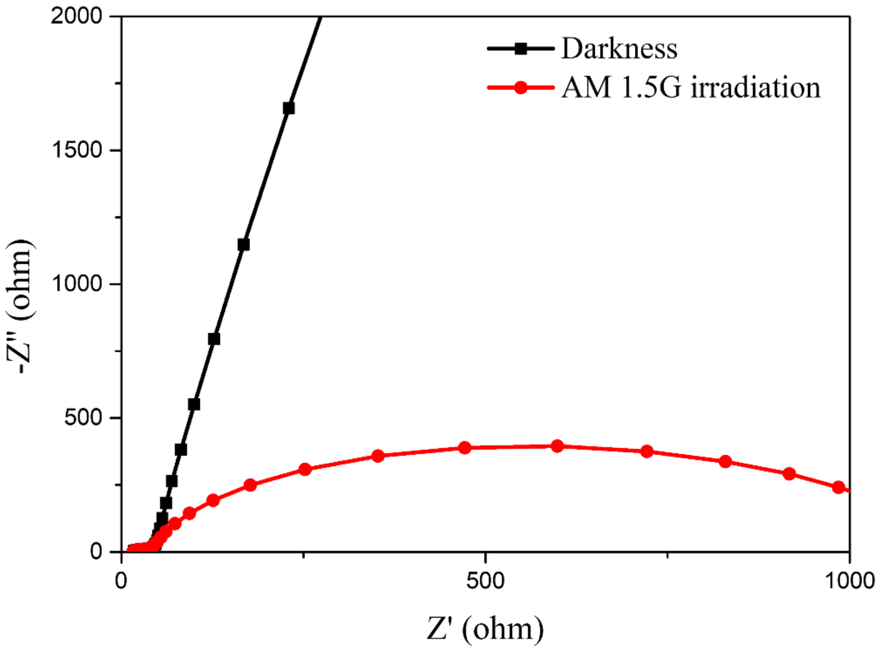

Figure A3.7 Nyquist plots of bare CdS NR arrays at open circuit potential under darkness and AM 1.5G irradiation.

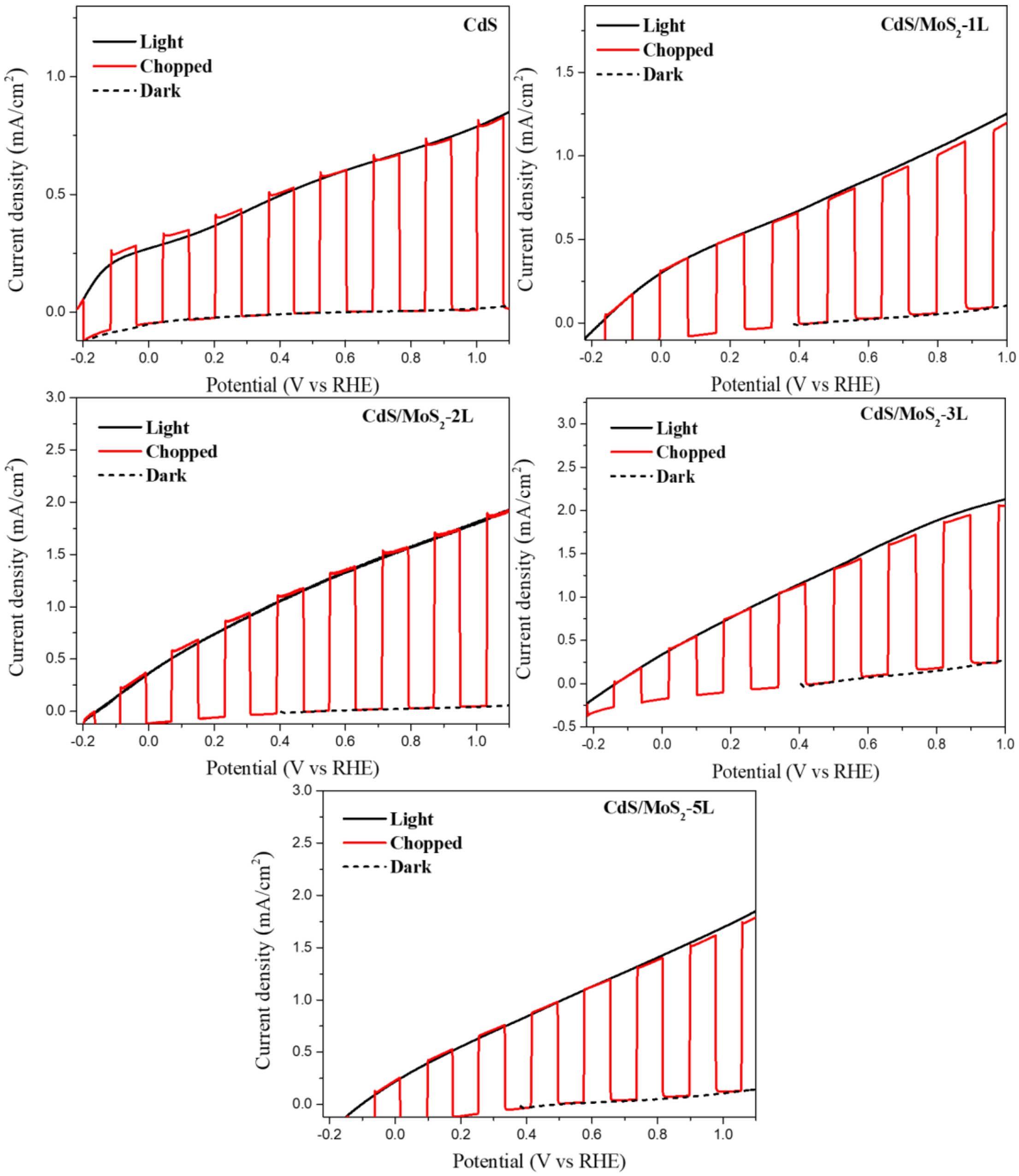

Figure A3.8 The polarization curves of bare CdS and CdS/MoS$_2$ heterojunction NRs under darkness, continuous and chopped solar illumination.

Table S3.1 The PEC performance comparison over recently reported CdS/MoS_2 heterojunctions and CdS-based photosystems.

Photocatalysts	Light source and intensity	Electrolyte	photocurrent density	Ref.
MoS_2/CdS heterostructure	AM 1.5G 100 mW cm^{-2}	10% lactic acid	1.2 mA cm^{-2} (0.4 V vs RHE)	[181]
MoS_2/CdS heterostructure	$\lambda \geq 400$ nm 300 W Xe lamp	1.33 M of lactic acid	~1.25 mA cm^{-2} (0 V vs Ag/AgCl)	[159]
MoS_2/CdS heterostructure	$\lambda \geq 420$ nm 300 W Xe lamp	0.2 M Na_2SO_4	~55 µA cm^{-2} (0 V vs Ag/AgCl)	[293]
MoS_2/CdS heterostructure	AM 1.5G 100 mW cm^{-2}	0.5 M Na_2SO_4	~1.6 µA cm^{-2} (0 V vs Ag/AgCl)	[294]
MoS_2/CdS heterostructure	300 W Xe lamp	0.5 M Na_2SO_4	~4 µA cm^{-2} (0.5 V vs Ag/AgCl)	[295]
MoS_2/CdS heterostructure	300 W Xe lamp	0.5 M Na_2SO_4	~18 µA cm^{-2} (0 V vs Ag/AgCl)	[296]
MoS_2/CdS heterostructure	300 W Xe lamp	0.5 M Na_2SO_4	~0.3 µA cm^{-2} (0 V vs Ag/AgCl)	[297]
MoS_2/Cu-CdS heterostructure	300 W Xe lamp	10% lactic acid	~43 µA cm^{-2} (0.5 V vs Ag/AgCl)	[298]
ZnO/Au/CdS heterostructure	150 W Xe lamp 75 mW cm^{-2}	0.25 M NaS_2 + 0.35 M Na_2SO_3	3.8 mA cm^{-2} (0 V vs Ag/AgCl)	[265]
β-$Ni(OH)_2$@CdS nanorod array	$\lambda \geq 420$ nm 100 mW cm^{-2}	5 M NaOH + 10 vol% ethanol	1.2 mA cm^{-2} (0 V vs Ag/AgCl)	[238]
MoS_2/CdS heterostructure	AM 1.5G 100 mW cm^{-2}	0.25 M NaS_2 + 0.35 M Na_2SO_3	2.14 mA cm^{-2} (0 V vs Ag/AgCl)	This work

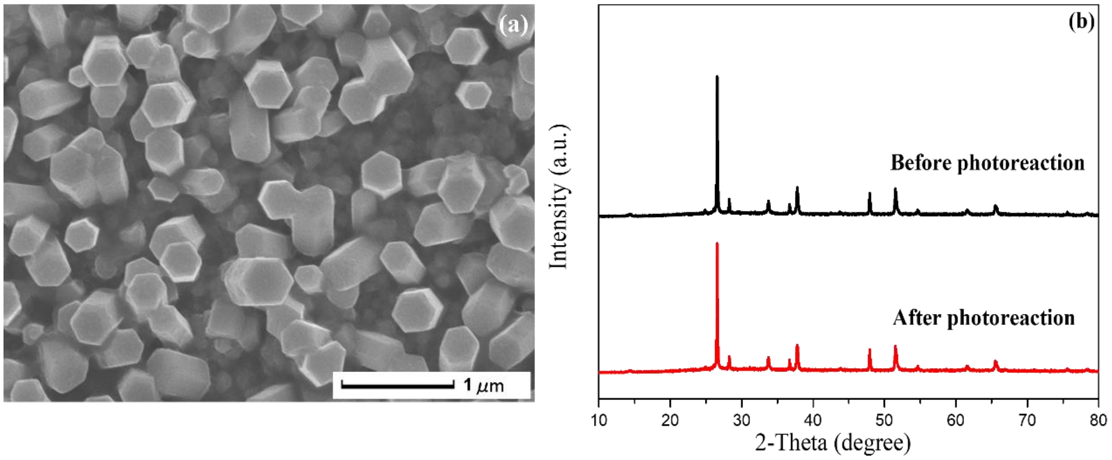

Figure A3.9 The SEM image and XRD pattern over the representative CdS/MoS_2 heterostructure before and after photostability tests.

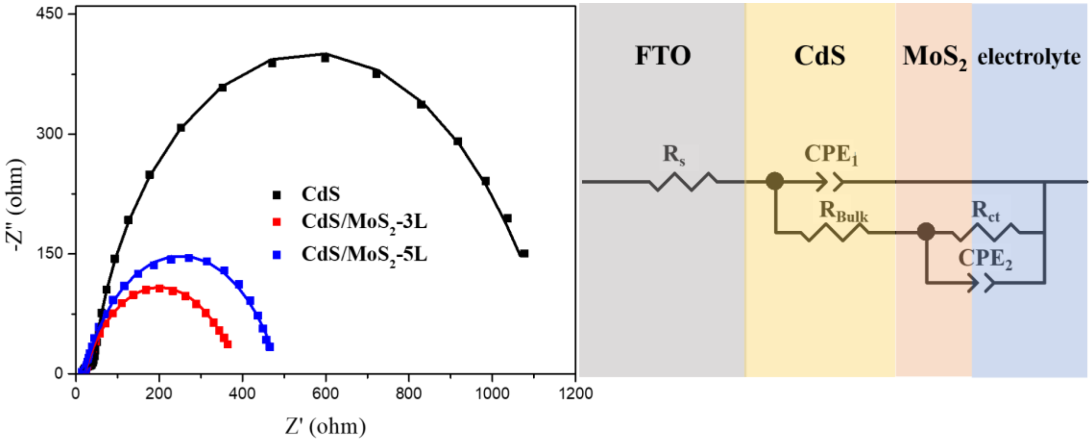

Figure A3.10 (a) Nyquist impedance spectroscopy of bare CdS and CdS/MoS_2-3, 5L heterojunctions with the measured plots as symbols and fitted curves as lines. (b) The corresponding equivalent circuit and estimated electronic structure based on the fitted EIS curves.

Table A3.2. The resistance values of all components over each photoanode based on the fitted equivalent circuits.

	R_s	R_{Bulk}	R_{ct}
Bare CdS	15.16	38.08	1110
CdS/MoS_2-3L	13.77	10.6	366.33
CdS/MoS_2-5L	12.51	10.5	467.2

Table A3.3. The summarized biexponential parameters of PL decay over the bare CdS and representative CdS/MoS_2-3L heterojunction.

	A_1	τ_1	A_2	τ_2	τ_{av} (ns)
Bare CdS	0.12	1.53	37.42	0.11	0.17
CdS/MoS_2-3L	0.22	1.85	21.13	0.15	0.36

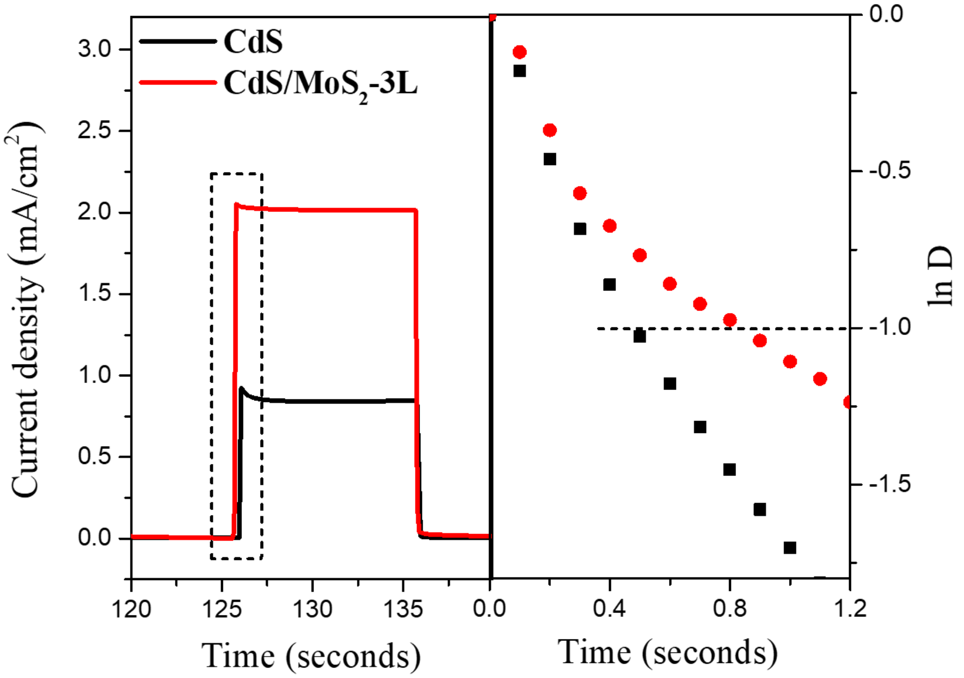

Figure A3.11. The normalized plots of ln D vs time for bare CdS and CdS/MoS$_2$ photoanode at 0 V vs Ag/AgCl.

In general, the transient photocurrent decay with the formed spike mainly originates from charge loss, which can be employed to evaluate the overall charge carrier recombination rates.[89] As displayed in the left region of Figure S10, the fabricated CdS/MoS$_2$ heterojunction photoanode presents a nearly disappearing transient spike compared to that of the pristine CdS, suggesting the less trapped electrons and rapid export of charge carriers. Further, the normalized plots and kinetic process were calculated according to equation S3.7, and shown in the right region of Figure S10. For better comparison, the transient decay time of each photoelectrode is defined at the time when ln D = -1. As expected, the representative CdS/MoS$_2$ photoanode exhibits a longer decay time of appropriately 0.83 s, meaning that using MoS$_2$ wrapping as a heterojunction can effectively reduce the trapping process of photogenerated electrons and facilitate the hole extraction.

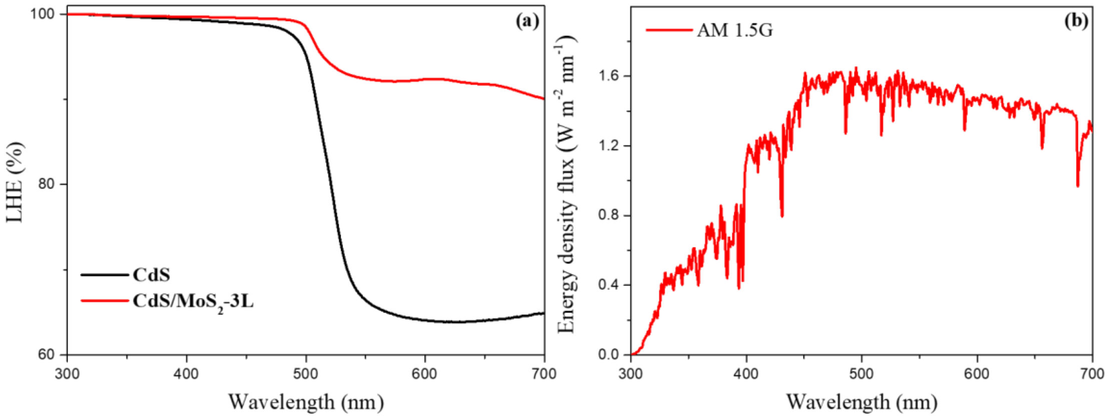

Figure A3.12 (a) LHE curves of the bare CdS and CdS/MoS$_2$-3L heterojunction photoanode; (b) The energy density flux of AM 1.5G.

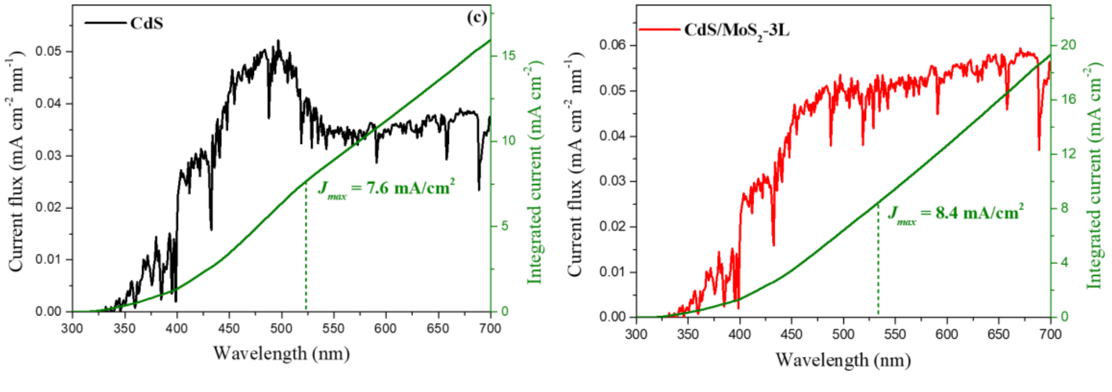

Figure A3.13 The integrated J_{max} values over the bare CdS and representative CdS/MoS$_2$-3L heterojunction photoanode.

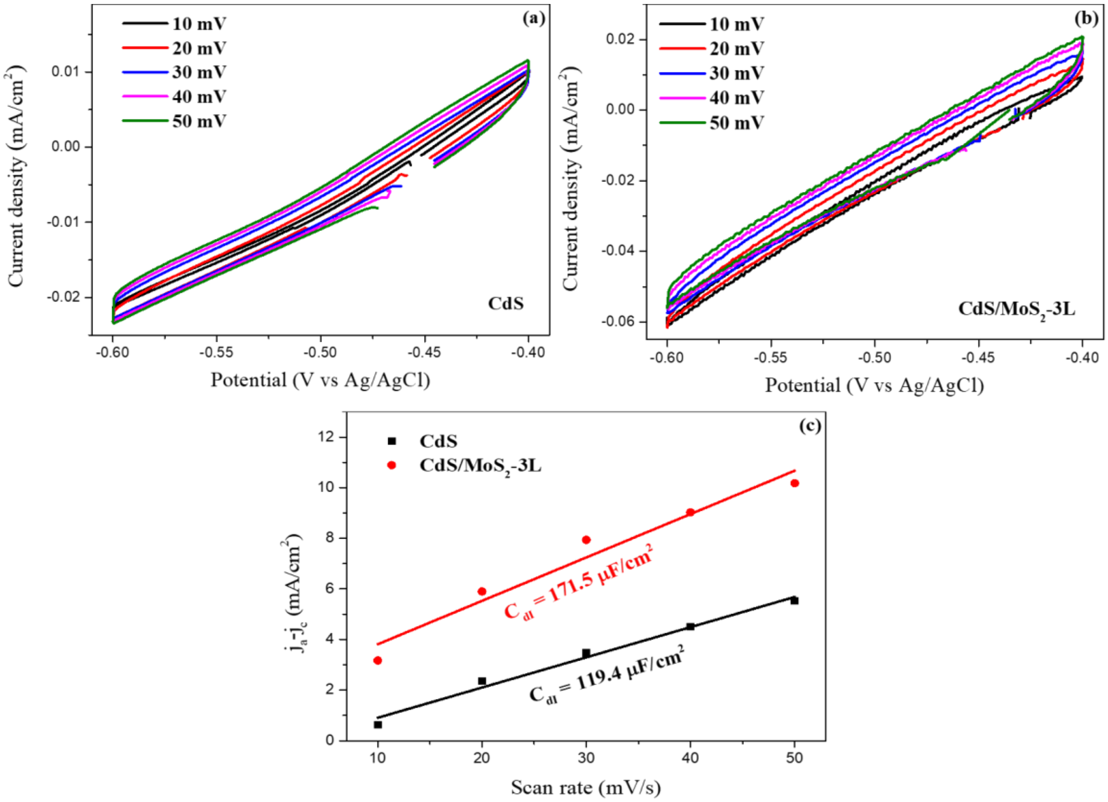

Figure A3.14 (a, b) CV curves of the bare CdS and CdS/MoS$_2$-3L photoanode at various scan rates from 10 to 50 mV/s in the non-Faradaic potential range (-0.6 to -0.4 V vs Ag/AgCl). (c) Current density differences ($\Delta j = j_a – j_c$) collected at -0.5 V as a function of scan rate for as-prepared photoanodes. j_a and j_c represents the anodic and cathodic currents, and the linear slope corresponds to the twice of the electrochemical double-layer capacitance (C_{dl}).

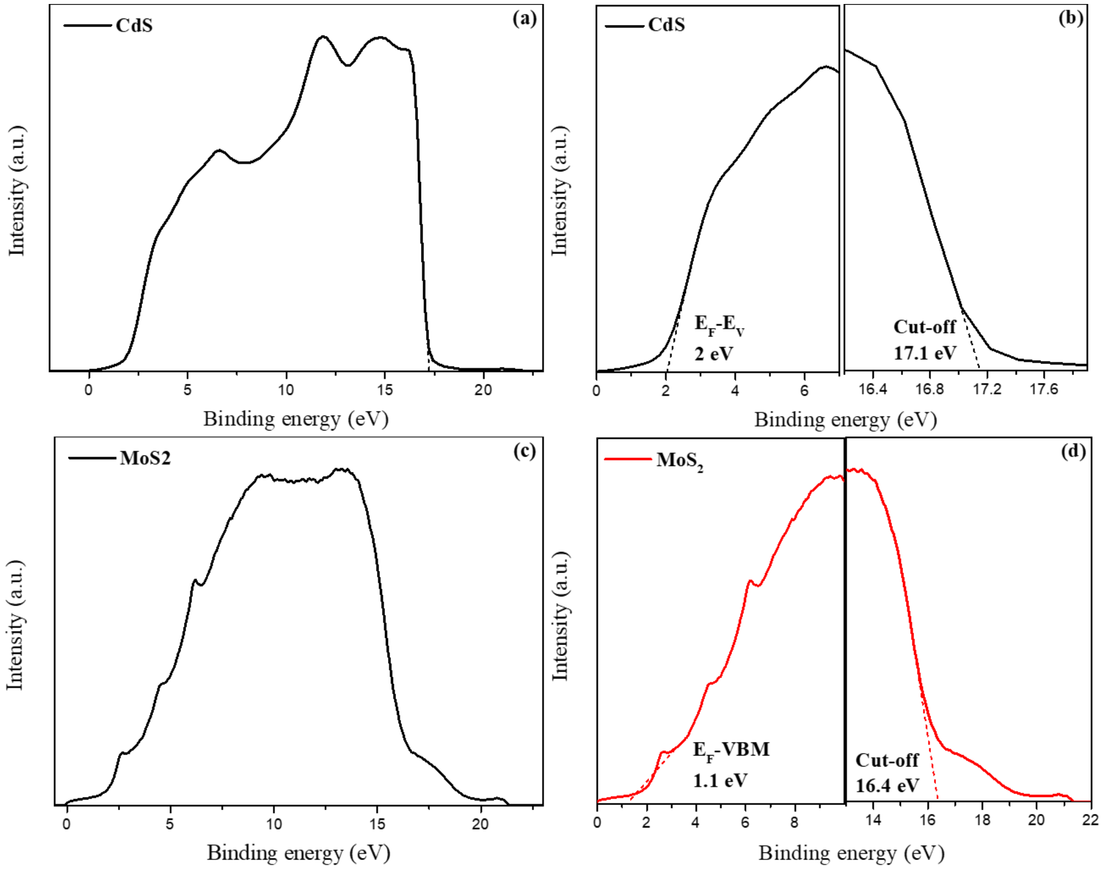

Figure A3.15 UPS spectra of the bare CdS (a, b) and MoS_2 nanoflakes (c, d). Here, $E_{Cut\text{-}off}$ depends on the spectrum edge of secondary electrons. E_F-E_V means the valence band energies relative to the Fermi levels.

ANNEXE B
SUPPLEMENTARY FILE FOR CHAPTER 4

Encapsulation of tin oxide layers on gold nanoparticles decorated one-dimensional CdS nanoarrays for pure Z-scheme photoanodes towards solar hydrogen evolution

Zhiyuan Peng, Yilu Su and Mohamed Siaj*

Department of Chemistry and Biochemistry, Université du Québec à Montréal, Montréal QC, H3C 3P8, Canada

*Corresponding author, E-mail: siaj.mohamed@uqam.ca

Formula used in this work

1. Nernst equation

Partial measured potentials are converted to the reversible hydrogen electrode (RHE) potentials using the following equation:

$$E_{RHE}=E_{Ag/AgCl}+0.059\,pH+E^{0}_{Ag/AgCl} \quad \text{(B4.1)}$$

Where E_{RHE} and $E_{Ag/AgCl}$ are related to the potential vs. RHE and vs. Ag/AgCl, $E^{O}_{Ag/AgCl}$ is 0.197 V at 25 ℃.

2. Incident photon-to-current efficiencies (IPCE)

Incident photon-to-current efficiencies (IPCE) can be calculated as follows:[291]

$$IPCE=\frac{1240\times J_{\lambda}\ (mV\cdot cm^{-2})}{\lambda\ (nm)\times P_{\lambda}(mW\cdot cm^{-2})}\times 100\% \quad \text{(B4.2)}$$

Where λ, J_{λ} and P_{λ} are respectively related to the incident-light wavelength, the measured photocurrent density and irradiation intensity.

3. Faradaic efficiency

The theoretical moles of hydrogen produced can be calculated according to the following equation:

$$n_{H_2}(theoretical)=\frac{Q}{zF}=\frac{I\times t}{zF} \quad \text{(B4.3)}$$

Where n_{H_2} represents the theoretical moles of hydrogen produced, Q is total charge passed during the testing process, z is the number of electrons for producing one molecule, which is 2 for H_2, F is the Faraday constant (96 485.33 C mol^{-1}), I is the photocurrent density and t is the testing time in seconds.

The corresponding Faradaic efficiency can be obtained as follows:

$$\eta_{Faradaic}=\frac{n_{H_2}(\text{measured})}{n_{H_2}(\text{theoretical})}\times 100\% \quad \text{(B4.4)}$$

Here, the measured H_2 evolution via gas chromatography after 3600 s is 8.809×10^{-5} mol and the theoretical H_2 evolution is 9.243×10^{-5} mol over the Z-scheme CdS/Au/SnO_2-S heterostructure. Consequently, the related Faradaic efficiency can be was calculated to be 95.3 %.

4. Mott-Schottky (M-S) analysis

The donor densities are estimated via the Mott-Schottky formula:[292]

$$N_D = \frac{2/e\varepsilon\varepsilon_0}{d(1/C^2)/dV} \tag{B4.5}$$

Where e is electron charge, ε_0 and ε represent vacuum permittivity (8.85×10^{-12} F m^{-1}) and relative dielectric constant of CdS (8.6). C and V correspond to the space charge capacitance and applied potential from M-S curves.

5. Light harvesting efficiency (LHE)

Light harvesting efficiency (LHE) of as-fabricated photoanode is calculated from UV-vis spectra based on the following formula:[89]

$$LHE = 1 - 10^{-A(\lambda)} \tag{B4.6}$$

Where $A(\lambda)$ is the absorbance at specific wavelength λ.

6. Theoretical maximum photocurrent (J_{Max})

Theoretical maximum photocurrents (J_{Max}) of as-obtained photoanodes are obtained according to the following equation:[89]

$$J_{abs} = \int \frac{\lambda}{1240} \cdot \varphi AM\ 1.5G(\lambda) \cdot LHE(\lambda) d\lambda \tag{B4.7}$$

In which λ, φAM 1.5G (λ) and LHE (λ) represent wavelength (nm), AM 1.5G solar spectrum and light harvesting efficiency, respectively.

7. OCVD electron lifetimes

The average charge lifetimes (τ_n) are evaluated according to the following equation:[238, 244]

$$\tau_n = \frac{K_B T}{\mathrm{e}} \left(\frac{\mathrm{d}V_{OC}}{\mathrm{d}_t}\right)^{-1} \tag{B4.8}$$

Where the K_BT, e and $\mathrm{d}V_{OC}/\mathrm{d}t$ are defined as the thermal energy, elementary charge, and derivative of OCVD transient.

8. Calculation of decay lifetime over the open-circuit voltage-time profiles

The related decay lifetimes of each V-t profiles are calculated through fitting to the following biexponential function with two time constants:[66, 269]

$$y(t) = A_0 + A_1 e^{-t/\tau_1} + A_2 e^{-t/\tau_2} \tag{B4.9}$$

$$\tau_m = (\tau_1 \tau_2)/(\tau_1 + \tau_2) \tag{B4.10}$$

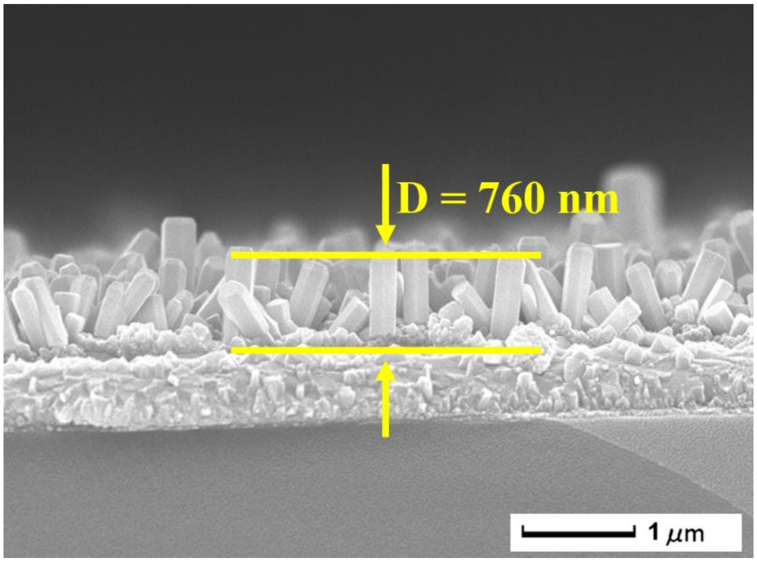

Figure B4.1 The cross-sectional SEM image of the pristine CdS nanorod array.

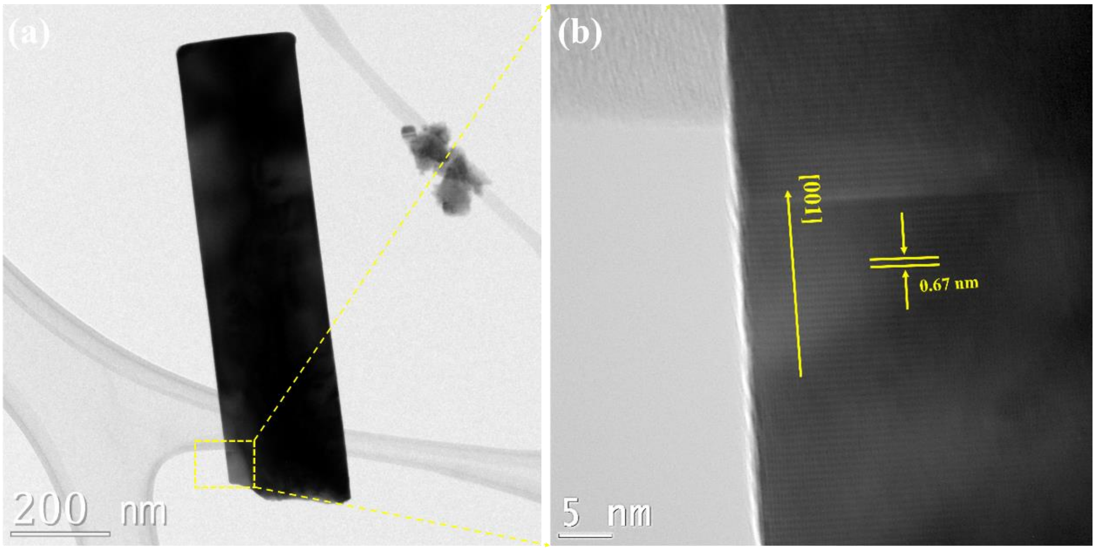

Figure B4.2 (a, b) The TEM and high-resolution TEM images of a single-crystalline CdS nanorod. The HRTEM image in Figure S2b is taken from the selected region in Figure S2a.

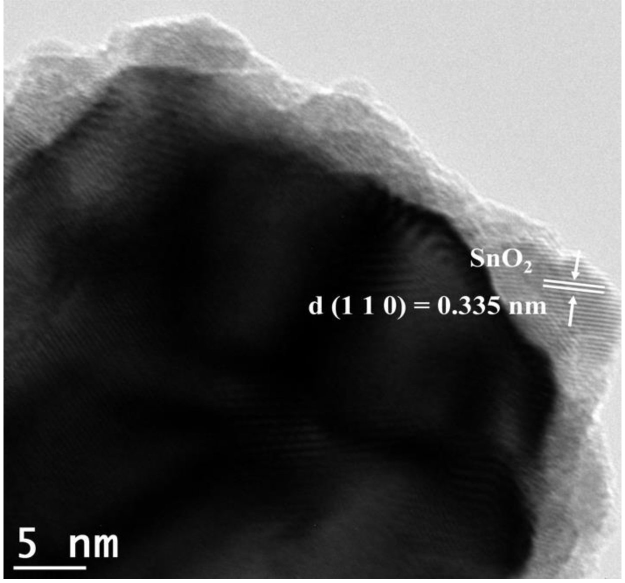

Figure B4.3 The high-resolution TEM image of the as-fabricated core-shell CdS/SnO$_2$ nanorod.

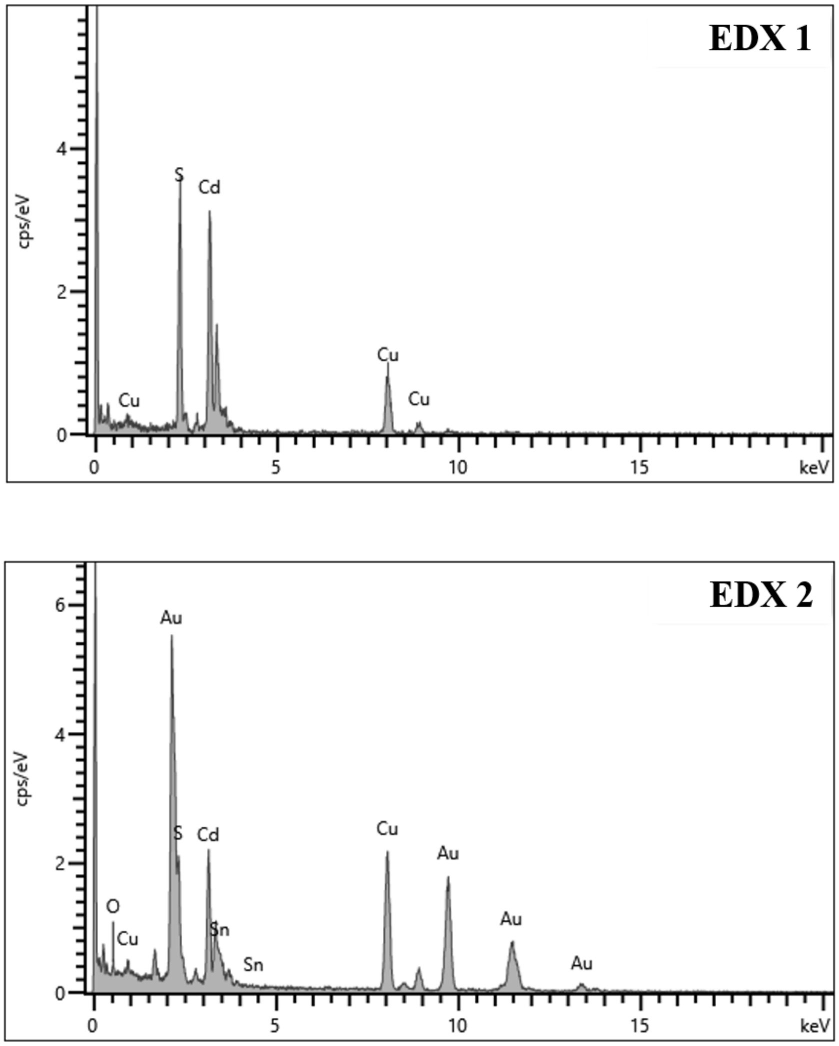

Figure B4.4 The TEM-EDX results with distinct regions taken from Figure 4f (EDX1 concentrated on the bare CdS region and EDX2 focused on the CdS/Au/SnO$_2$ region).

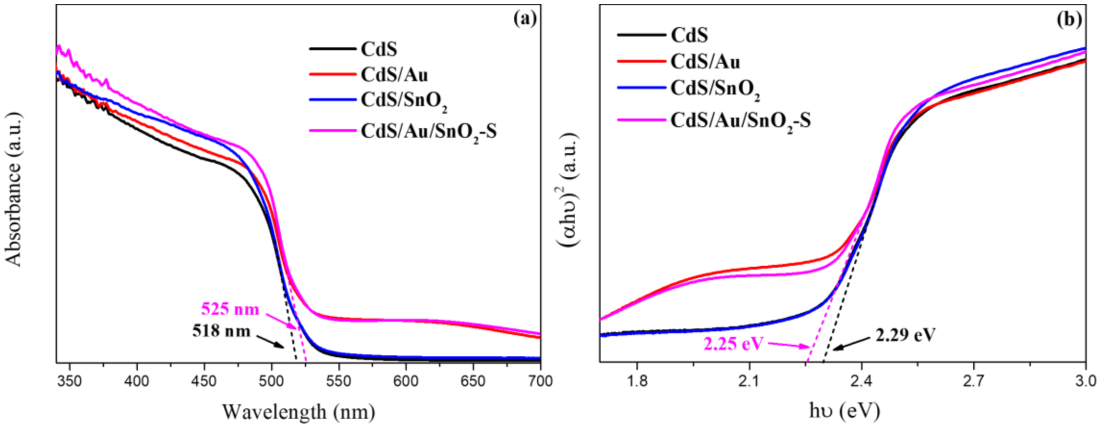

Figure B4.5 (a) UV-vis absorption spectra and (b) Tauc curves of the pristine CdS, CdS/Au, CdS/SnO$_2$, and CdS/Au/SnO$_2$-S photoanodes.

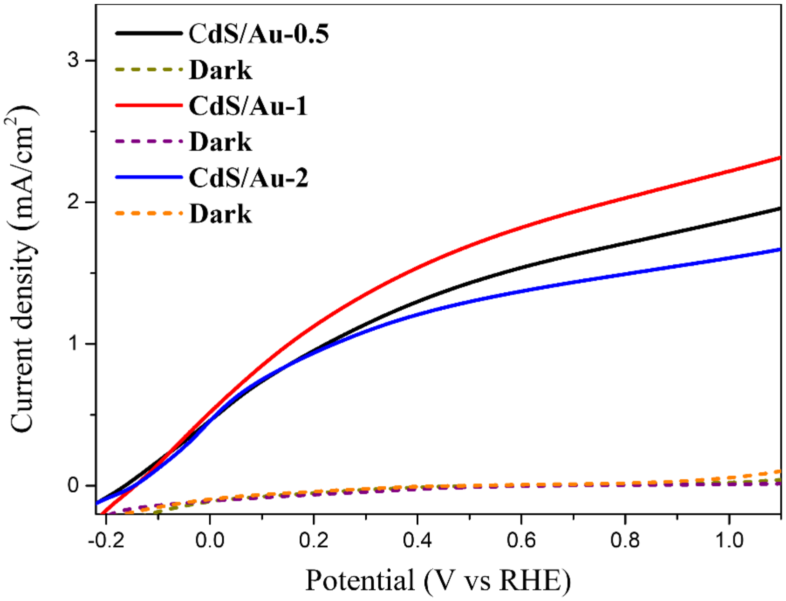

Figure B4.6 The LSV curves of CdS/Au-n photoanodes with different loading amount of Au NPs.

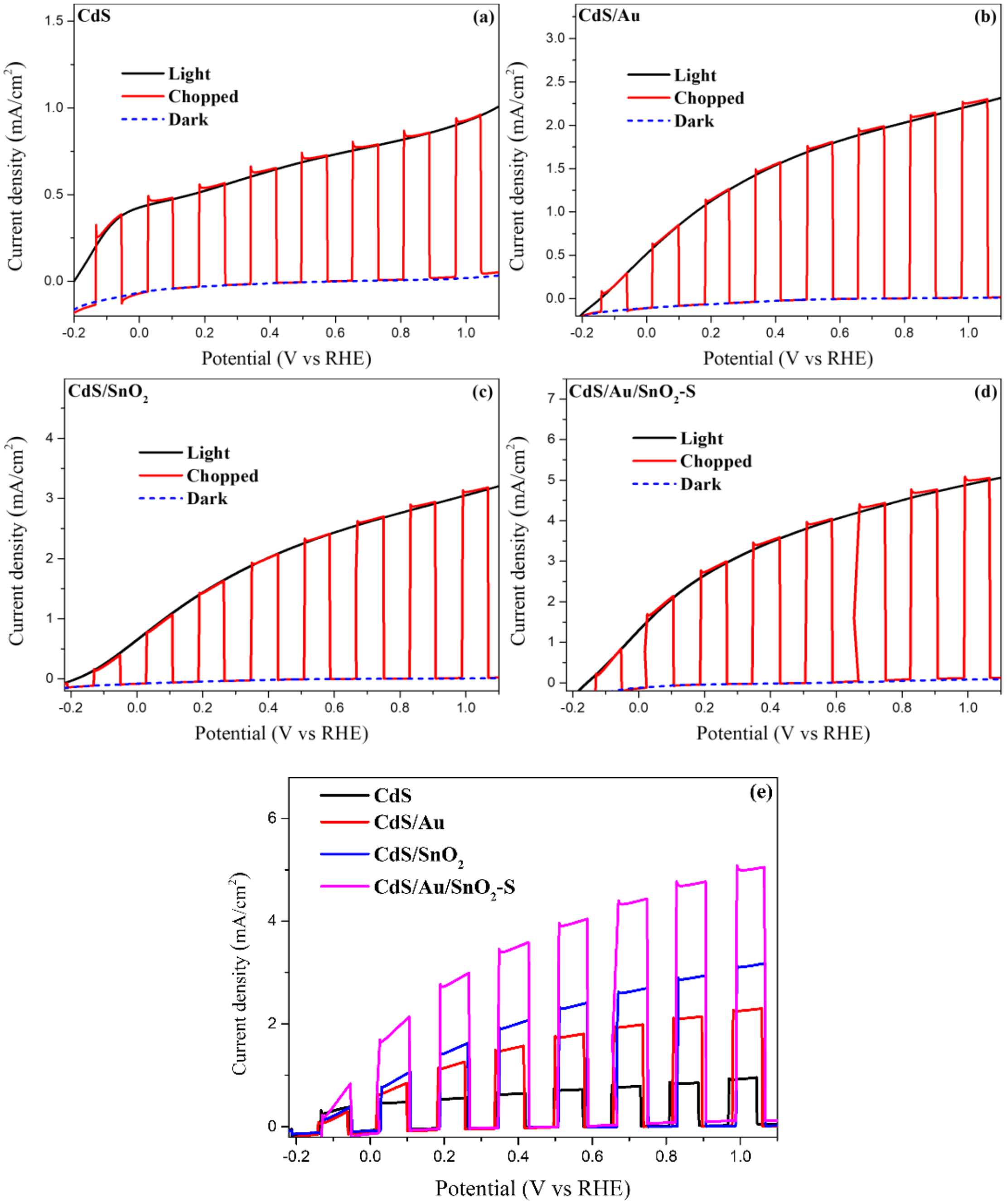

Figure B4.7 The LSV measurements for (a) CdS, (b) CdS/Au, (c) CdS/SnO$_2$ and (d) CdS/C$_{PDA}$/Au-S heterostructures under darkness, continuous and chopped solar illumination. (e) The compared chopped J-V curves of different photoanodes.

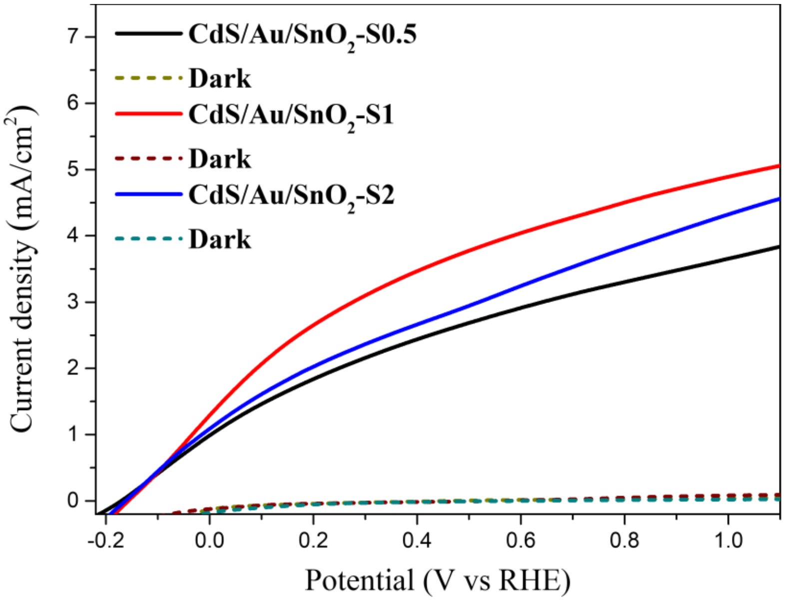

Figure B4.8 The LSV curves of CdS/Au/SnO_2-S photoanodes with different photodeposition times.

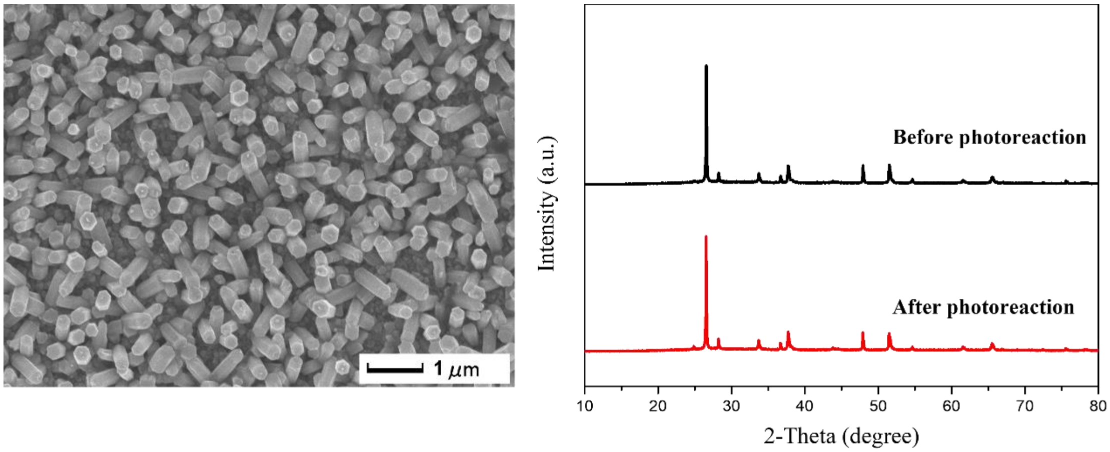

Figure B4.9 The SEM image and XRD pattern over the CdS/Au/SnO_2-S photoelectrode before and after the photostability test.

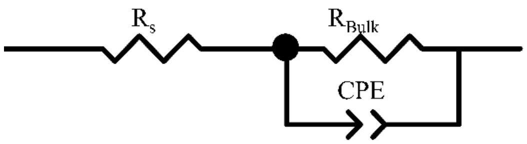

Figure B4.10 The equivalent circuit from EIS curve.

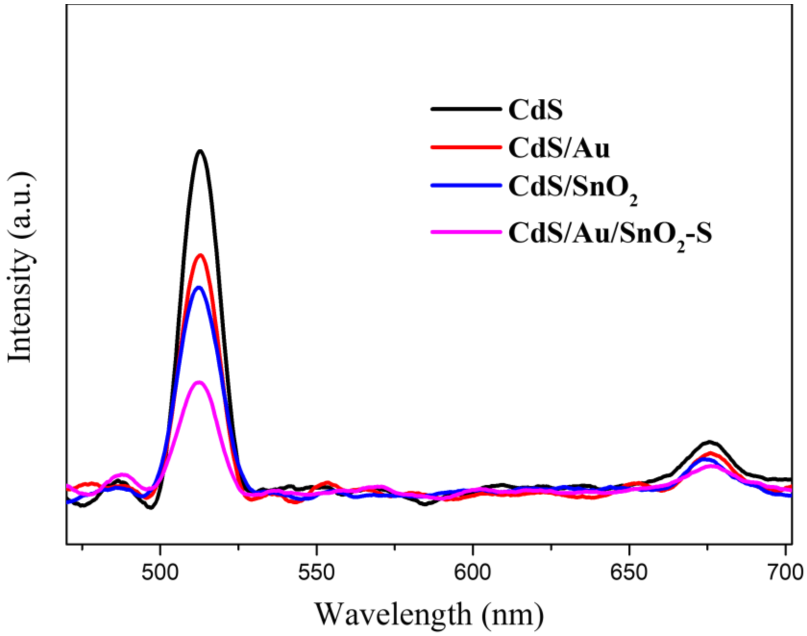

Figure B4.11 PL spectra of as-fabricated CdS, CdS/Au, CdS/SnO$_2$ and CdS/Au/SnO$_2$-S photoanodes.

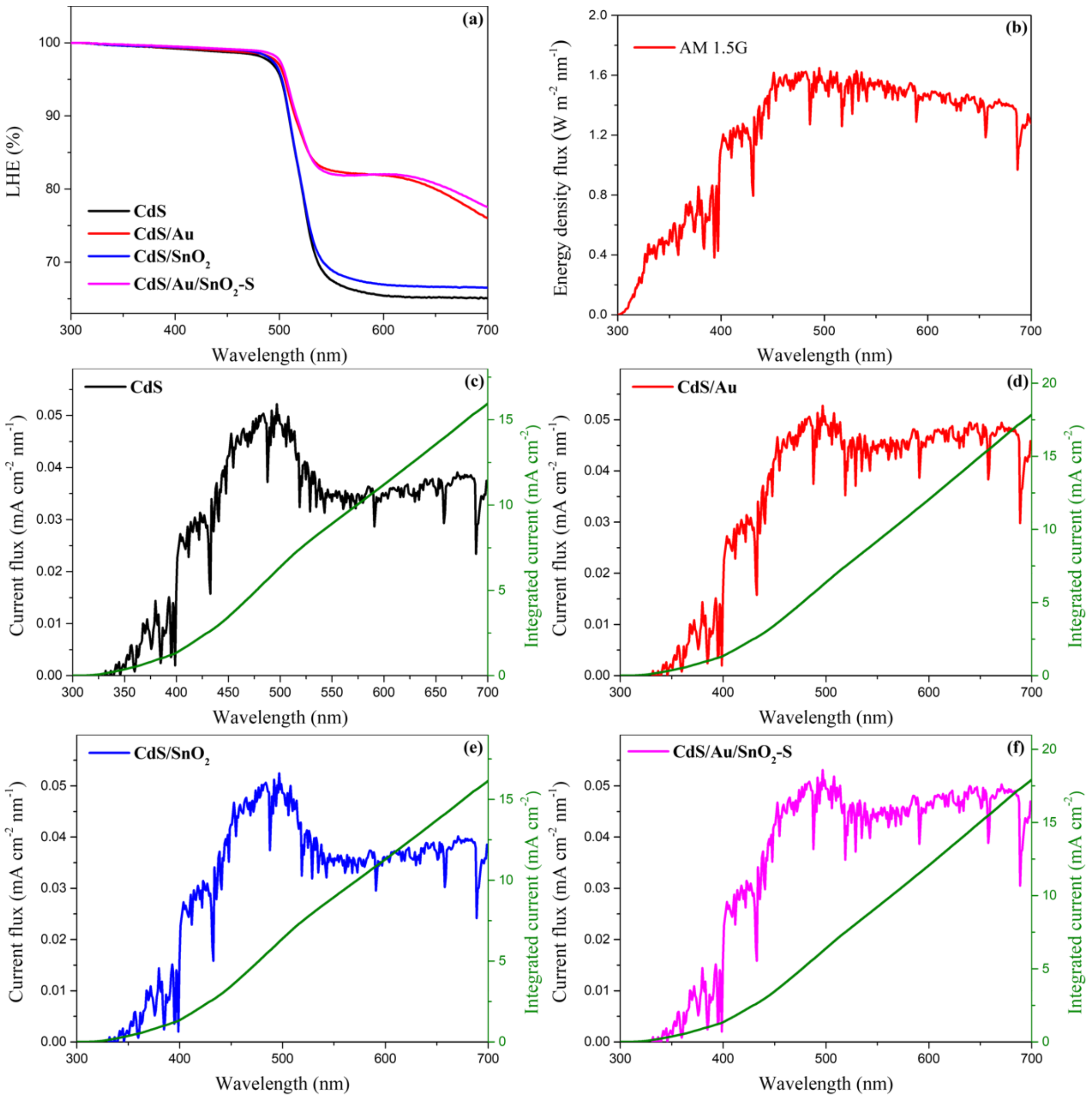

Figure B4.12 (a) LHE plots of bare CdS, CdS/ Au, CdS/SnO$_2$ and CdS/Au/SnO$_2$-S photoanodes; (b) The energy density flux of AM 1.5G; (c-f) The calculated J_{Max} values of CdS/ Au, CdS/SnO$_2$ and CdS/Au/SnO$_2$-S photoelectrodes。

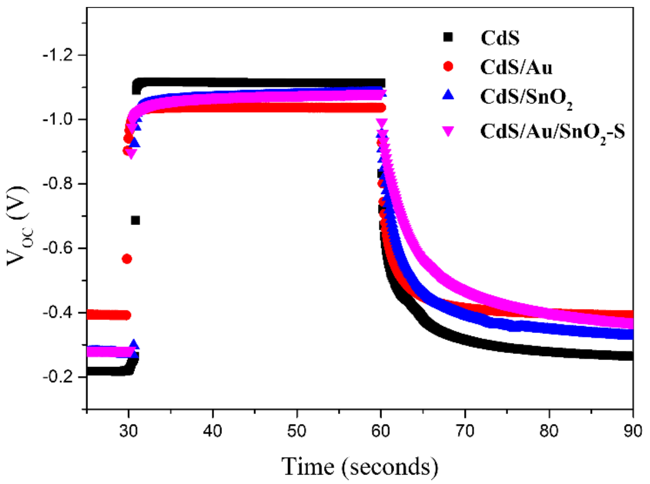

Figure B4.13 Transient OCVD measurements over the pristine CdS, CdS/Au, CdS/SnO$_2$, and CdS/Au/SnO$_2$-S photoanodes.

The above open-circuit voltage decay plots can be fitted by a biexponential function (Equation S9 and S10) and the corresponding decay lifetimes are determined to be 0.19, 0.31, 0.83, and 1.65 s for the pristine CdS, CdS/Au, CdS/SnO$_2$, and CdS/Au/SnO$_2$-S photoanodes, respectively. The significantly prolonged decay lifetime of the CdS/Au/SnO$_2$-S electrode indicates that the rational corporation of Au NPs and SnO$_2$ layer for Z-scheme heterojunction fabrication can effectively suppress the charge carrier recombination process and advance charge separation.

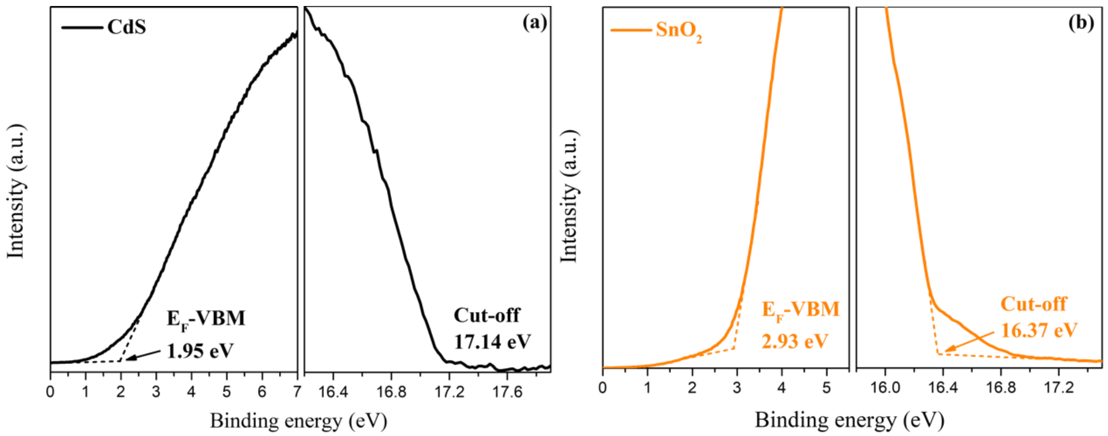

Figure B4.14. UPS spectra of bare CdS (a) and SnO_2 film (b).

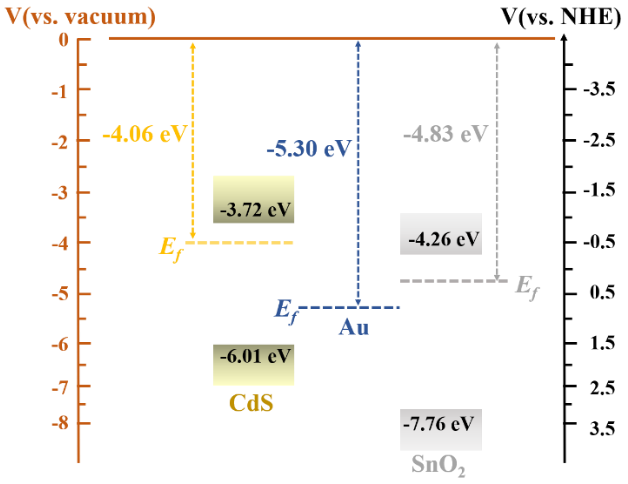

Figure B4.15. Schematic illustration for the diagram of the energy levels of CdS, Au and SnO_2.

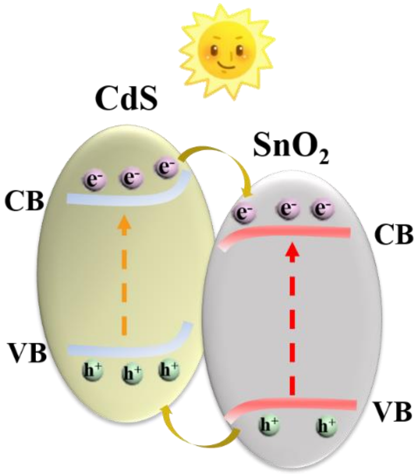

Figure B4.16. The Type-II charge transfer model between CdS and SnO_2 under sunlight irradiation.

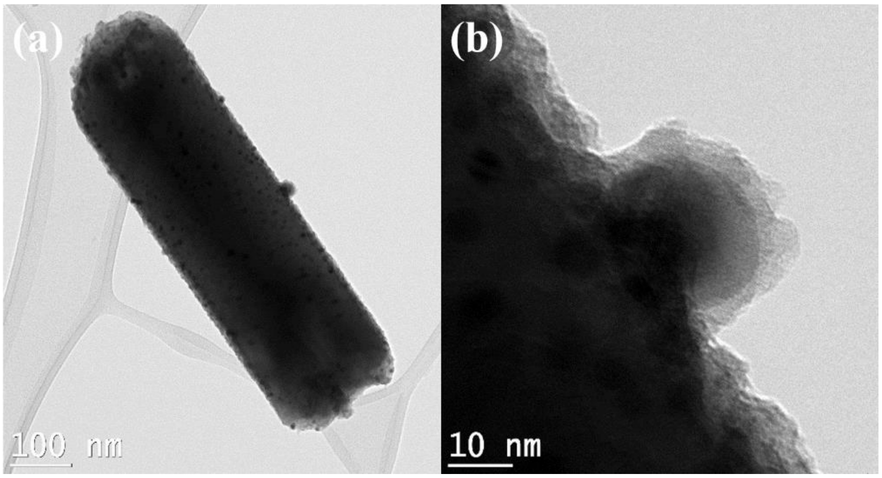

Figure B4.17. The low and high-magnification TEM images of the fully SnO_2-wrapped CdS/Au nanorod (CdS/Au/SnO_2-F).

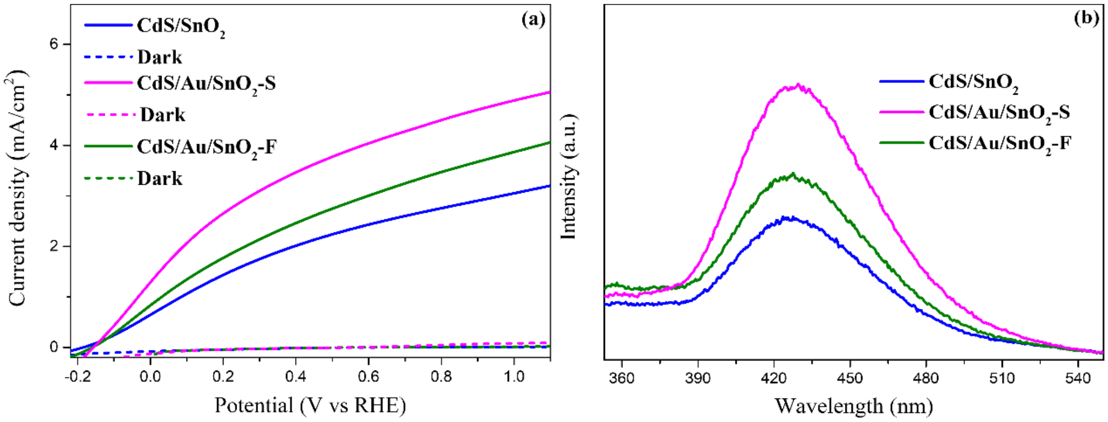

Figure B4.18 The comparison of LSV curves (a) and PL detection for the generation of hydroxyl radicals (b) over the fabricated direct Z-scheme CdS/SnO$_2$, CdS/Au/SnO$_2$-S and CdS/Au/SnO$_2$-F heterostructure.

Table B4.1 The PEC water splitting performance over recently reported similar CdS-based photoanodes.

Photoanodes	Light source and intensity	Electrolyte	photocurrent density	Ref.
β-$Ni(OH)_2$@CdS nanorod array	λ ≥ 420 nm 100 mW cm^{-2}	5 M NaOH + 10 vol% ethanol	1.2 mA cm^{-2} (0 V vs Ag/AgCl)	[238]
CdS@Ni_3S_2 core-shell nanorod	λ ≥ 400 nm 300 W Xe lamp	0.3 M NaS_2 + 0.2 M Na_2SO_3	5.8 mA cm^{-2} (-0.6 V vs Ag/AgCl)	[158]
ZnO/Au/CdS heterostructure	150 W Xe lamp 75 mW cm^{-2}	0.25 M NaS_2 + 0.35 M Na_2SO_3	3.8 mA cm^{-2} (0 V vs Ag/AgCl)	[265]
CdS/CdSe core-shell nanorod	AM 1.5G 100 mW cm^{-2}	0.5 M Na_2SO_3	5.8 mA cm^{-2} (0.7 V vs Ag/AgCl)	[150]
CdS/Cu_2O p-n heterostructure	300 W Xe lamp 100 mW cm^{-2}	0.25 M NaS_2 + 0.35 M Na_2SO_3	4.2 mA cm^{-2} (0 V vs Ag/AgCl)	[229]
CdS/$ZnFe_2O_4$/Cu_2O nanorod	visible light 100 mW cm^{-2}	0.35 M NaS_2 + 0.25 M Na_2SO_3	3.3 mA cm^{-2} (0 V vs Ag/AgCl)	[195]
Z-scheme CdS/CdO nanorod	AM 1.5G 100 mW cm^{-2}	0.35 M NaS_2 + 0.25 M Na_2SO_3	4.35 mA cm^{-2} (0 V vs SCE)	[135]
TiO_2@CdO/CdS nanorod array	AM 1.5G 100 mW cm^{-2}	0.3 M NaS_2 + 0.2 M Na_2SO_3	3.2 mA cm^{-2} (0 V vs RHE)	[93]
Bi_2S_3/CdS/TiO_2 nanotube array	AM 1.5G 100 mW cm^{-2}	0.25 M NaS_2 + 0.35 M Na_2SO_3	2.16 mA cm^{-2} (0 V vs Ag/AgCl)	[299]
CdS/Au/SnO_2 nanorod array	AM 1.5G 100 mW cm^{-2}	0.25 M NaS_2 + 0.35 M Na_2SO_3	4.69 mA cm^{-2} (0 V vs Ag/AgCl)	This work

ANNEXE C
SUPPLEMENTARY FILE FOR CHAPTER 5

One-Dimensional CdS/Carbon/Au Plasmonic Nanoarray Photoanodes via In-Situ Reduction-Graphitization Approach towards Efficient Solar Hydrogen Evolution

ZhiYuan Peng [a], Jianming Zhang [b], Peipei Liu [c], Jerome.Claverie [c], Mohamed Siaj [a,*]

d. Department of Chemistry and Biochemistry, Université du Québec à Montréal, Montréal QC, H3C 3P8, Canada
e. School of Chemistry and Chemical Engineering, Jiangsu University, Zhenjiang, Jiangsu, 212013, China
f. Département de Chimie, Université de Sherbrooke, 2500 Blvd de l'Université, Sherbrooke, J1K2R1 Qc, Canada

*Corresponding author, E-mail: siaj.mohamed@uqam.ca

Formula used in this work

1. Nernst equation

Partial measured potentials are converted to the reversible hydrogen electrode (RHE) potentials using the following equation:

$$E_{RHE}=E_{Ag/AgCl}+0.059\,pH+E^{0}_{Ag/AgCl} \tag{C5.1}$$

Where E_{RHE} and $E_{Ag/AgCl}$ are related to the potential vs. RHE and vs. Ag/AgCl, $E^{O}_{Ag/AgCl}$ is 0.197 V at 25 ℃.

2. Incident photon-to-current efficiencies (IPCE)

Incident photon-to-current efficiencies (IPCE) can be calculated as follows:[291]

$$IPCE=\frac{1240\times J_{\lambda}\ (mV\cdot cm^{-2})}{\lambda\ (nm)\times P_{\lambda}(mW\cdot cm^{-2})}\times 100\% \tag{C5.2}$$

Where λ, J_{λ} and P_{λ} are respectively related to the incident-light wavelength, the measured photocurrent density and irradiation intensity.

3. Faradaic efficiency

The theoretical moles of hydrogen produced can be calculated according to the following equation:

$$n_{H_2}(theoretical)=\frac{Q}{zF}=\frac{I\times t}{zF} \tag{C5.3}$$

Where n_{H_2} represents the theoretical moles of hydrogen produced, Q is total charge passed during the testing process, z is the number of electrons for producing one molecule, which is 2 for H_2, F is the Faraday constant (96 485.33 C mol^{-1}), I is the photocurrent density and t is the testing time in seconds.

The corresponding Faradaic efficiency can be obtained as follows:

$$\eta_{Faradaic}=\frac{n_{H_2}(\text{measured})}{n_{H_2}(\text{theoretical})}\times 100\% \tag{C5.4}$$

Here, the measured H_2 evolution via gas chromatography after 3600 s is 1.104×10^{-4} mol and the theoretical H_2 evolution is 1.146×10^{-4} mol. Consequently, the related Faradaic efficiency can be was calculated to be 96.3 %.

4. The normalized plots of In D vs. t.

The normalized plots and kinetic process are conducted using the following equation:[94]

$$D=\frac{(I_t-I_s)}{(I_i-I_s)} \tag{C5.5}$$

Where I_t is the photocurrent at the time t, I_s represents the stable-state photocurrent and I_i denotes the photocurrent spikes.

5. Mott-Schottky (M-S) analysis

The donor densities are estimated via the Mott-Schottky formula:[292]

$$N_D=\frac{2/e\varepsilon\varepsilon_0}{d(1/C^2)/dV} \tag{C5.6}$$

Where e is electron charge, ε_0 and ε represent vacuum permittivity (8.85×10^{-12} F m^{-1}) and relative dielectric constant of CdS (8.6). C and V correspond to the space charge capacitance and applied potential from M-S curves.

6. Light harvesting efficiency (LHE)

Light harvesting efficiency (LHE) of as-fabricated photoanode is calculated from UV-vis spectra based on the following formula:[89]

$$LHE=1-10^{-A(\lambda)} \tag{C5.7}$$

Where $A(\lambda)$ is the absorbance at specific wavelength λ.

7. Theoretical maximum photocurrent (J_{Max})

Theoretical maximum photocurrents (J_{Max}) of as-obtained photoanodes are obtained according to the following equation:

$$J_{abs} = \int \frac{\lambda}{1240} \cdot \varphi AM\ 1.5G(\lambda) \cdot LHE(\lambda) d\lambda \qquad \text{(C5.8)}$$

In which λ, φAM 1.5G (λ) and LHE (λ) represent wavelength (nm), AM 1.5G solar spectrum and light harvesting efficiency, respectively.

8. OCVD electron lifetimes

The average charge lifetimes (τ_n) are evaluated according to the following equation:[238, 244]

$$\tau_n = \frac{K_B T}{\mathrm{e}} (\frac{\mathrm{d}V_{OC}}{\mathrm{d}_t})^{-1} \qquad \text{(C5.9)}$$

Where the K_BT, e and $\mathrm{d}V_{OC}/\mathrm{d}t$ are defined as the thermal energy, elementary charge, and derivative of OCVD transient.

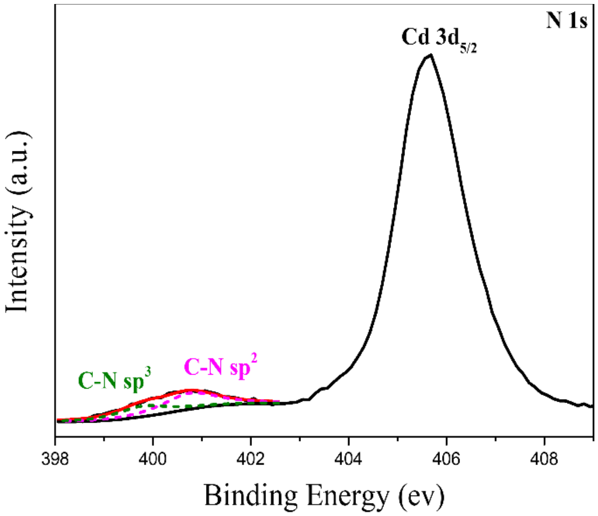

Figure C5.1 The high-resolution XPS spectrum of N 1s.

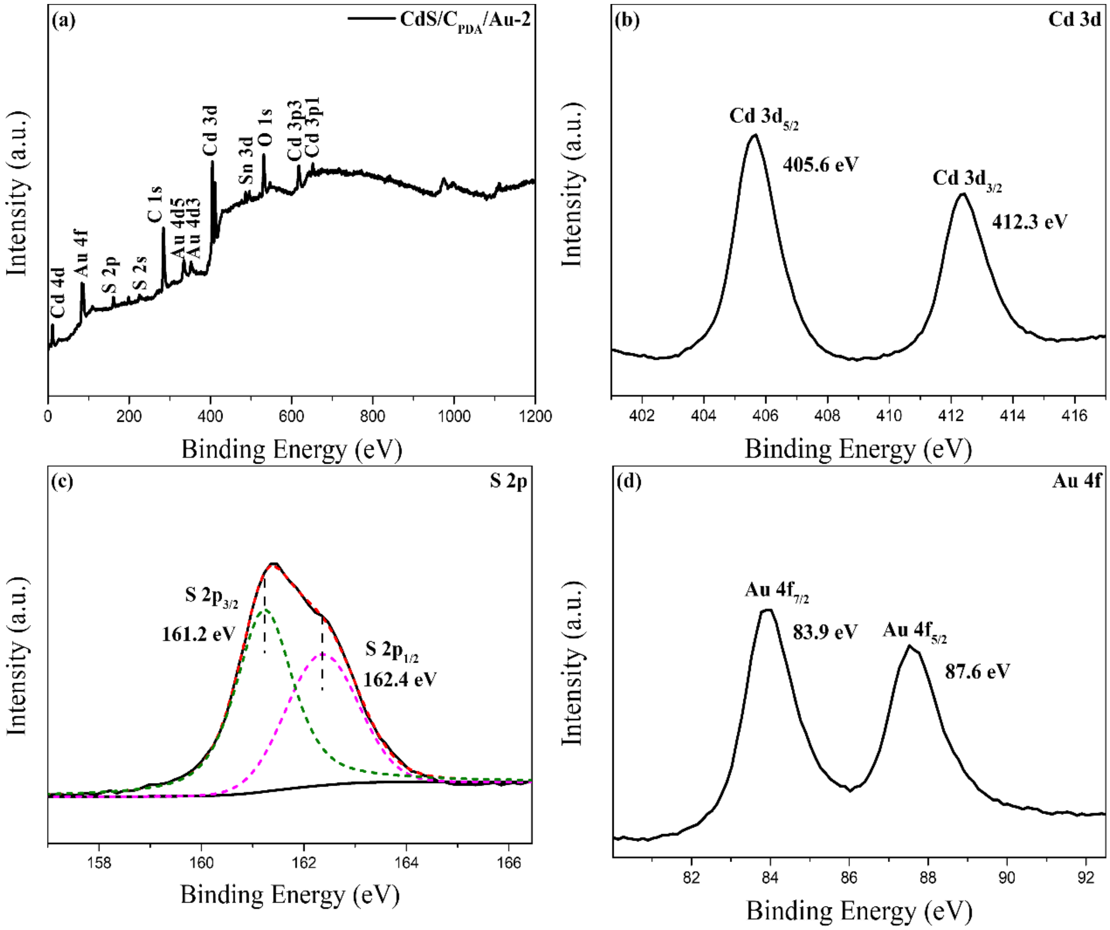

Figure C5.2 (a) The XPS survey spectrum of the CdS/C$_{PDA}$/Au-2 electrode; The high-resolution XPS spectrum of (b) Cd 3d, (c) S 2p and (d) Au 4f.

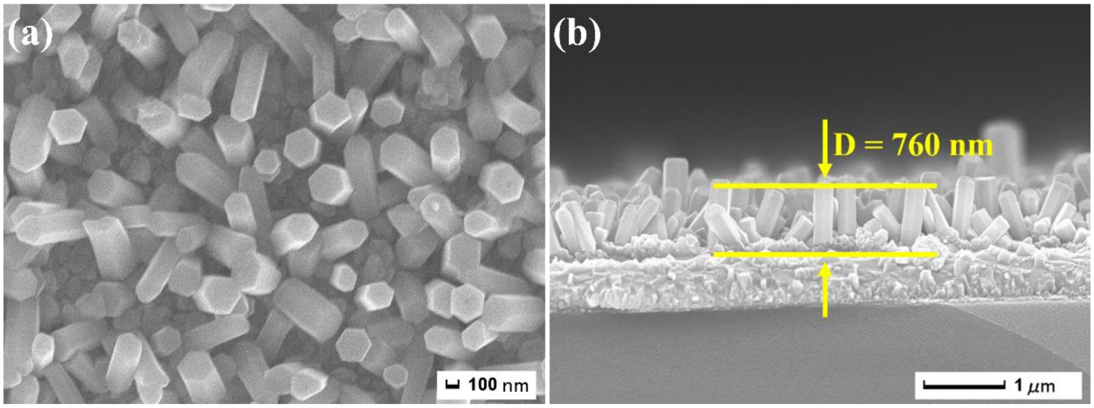

Figure C5.3 (a) The magnified and (b) cross-sectional SEM images of CdS photoanode.

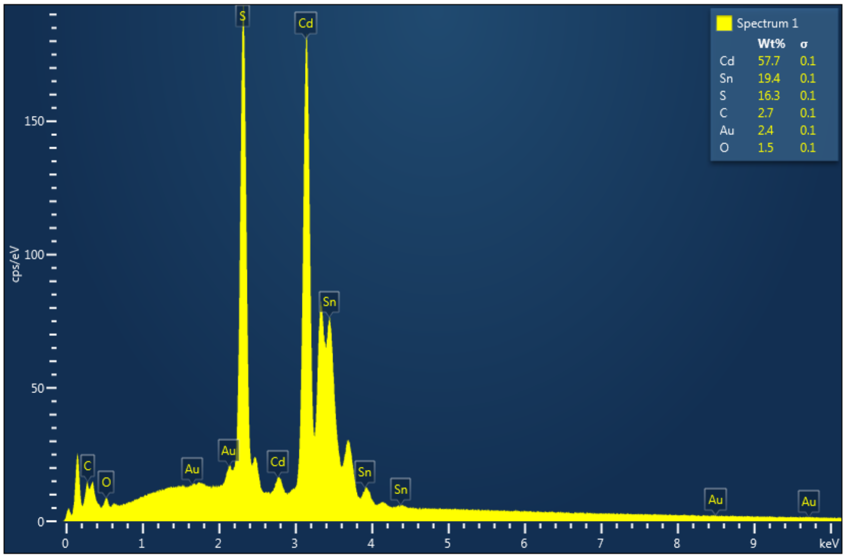

	Wt%	σ
Cd	57.7	0.1
Sn	19.4	0.1
S	16.3	0.1
C	2.7	0.1
Au	2.4	0.1
O	1.5	0.1

Figure C5.4 The EDS analysis of CdS/C_{PDA}/Au-2 sample.

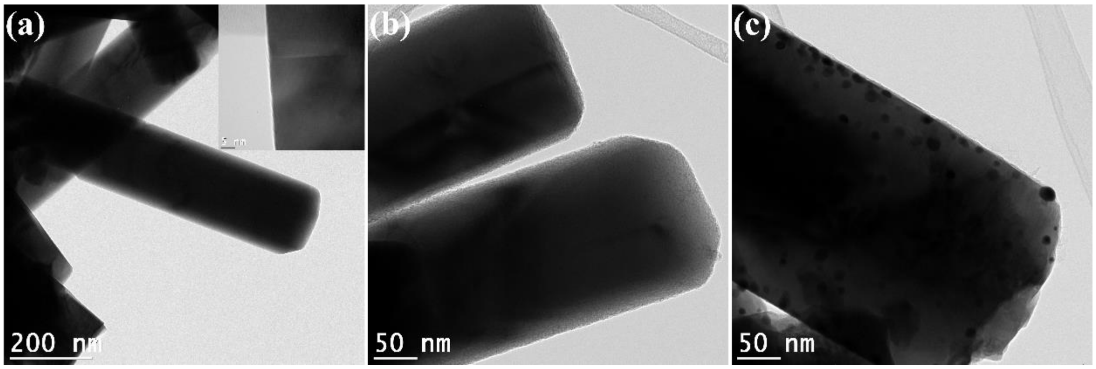

Figure C5.5 The TEM images of (a) bare CdS, (b) CdS/C_{PDA} and (c) CdS/C_{PDA}/Au-2 photoelectrodes.

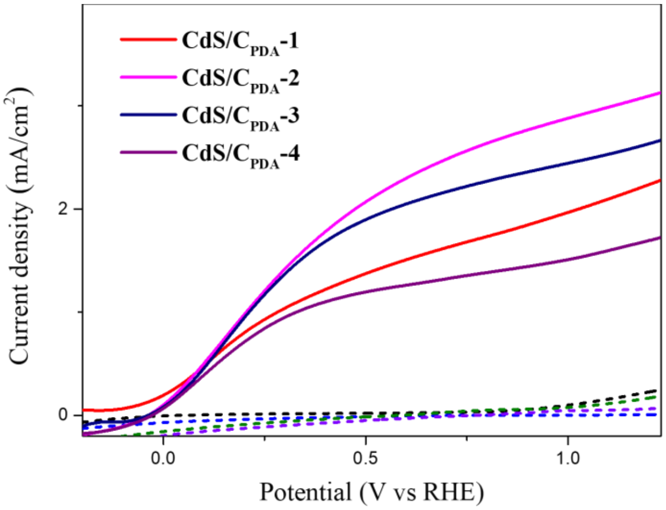

Figure C5.6 The LSV curves of CdS/C_{PDA}-n with controlled DA-polymerization times.

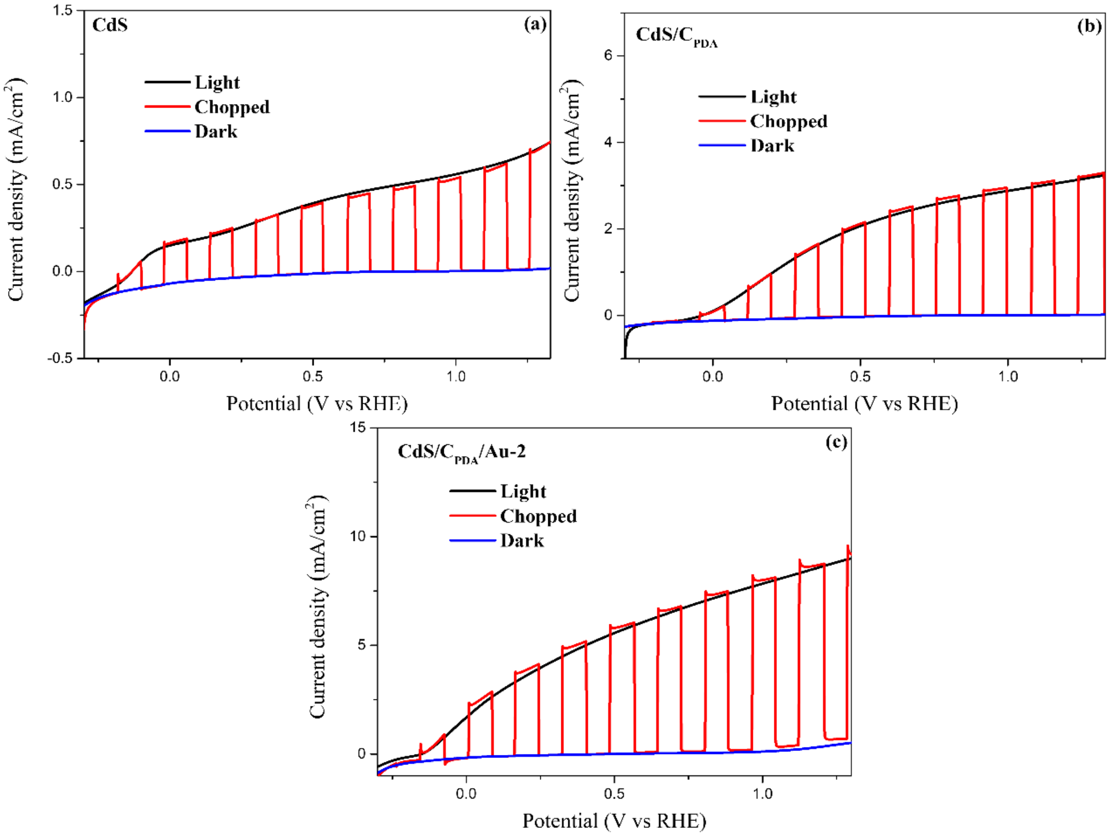

Figure C5.7 The LSV measurements for (a) CdS, (b) CdS/C$_{PDA}$ and (c) CdS/C$_{PDA}$/Au-2 under darkness, continuous and chopped solar illumination.

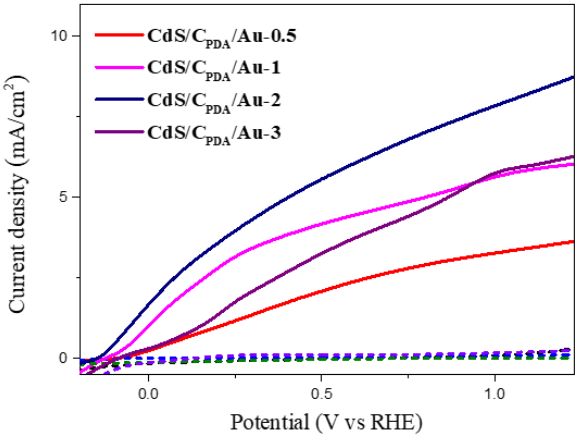

Figure C5.8 The LSV curves of CdS/C$_{PDA}$/Au-n photoanodes with different loading amount of Au NPs.

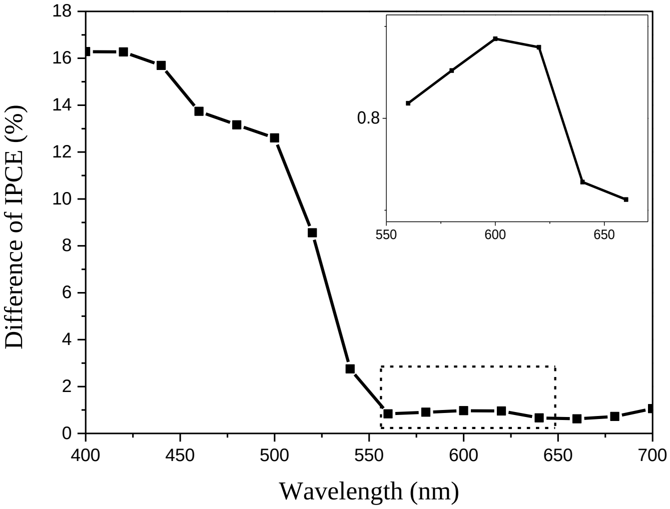

Figure C5.9 The IPCE difference between CdS/C_{PDA} and CdS/C_{PDA}/Au-2

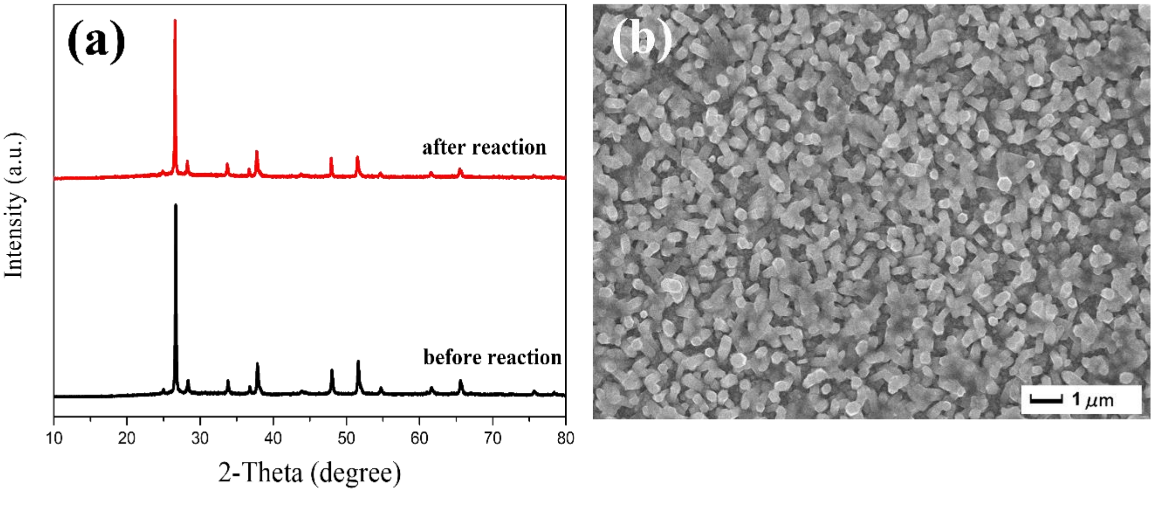

Figure C5.10 The XRD (a) and SEM result (b) over CdS/C_{PDA}/Au photoelectrode before and after durability tests.

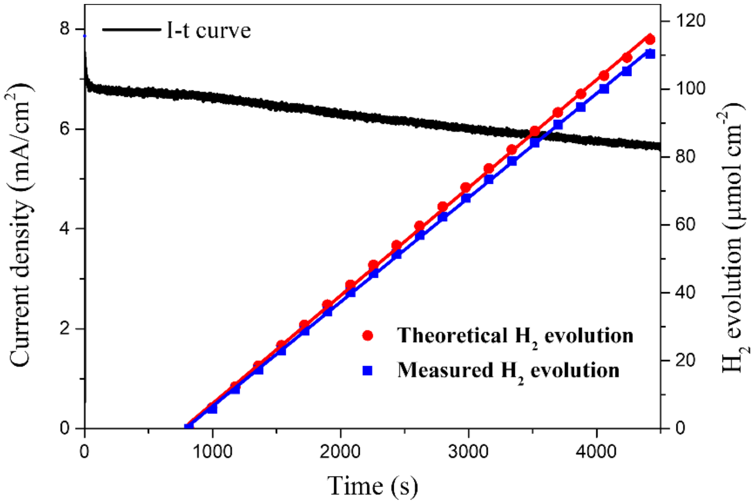

Figure C5.11 H_2 evolution over CdS/C_{PDA}/Au-2 sample as a function of time at 0 V vs Ag/AgCl under AM 1.5 G illumination (working surface area ~ 1 cm^2). Theoretical H_2 evolution is also calculated from the above chronoamperometric photoelectrolysis measurement (I-t curve).

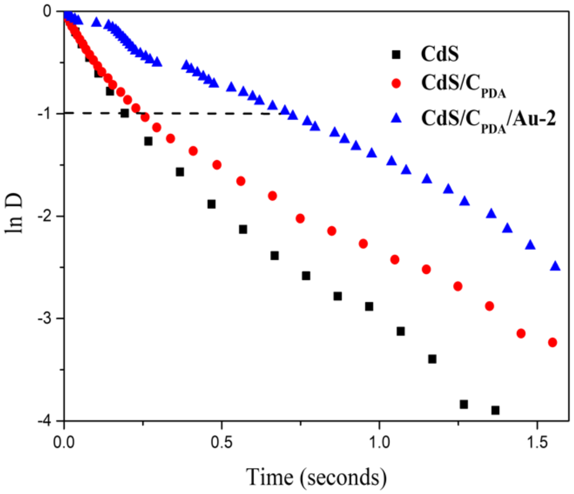

Figure C5.12 The normalized plots of ln D vs time for bare CdS, CdS/C_{PDA} and CdS/C_{PDA}/Au-2 photoelectrodes at 0 V vs Ag/AgCl.

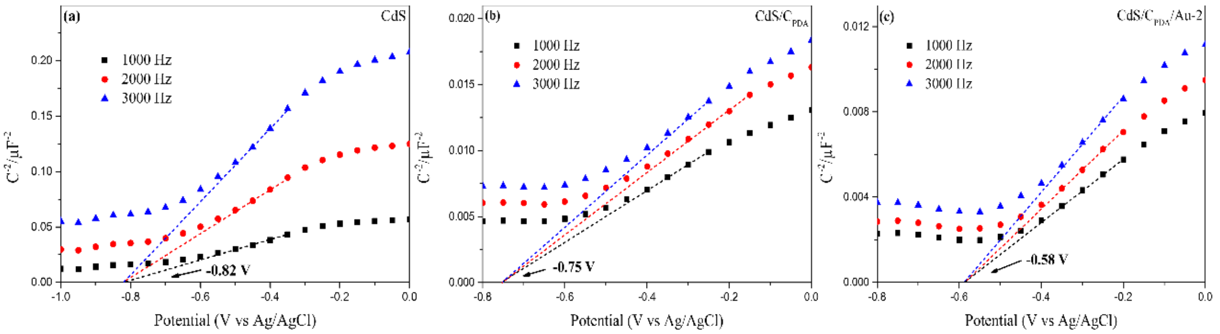

Figure C5.13 Mott-Schottky plots of as-prepared CdS, CdS/C$_{PDA}$ and CdS/C$_{PDA}$/Au-2 photoanodes at the frequency of 1 kHz, 2 kHz and 3kHz in darkness within the potential of -1-0 V vs Ag/AgCl.

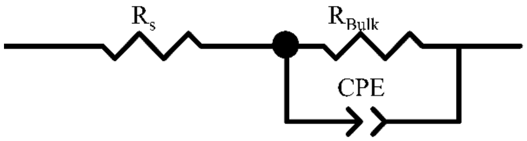

Figure C5.14 Equivalent circuit from EIS curve.

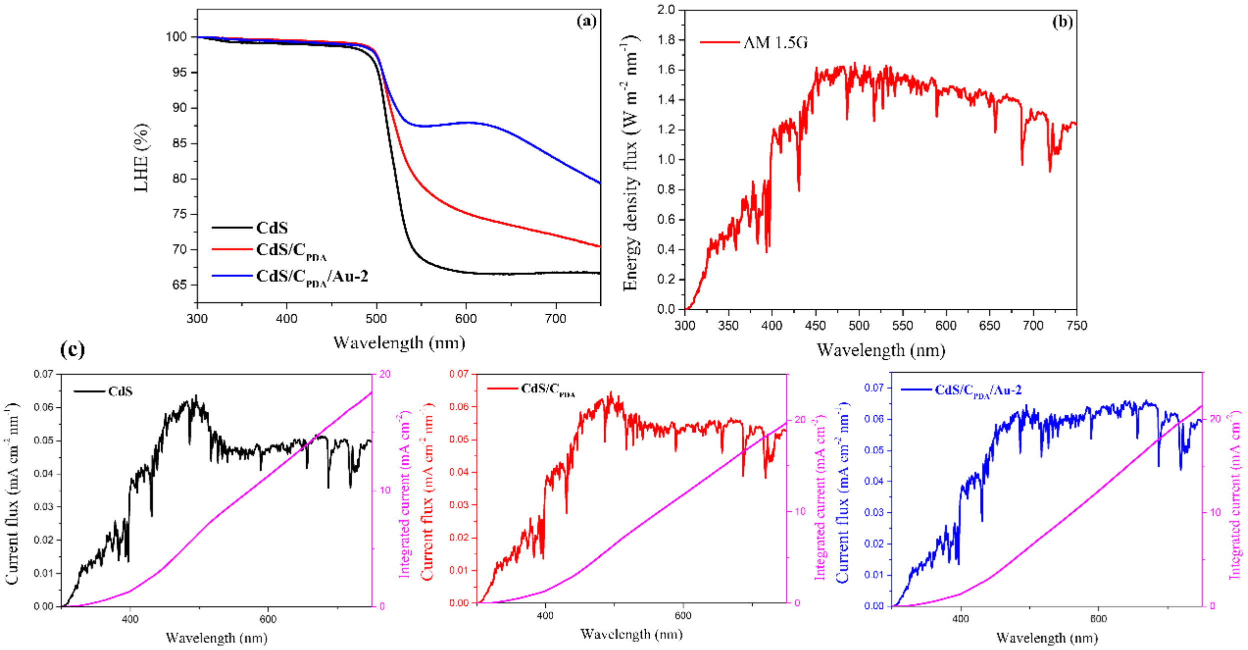

Figure C5.15 (a) LHE plots of bare CdS, CdS/C$_{PDA}$ and CdS/C$_{PDA}$/Au-2 photoanode; (b) The energy density flux of AM 1.5G; (c) The calculated J_{Max} values of bare CdS, CdS/C$_{PDA}$ and CdS/C$_{PDA}$/Au-2 photoanode.

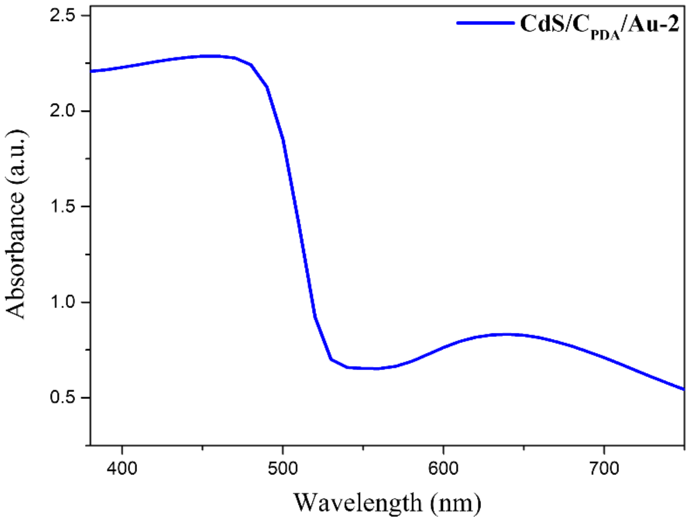

Figure C5.16 The simulated absorption spectrum of CdS/C_{PDA}/Au-2 electrode.

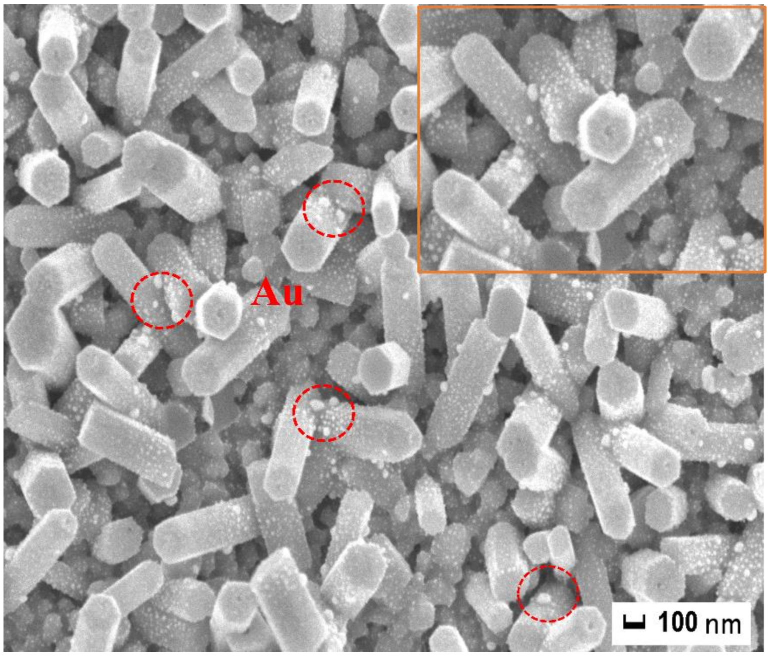

Figure C5.17 The SEM image of the CdS/Au photoelectrode.

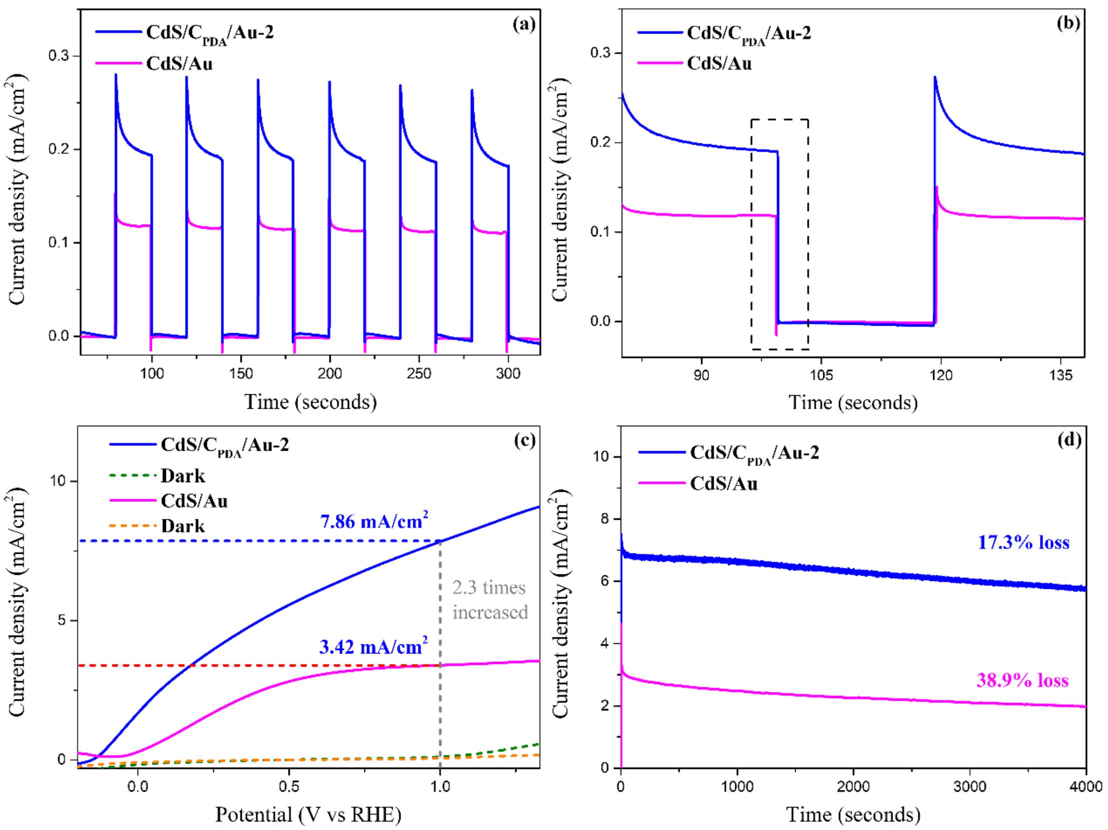

Figure C5.18 (a) chronoamperometric I-t measurements over CdS/Au and CdS/C$_{PDA}$/Au-2 photoanode under simulated solar light irradiation equipped with a 600 nm long-wave-pass filter.; (b) Partially enlarged I-t curves; (c) LSV curves under darkness and one sun irradiation (100 mW/cm^2); (d) Photostability and durability measurement at 0 V vs Ag/AgCl.

Table C5.1 The overpotentials and the corresponding photocurrent densities (at 1.23 V vs RHE) of as-obtained photoanodes under simulated solar light illumination.

Photoanodes	Overpotentials (V vs RHE)	Photocurrent densities (mA/cm^2) at 1.23 V vs RHE
CdS	-0.117	0.69
CdS/C$_{PDA}$	-0.016	3.12
CdS/C$_{PDA}$/Au-2	-0.142	8.74

Table C5.2 The PEC water splitting performance over previously reported CdS-based photoanodes.

Photoanodes	Light source and intensity	Electrolyte	photocurrent density	Ref.
β-Ni(OH)$_2$@CdS nanorod array	λ ≥ 420 nm 100 mW cm^{-2}	5 M NaOH + 10 vol% ethanol	1.2 mA cm^{-2} (0 V vs Ag/AgCl)	238
CdS@Ni$_3$S$_2$ core-shell nanorod	λ ≥ 400 nm 300 W Xe lamp	0.3 M NaS$_2$ + 0.2 M Na$_2$SO$_3$	5.8 mA cm^{-2} (-0.6 V vs Ag/AgCl)	158
ZnO/Au/CdS heterostructure	150 W Xe lamp 75 mW cm^{-2}	0.25 M NaS$_2$ + 0.35 M Na$_2$SO$_3$	3.8 mA cm^{-2} (0 V vs Ag/AgCl)	265
CdS/CdSe core-shell nanorod	AM 1.5G 100 mW cm^{-2}	0.5 M Na$_2$SO$_3$	5.8 mA cm^{-2} (0.7 V vs Ag/AgCl)	150
CdS/Cu$_2$O p-n heterostructure	300 W Xe lamp 100 mW cm^{-2}	0.25 M NaS$_2$ + 0.35 M Na$_2$SO$_3$	4.2 mA cm^{-2} (0 V vs Ag/AgCl)	229
CdS/ZnFe$_2$O$_4$/Cu$_2$O nanorod	visible light 100 mW cm^{-2}	0.35 M NaS$_2$ + 0.25 M Na$_2$SO$_3$	3.3 mA cm^{-2} (0 V vs Ag/AgCl)	195
Z-scheme CdS/CdO nanorod	AM 1.5G 100 mW cm^{-2}	0.35 M NaS$_2$ + 0.25 M Na$_2$SO$_3$	4.35 mA cm^{-2} (0 V vs SCE)	135
TiO$_2$@CdO/CdS nanorod array	AM 1.5G 100 mW cm^{-2}	0.3 M NaS$_2$ + 0.2 M Na$_2$SO$_3$	3.2 mA cm^{-2} (0 V vs RHE)	93
CdS/ZnS core–shell nanorod	AM 1.5G 100 mW cm^{-2}	0.25 M NaS$_2$ + 0.35 M Na$_2$SO$_3$	7.8 mA cm^{-2} (0 V vs SCE)	300
Bi$_2$S$_3$/CdS/TiO$_2$ nanotube array	AM 1.5G 100 mW cm^{-2}	0.25 M NaS$_2$ + 0.35 M Na$_2$SO$_3$	2.16 mA cm^{-2} (0 V vs Ag/AgCl)	299
CdS/C$_{PDA}$/Au nanorod array	AM 1.5G 100 mW cm^{-2}	0.25 M NaS$_2$ + 0.35 M Na$_2$SO$_3$	7.4 mA cm^{-2} (0 V vs Ag/AgCl)	This work

Table C5.3 The flat-band potentials (E_{fb}) and carrier densities (N_D) of different photoelectrodes.

Photoelectrode	CdS	CdS/C$_{PDA}$	CdS/C$_{PDA}$/Au
E_{fb} (V vs Ag/AgCl)	-0.82	-0.75	-0.58
N_D (cm^{-3})	1.4 × 10^{18}	7.9 × 10^{18}	1.2 × 10^{19}

LIST OF PUBLICATIONS

Articles published in peer-revies journals:

1. **Z. Peng**, Y. Su, M. Jafari, M. Siaj. Engineering interfacial band hole extraction on chemical-vapor-deposited MoS_2/CdS core-shell heterojunction photoanode: The junction thickness effects on photoelectrochemical performance, *J. Mater. Sci. Technol.* 167 (2023) 107-118.
2. **Z. Peng**, Y. Su, M. Siaj, Encapsulation of tin oxide layers on gold nanoparticles decorated one-dimensional CdS nanoarrays for pure Z-scheme photoanodes towards solar hydrogen evolution, *Appl. Catal. B: Environ.* 330 (2023) 122614.
3. **Z. Peng**, J. Zhang, P. Liu, J. Claverie, M. Siaj, One-dimensional CdS/carbon/Au plasmonic nanoarray photoanodes via in situ reduction–graphitization approach toward efficient solar hydrogen evolution, *ACS Appl. Mater. Interfaces* 13 (2021) 34658-34670.
4. **Z. Peng**, Y. Su, I. Ennaji, A. Khojastehnezhad, M. Siaj, Encapsulation of few-layered MoS_2 on electrochemical-treated BiVO4 nanoarray photoanode: Simultaneously improved charge separation and hole extraction towards efficient photoelectrochemical water splitting, *J. Chem. Eng.* 477 (2023) 147082.
5. S. Poorahong, C. Somnin, I. Malam Mahamadou, C. Dubois, S. Chergui, **Z. Peng**, Y. Su, T. Xuan Tran, C. Thammakhet-Buranachai, A. Mazzah, Nanoporous graphite-like membranes decorated with $MoSe_2$ nanosheets for hydrogen evolution, *ACS Appl. Nano Mater.* 5 (2022) 2769-2778.
6. A. Khojastehnezhad, G. Hichem, J. Maziar, **Z. Peng**, M. Siaj. Size-Dependent Catalytic Activity of Palladium Nanoparticles Decorated on Core-Shell Magnetic Microporous Organic Networks, *ACS Appl. Nano Mater.* 6 (2023) 17706-17717
7. A. Khojastehnezhad, R. Khaled, S. Mohammad, G. Hichem, **Z. Peng,** S. Samaneh, S. Ahmad, T. Rachid, H. Belkheir, E. Hani, M. Siaj. Rapid, Mild and Catalytic Synthesis of 2D and 3D COFs with Promising Supercapacitor Applications, *ACS Appl. Energy Mater, Accepted.*
8. P. Liu, A. Dörfler, A.A. Tabrizi, L. Skokan, D. Rawach, P. Wang, **Z. Peng,** J. Zhang, A.P. Ruediger, J.P. Claverie, In Operando Photoswitching of Cu Oxidation States in Cu-Based Plasmonic Heterogeneous Photocatalysis for Efficient H_2 Evolution, ACS Appl. Mater. Interfaces (2023).
9. **Z. Peng**, Y. Jiang, X. Wang, R. Zhang, H. Xu, Y. Xiao, X. Jing, J. Zhang, Y. Liu, L. Ni, Novel $CdIn_2S_4$ nano-octahedra/TiO_2 hollow hybrid heterostructure: In-situ synthesis, synergistic effect and enhanced dual-functional photocatalytic activities, Ceram. Int. 45 (2019) 15942-15953.
10. **Z. Peng**, Y. Jiang, Y. Xiao, H. Xu, W. Zhang, L. Ni, $CdIn_2S_4$ surface-decorated Ta_3N_5 core-shell

heterostructure for improved spatial charge transfer: In-situ growth, synergistic effect and efficient dual-functional photocatalytic performance, Appl. Surf. Sci. 487 (2019) 1084-1095.

11. Y. Xiao, **Z. Peng**, S. Zhang, Y. Jiang, X. Jing, X. Yang, J. Zhang, L. Ni, Z-scheme $CdIn_2S_4$/BiOCl nanosheet face-to-face heterostructure: In-situ synthesis and enhanced interfacial charge transfer for high-efficient photocatalytic performance, J. Mater. Sci. 54 (2019) 9573-9590.
12. Y. Xiao, **Z. Peng**, W. Zhang, Y. Jiang, L. Ni, Self-assembly of Ag_2O quantum dots on the surface of $ZnIn_2S_4$ nanosheets to fabricate p-n heterojunctions with wonderful bifunctional photocatalytic performance, Appl. Surf. Sci. 494 (2019) 519-531.
13. Y. Jiang, **Z. Peng**, F. Wu, Y. Xiao, X. Jing, L. Wang, Z. Liu, J. Zhang, Y. Liu, L. Ni, A novel 3D/2D $CdIn_2S_4$ nano-octahedron/ZnO nanosheet heterostructure: Facile synthesis, synergistic effect and enhanced tetracycline hydrochloride photodegradation mechanism, Dalton Trans. 47 (2018) 8724-8737. (Supervisor as the first author)
14. Y. Jiang, **Z. Peng**, S. Zhang, F. Li, Z. Liu, J. Zhang, Y. Liu, K. Wang, Facile in-situ Solvothermal Method to synthesize double shell $ZnIn_2S_4$ nanosheets/TiO_2 hollow nanosphere with enhanced photocatalytic activities, Ceram. Int. 44 (2018) 6115-6126. (Supervisor as the first author)
15. Y. Jiang, X. Jing, K. Zhu, **Z. Peng**, J. Zhang, Y. Liu, W. Zhang, L. Ni, Z. Liu, Ta_3N_5 nanoparticles/TiO_2 hollow sphere (0D/3D) heterojunction: facile synthesis and enhanced photocatalytic activities of levofloxacin degradation and H_2 evolution, Dalton Trans. 47 (2018) 13113-13125.
16. Y. Jiang, P. Liu, S. Tian, Y. Liu, **Z. Peng**, F. Li, L. Ni, Z. Liu, Sustainable visible-light-driven Z-scheme porous $Zn_3(VO_4)_2$/g-C_3N_4 heterostructure toward highly photoredox pollutant and mechanism insight, J. Taiwan Inst. Chem. Eng. 78 (2017) 517-529.

Conference Presentations :

1. Quebec Centre for Advanced Materials Annual Meeting – 7th edition, May 2023, oral presentation.
2. Quebec Centre for Advanced Materials Annual Meeting – 5th edition, 2021, poster presentation.

Awards and Honors:

1. CSC Scholarship (2019-2023) provided by China Scholarship Council.
2. RBC Royal Band scholarship-Doctorate Scholarship (2021).

BIBLIOGRAPHIE

(1) Ashraf, M.; Ayaz, M.; Khan, M.; Adil, S. F.; Farooq, W.; Ullah, N.; Nawaz Tahir, M. Recent Trends in Sustainable Solar Energy Conversion Technologies: Mechanisms, Prospects, and Challenges. *Energy Fuels* **2023,** *37* (9), 6283-6301.

(2) Smil, V. *Energy Transitions: Global and National Perspectives*, Bloomsbury Publishing USA: **2016**.

(3) Poizot, P.; Dolhem, F. Clean Energy New Deal for a Sustainable World: From Non-CO_2 Generating Energy Sources to Greener Electrochemical Storage Devices. *Energy Environ. Sci.* **2011,** *4* (6), 2003-2019.

(4) Wang, X.; Lu, Y.; Chen, C.; Yi, X.; Cui, H. Total-Factor Energy Efficiency of Ten Major Global Energy-Consuming Countries. *J. Environ. Sci.* **2024,** *137*, 41-52.

(5) Martens, J. A.; Bogaerts, A.; De Kimpe, N.; Jacobs, P. A.; Marin, G. B.; Rabaey, K.; Saeys, M.; Verhelst, S. The Chemical Route to a Carbon *Dioxide* Neutral World. *ChemSusChem* **2017,** *10* (6), 1039-1055.

(6) Seh, Z. W.; Kibsgaard, J.; Dickens, C. F.; Chorkendorff, I.; Nørskov, J. K.; Jaramillo, T. F. Combining Theory and Experiment in Electrocatalysis: Insights into Materials Design. *Science* **2017,** *355* (6321), eaad4998.

(7) Satyapal, S. In *Us Department of Energy Hydrogen and Fuel Cell Technologies Office and Global Perspectives*, Presentation at the Innovation for Cool Earth Forum (ICEF) 7th Annual Meeting (virtual), **2020**.

(8) Liu, J.; Luo, Z.; Mao, X.; Dong, Y.; Peng, L.; Sun-Waterhouse, D.; Kennedy, J. V.; Waterhouse, G. I. Recent Advances in Self-Supported Semiconductor Heterojunction Nanoarrays as Efficient Photoanodes for Photoelectrochemical Water Splitting. *Small* **2022,** *18* (48), 2204553.

(9) Clarizia, L.; Nadagouda, M. N.; Dionysiou, D. D. Recent Advances and Challenges of Photoelectrochemical Cells for Hydrogen Production. *Curr. Opin. Green Sustain. Chem.* **2023,** *41*, 100825.

(10) Bullock, M.; More, K. *Basic Energy Sciences Roundtable: Foundational Science for Carbon-Neutral Hydrogen Technologies*; USDOE Office of Science (SC), Basic Energy Sciences (BES): **2021**.

(11) Wu, X.-Y.; Luo, Y.; Hess, F.; Lipiński, W., Sustainable Hydrogen for Energy, Fuel and Commodity Applications. Frontiers Media SA: **2021**; Vol. 9, p 698669.

(12) Kim, J. H.; Hansora, D.; Sharma, P.; Jang, J.-W.; Lee, J. S. Toward Practical Solar Hydrogen Production–an Artificial Photosynthetic Leaf-to-Farm Challenge. *Chem. Soc. Rev.* **2019,** *48* (7), 1908-1971.

(13) Hisatomi, T.; Kubota, J.; Domen, K. Recent Advances in Semiconductors for Photocatalytic and Photoelectrochemical Water Splitting. *Chem. Soc. Rev.* **2014,** *43* (22), 7520-7535.

(14) Lewis, N. S.; Nocera, D. G. Powering the Planet: Chemical Challenges in Solar Energy Utilization. *PNAS* **2006,** *103* (43), 15729-15735.

(15) Zhao, Y.; Niu, Z.; Zhao, J.; Xue, L.; Fu, X.; Long, J. Recent Advancements in Photoelectrochemical Water Splitting for Hydrogen Production. *EER* **2023,** *6* (1), 14.

(16) Li, X.-B.; Tung, C.-H.; Wu, L.-Z. Semiconducting Quantum Dots for Artificial Photosynthesis. *Nat. Rev. Chem.* **2018,** *2* (8), 160-173.

(17) Walter, M. G.; Warren, E. L.; McKone, J. R.; Boettcher, S. W.; Mi, Q.; Santori, E. A.; Lewis, N. S. Solar Water Splitting Cells. *Chem. Rev.* **2010,** *110* (11), 6446-6473.

(18) Yang, W.; Prabhakar, R. R.; Tan, J.; Tilley, S. D.; Moon, J. Strategies for Enhancing the Photocurrent, Photovoltage, and Stability of Photoelectrodes for Photoelectrochemical Water Splitting. *Chem. Soc. Rev.* **2019,** *48* (19), 4979-5015.

(19) Chen, S.; Takata, T.; Domen, K. Particulate Photocatalysts for Overall Water Splitting. *Nat. Rev. Mater.* **2017,** *2* (10), 1-17.

(20) Liu, J.; Liu, Y.; Liu, N.; Han, Y.; Zhang, X.; Huang, H.; Lifshitz, Y.; Lee, S.-T.; Zhong, J.; Kang, Z. Metal-Free Efficient Photocatalyst for Stable Visible Water Splitting Via a Two-Electron Pathway. *Science* **2015,** *347* (6225), 970-974.

(21) Jia, J.; Seitz, L. C.; Benck, J. D.; Huo, Y.; Chen, Y.; Ng, J. W. D.; Bilir, T.; Harris, J. S.; Jaramillo, T. F. Solar Water Splitting by Photovoltaic-Electrolysis with a Solar-to-Hydrogen Efficiency over 30%. *Nat. Commun.* **2016,** *7* (1), 13237.

(22) Cheng, W.-H.; Richter, M. H.; May, M. M.; Ohlmann, J.; Lackner, D.; Dimroth, F.; Hannappel, T.; Atwater, H. A.; Lewerenz, H.-J. Monolithic Photoelectrochemical Device for Direct Water Splitting with 19% Efficiency. *ACS Energy Letters* **2018,** *3* (8), 1795-1800.

(23) Kang, D.; Young, J. L.; Lim, H.; Klein, W. E.; Chen, H.; Xi, Y.; Gai, B.; Deutsch, T. G.; Yoon, J. Printed Assemblies of Gaas Photoelectrodes with Decoupled Optical and Reactive Interfaces for Unassisted Solar Water Splitting. *Nature Energy* **2017,** *2* (5), 1-5.

(24) Song, H.; Luo, S.; Huang, H.; Deng, B.; Ye, J. Solar-Driven Hydrogen Production: Recent Advances, Challenges, and Future Perspectives. *ACS Energy Letters* **2022,** *7* (3), 1043-1065.

(25) Lewis, N. S. Research Opportunities to Advance Solar Energy Utilization. *Science* **2016,** *351* (6271), aad1920.

(26) Pinaud, B. A.; Benck, J. D.; Seitz, L. C.; Forman, A. J.; Chen, Z.; Deutsch, T. G.; James, B. D.; Baum, K. N.; Baum, G. N.; Ardo, S. Technical and Economic Feasibility of Centralized Facilities for Solar Hydrogen Production Via Photocatalysis and Photoelectrochemistry. *Energy Environ. Sci.* **2013,** *6* (7), 1983-2002.

(27) Levene, J. I.; Mann, M. K.; Margolis, R. M.; Milbrandt, A. An Analysis of Hydrogen Production from Renewable Electricity Sources. *Solar energy* **2007,** *81* (6), 773-780.

(28) Grätzel, M. Photoelectrochemical Cells. *Nature* **2001,** *414* (6861), 338-344.

(29) Boddy, P. Oxygen Evolution on Semiconducting TiO_2. *J. Electrochem. Soc.* **1968,** *115* (2), 199.

(30) Fujishima, A.; Honda, K. Electrochemical Photolysis of Water at a Semiconductor Electrode. *Nature* **1972,** *238* (5358), 37-38.

(31) Mayer, M. T. Photovoltage at Semiconductor–Electrolyte Junctions. *Curr. Opin. Electrochem.* **2017,** *2* (1), 104-110.

(32) Peng, K.; Wang, X.; Lee, S.-T. Silicon Nanowire Array Photoelectrochemical Solar Cells. *Appl. Phys. Lett.* **2008,** *92* (16).

(33) Jiang, C.; Moniz, S. J.; Wang, A.; Zhang, T.; Tang, J. Photoelectrochemical Devices for Solar Water Splitting–Materials and Challenges. *Chem. Soc. Rev.* **2017,** *46* (15), 4645-4660.

(34) Tachibana, Y.; Vayssieres, L.; Durrant, J. R. Artificial Photosynthesis for Solar Water-Splitting. *Nat. Photonics* **2012,** *6* (8), 511-518.

(35) Hensel, J.; Wang, G.; Li, Y.; Zhang, J. Z. Synergistic Effect of CdSe Quantum Dot Sensitization and Nitrogen Doping of TiO_2 Nanostructures for Photoelectrochemical Solar Hydrogen Generation. *Nano Lett.* **2010,** *10* (2), 478-483.

(36) Adhikari, R.; Jin, L.; Navarro-Pardo, F.; Benetti, D.; AlOtaibi, B.; Vanka, S.; Zhao, H.; Mi, Z.; Vomiero, A.; Rosei, F. High Efficiency, Pt-Free Photoelectrochemical Cells for Solar Hydrogen Generation Based on "Giant" Quantum Dots. *Nano Energy* **2016,** *27*, 265-274.

(37) Clarizia, L.; Spasiano, D.; Di Somma, I.; Marotta, R.; Andreozzi, R.; Dionysiou, D. D. Copper Modified-TiO_2 Catalysts for Hydrogen Generation through Photoreforming of Organics. A Short Review. *Int. J. Hydrogen Energy* **2014,** *39* (30), 16812-16831.

(38) Joy, J.; Mathew, J.; George, S. C. Nanomaterials for Photoelectrochemical Water Splitting–Review. *Int. J. Hydrogen Energy* **2018,** *43* (10), 4804-4817.

(39) He, Y.; Hamann, T.; Wang, D. Thin Film Photoelectrodes for Solar Water Splitting. *Chem. Soc. Rev.* **2019,** *48* (7), 2182-2215.

(40) Khanna, V. K. Carrier Lifetimes and Recombination–Generation Mechanisms in Semiconductor Device Physics. *Eur. J. Phys.* **2004,** *25* (2), 221.

(41) Cesar, I.; Sivula, K.; Kay, A.; Zboril, R.; Grätzel, M. Influence of Feature Size, Film Thickness, and Silicon Doping on the Performance of Nanostructured Hematite Photoanodes for Solar Water Splitting. *J. Phys. Chem. C* **2009,** *113* (2), 772-782.

(42) Gärtner, W. W. Depletion-Layer Photoeffects in Semiconductors. *Physical Review* **1959,** *116* (1), 84.

(43) Peter, L. M.; Wijayantha, K. U.; Tahir, A. A. Kinetics of Light-Driven Oxygen Evolution at α-Fe_2O_3 Electrodes. *Faraday Discuss.* **2012,** *155*, 309-322.

(44) Sonnet, A. M.; Hinkle, C. L.; Heh, D.; Bersuker, G.; Vogel, E. M. Impact of Semiconductor and Interface-State Capacitance on Metal/high-k/GaAs Capacitance–Voltage Characteristics. *IEEE Trans. Electron Devices* **2010,** *57* (10), 2599-2606.

(45) Sivula, K.; Zboril, R.; Le Formal, F.; Robert, R.; Weidenkaff, A.; Tucek, J.; Frydrych, J.; Gratzel, M. Photoelectrochemical Water Splitting with Mesoporous Hematite Prepared by a Solution-Based Colloidal Approach. *J. Am. Chem. Soc.* **2010,** *132* (21), 7436-7444.

(46) Meng, L.; Rao, D.; Tian, W.; Cao, F.; Yan, X.; Li, L. Simultaneous Manipulation of O-Doping and Metal Vacancy in Atomically Thin $Zn_{10}In_{16}S_{34}$ Nanosheet Arrays toward Improved Photoelectrochemical Performance. *Angew. Chem. Int. Ed.* **2018,** *57* (51), 16882-16887.

(47) Zhang, Y.; Li, Y.; Ni, D.; Chen, Z.; Wang, X.; Bu, Y.; Ao, J. P. Improvement of $BiVO_4$ Photoanode Performance During Water Photo-Oxidation Using Rh-Doped $SrTiO_3$ Perovskite as a Co-Catalyst. *Adv. Funct. Mater.* **2019,** *29* (32), 1902101.

(48) Gangwar, J.; Gupta, B. K.; Tripathi, S. K.; Srivastava, A. K. Phase Dependent Thermal and Spectroscopic Responses of Al_2O_3 Nanostructures with Different Morphogenesis. *Nanoscale* **2015,** *7* (32), 13313-13344.

(49) Qiu, Y.; Liu, W.; Chen, W.; Chen, W.; Zhou, G.; Hsu, P.-C.; Zhang, R.; Liang, Z.; Fan, S.; Zhang, Y. Efficient Solar-Driven Water Splitting by Nanocone $BiVO_4$-Perovskite Tandem Cells. *Science Advances* **2016,** *2* (6), e1501764.

(50) Li, Y.; Liu, Z.; Guo, Z.; Ruan, M.; Li, X.; Liu, Y. Efficient WO_3 Photoanode Modified by Pt Layer and Plasmonic Ag for Enhanced Charge Separation and Transfer to Promote Photoelectrochemical Performances. *ACS Sustain. Chem. Eng.* **2019,** *7* (14), 12582-12590.

(51) Li, S.; Xu, W.; Meng, L.; Tian, W.; Li, L. Recent Progress on Semiconductor Heterojunction-Based Photoanodes for Photoelectrochemical Water Splitting. *Small Science* **2022,** *2* (5), 2100112.

(52) Chen, F.; Deng, Z.; Li, X.; Zhang, J.; Zhao, J. Visible Light Detoxification by 2, 9, 16, 23-Tetracarboxyl Phthalocyanine Copper Modified Amorphous Titania. *Chem. Phys. Lett.* **2005,** *415* (1-3), 85-88.

(53) Lin, H.; Long, X.; An, Y.; Zhou, D.; Yang, S. Three-Dimensional Decoupling Co-Catalyst from a Photoabsorbing Semiconductor as a New Strategy to Boost Photoelectrochemical Water Splitting. *Nano Lett.* **2019,** *19* (1), 455-460.

(54) Yang, J.; Wang, D.; Han, H.; Li, C. Roles of Cocatalysts in Photocatalysis and Photoelectrocatalysis. *Acc. Chem. Res.* **2013,** *46* (8), 1900-1909.

(55) Wang, H.; Zhang, L.; Chen, Z.; Hu, J.; Li, S.; Wang, Z.; Liu, J.; Wang, X. Semiconductor Heterojunction Photocatalysts: Design, Construction, and Photocatalytic Performances. *Chem. Soc. Rev.* **2014,** *43* (15), 5234-5244.

(56) Zhou, H.; Qu, Y.; Zeid, T.; Duan, X. Towards Highly Efficient Photocatalysts Using Semiconductor Nanoarchitectures. *Energy Environ. Sci.* **2012,** *5* (5), 6732-6743.

(57) Garnett, E.; Yang, P. Light Trapping in Silicon Nanowire Solar Cells. *Nano Lett.* **2010,** *10* (3), 1082-1087.

(58) Kibria, M.; Mi, Z. Artificial Photosynthesis Using Metal/Nonmetal-Nitride Semiconductors: Current Status, Prospects, and Challenges. *J. Mater. Chem. A* **2016,** *4* (8), 2801-2820.

(59) Gueymard, C. A. The Sun's Total and Spectral Irradiance for Solar Energy Applications and Solar Radiation Models. *Solar energy* **2004,** *76* (4), 423-453.

(60) Kang, Z.; Liu, Y.; Tsang, C. H. A.; Ma, D. D. D.; Fan, X.; Wong, N. B.; Lee, S. T. Water-Soluble Silicon Quantum Dots with Wavelength-Tunable Photoluminescence. *Adv. Mater.* **2009,** *21* (6), 661-664.

(61) Ohmori, T.; Mametsuka, H.; Suzuki, E. Photocatalytic Hydrogen Evolution on InP Suspension with Inorganic Sacrificial Reducing Agent. *Int. J. Hydrogen Energy* **2000,** *25* (10), 953-955.

(62) Costi, R.; Cohen, G.; Salant, A.; Rabani, E.; Banin, U. Electrostatic Force Microscopy Study of Single Au−CdSe Hybrid Nanodumbbells: Evidence for Light-Induced Charge Separation. *Nano Lett.* **2009,** *9* (5), 2031-2039.

(63) Maeda, K.; Takata, T.; Hara, M.; Saito, N.; Inoue, Y.; Kobayashi, H.; Domen, K. Gan: ZnO Solid Solution as a Photocatalyst for Visible-Light-Driven Overall Water Splitting. *J. Am. Chem. Soc.* **2005,** *127* (23), 8286-8287.

(64) Maiolo, J. R.; Kayes, B. M.; Filler, M. A.; Putnam, M. C.; Kelzenberg, M. D.; Atwater, H. A.; Lewis, N. S. High Aspect Ratio Silicon Wire Array Photoelectrochemical Cells. *J. Am. Chem. Soc.* **2007,** *129* (41), 12346-12347.

(65) Dai, P.; Xie, J.; Mayer, M. T.; Yang, X.; Zhan, J.; Wang, D. Solar Hydrogen Generation by Silicon Nanowires Modified with Platinum Nanoparticle Catalysts by Atomic Layer Deposition. *Angew. Chem.* **2013,** *125* (42), 11325-11329.

(66) Wang, W.; Jin, C.; Qi, L. Hierarchical CdS Nanorod@ SnO_2 Nanobowl Arrays for Efficient and Stable Photoelectrochemical Hydrogen Generation. *Small* **2018,** *14* (33), 1801352.

(67) Yang, C.; Wang, Z.; Lin, T.; Yin, H.; Lü, X.; Wan, D.; Xu, T.; Zheng, C.; Lin, J.; Huang, F. Core-Shell Nanostructured "Black" Rutile Titania as Excellent Catalyst for Hydrogen Production Enhanced by Sulfur Doping. *J. Am. Chem. Soc.* **2013,** *135* (47), 17831-17838.

(68) Mayer, M. T.; Du, C.; Wang, D. Hematite/Si Nanowire Dual-Absorber System for Photoelectrochemical Water Splitting at Low Applied Potentials. *J. Am. Chem. Soc.* **2012,** *134* (30), 12406-12409.

(69) Li, Y.; Wang, R.; Li, H.; Wei, X.; Feng, J.; Liu, K.; Dang, Y.; Zhou, A. Efficient and Stable Photoelectrochemical Seawater Splitting with TiO_2@g-C_3N_4 Nanorod Arrays Decorated by Co-Pi. *J. Phys. Chem. C* **2015,** *119* (35), 20283-20292.

(70) Moniz, S. J.; Shevlin, S. A.; Martin, D. J.; Guo, Z.-X.; Tang, J. Visible-Light Driven Heterojunction Photocatalysts for Water Splitting–a Critical Review. *Energy Environ. Sci.* **2015,** *8* (3), 731-759.

(71) San Martín, S.; Rivero, M. J.; Ortiz, I. Unravelling the Mechanisms That Drive the Performance of Photocatalytic Hydrogen Production. *Catalysts* **2020,** *10* (8), 901.

(72) Abdullah, H.; Shuwanto, H.; Lie, J.; Silanpää, M. Critical Parameters and Essential Strategies in Designing Photoanodes to Overcome the Sluggish Water Oxidation Reaction. *J. Environ. Chem. Eng.* **2023**, 109356.

(73) Wang, Y.; Wang, Q.; Zhan, X.; Wang, F.; Safdar, M.; He, J. Visible Light Driven Type II Heterostructures and Their Enhanced Photocatalysis Properties: A Review. *Nanoscale* **2013,** *5* (18), 8326-8339.

(74) Cao, S.; Yan, X.; Kang, Z.; Liang, Q.; Liao, X.; Zhang, Y. Band Alignment Engineering for Improved Performance and Stability of $ZnFe_2O_4$ Modified CdS/ZnO Nanostructured Photoanode for PEC Water Splitting. *Nano Energy* **2016,** *24*, 25-31.

(75) Li, C.; Wang, T.; Luo, Z.; Liu, S.; Gong, J. Enhanced Charge Separation through ALD-Modified Fe_2O_3/Fe_2TiO_5 Nanorod Heterojunction for Photoelectrochemical Water Oxidation. *Small* **2016,** *12* (25), 3415-3422.

(76) Shi, X.; Choi, I. Y.; Zhang, K.; Kwon, J.; Kim, D. Y.; Lee, J. K.; Oh, S. H.; Kim, J. K.; Park, J. H. Efficient Photoelectrochemical Hydrogen Production from Bismuth Vanadate-Decorated Tungsten Trioxide Helix Nanostructures. *Nat. Commun.* **2014,** *5* (1), 4775.

(77) Li, J.; Hoffmann, M. W.; Shen, H.; Fabrega, C.; Prades, J. D.; Andreu, T.; Hernandez-Ramirez, F.; Mathur, S. Enhanced Photoelectrochemical Activity of an Excitonic Staircase in CdS@TiO_2 and CdS @Anatase@ Rutile TiO_2 Heterostructures. *J. Mater. Chem.* **2012,** *22* (38), 20472-20476.

(78) Luo, J.; Ma, L.; He, T.; Ng, C. F.; Wang, S.; Sun, H.; Fan, H. J. TiO_2/(CdS, CdSe, CdSeS) Nanorod Heterostructures and Photoelectrochemical Properties. *J. Phys. Chem. C* **2012,** *116* (22), 11956-11963.

(79) Wang, X.; Yin, L.; Liu, G.; Wang, L.; Saito, R.; Lu, G. Q. M.; Cheng, H.-M. Polar Interface-Induced Improvement in High Photocatalytic Hydrogen Evolution over ZnO–CdS Heterostructures. *Energy Environ. Sci.* **2011,** *4* (10), 3976-3979.

(80) Liu, X.; Wang, C.; Xu, J.; Liu, X.; Zou, R.; Ouyang, L.; Xu, X.; Chen, X.; Xing, H. Fabrication of ZnO/CdS/Cu_2ZnSnS_4 p–n Heterostructure Nanorod Arrays Via a Solution-Based Route. *CrystEngComm* **2013,** *15* (6), 1139-1145.

(81) Peng, Z.; Su, Y.; Jafari, M.; Siaj, M. Engineering Interfacial Band Hole Extraction on Chemical-Vapor-Deposited MoS_2/CdS Core-Shell Heterojunction Photoanode: The Junction Thickness Effects on Photoelectrochemical Performance. *J Mater Sci Technol.* **2023,** *167*, 107-118.

(82) Pihosh, Y.; Turkevych, I.; Mawatari, K.; Asai, T.; Hisatomi, T.; Uemura, J.; Tosa, M.; Shimamura, K.; Kubota, J.; Domen, K. Nanostructured $WO_3/BiVO_4$ Photoanodes for Efficient Photoelectrochemical Water Splitting. *Small* **2014,** *10* (18), 3692-3699.

(83) Fuku, K.; Miyase, Y.; Miseki, Y.; Funaki, T.; Gunji, T.; Sayama, K. Photoelectrochemical Hydrogen Peroxide Production from Water on a $WO_3/BiVO_4$ Photoanode and from O_2 on an Au Cathode without External Bias. *Chem. Asian J.* **2017,** *12* (10), 1111-1119.

(84) Hwang, I.; Seol, M.; Kim, H.; Yong, K. Improvement of Photocurrent Generation of Ag_2S Sensitized Solar Cell through Co-Sensitization with Cds. *Appl. Phys. Lett.* **2013,** *103* (2).

(85) Dong, Q.; Li, M.; Sun, M.; Si, F.; Gao, Q.; Cai, X.; Xu, Y.; Yuan, T.; Zhang, S.; Peng, F. Phase-Controllable Growth Nixpy Modified CdS@ Ni_3S_2 Electrodes for Efficient Electrocatalytic and Enhanced Photoassisted Electrocatalytic Overall Water Splitting. *Small Methods* **2021,** *5* (11), 2100878.

(86) Tang, R.; Zhou, S.; Yuan, Z.; Yin, L. Metal–Organic Framework Derived Co_3O_4/TiO_2/Si Heterostructured Nanorod Array Photoanodes for Efficient Photoelectrochemical Water Oxidation. *Adv. Funct. Mater.* **2017,** *27* (37), 1701102.

(87) Hussain, S.; Patil, S. A.; Memon, A. A.; Vikraman, D.; Naqvi, B. A.; Jeong, S. H.; Kim, H.-S.; Kim, H.-S.; Jung, J. CuS/WS_2 and CuS/MoS_2 Heterostructures for High Performance Counter Electrodes in Dye-Sensitized Solar Cells. *Solar Energy* **2018,** *171*, 122-129.

(88) Qiao, L.; Liao, M.; Fang, K.; He, X.; Zhang, Y. Enhancement of Photoelectrochemical Hydrogen Evolution of p-Type Silicon Nanowires Array by Loading MoS_2. *Silicon* **2019,** *11* (4), 1963-1970.

(89) Gao, L.; Long, X.; Wei, S.; Wang, C.; Wang, T.; Li, F.; Hu, Y.; Ma, J.; Jin, J. Facile Growth of $AgVO_3$ Nanoparticles on Mo-Doped $BiVO_4$ Film for Enhanced Photoelectrochemical Water Oxidation. *Chem. Eng. J.* **2019,** *378*, 122193.

(90) Zuo, Y.; Chen, J.; Yang, H.; Zhang, M.; Wang, Y.; He, G.; Sun, Z. Facile Synthesis of $TiO_2/In_2S_3/CdS$ Ternary Porous Heterostructure Arrays with Enhanced Photoelectrochemical and Visible-Light Photocatalytic Properties. *J. Mater. Chem. C **2019***, *7* (29), 9065-9074.

(91) Kuang, P.-Y.; Zheng, X.-J.; Lin, J.; Huang, X.-B.; Li, N.; Li, X.; Liu, Z.-Q. Facile Construction of Dual P–N Junctions in $CdS/Cu_2O/ZnO$ Photoanode with Enhanced Charge Carrier Separation and Transfer Ability. *ACS omega* **2017,** *2* (3), 852-863.

(92) Zhang, F.; Chen, Y.; Zhou, W.; Ren, C.; Gao, H.; Tian, G. Hierarchical $SnS_2/CuInS_2$ Nanosheet Heterostructure Films Decorated with C_{60} for Remarkable Photoelectrochemical Water Splitting. *ACS Appl. Mater. Interfaces* **2019,** *11* (9), 9093-9101.

(93) Li, C.-H.; Hsu, C.-W.; Lu, S.-Y. TiO_2 Nanocrystals Decorated Z-Schemed Core-Shell CdS-CdO Nanorod Arrays as High Efficiency Anodes for Photoelectrochemical Hydrogen Generation. *J. Colloid Interface Sci.* **2018,** *521*, 216-225.

(94) Khoomortezaei, S.; Abdizadeh, H.; Golobostanfard, M. R. Triple Layer Heterojunction $WO_3/BiVO_4/BiFeO_3$ Porous Photoanode for Efficient Photoelectrochemical Water Splitting. *ACS Appl. Energy Mater.* **2019,** *2* (9), 6428-6439.

(95) Jeong, Y. J.; Hwang, S. W.; Chaikasetsin, S.; Han, H. S.; Cho, I. S. Dual Textured $BiVO_4$/Sb: SnO_2 Heterostructure for Enhanced Photoelectrochemical Water-Splitting. *Chem. Eng. J.* **2022,** *435*, 135183.

(96) Wang, Y.; Chen, C.; Tian, W.; Xu, W.; Li, L. Designing $WO_3/CdIn_2S_4$ Type-II Heterojunction with Both Efficient Light Absorption and Charge Separation for Enhanced Photoelectrochemical Water Splitting. *Nanotechnology* **2019,** *30* (49), 495402.

(97) DİKİCİ, T.; YURDDAŞKAL, M. Nanoyapılı TiO_2 Film Yüzeyinde TiO_2/ZnO Ve TiO_2/CuO Heteroyapıların Oluşturulması Ve Fotokatalitik Aktivitelerinin İncelenmesi. *Erzincan University J. Sci. Technol.* **2019,** *12* (1), 63-73.

(98) Bard, A. J. Photoelectrochemistry and Heterogeneous Photo-Catalysis at Semiconductors. *J. Photochem.* **1979,** *10* (1), 59-75.

(99) Tada, H.; Mitsui, T.; Kiyonaga, T.; Akita, T.; Tanaka, K. All-Solid-State Z-Scheme in CdS–Au–TiO_2 Three-Component Nanojunction System. *Nat. Mater.* **2006,** *5* (10), 782-786.

(100) Yu, J.; Wang, S.; Low, J.; Xiao, W. Enhanced Photocatalytic Performance of Direct Z-Scheme g-C_3N_4–TiO_2 Photocatalysts for the Decomposition of Formaldehyde in Air. *Phys. Chem. Chem. Phys.* **2013,** *15* (39), 16883-16890.

(101) Huang, X.; Wang, J.; Li, T.; Wang, J.; Xu, M.; Yu, W.; El Abed, A.; Zhang, X. Review on Optofluidic Microreactors for Artificial Photosynthesis. *Beilstein J. Nanotechnol.* **2018,** *9* (1), 30-41.

(102) Wen, P.; Sun, Y.; Li, H.; Liang, Z.; Wu, H.; Zhang, J.; Zeng, H.; Geyer, S. M.; Jiang, L. A Highly Active Three-Dimensional Z-Scheme ZnO/Au/g-C_3N_4 Photocathode for Efficient Photoelectrochemical Water Splitting. *Appl. Catal. B: Environ.* **2020,** *263*, 118180.

(103) Jiao, Z.; Guan, X.; Wang, M.; Wang, Q.; Xu, B.; Bi, Y.; Zhao, X. S. Undamaged Depositing Large-Area ZnO Quantum Dots/rGO Films on Photoelectrodes for the Construction of Pure Z-Scheme. *Chem. Eng. J.* **2019,** *356*, 781-790.

(104) Zhang, R.; Hao, G.; Li, H.; Ye, X.; Gao, S.; Yuan, X.; Liu, C. A Black Phosphorus/$BiVO_4$ (010) Heterostructure for Promising Photocatalytic Performance: First-Principles Study. *J. Phys. Chem. Solids* **2020,** *143*, 109466.

(105) Liu, F.; Shi, R.; Wang, Z.; Weng, Y.; Che, C. M.; Chen, Y. Direct Z-Scheme Hetero-Phase Junction of Black/Red Phosphorus for Photocatalytic Water Splitting. *Angew. Chem.* **2019,** *131* (34), 11917-11921.

(106) Liao, A.; Zhou, Y.; Xiao, L.; Zhang, C.; Wu, C.; Asiri, A. M.; Xiao, M.; Zou, Z. Direct Z Scheme-Fashioned Photoanode Systems Consisting of Fe_2O_3 Nanorod Arrays and Underlying Thin Sb_2Se_3 Layers toward Enhanced Photoelectrochemical Water Splitting Performance. *Nanoscale* **2019,** *11* (1), 109-114.

(107) Baral, B.; Parida, K. {040/110} Facet Isotype Heterojunctions with Monoclinic Scheelite $BiVO_4$. *Inorg. Chem.* **2020,** *59* (14), 10328-10342.

(108) Hisatomi, T.; Brillet, J.; Cornuz, M.; Le Formal, F.; Tétreault, N.; Sivula, K.; Grätzel, M. A Ga_2O_3 Underlayer as an Isomorphic Template for Ultrathin Hematite Films toward Efficient Photoelectrochemical Water Splitting. *Faraday Discuss.* **2012,** *155*, 223-232.

(109) Thalluri, S. M.; Bai, L.; Lv, C.; Huang, Z.; Hu, X.; Liu, L. Strategies for Semiconductor/Electrocatalyst Coupling toward Solar-Driven Water Splitting. *Adv. Sci.* **2020,** *7* (6), 1902102.

(110) Ding, C.; Shi, J.; Wang, Z.; Li, C. Photoelectrocatalytic Water Splitting: Significance of Cocatalysts, Electrolyte, and Interfaces. *ACS catalysis* **2017,** *7* (1), 675-688.

(111) Dai, Y.; Cheng, P.; Xie, G.; Li, C.; Akram, M. Z.; Guo, B.; Boddula, R.; Shi, X.; Gong, J.; Gong, J. R. Modulating Photoelectrochemical Water-Splitting Activity by Charge-Storage Capacity of Electrocatalysts. *J. Phys. Chem. C* **2019,** *123* (47), 28753-28762.

(112) Chen, S.; Huang, D.; Xu, P.; Xue, W.; Lei, L.; Cheng, M.; Wang, R.; Liu, X.; Deng, R. Semiconductor-Based Photocatalysts for Photocatalytic and Photoelectrochemical Water Splitting: Will We Stop with Photocorrosion? *J. Mater. Chem. A* **2020,** *8* (5), 2286-2322.

(113) Hinnemann, B.; Moses, P. G.; Bonde, J.; Jørgensen, K. P.; Nielsen, J. H.; Horch, S.; Chorkendorff, I.; Nørskov, J. K. Biomimetic Hydrogen Evolution: MoS_2 Nanoparticles as Catalyst for Hydrogen Evolution. *J. Am. Chem. Soc.* **2005,** *127* (15), 5308-5309.

(114) Li, D.; Shi, J.; Li, C. Transition-Metal-Based Electrocatalysts as Cocatalysts for Photoelectrochemical Water Splitting: A Mini Review. *Small* **2018,** *14* (23), 1704179.

(115) Xu, X. T.; Pan, L.; Zhang, X.; Wang, L.; Zou, J. J. Rational Design and Construction of Cocatalysts for Semiconductor-Based Photo-Electrochemical Oxygen Evolution: A Comprehensive Review. *Adv. Sci.* **2019,** *6* (2), 1801505.

(116) Mei, B.; Han, K.; Mul, G. Driving Surface Redox Reactions in Heterogeneous Photocatalysis: The Active State of Illuminated Semiconductor-Supported Nanoparticles During Overall Water-Splitting. *ACS catalysis* **2018,** *8* (10), 9154-9164.

(117) Jang, J.-W.; Du, C.; Ye, Y.; Lin, Y.; Yao, X.; Thorne, J.; Liu, E.; McMahon, G.; Zhu, J.; Javey, A. Enabling Unassisted Solar Water Splitting by Iron Oxide and Silicon. *Nat. Commun.* **2015,** *6* (1), 7447.

(118) Dai, P.; Li, W.; Xie, J.; He, Y.; Thorne, J.; McMahon, G.; Zhan, J.; Wang, D. Forming Buried Junctions to Enhance the Photovoltage Generated by Cuprous Oxide in Aqueous Solutions. *Angew. Chem.* **2014,** *126* (49), 13711-13715.

(119) Li, M.; Deng, J.; Pu, A.; Zhang, P.; Zhang, H.; Gao, J.; Hao, Y.; Zhong, J.; Sun, X. Hydrogen-Treated Hematite Nanostructures with Low Onset Potential for Highly Efficient Solar Water Oxidation. *J. Mater. Chem. A* **2014,** *2* (19), 6727-6733.

(120) Wang, Q.; Domen, K. Particulate Photocatalysts for Light-Driven Water Splitting: Mechanisms, Challenges, and Design Strategies. *Chem. Rev.* **2019,** *120* (2), 919-985.

(121) Hodes, G.; Cahen, D.; Manassen, J. Tungsten Trioxide as a Photoanode for a Photoelectrochemical Cell (Pec). *Nature* **1976,** *260* (5549), 312-313.

(122) Henrich, V. E.; Cox, P. A. *The Surface Science of Metal Oxides*, Cambridge university press: **1994.**

(123) Sivula, K.; Van De Krol, R. Semiconducting Materials for Photoelectrochemical Energy Conversion. *Nat. Rev. Mater.* **2016,** *1* (2), 1-16.

(124) De Respinis, M.; Fravventura, M.; Abdi, F. F.; Schreuders, H.; Savenije, T. J.; Smith, W. A.; Dam, B.; van de Krol, R. Oxynitrogenography: Controlled Synthesis of Single-Phase Tantalum Oxynitride Photoabsorbers. *Chem. Mater.* **2015,** *27* (20), 7091-7099.

(125) Zhai, T.; Fang, X.; Li, L.; Bando, Y.; Golberg, D. One-Dimensional Cds Nanostructures: Synthesis, Properties, and Applications. *Nanoscale* **2010,** *2* (2), 168-187.

(126) Xu, Y.; Huang, Y.; Zhang, B. Rational Design of Semiconductor-Based Photocatalysts for Advanced Photocatalytic Hydrogen Production: The Case of Cadmium Chalcogenides. *Inorganic Chemistry Frontiers* **2016,** *3* (5), 591-615.

(127) Tang, Z.-R.; Han, B.; Han, C.; Xu, Y.-J. One Dimensional CdS Based Materials for Artificial Photoredox Reactions. *J. Mater. Chem. A* **2017,** *5* (6), 2387-2410.

(128) Zhai, T.; Fang, X.; Zeng, H.; Xu, X.; Bando, Y.; Golberg, D. Vapor-Phase Synthesis of One-Dimensional ZnS, CdS, and $Zn_xCd_{1-X}S$ Nanostructures. *Pure Appl. Chem.* **2010,** *82* (11), 2027-2053.

(129) Pareek, A.; Borse, P. H. Hurdles and Recent Developments for CdS and Chalcogenide-Based Electrode in "Solar Electro Catalytic" Hydrogen Generation: A Review. *Int. J. Electrochem. Sci.* **2022,** *2* (6), e2100114.

(130) Kwak, W.-C.; Kim, T. G.; Lee, W.; Han, S.-H.; Sung, Y.-M. Template-Free Liquid-Phase Synthesis of High-Density CdS Nanowire Arrays on Conductive Glass. *J. Phys. Chem. C* **2009,** *113* (4), 1615-1619.

(131) Chen, F.; Zhou, R.; Yang, L.; Shi, M.; Wu, G.; Wang, M.; Chen, H. One-Step Fabrication of CdS Nanorod Arrays Via Solution Chemistry. *J. Phys. Chem. C* **2008,** *112* (35), 13457-13462.

(132) Barth, S.; Hernandez-Ramirez, F.; Holmes, J. D.; Romano-Rodriguez, A. Synthesis and Applications of One-Dimensional Semiconductors. *Prog. Mater Sci.* **2010,** *55* (6), 563-627.

(133) Tang, Q.; Chen, X.; Li, T.; Zhao, A.; Qian, Y.; Yu, D.; Yu, W. Template-Free Growth of Vertically Aligned CdS Nanowire Array Exhibiting Good Field Emission Property. *Chem. Lett.* **2004,** *33* (9), 1088-1089.

(134) Liang, Y.; Zhen, C.; Zou, D.; Xu, D. Preparation of Free-Standing Nanowire Arrays on Conductive Substrates. *J. Am. Chem. Soc.* **2004,** *126* (50), 16338-16339.

(135) Cho, K.-H.; Sung, Y.-M. The Formation of Z-Scheme CdS/CdS Nanorods on FTO Substrates: The Shell Thickness Effects on the Flat Band Potentials. *Nano Energy* **2017,** *36*, 176-185.

(136) Zhu, T.; Liang, Y.; Wang, Y.; Wang, J.; Wang, W.; Fu, J.; Yao, L.; Cheng, Y.; Han, H. p-Type β-$Ni(OH)_2$ Nanoparticles Sensitize CdS Nanorod Array Photoanode to Prolong Charge Carrier Lifetime and Highly Improve Bias-Free Visible-Light-Driven H_2 Evaluation. *Appl. Catal. B: Environ.* **2020,** *271*, 118945.

(137) Bard, A. J.; Fox, M. A. Artificial Photosynthesis: Solar Splitting of Water to Hydrogen and Oxygen. *Acc. Chem. Res.* **1995,** *28* (3), 141-145.

(138) Yang, Z.; Li, M.; Chen, S.; Yang, S.; Peng, F.; Liao, J.; Fang, Y.; Zhang, S.; Zhang, S. Cocatalyst Engineering with Robust Tunable Carbon-Encapsulated Mo-Rich Mo/Mo_2C Heterostructure Nanoparticle for Efficient Photocatalytic Hydrogen Evolution. *Adv. Funct. Mater.* **2023**, 2212746.

(139) Landman, A.; Dotan, H.; Shter, G. E.; Wullenkord, M.; Houaijia, A.; Maljusch, A.; Grader, G. S.; Rothschild, A. Photoelectrochemical Water Splitting in Separate Oxygen and Hydrogen Cells. *Nat. Mater.* **2017,** *16* (6), 646-651.

(140) Paracchino, A.; Laporte, V.; Sivula, K.; Grätzel, M.; Thimsen, E. Highly Active Oxide Photocathode for Photoelectrochemical Water Reduction. *Nat. Mater.* **2011,** *10* (6), 456-461.

(141) Zhang, X.-Y.; Li, H.-P.; Cui, X.-L.; Lin, Y. Graphene/Tio 2 Nanocomposites: Synthesis, Characterization and Application in Hydrogen Evolution from Water Photocatalytic Splitting. *J. Mater. Chem.* **2010,** *20* (14), 2801-2806.

(142) Li, F.; Li, J.; Gao, L.; Hu, Y.; Long, X.; Wei, S.; Wang, C.; Jin, J.; Ma, J. Construction of an Efficient Hole Migration Pathway on Hematite for Efficient Photoelectrochemical Water Oxidation. *J. Mater. Chem. A* **2018,** *6* (46), 23478-23485.

(143) Kim, K.; Moon, J. H. Three-Dimensional Bicontinuous $BiVO_4$/ZnO Photoanodes for High Solar Water-Splitting Performance at Low Bias Potential. *ACS Appl. Mater. Interfaces* **2018,** *10* (40), 34238-34244.

(144) Li, Y.; Liu, Z.; Zhang, J.; Guo, Z.; Xin, Y.; Zhao, L. 1D/0D WO_3/CdS Heterojunction Photoanodes Modified with Dual Co-Catalysts for Efficient Photoelectrochemical Water Splitting. *J. Alloys Compd.* **2019,** *790*, 493-501.

(145) Han, N.; Liu, P.; Jiang, J.; Ai, L.; Shao, Z.; Liu, S. Recent Advances in Nanostructured Metal Nitrides for Water Splitting. *J. Mater. Chem. A* **2018,** *6* (41), 19912-19933.

(146) Zhang, K.; Guo, L. Metal Sulphide Semiconductors for Photocatalytic Hydrogen Production. *Catal. Sci. Technol.* **2013,** *3* (7), 1672-1690.

(147) Ghosh, D.; Devi, P.; Kushwaha, O. S.; Kumar, R.; Kumar, P. In Operando Generation and Storage of Hydrogen by Coupling Monolithically Integrated Photoelectrochemical Cell with Clathrate Hydrates Molecular Storage. *ACS Applied Energy Materials* **2020,** *3* (7), 6834-6844.

(148) Wu, K.; Du, Y.; Tang, H.; Chen, Z.; Lian, T. Efficient Extraction of Trapped Holes from Colloidal CdS Nanorods. *J. Am. Chem. Soc.* **2015,** *137* (32), 10224-10230.

(149) Bao, N.; Shen, L.; Takata, T.; Domen, K. Self-Templated Synthesis of Nanoporous CdS Nanostructures for Highly Efficient Photocatalytic Hydrogen Production under Visible Light. *Chem. Mater.* **2008,** *20* (1), 110-117.

(150) Wang, M.; Jiang, J.; Shi, J.; Guo, L. CdS/CdSe Core–Shell Nanorod Arrays: Energy Level Alignment and Enhanced Photoelectrochemical Performance. *ACS Appl. Mater. Interfaces* **2013,** *5* (10), 4021-4025.

(151) Peng, Z.; Zhang, J.; Liu, P.; Claverie, J.; Siaj, M. One-Dimensional CdS/Carbon/Au Plasmonic Nanoarray Photoanodes Via in Situ Reduction-Graphitization Approach toward Efficient Solar Hydrogen Evolution. *ACS Appl. Mater. Interfaces* **2021,** *13* (29), 34658-34670.

(152) Habas, S. E.; Yang, P.; Mokari, T. Selective Growth of Metal and Binary Metal Tips on CdS Nanorods. *J. Am. Chem. Soc.* **2008,** *130* (11), 3294-3295.

(153) Park, H.; Reddy, D. A.; Kim, Y.; Lee, S.; Ma, R.; Kim, T. K. Synthesis of Ultra-Small Palladium Nanoparticles Deposited on CdS Nanorods by Pulsed Laser Ablation in Liquid: Role of Metal Nanocrystal Size in the Photocatalytic Hydrogen Production. *Chem. Eur. J.* **2017,** *23* (53), 13112-13119.

(154) Zhang, Y. J.; Zhang, L. Preparation of Ru-Loaded CdS/Al-Hms Nanocomposites and Production of Hydrogen by Photocatalytic Degradation of Formic Acid. *Appl. Surf. Sci.* **2009,** *255* (9), 4863-4866.

(155) Xiang, D.; Yang, L.; Hou, Y.; Zhu, J.; Yang, M. Hybrid CdS-Au Nanochains with Enhanced Photoelectrochemistry. *Vacuum* **2019,** *168*, 108866.

(156) Fang, Z.; Wang, Y.; Song, J.; Sun, Y.; Zhou, J.; Xu, R.; Duan, H. Immobilizing CdS Quantum Dots and Dendritic Pt Nanocrystals on Thiolated Graphene Nanosheets toward Highly Efficient Photocatalytic H_2 Evolution. *Nanoscale* **2013,** *5* (20), 9830-9838.

(157) Hieu, H.; Nghia, N.; Vuong, N.; Van Bui, H. Omnidirectional Au-Embedded ZnO/CdS Core/Shell Nanorods for Enhanced Photoelectrochemical Water-Splitting Efficiency. *Chem. Commun.* **2020,** *56* (28), 3975-3978.

(158) Guan, H.; Zhang, S.; Cai, X.; Gao, Q.; Yu, X.; Zhou, X.; Peng, F.; Fang, Y.; Yang, S. CdS@ Ni_3S_2 Core–Shell Nanorod Arrays on Nickel Foam: A Multifunctional Catalyst for Efficient Electrochemical Catalytic, Photoelectrochemical and Photocatalytic H_2 Production Reaction. *J. Mater. Chem. A* **2019,** *7* (6), 2560-2574.

(159) Yin, X.-L.; Li, L.-L.; Jiang, W.-J.; Zhang, Y.; Zhang, X.; Wan, L.-J.; Hu, J.-S. MoS_2/CdS Nanosheets-on-Nanorod Heterostructure for Highly Efficient Photocatalytic H_2 Generation under Visible Light Irradiation. *ACS Appl. Mater. Interfaces* **2016,** *8* (24), 15258-15266.

(160) Zhao, L.; Jia, J.; Yang, Z.; Yu, J.; Wang, A.; Sang, Y.; Zhou, W.; Liu, H. One-Step Synthesis of CdS Nanoparticles/MoS_2 Nanosheets Heterostructure on Porous Molybdenum Sheet for Enhanced Photocatalytic H_2 Evolution. *Appl. Catal. B Environ.* **2017,** *210*, 290-296.

(161) Xu, J.; Cao, X. Characterization and Mechanism of MoS_2/CdS Composite Photocatalyst Used for Hydrogen Production from Water Splitting under Visible Light. *Chem. Eng. J.* **2015,** *260*, 642-648.

(162) Duan, X.; Wang, C.; Pan, A.; Yu, R.; Duan, X. Two-Dimensional Transition Metal Dichalcogenides as Atomically Thin Semiconductors: Opportunities and Challenges. *Chem. Soc. Rev.* **2015,** *44* (24), 8859-8876.

(163) Poorahong, S.; Izquierdo, R.; Siaj, M. An Efficient Porous Molybdenum Diselenide Catalyst for Electrochemical Hydrogen Generation. *Journal of Materials Chemistry A* **2017,** *5* (39), 20993-21001.

(164) Poorahong, S.; Somnin, C.; Malam Mahamadou, I.; Dubois, C.; Chergui, S.; Peng, Z.; Su, Y.; Xuan Tran, T.; Thammakhet-Buranachai, C.; Mazzah, A. Nanoporous Graphite-Like Membranes Decorated with $MoSe_2$ Nanosheets for Hydrogen Evolution. *ACS Applied Nano Materials* **2022,** *5* (2), 2769-2778.

(165) Poorahong, S.; Harding, D. J.; Siaj, M. Hollow Molybdenum Oxide-Graphene Oxide Spheres as a Binder-Free Electrocatalyst Membrane with Enhanced Hydrogen Evolution Efficiency. *Mater. Lett.* **2020,** *272*, 127872.

(166) Tran, X. T.; Poorahong, S.; Siaj, M. One-Pot Hydrothermal Synthesis and Selective Etching Method of a Porous $MoSe_2$ Sand Rose-Like Structure for Electrocatalytic Hydrogen Evolution Reaction. *RSC advances* **2017,** *7* (82), 52345-52351.

(167) Yuan, Y. J.; Lu, H. W.; Yu, Z. T.; Zou, Z. G. Noble-Metal-Free Molybdenum Disulfide Cocatalyst for Photocatalytic Hydrogen Production. *ChemSusChem* **2015,** *8* (24), 4113-4127.

(168) Raybaud, P.; Hafner, J.; Kresse, G.; Kasztelan, S.; Toulhoat, H. Ab Initio Study of the H_2–H_2S/MoS_2 Gas–Solid Interface: The Nature of the Catalytically Active Sites. *J. Catal.* **2000,** *189* (1), 129-146.

(169) Karunadasa, H. I.; Montalvo, E.; Sun, Y.; Majda, M.; Long, J. R.; Chang, C. J. A Molecular MoS_2 Edge Site Mimic for Catalytic Hydrogen Generation. *Science* **2012,** *335* (6069), 698-702.

(170) Liu, Y.; Yu, Y.-X.; Zhang, W.-D. MoS_2/CdS Heterojunction with High Photoelectrochemical Activity for H_2 Evolution under Visible Light: The Role of MoS_2. *J. Phys. Chem. C* **2013,** *117* (25), 12949-12957.

(171) Dolai, S.; Maiti, P.; Ghorai, A.; Bhunia, R.; Paul, P. K.; Ghosh, D. Exfoliated Molybdenum Disulfide-Wrapped CdS Nanoparticles as a Nano-Heterojunction for Photo-Electrochemical Water Splitting. *ACS Appl. Mater. Interfaces* **2020,** *13* (1), 438-448.

(172) Zong, X.; Wu, G.; Yan, H.; Ma, G.; Shi, J.; Wen, F.; Wang, L.; Li, C. Photocatalytic H_2 Evolution on MoS_2/CdS Catalysts under Visible Light Irradiation. *J. Phys. Chem. C* **2010,** *114* (4), 1963-1968.

(173) Zhang, W.; Cao, Y.; Tian, P.; Guo, F.; Tian, Y.; Zheng, W.; Ji, X.; Liu, J. Soluble, Exfoliated Two-Dimensional Nanosheets as Excellent Aqueous Lubricants. *ACS Appl. Mater. Interfaces* **2016,** *8* (47), 32440-32449.

(174) Ding, Q.; Zhai, J.; Cabán-Acevedo, M.; Shearer, M. J.; Li, L.; Chang, H. C.; Tsai, M. L.; Ma, D.; Zhang, X.; Hamers, R. J. Designing Efficient Solar-Driven Hydrogen Evolution Photocathodes Using Semitransparent Moqxcly (Q= S, Se) Catalysts on Si Micropyramids. *Adv. Mater.* **2015,** *27* (41), 6511-6518.

(175) Hu, D.; Xiang, J.; Zhou, Q.; Su, S.; Zhang, Z.; Wang, X.; Jin, M.; Nian, L.; Nözel, R.; Zhou, G. One-Step Chemical Vapor Deposition of MoS_2 Nanosheets on Sinws as Photocathodes for Efficient and Stable Solar-Driven Hydrogen Production. *Nanoscale* **2018,** *10* (7), 3518-3525.

(176) Pi, Y.; Li, Z.; Xu, D.; Liu, J.; Li, Y.; Zhang, F.; Zhang, G.; Peng, W.; Fan, X. 1t-Phase MoS_2 Nanosheets on TiO_2 Nanorod Arrays: 3d Photoanode with Extraordinary Catalytic Performance. *ACS Sustain. Chem. Eng.* **2017,** *5* (6), 5175-5182.

(177) Liu, Q.; Shang, Q.; Khalil, A.; Fang, Q.; Chen, S.; He, Q.; Xiang, T.; Liu, D.; Zhang, Q.; Luo, Y. In Situ Integration of a Metallic 1t-MoS_2/CdS Heterostructure as a Means to Promote Visible-Light-Driven Photocatalytic Hydrogen Evolution. *ChemCatChem* **2016,** *8* (16), 2614-2619.

(178) Joe, J.; Bae, C.; Kim, E.; Ho, T. A.; Yang, H.; Park, J. H.; Shin, H. Mixed-Phase (2H and 1T) MoS_2 Catalyst for a Highly Efficient and Stable Si Photocathode. *Catalysts* **2018,** *8* (12), 580.

(179) Ago, H.; Endo, H.; Solís-Fernández, P.; Takizawa, R.; Ohta, Y.; Fujita, Y.; Yamamoto, K.; Tsuji, M. Controlled Van Der Waals Epitaxy of Monolayer MoS_2 Triangular Domains on Graphene. *ACS Appl. Mater. Interfaces* **2015,** *7* (9), 5265-5273.

(180) Shi, H.; Yan, R.; Bertolazzi, S.; Brivio, J.; Gao, B.; Kis, A.; Jena, D.; Xing, H. G.; Huang, L. Exciton Dynamics in Suspended Monolayer and Few-Layer MoS_2 2D Crystals. *ACS Nano* **2013,** *7* (2), 1072-1080.

(181) Ho, T. A.; Bae, C.; Joe, J.; Yang, H.; Kim, S.; Park, J. H.; Shin, H. Heterojunction Photoanode of Atomic-Layer-Deposited MoS_2 on Single-Crystalline CdS Nanorod Arrays. *ACS Appl. Mater. Interfaces* **2019,** *11* (41), 37586-37594.

(182) Wang, Y.; Zhang, X.; Liu, Y.; Zhao, Y.; Xie, C.; Song, Y.; Yang, P. Crystallinity and Phase Controlling of g-C_3N_4/CdS Hetrostructures Towards High Efficient Photocatalytic H_2 Generation. *Int. J. Hydrogen Energy* **2019,** *44* (57), 30151-30159.

(183) Fan, X.; Zhou, Y.; Zhang, G.; Liu, T.; Dong, W. In Situ Photoelectrochemical Activation of Sulfite by MoS_2 Photoanode for Enhanced Removal of Ammonium Nitrogen from Wastewater. *Appl. Catal. B Environ.* **2019,** *244*, 396-406.

(184) Umukoro, E. H.; Kumar, N.; Ngila, J. C.; Arotiba, O. A. Expanded Graphite Supported P-N MoS_2-SnO_2 Heterojunction Nanocomposite Electrode for Enhanced Photo-Electrocatalytic Degradation of a Pharmaceutical Pollutant. *J. Electroanal. Chem.* **2018,** *827*, 193-203.

(185) Lu, X.; Chen, W.; Yao, Y.; Wen, X.; Hart, J. N.; Tsounis, C.; Toe, C. Y.; Scott, J.; Ng, Y. H. Photogenerated Charge Dynamics of CdS Nanorods with Spatially Distributed MoS_2 for Photocatalytic Hydrogen Generation. *Chem. Eng. J.* **2021,** *420*, 127709.

(186) Chen, J.; Wu, X. J.; Yin, L.; Li, B.; Hong, X.; Fan, Z.; Chen, B.; Xue, C.; Zhang, H. One-Pot Synthesis of CdS Nanocrystals Hybridized with Single-Layer Transition-Metal Dichalcogenide Nanosheets for Efficient Photocatalytic Hydrogen Evolution. *Angew. Chem.* **2015,** *127* (4), 1226-1230.

(187) Ho, T. A.; Bae, C.; Lee, S.; Kim, M.; Montero-Moreno, J. M.; Park, J. H.; Shin, H. Edge-on MoS_2 Thin Films by Atomic Layer Deposition for Understanding the Interplay between the Active Area and Hydrogen Evolution Reaction. *Chem. Mater.* **2017,** *29* (17), 7604-7614.

(188) Li, Y.; Wang, H.; Xie, L.; Liang, Y.; Hong, G.; Dai, H. MoS_2 Nanoparticles Grown on Graphene: An Advanced Catalyst for the Hydrogen Evolution Reaction. *J. Am. Chem. Soc.* **2011,** *133* (19), 7296-7299.

(189) Yu, Z.; Ong, Z. Y.; Li, S.; Xu, J. B.; Zhang, G.; Zhang, Y. W.; Shi, Y.; Wang, X. Analyzing the Carrier Mobility in Transition-Metal Dichalcogenide MoS_2 Field-Effect Transistors. *Adv. Funct. Mater.* **2017,** *27* (19), 1604093.

(190) Yang, S.; Guan, H.; Zhong, Y.; Quan, J.; Luo, N.; Gao, Q.; Xu, Y.; Peng, F.; Zhang, S.; Fang, Y. $CdS@Ni_3S_2$ for Efficient and Stable Photo-Assisted Electrochemical (P-EC) Overall Water Splitting. *Chem. Eng. J.* **2021,** *405*, 126231.

(191) Lu, X.; Toe, C. Y.; Ji, F.; Chen, W.; Wen, X.; Wong, R. J.; Seidel, J.; Scott, J.; Hart, J. N.; Ng, Y. H. Light-Induced Formation of MoO_XS_Y Clusters on CdS Nanorods as Cocatalyst for Enhanced Hydrogen Evolution. *ACS Appl. Mater. Interfaces* **2020,** *12* (7), 8324-8332.

(192) Long, X.; Gao, L.; Li, F.; Hu, Y.; Wei, S.; Wang, C.; Wang, T.; Jin, J.; Ma, J. Bamboo Shoots Shaped $FeVO_4$ Passivated ZnO Nanorods Photoanode for Improved Charge Separation/Transfer Process Towards Efficient Solar Water Splitting. *Appl. Catal. B Environ.* **2019,** *257*, 117813.

(193) Eda, G.; Yamaguchi, H.; Voiry, D.; Fujita, T.; Chen, M.; Chhowalla, M. Photoluminescence from Chemically Exfoliated MoS_2. *Nano Lett.* **2011,** *11* (12), 5111-5116.

(194) Masoumi, Z.; Tayebi, M.; Kolaei, M.; Tayyebi, A.; Ryu, H.; Jang, J. I.; Lee, B.-K. Simultaneous Enhancement of Charge Separation and Hole Transportation in a W: A-Fe_2O_3/MoS_2 Photoanode: A Collaborative Approach of MoS_2 as a Heterojunction and W as a Metal Dopant. *ACS Appl. Mater. Interfaces* **2021,** *13* (33), 39215-39229.

(195) Yao, L.; Wang, W.; Zhu, T.; Wang, Y.; Liang, Y.; Fu, J.; Wang, J.; Cheng, Y.; Liu, S. A Rational Design of CdS/$ZnFe_2O_4$/Cu_2O Core-Shell Nanorod Array Photoanode with Stair-Like Type-II Band Alignment for Highly Efficient Bias-Free Visible-Light-Driven H_2 Generation. *Appl. Catal. B: Environ* **2020,** *268*, 118460.

(196) Krysa, J.; Zlamal, M.; Kment, S.; Brunclikova, M.; Hubicka, Z. TiO_2 and Fe_2O_3 Films for Photoelectrochemical Water Splitting. *Molecules* **2015,** *20* (1).

(197) Ma, X.-C.; Dai, Y.; Yu, L.; Huang, B.-B. Energy Transfer in Plasmonic Photocatalytic Composites. *Light: Science & Applications* **2016,** *5* (2), e16017-e16017.

(198) Wei, Z.-Q.; Dai, X.-C.; Hou, S.; Li, Y.-B.; Huang, M.-H.; Li, T.; Xu, S.; Xiao, F.-X. Branched Polymer-Incorporated Multi-Layered Heterostructured Photoanode: Precisely Tuning Directional Charge Transfer toward Solar Water Oxidation. *J. Mater. Chem. A.* **2020,** *8* (1), 177-189.

(199) Gao, T.; Wang, T. Catalyst-Assisted Vapor− Liquid− Solid Growth of Single-Crystal CdS Nanobelts and Their Luminescence Properties. *J. Phys. Chem. B* **2004,** *108* (52), 20045-20049.

(200) Fu, J.; Fan, Z.; Nakabayashi, M.; Ju, H.; Pastukhova, N.; Xiao, Y.; Feng, C.; Shibata, N.; Domen, K.; Li, Y. Interface Engineering of Ta_3N_5 Thin Film Photoanode for Highly Efficient Photoelectrochemical Water Splitting. *Nat. Commun.* **2022,** *13* (1), 729.

(201) Li, Y.; Zhang, J. Z. Hydrogen Generation from Photoelectrochemical Water Splitting Based on Nanomaterials. *Laser & Photonics Reviews* **2010,** *4* (4), 517-528.

(202) Lu, Q.; Yu, Y.; Ma, Q.; Chen, B.; Zhang, H. 2D Transition-Metal-Dichalcogenide-Nanosheet-Based Composites for Photocatalytic and Electrocatalytic Hydrogen Evolution Reactions. *Adv. Mater.* **2016,** *28* (10), 1917-1933.

(203) Shao, D.; Cheng, Y.; He, J.; Feng, D.; Zheng, L.; Zheng, L.; Zhang, X.; Xu, J.; Wang, W.; Wang, W. A Spatially Separated Organic–Inorganic Hybrid Photoelectrochemical Cell for Unassisted Overall Water Splitting. *ACS Catalysis* **2017,** *7* (8), 5308-5315.

(204) Kargar, A.; Sun, K.; Jing, Y.; Choi, C.; Jeong, H.; Jung, G. Y.; Jin, S.; Wang, D. 3D Branched Nanowire Photoelectrochemical Electrodes for Efficient Solar Water Splitting. *ACS Nano* **2013,** *7* (10), 9407-9415.

(205) Wang, T.; Luo, Z.; Li, C.; Gong, J. Controllable Fabrication of Nanostructured Materials for Photoelectrochemical Water Splitting Via Atomic Layer Deposition. *Chem. Soc. Rev.* **2014,** *43* (22), 7469-7484.

(206) Zhang, X.; Zhai, P.; Zhang, Y.; Wu, Y.; Wang, C.; Ran, L.; Gao, J.; Li, Z.; Zhang, B.; Fan, Z. Engineering Single-Atomic Ni-N_4-O Sites on Semiconductor Photoanodes for High-Performance Photoelectrochemical Water Splitting. *J. Am. Chem. Soc.* **2021,** *143* (49), 20657-20669.

(207) Baek, J. H.; Kim, B. J.; Han, G. S.; Hwang, S. W.; Kim, D. R.; Cho, I. S.; Jung, H. S. $BiVO_4/WO_3/SnO_2$ Double-Heterojunction Photoanode with Enhanced Charge Separation and Visible-Transparency for Bias-Free Solar Water-Splitting with a Perovskite Solar Cell. *ACS Appl. Mater. Interfaces* **2017,** *9* (2), 1479-1487.

(208) Li, H.; Zhou, Y.; Tu, W.; Ye, J.; Zou, Z. State-of-the-Art Progress in Diverse Heterostructured Photocatalysts toward Promoting Photocatalytic Performance. *Adv. Funct. Mater.* **2015,** *25* (7), 998-1013.

(209) Zhou, P.; Yu, J.; Jaroniec, M. All-Solid-State Z-Scheme Photocatalytic Systems. *Adv. Mater.* **2014,** *26* (29), 4920-4935.

(210) Tada, H.; Mitsui, T.; Kiyonaga, T.; Akita, T.; Tanaka, K. All-Solid-State Z-Scheme in CdS–Au–TiO_2 Three-Component Nanojunction System. *Nat. Mater.* **2006,** *5* (10), 782-786.

(211) Li, J.-M.; Cheng, H.-Y.; Chiu, Y.-H.; Hsu, Y.-J. ZnO–Au–SnO_2 Z-Scheme Photoanodes for Remarkable Photoelectrochemical Water Splitting. *Nanoscale* **2016,** *8* (34), 15720-15729.

(212) Zheng, D.; Pang, C.; Wang, X. The Function-Led Design of Z-Scheme Photocatalytic Systems Based on Hollow Carbon Nitride Semiconductors. *Chem. Commun.* **2015,** *51* (98), 17467-17470.

(213) Huang, M.; Chen, C.; Wang, T.; Sui, Q.; Zhang, K.; Li, B. Cadmium-Sulfide/Gold/Graphitic-Carbon-Nitride Sandwich Heterojunction Photocatalyst with Regulated Electron Transfer for Boosting Carbon-Dioxide Reduction to Hydrocarbon. *J. Colloid Interface Sci.* **2022,** *613*, 575-586.

(214) Wang, X.; Li, S.; Ma, Y.; Yu, H.; Yu, J. $H_2WO_4 \cdot H_2O$/Ag/AgCl Composite Nanoplates: A Plasmonic Z-Scheme Visible-Light Photocatalyst. *J. Phys. Chem. C* **2011,** *115* (30), 14648-14655.

(215) Chen, Z.; Bing, F.; Liu, Q.; Zhang, Z.; Fang, X. Novel Z-Scheme Visible-Light-Driven Ag_3PO_4/Ag/SiC Photocatalysts with Enhanced Photocatalytic Activity. *J. Mater. Chem. A.* **2015,** *3* (8), 4652-4658.

(216) Wang, Y.; Tang, J.; Peng, Z.; Wang, Y.; Jia, D.; Kong, B.; Elzatahry, A. A.; Zhao, D.; Zheng, G. Fully Solar-Powered Photoelectrochemical Conversion for Simultaneous Energy Storage and Chemical Sensing. *Nano Lett.* **2014,** *14* (6), 3668-3673.

(217) Wei, Y.; Jiao, J.; Zhao, Z.; Zhong, W.; Li, J.; Liu, J.; Jiang, G.; Duan, A. 3D Ordered Macroporous TiO_2-Supported Pt@ CdS Core–Shell Nanoparticles: Design, Synthesis and Efficient Photocatalytic Conversion of CO_2 with Water to Methane. *J. Mater. Chem. A.* **2015,** *3* (20), 11074-11085.

(218) Pan, Z.; Hisatomi, T.; Wang, Q.; Chen, S.; Iwase, A.; Nakabayashi, M.; Shibata, N.; Takata, T.; Katayama, M.; Minegishi, T. Photoreduced Graphene Oxide as a Conductive Binder to Improve the Water Splitting Activity of Photocatalyst Sheets. *Adv. Funct. Mater.* **2016,** *26* (38), 7011-7019.

(219) Chen, S.; Qi, Y.; Hisatomi, T.; Ding, Q.; Asai, T.; Li, Z.; Ma, S. S. K.; Zhang, F.; Domen, K.; Li, C. Efficient Visible-Light-Driven Z-Scheme Overall Water Splitting Using a $MgTa_2O_{6-X}N_y$/TaON Heterostructure Photocatalyst for H_2 Evolution. *Angew. Chem.* **2015,** *127* (29), 8618-8621.

(220) Kim, Y.; Shin, D.; Chang, W. J.; Jang, H. L.; Lee, C. W.; Lee, H. E.; Nam, K. T. Hybrid Z-Scheme Using Photosystem I and $BiVO_4$ for Hydrogen Production. *Adv. Funct. Mater.* **2015,** *25* (16), 2369-2377.

(221) Xian, J.; Li, D.; Chen, J.; Li, X.; He, M.; Shao, Y.; Yu, L.; Fang, J. TiO_2 Nanotube Array/Graphene/ CdS Quantum Dots Composite Film in Z-Scheme with Enhanced Photoactivity and Photostability. *ACS Appl. Mater. Interfaces* **2014,** *6* (15), 13157-13166.

(222) Iwase, A.; Ng, Y. H.; Ishiguro, Y.; Kudo, A.; Amal, R. Reduced Graphene Oxide as a Solid-State Electron Mediator in Z-Scheme Photocatalytic Water Splitting under Visible Light. *J. Am. Chem. Soc.* **2011,** *133* (29), 11054-11057.

(223) Liu, C.; Tang, J.; Chen, H. M.; Liu, B.; Yang, P. A Fully Integrated Nanosystem of Semiconductor Nanowires for Direct Solar Water Splitting. *Nano Lett.* **2013,** *13* (6), 2989-2992.

(224) Chen, Y.-S.; Manser, J. S.; Kamat, P. V. All Solution-Processed Lead Halide Perovskite-$BiVO_4$ Tandem Assembly for Photolytic Solar Fuels Production. *J. Am. Chem. Soc.* **2015,** *137* (2), 974-981.

(225) Wang, W.; Wang, H.; Zhu, Q.; Qin, W.; Han, G.; Shen, J. R.; Zong, X.; Li, C. Spatially Separated Photosystem II and a Silicon Photoelectrochemical Cell for Overall Water Splitting: A Natural–Artificial Photosynthetic Hybrid. *Angew. Chem.* **2016,** *128* (32), 9375-9379.

(226) Gopannagari, M.; Kumar, D. P.; Reddy, D. A.; Hong, S.; Song, M. I.; Kim, T. K. In Situ Preparation of Few-Layered WS_2 Nanosheets and Exfoliation into Bilayers on CdS Nanorods for Ultrafast Charge Carrier Migrations toward Enhanced Photocatalytic Hydrogen Production. *J. Catal.* **2017,** *351*, 153-160.

(227) Li, Q.; Guo, B.; Yu, J.; Ran, J.; Zhang, B.; Yan, H.; Gong, J. R. Highly Efficient Visible-Light-Driven Photocatalytic Hydrogen Production of CdS-Cluster-Decorated Graphene Nanosheets. *J. Am. Chem. Soc.* **2011,** *133* (28), 10878-10884.

(228) Peng, Z.; Zhang, J.; Liu, P.; Claverie, J.; Siaj, M. One-Dimensional CdS/Carbon/Au Plasmonic Nanoarray Photoanodes Via in Situ Reduction–Graphitization Approach toward Efficient Solar Hydrogen Evolution. *ACS Appl. Mater. Interfaces* **2021,** *13* (29), 34658-34670.

(229) Wang, L.; Wang, W.; Chen, Y.; Yao, L.; Zhao, X.; Shi, H.; Cao, M.; Liang, Y. Heterogeneous P–N Junction CdS/Cu_2O Nanorod Arrays: Synthesis and Superior Visible-Light-Driven Photoelectrochemical Performance for Hydrogen Evolution. *ACS Appl. Mater. Interfaces* **2018,** *10* (14), 11652-11662.

(230) Sun, M.; Fu, W.; Li, Q.; Yin, G.; Chi, K.; Zhou, X.; Ma, J.; Yang, L.; Mu, Y.; Chen, Y. Facile Fabrication of CdS Nanorod Arrays on the Transparent Conducting Substrates and Their Photoelectrochemical Properties. *J. Cryst. Growth* **2013,** *377*, 112-117.

(231) Huang, Y.; Xu, Y.; Zhang, J.; Yin, X.; Guo, Y.; Zhang, B. Hierarchical Ultrathin-Branched CdS Nanowire Arrays with Enhanced Photocatalytic Performance. *J. Mater. Chem. A.* **2015,** *3* (38), 19507-19516.

(232) Fu, Y.; Cao, F.; Wu, F.; Diao, Z.; Chen, J.; Shen, S.; Li, L. Phase-Modulated Band Alignment in CdS Nanorod/SnS_x Nanosheet Hierarchical Heterojunctions toward Efficient Water Splitting. *Adv. Funct. Mater.* **2018,** *28* (16), 1706785.

(233) Zhang, D.; Liu, L.; Zhang, L.; Qi, K.; Zhang, H.; Cui, X. An Anti-Photocorrosive Photoanode Based on a CdS/Ni_xS_y@NF Heterostructure for Visible-Light-Driven Water Splitting. *Appl. Surf. Sci.* **2017,** *420*, 161-166.

(234) Hong, S.; Kumar, D. P.; Reddy, D. A.; Choi, J.; Kim, T. K. Excellent Photocatalytic Hydrogen Production over CdS Nanorods Via Using Noble Metal-Free Copper Molybdenum Sulfide (Cu_2MoS_4) Nanosheets as Co-Catalysts. *Appl. Surf. Sci.* **2017,** *396*, 421-429.

(235) Yu, G.; Wang, X.; Cao, J.; Wu, S.; Yan, W.; Liu, G. Plasmonic Au Nanoparticles Embedding Enhances the Activity and Stability of CdS for Photocatalytic Hydrogen Evolution. *Chem. Commun.* **2016,** *52* (11), 2394-2397, DOI: 10.1039/c5cc10066f.

(236) Zhang, X.; Liu, Y.; Kang, Z. 3d Branched Zno Nanowire Arrays Decorated with Plasmonic Au Nanoparticles for High-Performance Photoelectrochemical Water Splitting. *ACS Appl. Mater. Interfaces* **2014,** *6* (6), 4480-4489.

(237) Linic, S.; Christopher, P.; Ingram, D. B. Plasmonic-Metal Nanostructures for Efficient Conversion of Solar to Chemical Energy. *Nat. Mater.* **2011,** *10* (12), 911-921, DOI: 10.1038/nmat3151.

(238) Zhu, T.; Liang, Y.; Wang, Y.; Wang, J.; Wang, W.; Fu, J.; Yao, L.; Cheng, Y.; Han, H. P-Type B-Ni $(OH)_2$ Nanoparticles Sensitize CdS Nanorod Array Photoanode to Prolong Charge Carrier Lifetime and Highly Improve Bias-Free Visible-Light-Driven HS Evaluation. *Appl. Catal. B: Environ* **2020**, 118945.

(239) Qin, L.; Huang, D.; Xu, P.; Zeng, G.; Lai, C.; Fu, Y.; Yi, H.; Li, B.; Zhang, C.; Cheng, M. In-Situ Deposition of Gold Nanoparticles onto Polydopamine-Decorated g-C_3N_4 for Highly Efficient Reduction of Nitroaromatics in Environmental Water Purification. *J. Colloid Interface Sci.* **2019,** *534*, 357-369.

(240) Lin, C.; Fu, J.; Liu, S. Facile Preparation of Au Nanoparticle-Embedded Polydopamine Hollow Microcapsule and Its Catalytic Activity for the Reduction of Methylene Blue. *J. Macromol. Sci. A* **2019,** *56* (12), 1104-1113.

(241) Huang, M.; Wang, T.; Wu, Z.; Shang, Y.; Zhao, Y.; Li, B. Rational Fabrication of Cadmium-Sulfide/Graphitic-Carbon-Nitride/Hematite Photocatalyst with Type II and Z-Scheme Tandem Heterojunctions to Promote Photocatalytic Carbon Dioxide Reduction. *J. Colloid Interface Sci.* **2022,** *628*, 129-140.

(242) Zheng, Z.; Han, F.; Xing, B.; Han, X.; Li, B. Synthesis of Fe_3O_4@CdS@CQDs Ternary Core–Shell Heterostructures as a Magnetically Recoverable Photocatalyst for Selective Alcohol Oxidation Coupled with H_2O_2 Production. *J. Colloid Interface Sci.* **2022,** *624*, 460-470.

(243) Mu, J.; Teng, F.; Miao, H.; Wang, Y.; Hu, X. In-Situ Oxidation Fabrication of 0D/2D SnO_2/SnS_2 Novel Step-Scheme Heterojunctions with Enhanced Photoelectrochemical Activity for Water Splitting. *Appl. Surf. Sci.* **2020,** *501*, 143974.

(244) Zhang, Z.; Choi, M.; Baek, M.; Deng, Z.; Yong, K. Plasmonic and Passivation Effects of Au Decorated RGO@ CdSe Nanofilm Uplifted by CdSe@ ZnO Nanorods with Photoelectrochemical Enhancement. *Nano Energy* **2016,** *21*, 185-197.

(245) Yu, J.; Jin, J.; Cheng, B.; Jaroniec, M. A Noble Metal-Free Reduced Graphene Oxide–CdS Nanorod Composite for the Enhanced Visible-Light Photocatalytic Reduction of CO_2 to Solar Fuel. *J. Mater. Chem. A* **2014,** *2* (10), 3407-3416.

(246) Zhu, X.; Guijarro, N.; Liu, Y.; Schouwink, P.; Wells, R. A.; Le Formal, F.; Sun, S.; Gao, C.; Sivula, K. Spinel Structural Disorder Influences Solar-Water-Splitting Performance of $ZnFe_2O_4$ Nanorod Photoanodes. *Adv. Mater.* **2018,** *30* (34), 1801612.

(247) Xu, H.; Fan, W.; Zhao, Y.; Chen, B.; Gao, Y.; Chen, X.; Xu, D.; Shi, W. Amorphous Iron (III)-Borate Decorated Electrochemically Treated-$BiVO_4$ Photoanode for Efficient Photoelectrochemical Water Splitting. *Chem. Eng. J.* **2021,** *411*, 128480.

(248) Zhang, B.; Huang, X.; Zhang, Y.; Lu, G.; Chou, L.; Bi, Y. Unveiling the Activity and Stability Origin of $BiVO_4$ Photoanodes with FeNi Oxyhydroxides for Oxygen Evolution. *Angew. Chem. Int. Ed.* **2020,** *59* (43), 18990-18995.

(249) DuChene, J. S.; Sweeny, B. C.; Johnston-Peck, A. C.; Su, D.; Stach, E. A.; Wei, W. D. Prolonged Hot Electron Dynamics in Plasmonic-Metal/Semiconductor Heterostructures with Implications for Solar Photocatalysis. *Angew. Chem. Int. Ed.* **2014,** *53* (30), 7887-7891.

(250) Zhong, M.; Hisatomi, T.; Kuang, Y.; Zhao, J.; Liu, M.; Iwase, A.; Jia, Q.; Nishiyama, H.; Minegishi, T.; Nakabayashi, M. Surface Modification of CoO_x Loaded $BiVO_4$ Photoanodes with Ultrathin P-Type NiO Layers for Improved Solar Water Oxidation. *J. Am. Chem. Soc.* **2015,** *137* (15), 5053-5060.

(251) Chen, Y.; Wang, L.; Gao, R.; Zhang, Y.-C.; Pan, L.; Huang, C.; Liu, K.; Chang, X.-Y.; Zhang, X.; Zou, J.-J. Polarization-Enhanced Direct Z-Scheme ZnO-WO_{3-x} Nanorod Arrays for Efficient Piezoelectric-Photoelectrochemical Water Splitting. *Appl. Catal. B: Environ.* **2019,** *259*, 118079.

(252) Ran, L.; Qiu, S.; Zhai, P.; Li, Z.; Gao, J.; Zhang, X.; Zhang, B.; Wang, C.; Sun, L.; Hou, J. Conformal Macroporous Inverse Opal Oxynitride-Based Photoanode for Robust Photoelectrochemical Water Splitting. *J. Am. Chem. Soc.* **2021,** *143* (19), 7402-7413.

(253) Song, Y.; Zhang, X.; Zhang, Y.; Zhai, P.; Li, Z.; Jin, D.; Cao, J.; Wang, C.; Zhang, B.; Gao, J. Engineering MoO_x/MXene Hole Transfer Layers for Unexpected Boosting of Photoelectrochemical Water Oxidation. *Angew. Chem.* **2022,** *134* (16), e202200946.

(254) Osterloh, F. E. Inorganic Nanostructures for Photoelectrochemical and Photocatalytic Water Splitting. *Chem. Soc. Rev.* **2013,** *42* (6), 2294-2320.

(255) Chen, X.; Shen, S.; Guo, L.; Mao, S. S. Semiconductor-Based Photocatalytic Hydrogen Generation. *Chem. Rev.* **2010,** *110* (11), 6503-6570.

(256) Kronawitter, C. X.; Vayssieres, L.; Shen, S.; Guo, L.; Wheeler, D. A.; Zhang, J. Z.; Antoun, B. R.; Mao, S. S. A Perspective on Solar-Driven Water Splitting with All-Oxide Hetero-Nanostructures. *Energy Environ. Sci.* **2011,** *4* (10), 3889-3899.

(257) Huang, S.; Ouyang, T.; Zheng, B. F.; Dan, M.; Liu, Z. Q. Enhanced Photoelectrocatalytic Activities for CH_3OH-to-HCHO Conversion on Fe_2O_3/MoO_3: Fe-O-Mo Covalency Dominates the Intrinsic Activity. *Angew. Chem. Int. Ed.* **2021**.

(258) He, S.; Yan, C.; Chen, X.-Z.; Wang, Z.; Ouyang, T.; Guo, M.-L.; Liu, Z.-Q. Construction of Core-Shell Heterojunction Regulating A-Fe_2O_3 Layer on CeO_2 Nanotube Arrays Enables Highly Efficient Z-Scheme Photoelectrocatalysis. *Appl. Catal. B: Environ.* **2020,** *276*, 119138.

(259) Marsen, B.; Cole, B.; Miller, E. L. Photoelectrolysis of Water Using Thin Copper Gallium Diselenide Electrodes. *Sol. Energy Mater. Sol. Cells* **2008,** *92* (9), 1054-1058.

(260) Chen, D.; Liu, Z.; Guo, Z.; Yan, W.; Xin, Y. Enhancing Light Harvesting and Charge Separation of Cu_2O Photocathodes with Spatially Separated Noble-Metal Cocatalysts Towards Highly Efficient Water Splitting. *J. Mater. Chem. A* **2018,** *6* (41), 20393-20401.

(261) Chen, Y.; Li, J.-F.; Liao, P.-Y.; Zeng, Y.-S.; Wang, Z.; Liu, Z.-Q. Cascaded Electron Transition in $CuWO_4$/CdS/CDs Heterostructure Accelerating Charge Separation Towards Enhanced Photocatalytic Activity. *Chin. Chem. Lett.* **2020,** *31* (6), 1516-1519.

(262) Ye, Y.-Q.; Gu, G.-H.; Wang, X.-T.; Ouyang, T.; Chen, Y.; Liu, Z.-Q. 3D Cross-Linked BiOI Decorated ZnO/CdS Nanorod Arrays: A Cost-Effective Hydrogen Evolution Photoanode with High Photoelectrocatalytic Activity. *Int. J. Hydrogen Energy* **2019,** *44* (39), 21865-21872.

(263) Wang, X.; Liow, C.; Qi, D.; Zhu, B.; Leow, W. R.; Wang, H.; Xue, C.; Chen, X.; Li, S. Programmable Photo-Electrochemical Hydrogen Evolution Based on Multi-Segmented CdS-Au Nanorod Arrays. *Adv. Mater.* **2014,** *26* (21), 3506-3512.

(264) Zhang, J.; Vasei, M.; Sang, Y.; Liu, H.; Claverie, J. P. TiO_2@ Carbon Photocatalysts: The Effect of Carbon Thickness on Catalysis. *ACS Appl. Mater. Interfaces* **2016,** *8* (3), 1903-1912.

(265) Ma, Q.; Peng, X.; Zhu, M.; Wang, X.; Wang, Y.; Gao, Y.; Wang, H. Enhanced Photoelectrochemical Performance with Plasmon-Induced Hot Electron Injection of Gold Nanoparticle. *J. Phys. D: Appl. Phys.* **2019,** *52* (12), 125503.

(266) Pareek, A.; Thotakuri, R.; Dom, R.; Kim, H. G.; Borse, P. H. Nanostructure Zn–Cu Co-Doped CdS Chalcogenide Electrodes for Opto-Electric-Power and H_2 Generation. *Int. J. Hydrogen Energy* **2017,** *42* (1), 125-132.

(267) Koo, B.; Byun, S.; Nam, S. W.; Moon, S. Y.; Kim, S.; Park, J. Y.; Ahn, B. T.; Shin, B. Reduced Graphene Oxide as a Catalyst Binder: Greatly Enhanced Photoelectrochemical Stability of Cu (In, Ga) Se_2 Photocathode for Solar Water Splitting. *Adv. Funct. Mater.* **2018,** *28* (16), 1705136.

(268) Wei, W.; Tian, Q.; Sun, H.; Liu, P.; Zheng, Y.; Fan, M.; Zhuang, J. Efficient Visible-Light-Driven Photocatalytic H_2 Evolution over $MoO_{2\text{-}C}$/CdS Ternary Heterojunction with Unique Interfacial Microstructures. *Appl. Catal. B: Environ.* **2020,** *260*, 118153.

(269) Pu, Y.-C.; Wang, G.; Chang, K.-D.; Ling, Y.; Lin, Y.-K.; Fitzmorris, B. C.; Liu, C.-M.; Lu, X.; Tong, Y.; Zhang, J. Z. Au Nanostructure-Decorated TiO_2 Nanowires Exhibiting Photoactivity across Entire UV-Visible Region for Photoelectrochemical Water Splitting. *Nano Lett.* **2013,** *13* (8), 3817-3823.

(270) Guan, P.; Bai, H.; Wang, F.; Yu, H.; Xu, D.; Fan, W.; Shi, W. In-Situ Anchoring Ag through Organic Polymer for Configuring Efficient Plasmonic $BiVO_4$ Photoanode. *Chem. Eng. J.* **2019,** *358*, 658-665.

(271) Zheng, B.-F.; Ouyang, T.; Wang, Z.; Long, J.; Chen, Y.; Liu, Z.-Q. Enhanced Plasmon-Driven Photoelectrocatalytic Methanol Oxidation on Au Decorated a-Fe_2O_3 Nanotube Arrays. *Chem. Commun.* **2018,** *54* (69), 9583-9586.

(272) Wei, R.-B.; Kuang, P.-Y.; Cheng, H.; Chen, Y.-B.; Long, J.-Y.; Zhang, M.-Y.; Liu, Z.-Q. Plasmon-Enhanced Photoelectrochemical Water Splitting on Gold Nanoparticle Decorated ZnO/CdS Nanotube Arrays. *ACS Sustain. Chem. Eng.* **2017,** *5* (5), 4249-4257.

(273) Pocklanova, R.; Rathi, A. K.; Gawande, M. B.; Datta, K. K. R.; Ranc, V.; Cepe, K.; Petr, M.; Varma, R. S.; Kvitek, L.; Zboril, R. Gold Nanoparticle-Decorated Graphene Oxide: Synthesis and Application in Oxidation Reactions under Benign Conditions. *J. Mol. Catal. A: Chem.* **2016,** *424*, 121-127.

(274) Huang, K.; Li, C.; Zhang, X.; Meng, X.; Wang, L.; Wang, W.; Li, Z. TiO_2 Nanorod Arrays Decorated by Nitrogen-Doped Carbon and g-C_3N_4 with Enhanced Photoelectrocatalytic Activity. *Appl. Surf. Sci.* **2020**, 146219.

(275) Fan, K.; Chen, H.; He, B.; Yu, J. Cobalt Polyoxometalate on N-Doped Carbon Layer to Boost Photoelectrochemical Water Oxidation of $BiVO_4$. *Chem. Eng. J.* **2020,** *392*, 123744.

(276) Sun, X.; Jiang, J.; Yang, Y.; Shan, Y.; Gong, L.; Wang, M. Enhancing the Performance of Si-Based Photocathodes for Solar Hydrogen Production in Alkaline Solution by Facilely Intercalating a Sandwich N-Doped Carbon Nanolayer to the Interface of Si and TiO_2. *ACS Appl. Mater. Interfaces* **2019,** *11* (21), 19132-19140.

(277) Chung, D. Y.; Jun, S. W.; Yoon, G.; Kim, H.; Yoo, J. M.; Lee, K.-S.; Kim, T.; Shin, H.; Sinha, A. K.; Kwon, S. G. Large-Scale Synthesis of Carbon-Shell-Coated FeP Nanoparticles for Robust Hydrogen Evolution Reaction Electrocatalyst. *J. Am. Chem. Soc.* **2017,** *139* (19), 6669-6674.

(278) Dzhagan, V.; Valakh, M. Y.; Raevskaya, A.; Stroyuk, A.; Kuchmiy, S. Y.; Zahn, D. Resonant Raman Scattering Study of CdSe Nanocrystals Passivated with CdS and ZnS. *Nanotechnology* **2007,** *18* (28), 285701.

(279) Ferrari, A. C.; Robertson, J. Interpretation of Raman Spectra of Disordered and Amorphous Carbon. *Phys. Rev. B* **2000,** *61* (20), 14095.

(280) Sim, U.; Yang, T.-Y.; Moon, J.; An, J.; Hwang, J.; Seo, J.-H.; Lee, J.; Kim, K. Y.; Lee, J.; Han, S. N-Doped Monolayer Graphene Catalyst on Silicon Photocathode for Hydrogen Production. *Energy Environ. Sci.* **2013,** *6* (12), 3658-3664.

(281) Chen, D.; Dai, S.; Su, X.; Xin, Y.; Zou, S.; Wang, X.; Kang, Z.; Shen, M. N-Doped Nanodots/Np^+-Si Photocathodes for Efficient Photoelectrochemical Hydrogen Generation. *Chem. Commun.* **2015,** *51* (83), 15340-15343.

(282) Li, H.; Shen, L.; Yin, K.; Ji, J.; Wang, J.; Wang, X.; Zhang, X. Facile Synthesis of N-Doped Carbon-Coated $Li_4Ti_5O_{12}$ Microspheres Using Polydopamine as a Carbon Source for High Rate Lithium Ion Batteries. *J. Mater. Chem. A* **2013,** *1* (24), 7270-7276.

(283) Wei, Y.; Kong, J.; Yang, L.; Ke, L.; Tan, H. R.; Liu, H.; Huang, Y.; Sun, X. W.; Lu, X.; Du, H. Polydopamine-Assisted Decoration of ZnO Nanorods with Ag Nanoparticles: An Improved Photoelectrochemical Anode. *J. Mater. Chem. A* **2013,** *1* (16), 5045-5052.

(284) Sun, L.; He, X.; Zeng, S.; Yuan, Y.; Li, R.; Zhan, W.; Chen, J.; Wang, X.; Han, X. Double Insurance of Continuous Band Structure and N-C Layer Induced Prolonging of Carrier Lifetime to Enhance the Long-Wavelength Visible-Light Catalytic Activity of N-Doped In_2O_3. *Inorg. Chem.* **2021,** *60* (2), 1160-1171.

(285) Hagfeldt, A.; Lindström, H.; Södergren, S.; Lindquist, S.-E. Photoelectrochemical Studies of Colloidal TiO_2 Films: The Effect of Oxygen Studied by Photocurrent Transients. *J. Electroanal. Chem.* **1995,** *381* (1-2), 39-46.

(286) Tafalla, D.; Salvador, P.; Benito, R. Kinetic Approach to the Photocurrent Transients in Water Photoelectrolysis at N-TiO_2 Electrodes: Ii. Analysis of the Photocurrent-Time Dependence. *J. Electrochem. Soc.* **1990,** *137* (6), 1810.

(287) Kumar, D. P.; Hong, S.; Reddy, D. A.; Kim, T. K. Ultrathin MoS_2 Layers Anchored Exfoliated Reduced Graphene Oxide Nanosheet Hybrid as a Highly Efficient Cocatalyst for CdS Nanorods Towards Enhanced Photocatalytic Hydrogen Production. *Appl. Catal. B: Environ* **2017,** *212*, 7-14.

(288) Iqbal, S.; Pan, Z.; Zhou, K. Enhanced Photocatalytic Hydrogen Evolution from in Situ Formation of Few-Layered MoS_2/CdS Nanosheet-Based Van Der Waals Heterostructures. *Nanoscale* **2017,** *9* (20), 6638-6642.

(289) Courtin, J.; Le Gall, S.; Chrétien, P.; Moréac, A.; Delhaye, G.; Lépine, B.; Tricot, S.; Turban, P.; Schieffer, P.; Le Breton, J.-C. A Low Schottky Barrier Height and Transport Mechanism in Gold–Graphene–Silicon (001) Heterojunctions. *Nanoscale Advances* **2019,** *1* (9), 3372-3378.

(290) Quang, N. D.; Majumder, S.; Kim, C.; Kim, D. Incorporation of an Au-Rgo Layer to Enhance the Photocatalytic Application of Optimized CdS Thin Film. *J. Electrochem. Soc.* **2019,** *166* (5), H3112.

(291) Jing, L.; Zhou, J.; Durrant, J. R.; Tang, J.; Liu, D.; Fu, H. Dynamics of Photogenerated Charges in the Phosphate Modified TiO_2 and the Enhanced Activity for Photoelectrochemical Water Splitting. *Energy Environ. Sci.* **2012,** *5* (4), 6552-6558.

(292) Han, X.; Wei, Y.; Su, J.; Zhao, Y. Low-Cost Oriented Hierarchical Growth of $BiVO_4$/RGO/NiFe Nanoarrays Photoanode for Photoelectrochemical Water Splitting. *ACS Sustainable Chem. Eng.* **2018,** *6* (11), 14695-14703.

(293) Zheng, X.; Han, H.; Liu, J.; Yang, Y.; Pan, L.; Zhang, S.; Meng, S.; Chen, S. Sulfur Vacancy-Mediated Electron–Hole Separation at MoS_2/CdS Heterojunctions for Boosting Photocatalytic N_2 Reduction. *ACS Appl. Energy Mater.* **2022,** *5* (4), 4475-4485.

(294) Liu, H.; Tan, P.; Liu, Y.; Zhai, H.; Du, W.; Liu, X.; Pan, J. Ultrafast Interfacial Charge Evolution of the Type-II Cadmium Sulfide/Molybdenum Disulfide Heterostructure for Photocatalytic Hydrogen Production. *J. Colloid Interface Sci.* **2022,** *619*, 246-256.

(295) Zhao, H.; Fu, H.; Yang, X.; Xiong, S.; Han, D.; An, X. MoS_2/CdS Rod-Like Nanocomposites as High-Performance Visible Light Photocatalyst for Water Splitting Photocatalytic Hydrogen Production. *Int. J. Hydrogen Energy* **2022**.

(296) Liu, C.; Ma, J.; Zhang, F.-J.; Wang, Y.-R.; Kong, C. Facile Formation of Mo-Vacancy Defective MoS_2/CdS Nanoparticles Enhanced Efficient Hydrogen Production. *Colloids Surf. Physicochem. Eng. Aspects* **2022,** *643*, 128743.

(297) Xu, J.; Yan, X.; Qi, Y.; Fu, Y.; Wang, C.; Wang, L. Novel Phosphidated MoS_2 Nanosheets Modified CdS Semiconductor for an Efficient Photocatalytic H_2 Evolution. *Chem. Eng. J.* **2019,** *375*, 122053.

(298) Tian, H.; Liang, J.; Ma, X.; Cao, L.; Hu, X.; Gao, M.; Yang, H.; Liang, Z. Enhanced Photoelectrocatalytic H_2 Evolution over Two-Dimensional MoS_2 Nanosheets Loaded on Cu-Doped CdS Nanorods. *ChemElectroChem* **2019,** *6* (3), 714-723.

(299) Lv, P.; Fu, W.; Yang, H.; Sun, H.; Chen, Y.; Ma, J.; Zhou, X.; Tian, L.; Zhang, W.; Li, M. Simple Synthesis Method of Bi_2S_3/CdS Quantum Dots Cosensitized TiO_2 Nanotubes Array with Enhanced Photoelectrochemical and Photocatalytic Activity. *CrystEngComm* **2013,** *15* (37), 7548-7555.

(300) Zhang, J.; Wang, L.; Liu, X.; Li, X. a.; Huang, W. High-Performance CdS–ZnS Core–Shell Nanorod Array Photoelectrode for Photoelectrochemical Hydrogen Generation. *J. Mater. Chem. A* **2015,** *3* (2), 535-541.